

TEM STUDY OF INTERFACIAL REACTIONS AND PRECIPITATION MECHANISMS IN Al_2O_3 SHORT FIBERS OR SiC PARTICLES REINFORCED Al-4Cu-1Mg-0.5Ag SQUEEZE-CAST COMPOSITES

THÈSE N° 2246 (2000)

PRÉSENTÉE AU DÉPARTEMENT DES MATÉRIAUX

ÉCOLE POLYTECHNIQUE FÉDÉRALE DE LAUSANNE

POUR L'OBTENTION DU GRADE DE DOCTEUR ÈS SCIENCES TECHNIQUES

PAR

Cyril CAYRON

Ingénieur civil des Mines, Ecole des Mines Nancy, DEA en physique des matériaux, Faculté de Nancy, France
de nationalité française

acceptée sur proposition du jury:

Prof. P.A. Buffat, directeur de thèse
Dr O. Beffort, rapporteur
Prof. Y. Brechet, rapporteur
Prof. A. Châtelain, rapporteur
Dr L. Sagalowicz, rapporteur

Lausanne, EPFL
2000

Contents

List of Acronyms	vii
Summary	viii
Version abrégée	x
Chapter 1 Introduction	1
1.1 General Context	1
1.2 Outline.....	2
Chapter 2 Aluminum Matrix Composites: Processing and Properties	5
2.1 Introduction to AMCs	6
2.1.1 Composites	6
2.1.2 Aluminum Matrix Composites (AMCs)	6
2.1.3 Fabrication of the AMCs.....	8
2.2 Mechanical Properties of the AMCs.....	8
2.2.1 Elasticity.....	8
2.2.2 Yielding / Flow.....	10
2.2.3 Fracture.....	11
2.2.4 Conclusions: Influence of the Microstructural Variables	13
2.3 The AlCuMgAg Based Composites.....	13
2.3.1 Materials.....	13
2.3.2 Direct Squeeze-Casting Process.....	15
2.3.3 Tensile Properties.....	16
2.4 Discussion	20

Chapter 3 Transmission Electron Microscopy	21
3.1 Historical Introduction	22
3.2 Preparation of the TEM Samples	22
3.3 Chemical Analyses by EDS	23
3.4 Electron Scattering: From Diffusion to Diffraction	25
3.4.1 Diffusion.....	25
3.4.2 Kinematical Diffraction.....	28
3.4.3 Bragg Law	30
3.4.4 Ewald Construction	30
3.4.5 Dynamical Diffraction.....	31
3.5 Conventional Transmission Electron Microscopy	31
3.5.1 Imaging Mode	31
3.5.2 Diffraction Mode.....	33
3.5.3 Special TEM Techniques	34
3.6 High Resolution Transmission Microscopy	35
3.6.1 Propagation through the sample	35
3.6.2 Transfer by the optical system	36
3.7 Quantitative Electron Crystallography.....	39
3.7.1 Phase Loss Problem in Diffraction.....	39
3.7.2 HREM “Direct” Methods.....	39
3.7.3 HREM Simulations	41
3.8 TEM Facilities.....	41
Chapter 4 Microstructure of WFA/Al₂O₃/sf and WFA/SiC/p Composites	43
4.1 Grains and Microsegregation	44
4.1.1 Grain Sizes and Morphologies	44
4.1.2 Primary Intermetallics Compounds.....	45
4.1.3 Chemical Composition of the Matrices.....	48
4.2 Interfacial Reactions	48
4.2.1 WFA/Al ₂ O ₃ /sf/s Composites.....	48
4.2.2 WFA/SiC/p Composites	50
4.2.3 Al(Mg)/SiC/p Composites.....	53
4.2.4 Diffusion of Si, Mg and Cu.....	57
4.3 Precipitation States.....	57
4.3.1 Hardness Curves	58
4.3.2 Modification of the Precipitation State	59
4.4 Identification of the Precipitates	61
4.4.1 θ' Plate-Shaped Precipitates	61

Contents

4.4.2 Rod-Shaped Precipitates	64
4.4.3 Evolution of the Precipitation by Overaging at 300°C/24h	68
4.5 Conclusions and Prospects	71
4.5.1 Grains and Microsegregation	71
4.5.2 Chemistry and Precipitation Modification of the Base Alloy	71
4.5.3 Effect of Binder on the WFA/Al ₂ O ₃ /sf AMC Tensile Properties	72
4.5.4 Prospects for the Improvements of Tensile Properties.....	74
Chapter 5 Introduction to Order-Disorder Transitions	77
5.1 Classification of the Phase Transitions	78
5.1.1 Chemistry	78
5.1.2 Thermodynamics.....	78
5.2 Landau's Phenomenological Approach	79
5.2.1 Second Order Transitions.....	80
5.2.2 First Order Transitions	80
5.3 Statistical Mechanics Approach.....	82
5.3.1 Canonical Ensembles	82
5.3.2 The Ising Model	82
5.3.3 Monte Carlo Simulations	83
5.3.4 Phase Diagrams	84
5.4 Ordering in Binary Alloys.....	86
5.4.1 Equivalence with the Ising Model.....	86
5.4.2 Order Parameters.....	86
5.4.3 Approximate Methods.....	88
5.5 Scattering and HREM Images of Disordered Particles.....	91
5.5.1 Diffuse Scattering and Disorder	91
5.5.2 Diffuse Scattering Simulations.....	93
5.5.3 Filtered HREM Images	93
5.5.4 Dark Field Superstructure Images.....	95
Chapter 6 Order-Disorder Transition in AlCuMgSi and AlMgSi Alloys ..	97
6.1 Structural Phase Transition in the AlCuMgSi Alloys.....	98
6.1.1 TEM Observations of the QP, QC and Q Phases.....	98
6.1.2 Link between the QP/QC/Q Lattices.....	99
6.1.3 Confirmation of the Structural Transition between the QP/QC/Q Phases	103
6.2 Structural Transition Model	105
6.2.1 Q structure: Sub-Unit Clusters and qh-Lattice.....	105
6.2.2 Difference between Q and Q'	108

Contents

6.2.3 Application of the Structural Model to the AlMgSi Alloys	109
6.3 Crystallographic Structures of the QC and β' Phases	111
6.3.1 Similarities between the QC and β' Phases	112
6.3.2 Microdiffraction and Computing Details	114
6.3.3 Basic Ideas about the Structures.....	115
6.3.4 Structural Refinements.....	116
6.3.5 Verification of the Structures by HREM.....	120
6.3.6 Discussion	121
6.3.7 First conclusions.....	124
6.4 Ordering Processes during the Precipitation.....	124
6.4.1 Monte Carlo Simulations	124
6.4.2 Ground State Problem	128
6.4.3 As-Cast State: Kinetics Effect.....	130
6.4.4 T6 State: Size Effect.....	130
6.5 Conclusion and Prospects	133
Chapter 7 Conclusions	137
Bibliography	139

Annex A Electronic Diffusion Factor, Radial Potential	147
A.1 Inversion of the Diffusion Factor Formula	147
A.2 Radial Atomic Potentials Deduced from Diffusion Factors Fit	148
A.3 Calculus of the Projected Potentials.....	149
A.4 Projected Atomic Potential Deduced from Diffusion Factors Fit.....	149
A.5 References	150
Annex B Precipitation in the 2xxx and 6xxx Aluminum Alloys	153
B.1 Precipitation in the 2xxx Alloys	153
B.1.1 In the AlCu Alloys.....	153
B.1.2 In the AlCuMg Alloys	154
B.1.3 In the AlCuMgAg Alloys	156
B.2 Precipitation in the 6xxx Alloys.....	157
B.2.1 Without Si in Excess.....	157
B.2.2 With Si in Excess.....	159
B.3 Precipitation in the AlCuMgSi Alloys	160
B.4 References	161
Annex C Simulation of Diffraction of Orientated Precipitates	165
C.1 Notions of Crystallography	165
C.1.1 Punctual Groups	165
C.1.2 Space Groups.....	165
C.1.3 Reciprocals Spaces and Associated Matrices	165
C.2 Simulation Program.....	166
C.3 References	168
Remerciements	169
Curriculum Vitae	171
Scientific Publications	173

List of Acronyms

APFIM	atom probe field ion microscopy
AMC	aluminum matrix composite
BCC	body-centered cubic
BF	bright field
CBED	convergent beam electron diffraction
CCD	charge-coupled device
CTE	coefficient of thermal expansion
CTF	contrast transfer function
DF	dark field
DSTEM	dedicated scanning transmission electron microscopy
EDS	energy dispersive spectrometry
EELS	electron energy loss spectroscopy
FCC	face-centered cubic
FEG	field emission gun
FEM	finite elements model
FFT	fast Fourier transform
GPI	gas pressure infiltration
GPZ	Guinier-Preston zone
GPBZ	Guinier-Preston-Bagaryatsky zone
HOLZ	high-order Laue zone
HREM	high resolution electron microscopy
LRO	long-range order
MMC	metal matrix composite
P/M	powder metallurgy
OR	orientation relationship
PFZ	precipitate-free zone
PS	power spectrum (modulus part of the FFT)
ROM	rule of mixture
SAED	selected area electron diffraction
SC	simple cubic
SEM	scanning electron microscopy
SQC	squeeze-casting
SRO	short-range order
TEM	transmission electron microscopy
WFA	Al-4Cu-1Mg-0.5Ag (notation in this work)
WP	whole pattern (ZOLZ + HOLZ)
ZOLZ	zero-order Laue zone

Summary

After more than a quarter of a century of active research, metal matrix composites (MMCs), and more particularly aluminum matrix composites (AMCs), are beginning to make a significant contribution to aerospace, automotive, and electronic industrial practice. This is the consequence of progresses in the development of processing techniques, and the result of advances in the understanding of the relationship between composite structure and mechanical behavior.

In the present work, two kinds of AMCs were elaborated by direct squeeze-casting for the assessment of their mechanical performance in view of potential applications for the automobile and electronic industry. They are based on a specifically designed precipitation hardening Al-4Cu-1Mg-0.5Ag alloy chosen for its promising mechanical properties at temperatures up to 200°C. Al₂O₃ Saffil short fibers (15%-vol) on the one hand and SiC particles (60%-vol) on the other hand act as reinforcements. In the aim of a better understanding of the mechanical properties of the composites, their microstructure has been studied by transmission electron microscopy (TEM).

The grain morphology and size, microsegregation and precipitation states of the composites have been investigated and compared with those of the unreinforced matrix alloy. Microsegregation, mainly of Al₂Cu, Al₇Cu₂Fe and Q-Al₅Cu₂Mg₈Si₆ phases, is observed in the as-cast composites at the interfaces between the matrix and the reinforcements. However, a solution heat treatment at 500°C for 2 hours leads to a significant dissolution of these phases. Although the unreinforced alloy was free of Si, this element is detected in the matrices of both composites. After a TEM study of the interfaces, it was deduced that Si is released from different interfacial reactions: (i) for the Al₂O₃ reinforced composites, from a reaction between the Mg from the matrix alloy and the SiO₂ from the Saffil fibers and the silica binder of the preform, and (ii) for the SiC reinforced composites, from a direct reaction between Al and the SiC particles with an indirect but important contribution of Mg to the reaction kinetics.

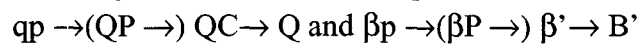
As consequence of the chemical modification of the alloy, the precipitation state in the matrices of the composites has drastically changed. It was shown by energy dispersive spectrometry chemical analyses (EDS), high resolution electron microscopy (HREM), dedicated scanning transmission electron microscopy (DSTEM) and microdiffraction techniques that the usual Ω and S' hardening phases of the matrix alloy are substituted by a fine and dense precipitation of nano-sized QP rods and θ' plates. The θ' plates lie on nano-sized rod-shaped precipitates identified as Si phase in the Al₂O₃ short fiber reinforced composite, and as QC phase in the SiC particle reinforced composite. The QP and QC phases are shown to be precursors of the stable Q-Al₅Cu₂Mg₈Si₆ phase. They have both a hexagonal structure with $a = 0.393$ nm and $c = 0.405$ nm, and with $a = 0.675$ nm and $c = 0.405$ nm, respectively for QP and QC.

Summary

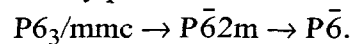
A structural phase transition between the QP, QC, Q rod-shaped precipitates in the matrices of the composites is observed and studied by TEM, DF superstructure imaging and in-situ experiment techniques. The details of this transition are shown to bring a new understanding to the precipitation mechanisms in the 6xxx alloys (AlMgSi alloys) in general. These ones are widely used as medium-strength structural alloys. The structures of the metastable phases that precipitate in these alloys have been largely described in literature, but the precipitation mechanisms at atomic scale has not been well understood so far.

In the present work, a model is developed from the crystallographic structure of the stable Q-phase determined by X-ray. It describes the QP, QC and Q structures as superordered structures formed by an order-disorder transition from a primitive phase named qp. The model predicts that a similar transition exists between all the metastable phases in the 6xxx alloys (β'' , β' , B', type-A, type-B). For example, β' is supposed to be structurally similar to QC, with Si substituting Cu in the unit-cell. The latent lattices implied in the transitions are noted QP and βP for the matrices of the composites (AlCuMgSi alloys) and for the 6xxx alloys respectively. Microdiffraction patterns and superstructure DF images acquired on a CCD camera confirm the similarity between the QC and β' phases. After refinement by comparison between the experimental and computed microdiffraction patterns, their crystallography is found to be hexagonal $P\bar{6}2m$.

Eventually, according to the model, the structural transitions in the AlCuMgSi and AlMgSi alloys are found to respectively follow the sequences



corresponding to the breaking symmetry path



This sequence is respected during the cooling of the materials from the liquid state, and structurally mixed precipitates can be observed in the as-cast state, due to the slow kinetics of the transition (order/disorder transition). This sequence is also respected during the aging of the materials, since the small size of the precipitates is expected to reduce the critical temperature of transition. Monte Carlo simulations on an Ising lattice are computed to illustrate and confirm those effects.

Version abrégée

Après plus d'un quart de siècle de recherche intense, les composites à matrices métalliques (CMM), et particulièrement les composites à matrice aluminium (CMA), prennent une place de plus en plus importante dans les réalisations des industries spatiales, automobiles et électroniques. Ceci résulte d'une part des derniers développements des méthodes d'élaboration, et d'autre part d'une compréhension de plus en plus approfondie des relations qui existent entre leur microstructure et leur comportement mécanique.

Dans ce travail, deux types de composites à matrice métallique ont été élaborés par moulage sous pression pour évaluer leurs performances mécaniques pour certaines applications dans l'industrie automobile et électronique. Ils sont basés sur un alliage Al-4Cu-1Mg-0.5Ag, habituellement durci par la précipitation des phases W et S' et choisi pour ses excellentes propriétés mécaniques jusqu'à des températures de 200°C. Ils sont renforcés avec des fibres courtes d'Al₂O₃ (15%-vol) ou des particules de SiC (60%-vol). Pour mieux comprendre leurs propriétés mécaniques, leur microstructure a été étudiée par microscopie électronique en transmission (MET).

La morphologie des grains, leurs tailles et la microségrégation dans les composites ont été observées et comparées avec celles de l'alliage non renforcé. La microségrégation, principalement constituée de phases Al₂Cu, Al₇Cu₂Fe et Q-Al₅Cu₂Mg₈Si₆ a été réduite de manière significative par le traitement thermique à 500°C pendant 2 hrs. Bien qu'absent de l'alliage de départ, du Si a été détecté dans les matrices des composites. Après une étude MET des précipités aux interfaces, il a été déduit que le Si provient de différentes réactions d'interface: (1) pour les composites aux renforts Al₂O₃, d'une réaction entre le Mg de l'alliage et le SiO₂ présent dans les fibres et dans le liant si un liant silice a été utilisé, et (2) pour les composites aux renforts SiC, d'une réaction entre l'Al et les particules de SiC avec un rôle indirect mais important du Mg sur la cinétique.

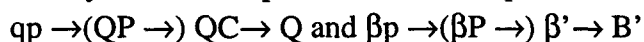
Par suite de la modification de la composition chimique de l'alliage, l'état de précipitation dans les matrices des composites a été complètement changé. Il a notamment été montré par des analyses chimiques par spectrométrie dispersive en énergies, par microscopie électronique haute résolution (MEHR), par microscopie à balayage en transmission et par microdiffraction, que la précipitation de Ω et S', habituellement rencontrée dans l'alliage, a été remplacée par une précipitation fine et dense de bâtonnets QP et de plaquettes θ' de tailles nanométriques. Les plaquettes de θ' reposent sur des précipités en forme de bâtonnet identifiés comme étant de la phase Si dans les composites renforcés par Al₂O₃ et comme étant de la phase QC phase dans les composites renforcés par les SiC. Il a été montré que les phases QP et QC sont les précurseurs de la phase stable Q-Al₅Cu₂Mg₈Si₆. Ils ont tous les deux une structure

hexagonale, avec respectivement $a = 0.393$ nm et $c = 0.405$ nm, et avec $a = 0.675$ nm et $c = 0.405$ nm. Durant ce travail des suggestions ont été faites pour améliorer les propriétés mécaniques des composites étudiés.

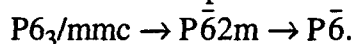
Les alliages 6xxx, c.a.d les alliages AlMgSi(Cu), sont largement répandus comme alliages structuraux à contrainte moyenne. Ils présentent les avantages cumulés d'une bonne soudabilité, de résistance à la corrosion, notamment à la corrosion sous contraintes. Ils sont utilisés en majorité pour les extrusions, avec de petites quantités disponibles pour les feuilles et les plaques. La structure des phases métastables qui précipitent dans ces alliages sont largement décrites dans la littérature, mais les mécanismes de précipitation à l'échelle atomique restent inconnus.

Dans ce travail, après des études par MET, par des images de superstructure en champ sombre et par des expériences in-situ, nous avons reporté l'existence d'une transition structurale entre les phases QP, QC et Q précipitées sous forme de bâtonnet dans les matrices des composites. Il a été montré que cette transition de phase apporte une compréhension nouvelle aux mécanismes de précipitation dans les alliages 6xxx en général. En effet, un modèle a été développé sur la base de la structure cristallographique de la phase stable Q déterminée par rayons X. Il décrit les phases QP, QC et Q comme des structures super-ordonnées d'une phase primitive appelée qp. Le modèle a prédit l'existence d'une transition similaire entre les phases métastables des alliages 6xxx (β'' , β' , B', type-A, type-B). Par exemple, la phase β' est supposée avoir une structure similaire à QC, avec du Si remplaçant le Cu dans la maille primitive. Les réseaux latents mis en jeu dans les transitions ont respectivement été notés QP et βP pour les matrices des composites (alliages AlCuMgSi) et pour les alliages 6xxx (alliages AlMgSi). Des clichés de microdiffraction obtenus sur caméra CCD ainsi que des images de superstructures en champ sombre ont permis de confirmer la similarité des phases QC et β' . Après raffinement par comparaison entre les clichés de microdiffraction expérimentaux et simulés, il a été trouvé que leur cristallographie est hexagonale $P\bar{6}2m$.

Finalement, selon notre modèle, les transitions structurales dans les alliages AlCuMgSi et AlMgSi alloys suivent respectivement les séquences



celles-ci correspondant à un cheminement en pertes de symétrie



La séquence a été respectée durant le refroidissement des matériaux depuis l'état liquide, et des structures mixtes ont pu être observées dans les états bruts, ceci parce que la cinétique de transition est lente (transition ordre/désordre). La séquence a aussi été respectée durant le vieillissement des matériaux, et ceci probablement parce que la petite taille des précipités abaisse la température critique de transition. Des simulations Monte Carlo sur un réseau d'Ising ont été programmées pour illustrer ces effets.

Chapter 1

Introduction

1.1 General Context

After more than a quarter of a century of active research, metal matrix composites (MMCs), and more particularly aluminum matrix composites (AMCs), are beginning to make a significant contribution to aerospace, automotive, and electronic industrial practice [1, 2, 3]. On the one hand, this is the consequence of developments in processing methods, and on the other hand, the result of advances in the understanding of the relationship between structure and mechanical behavior.

Two kinds of AMCs have been elaborated by direct squeeze-casting (SQC) at EMPA-Thun within the framework of a feasibility project [4]. The composites are based on an Al-4Cu-1Mg-0.5Ag aluminum alloy (called WFA hereafter) selected for its promising mechanical properties at high temperatures (up to 200°C) [5, 6]. The composites are reinforced with:

- (1) Al_2O_3 short fibers (15 vol-%) bounded by
 - (a) a SiO_2 binder (noted *s*)
 - (b) a Al_2O_3 binder (noted *a*)
- (2) SiC particles (60 vol-%).

The composites are denoted WFA/ Al_2O_3 /sf/s, WFA/ Al_2O_3 /sf/a and WFA/ SiC /p respectively.

The first part of the present work is devoted to the transmission electron microscopy (TEM) study of the microstructural parameters that affect the mechanical behavior of these two kinds of composites, i.e. the nature of the matrix/reinforcement interfaces and the modification of the matrix precipitation. Other parameters such as the matrix residual stresses and the matrix dislocations generated by thermal mismatches [1, 2, 7] are not considered in this work.

The second part is devoted to the TEM study of the rod-shaped precipitates appearing in the matrices of the composites as a consequence of chemical modifications. It will be shown that they are structurally identical to those present in 6xxx series commercial alloys (AlMgSiCu alloys) [8]. The structures of the metastable hardening phases have been

extensively described in literature [9], but the precipitation mechanisms at atomic scale remain unknown so far. A structural phase transition between the rod-shaped precipitates in the matrices of the composites and in a AlMgSi alloy will be demonstrated and studied by TEM. The aim of this second part is to bring a new understanding to the precipitation mechanisms in the AlMgSi(Cu) alloys in general.

1.2 Outline

The first part of the present work deals with the microstructure of composites.

Chapter 2 gives a brief introduction to AMCs; it describes their history and elaboration processes, and discusses their mechanical behavior and related models. It treats particularly the WFA/Al₂O₃/sf and WFA/SiC/p composites. The SQC process parameters used for their fabrication, the nature of the alloy and of the reinforcement components are detailed. The aim of chapter 2 is to evidence that the understanding of the mechanical properties of the composites requires a profound knowledge of their microstructure, and more particularly, of their interface and precipitation states.

Chapter 3 introduces the principles of classical TEM. It begins with a brief introduction to TEM history and describes the TEM sample preparation. The energy dispersive spectrometry (EDS) is succinctly presented. After a theoretical approach to electron diffraction physics, the chapter treats some of the conventional TEM techniques such as bright field and dark field imaging (BF and DF), selected area and convergent diffraction (SAED and CBED). High resolution electron microscopy (HREM) is introduced in a separate section. It is discussed how this technique combined with diffraction can be used to get crystallographic information. The aim of chapter 3 is to present all the TEM concepts and techniques that will be used to study the microstructure of the composites.

Chapter 4 presents the results of the microstructural investigations on the WFA/Al₂O₃/sf and WFA/SiC/p composites. It begins with a description of the grain sizes, microsegregation and primary intermetallic compounds. The interfacial reaction products are identified by TEM and the thermodynamics of the reactions, particularly in the WFA/SiC/p composites, are discussed. These interfacial reactions are shown to modify the chemical composition of the matrix alloy, and, in consequence, to affect the precipitation state of the composite matrices. Particular rod-shaped precipitates are observed and identified by EDS, TEM and HREM. The influence of the microstructural features on the composites' mechanical behavior is qualitatively discussed at the end of the chapter.

The second part of the present work deals with the description of a phase transition governing the precipitation of the rod-shaped precipitates.

Chapter 5 introduces the physics of order-disorder transitions. After giving a classification of the phase transitions, it presents two approaches: the Landau

phenomenological and the statistical mechanics approaches. The later includes the Ising model and the Monte Carlo simulations, and is used to present the order-disorder transition in binary alloys and to define the order parameters. The end of chapter 5 briefly discusses the effect of disorder on TEM and HREM images. The aim of this chapter is to introduce the main ideas, vocabulary and tools concerning the order-disorder phase transitions.

Chapter 6 begins by proving the existence of a structural phase transition between the rod-shaped precipitates. An atomistic model is then devised; it describes the transition as an order-disorder one and explains the many different structures of the metastable phases present in the commercial 6xxx alloy series (AlMgSiCu alloys). One of the direct application is to propose a crystallographic structure for some of these phases in quantitative agreement with TEM diffraction experiments. After a simplification of the model, Monte Carlo simulations on an Ising model are performed to illustrate the ordering processes in these precipitates. Chapter 6 concludes with a complete description of the model and by some experiments that could be done to validate the model.

Chapter 7 concludes the work on its two fundamental sides: the microstructure of the composites and the precipitation mechanisms in the AlMgSi(Cu) alloys.

Some annexes are given at the end of the work. Annex A deals with the formulae found to link the projected atomic potentials to the atomic diffusion factors. Annex B reports the earlier studies about the structures of the precipitates in the 2xxx alloys and in the 6xxx alloys. Annex C gives the crystallographic basis used to develop a program simulating SAED patterns of precipitates in orientation relationship (OR) with a matrix.

A reader in hurry can directly go to chapter 4 if he/she is interested in the microstructure of the composites, or to chapter 6 if he/she is interested in the precipitation in the AlMgSi(Cu) alloys, and refer to the other chapters and annexes if he/she needs some physical knowledge to follow his/her reading.

1.2. Outline

Chapter 2

Aluminum Matrix Composites:

Processing and Properties

The aim of this chapter is to show that the understanding of the mechanical properties of the WFA/Al₂O₃/sf and WFA/SiC/p composites requires a deep characterization of their microstructure. Section 2.1 presents the concepts related to the MMCs, particularly to the discontinuously reinforced AMCs (definitions, history, fabrication processes). Section 2.2 gives an introduction to the mechanical properties basis of AMCs. It will be shown that the existing models are efficient for the elastic behavior of the AMCs (even for misoriented short fibers composites), but are inaccurate to describe the plastic deformation due the complexity of the correlated mechanisms of deformation. Section 2.3 presents more particularly the WFA/Al₂O₃/sf and WFA/SiC/p composites (fabrication process and mechanical properties). The comparison between the results obtained for these AMCs and the general concepts of the sections 2.1 and 2.2 are discussed in section 2.4. It will be shown that the precipitation state and the nature of the interfaces play a key role in the mechanical behavior of the WFA/Al₂O₃/sf and WFA/SiC/p composites respectively.

2.1 Introduction to AMCs

2.1.1 Composites

The possibility of taking advantage of particular properties of the constituent materials to meet specific demands is the most important motivation for the development of composites. A composite is a material made with several different constituents intimately bonded. This definition is very large, and includes a lot of materials such as the Roman ways (constituted of different layers of stones, chalk and sand), wood, human body etc... A more restrictive definition is used by industries and materials scientists: a composite is a material that consists of constituents produced via a physical combination of pre-existing ingredient materials to obtain a new material with unique properties when compared to the monolithic material properties. This definition distinguishes a composite from other multiphase materials which are produced by bulk processes where one or more phases result from phase transformation ("in-situ" composites).

The terms *matrix* and *reinforcement* are often used. The matrix is a percolating "soft" phase (with in general excellent ductility, formability and thermal conductivity) in which are embedded the "hard" reinforcements (high stiffness and low thermal expansion). The reinforcements can be continuous or discontinuous, orientated or disorientated. The composites are classified by: (1) their matrix (polymer, ceramic, metal), (2) their reinforcement, which includes the chemical nature (oxides, carbides, nitrides), shape (continuous fibers, short fibers, whiskers, particulates) and orientation, (3) their processing routes.

2.1.2 Aluminum Matrix Composites (AMCs)

Aluminum is the most popular matrix for the metal matrix composites (MMCs). The Al alloys are quite attractive due to their low density, their capability to be strengthened by precipitation, their good corrosion resistance, high thermal and electrical conductivity, and their high damping capacity. *Aluminum matrix composites* (AMCs) have been widely studied since the 1920s and are now used in sporting goods, electronic packaging, armours and automotive industries. They offer a large variety of mechanical properties depending on the chemical composition of the Al-matrix. They are usually reinforced by Al_2O_3 , SiC, C but SiO_2 , B, BN, B_4C , AlN may also be considered. The aluminum matrices are in general Al-Si, Al-Cu, 2xxx or 6xxx alloys. As proposed by the American Aluminum Association the AMCs should be designated by their constituents: accepted designation of the matrix / abbreviation of the reinforcement's designation / arrangement and volume fraction in % with symbol of type (shape) of reinforcement. For example, an aluminum alloy AA6061 reinforced by particulates of alumina, 22 % volume fraction, is designated as "AA6061/ Al_2O_3 /22p".

In the 1980s, transportation industries began to develop discontinuously reinforced

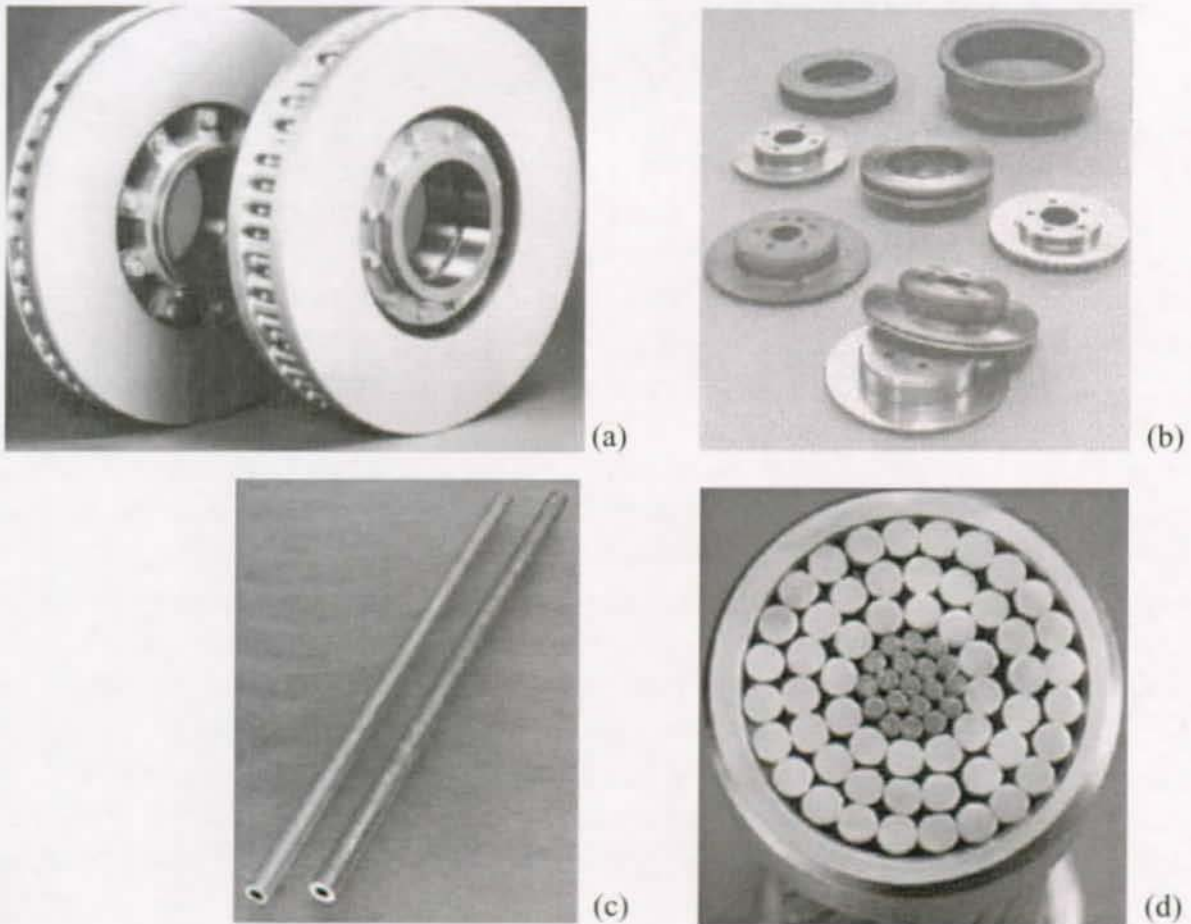


Fig. 2.1 Some industrial AMCs applications: (a) brake rotors for high speed train [10], (b) automotive braking systems [10], (c) automotive pushrods [11] and (d) cords for HV electrical wires [11].

AMCs. They are very attractive for their isotropic mechanical properties (higher than their unreinforced alloys) and their low costs (cheap processing routes and low prices of some of the discontinuous reinforcement such as SiC particles or Al_2O_3 short fibers).

Among the various and numerous applications [10, 11], a few arbitrary examples, are given in Fig. 2.1: (1) Brake rotors for German high speed train ICE-1 and ICE-2 developed by Knorr Bremse AG and made from a particulate reinforced aluminum alloy (AlSi7Mg+SiC particulates) supplied by Duralcan. Compared to conventional parts made out of cast iron with 120 kg/piece, the 76 kg of the AMC rotor offers an attractive weight saving potential. (2) The braking systems (discs, drums, calipers or back-plate) of the New Lupo from Volkswagen made from particulate reinforced aluminum alloy supplied by Duralcan. (3) AMC continuous fiber reinforced pushrods produced by 3M for racing engines. These pushrods weigh 40% as much as steel, are stronger and stiffer, and have high vibration damping. (4) AMC wires also developed by 3M for the core of a electrical conductors. The unique properties of this type of conductor offer substantial performance benefits when compared to the currently used steel wire reinforced conductors.

2. Aluminum Matrix Composites: Processing and Properties

2.1.3 Fabrication of the AMCs

There are many processes viable to fabricate AMCs; they can be classified in: solid-state, liquid-state and deposition processes.

In solid-state processes, the most spread method is *powder metallurgy* PM; it is usually used for high melting point matrices and avoids segregation effects and brittle reaction product formation prone to occur in liquid state processes. This method permits to obtain discontinuously particle reinforced AMCs with the highest mechanical properties [12]. These AMCs are used for military applications [13] but remain limited for large scale productions.

In liquid-state processes, one can distinguish the infiltration processes where the reinforcements form a preform which is infiltrated by the alloy melt (1) with pressure applied by a piston (*squeeze-casting* SQC described in section 2.3.2) or by an inert gas (*gas pressure infiltration* GPI) and (2) without pressure [14]. In the last case, one can distinguish (a) the reactive infiltration processes using the wetting between reinforcement and melt obtained by reactive atmosphere, elevated temperature, alloy modification or reinforcement coating (*reactive infiltration*) and (b) the dispersion processes, such as *stir-casting*, where the reinforcements are particles stirred into the liquid alloy. Process parameters and alloys are to be adjusted to avoid reaction with particles.

In deposition processes, droplets of molten metal are sprayed together with the reinforcing phase and collected on a substrate where the metal solidification is completed. This technique has the main advantage that the matrix microstructure exhibits very fine grain sizes and low segregation, but has several drawbacks: the technique can only be used with discontinuous reinforcements, the costs are high, and the products are limited to the simple shapes that by obtained by extrusion, rolling or forging.

2.2 Mechanical Properties of the AMCs.

In this section, the basic mechanical properties are succinctly introduced: elastic, yielding, fracture. The mechanical models and concepts presented in this section will be used to show that the mechanical behavior of the WFA/Al₂O₃/sf and WFA/SiC/p composites (section 2.3) cannot be completely understood without deeper microstructural investigations.

2.2.1 Elasticity

Different models exist for the elastic behavior of MMCs. All are based on the assumption of a perfect and intact reinforcement. Let us consider the simplest case of continuous aligned fiber composites with the *slab model*. The Young's modulus follows the "rule of mixture" ROM law:

Axial stiffness

$$\begin{aligned}\sigma_c &= (1 - V_f)\sigma_m + V_f\sigma_f \\ \Rightarrow E_c &= (1 - V_f)E_m + V_fE_f\end{aligned}\quad (2.1)$$

Transversal stiffness

$$\begin{aligned}\varepsilon_c &= (1 - V_f)\varepsilon_m + V_f\varepsilon_f \\ \Rightarrow E_c &= \left(\left(\frac{1 - V_f}{E_m} \right) + \frac{V_f}{E_f} \right)^{-1}\end{aligned}\quad (2.2)$$

with σ the stress, ε the strain and E the Young modulus, with the subscript m, f , and c for the matrix, fiber and composite respectively.

For short orientated fibers, a more elaborated model has been developed by Cox [15] and Kelly [16], *the shear lag model*. The main idea is the transfer of tensile strength from matrix to reinforcement by means of interfacial shear stresses. If load transfer is assumed at reinforcement ends, it is found that

$$E_c = (1 - V_f)E_m + V_fE_f \left[1 - \frac{\left(\frac{E_m}{E_f} - 1 \right) \tanh\left(\frac{\beta l}{2} \right)}{\frac{\beta l}{2}} \right] \quad (2.3)$$

with l fiber length and $\beta = \frac{2\sqrt{2}}{d} \sqrt{\frac{G_m}{E_f \ln(D/d)}}$,

with G_m shear modulus of the matrix, d diameter of the fiber and D interfiber distance $(D/d)^2 \approx 1/V_f$.

A generalization of the shear lag model for misorientated short fiber composites using semi-empirical coefficients is largely used [1, 17, 19]. The stiffness takes generally the form:

$$E_c = (1 - V_f)E_m + \eta_\theta \eta_l V_f E_f \quad (2.4)$$

with η_θ efficiency factor for the orientational distribution of the fibers (1, for unidirectionally aligned fibers, 0.375 for planar random array, and 0.2 for random distribution) and η_l relates to the fiber length [19]. For particle composites, another modification of the ROM is given in the Halpin-Tsai equations [20, 21]:

$$E_c = \frac{E_m(1 + 2sqV_p)}{1 - qV_p} \quad (2.5)$$

where $q = \frac{E_p/E_m - 1}{E_p/E_m + 2s}$ and s is the particle aspect ratio.

These semi-empirical models are often used for their simple expressions but are very pessimistic for composites with low reinforcement aspect ratios. A more rigorous model has been given by Eshelby [22, 23]. *The Eshelby method* is exact for ellipsoidal orientated inclusions and is a very good approximation for short fibers or particulate reinforced composites. Without going deeper in the details, it can be said that the method is based on representing the actual inclusion by one made of matrix material which has an appropriate misfit strain so that the stress field is the same as for the inclusion. It expresses the stiffness tensor of the composite in function of the matrix and inclusion ones.

2.2.2 Yielding / Flow.

The ideal¹ AMC stress-strain curve for continuous unidirectional fiber composites (with stress in the fiber direction) is presented in Fig. 2.2. Generally, this curve consists of two stages. During the stage I, both fiber and matrix remain elastic, during stage II, the matrix deforms plastically and fibers remain elastic. There is possibly a stage III where both matrix and fibers deform plastically, but generally the fibers break before their plastic deformation.

In the case of short fiber composites, the three stages are degenerated in one, and there is no definable linear region in the composite due to the existence of microplasticity at the fiber ends and to the random fiber orientation.

The yield stress is defined as the stress at a plastic strain of 0.2% and represents the limit of the elastic behavior of the composite. Flow stresses are stresses at greater plastic strains. In general the yield stress increases with the fiber volume fraction and a better orientation of the fibers along the tensile axis. The yield stress in compression is in general larger than in traction due to the residual stress caused by the CTE mismatch between the alloy and the fibers. The prediction of yielding and flow behavior is quite complex. During tensile loading, at a given strain, the stresses in the matrix are expected to be lower than in the unreinforced alloy due to the load transfer to the reinforcements, and therefore the matrix yielding is delayed in comparison with the unreinforced alloy (*work hardening* caused by the composite structure). The distribution of the reinforcements (orientation and homogeneity) plays a key role in this work hardening. Local plasticity occurs at fibers ends during the deformation (an effect accentuated by the thermal residual stresses). This stress concentration can lead to relaxation effects as dislocation motions, diffusion, recrystallization or to more catastrophic effects such as inclusion fracture, interfacial debonding and matrix cavitation. Some of these effects can be taken into account in the continuous models presented in section 2.2.1 or in finite elements models FEMs. However, these models remain not very accurate to predict the yield and flow stresses of composites (underestimation of the predicted yield stress), particularly for the misoriented short fiber composites. The underestimation can be explained by a *matrix hardening* as detailed by Taya [7]. The matrix hardening is mainly the consequence of three effects:

(1) smaller grain sizes in the AMC matrix than in the alloy due to the reinforcement tangle. The hardening follows the Hall-Petch law: $\Delta\sigma_m^Y \propto 1/\sqrt{D}$ where D is the grain size.

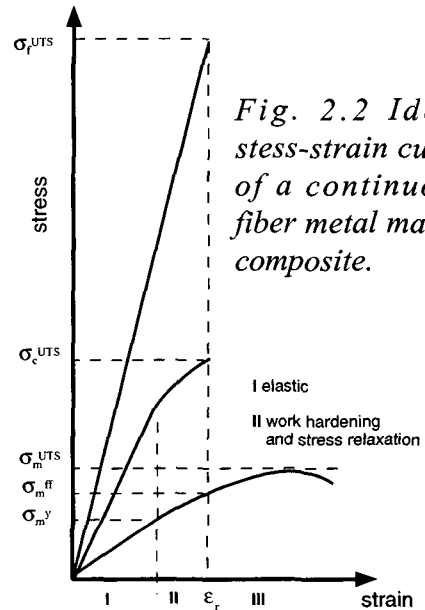


Fig. 2.2 Ideal stress-strain curve of a continuous fiber metal matrix composite.

1. The internal stresses are not taken into account and a perfect bonding is assumed so that $\epsilon_C = \epsilon_m = \epsilon_F$.

(2) higher dislocation density generated by the CTE mismatch between matrix and reinforcements. Arsenault *et al.* [24, 25] showed that the dislocation density ρ increases by

$$\Delta\rho = \frac{BV_f\varepsilon}{b(1-V_f)} \times \frac{1}{t} \quad (2.6)$$

where B is a geometric constant ε is the misfit strain given by $\varepsilon = \Delta\text{CTE}.t/2$, with b the Burgers vector and t the smallest dimension of the inclusion. The matrix yield stress enhancement follows the dislocation forest hardening:

$$\Delta\sigma_m^Y = \beta\mu b\sqrt{\rho} \quad (2.7)$$

where μ is the shear modulus of aluminum, and β a constant estimated at 1.25 for aluminum. The matrix hardening can be very important: as shown by Arsenault [24], with a temperature drop of 300°C, for inclusions below 1 μm , the dislocation density increases by $\Delta\rho \approx 10^{13} - 10^{14} \text{ m}^{-2}$ and the hardening by $\Delta\sigma_m^Y \approx 100\text{-}200 \text{ MPa}$. This effect remains significant for larger inclusion sizes if the aspect ratios are taken into account.

(3) another aspect has not been considered yet. Considering that $\sigma^Y \approx 20 \text{ MPa}$ for pure aluminum and $\sigma^e = 400 \text{ MPa}$ for 2xxx alloys (shearing/by-passing mechanisms [27]), both alloys being cast in the same conditions, it is clear that any possible change of the precipitation state of the alloy when it is reinforced can have a great influence on the final AMC mechanical properties. It is often reported in literature that a change of the density or of the spatial distribution of the precipitation occurs due to the increased dislocation density. As shown in chapter 4, the precipitation nature (phases) can also be completely modified as consequence of interfacial reactions.

2.2.3 Fracture

The fracture strength is the ultimate tensile strength before the rupture of the material. Since it represents the limit of the flow behavior of the MMC, its prediction is also very complex.

For aligned continuous fibers composites, without considering the matrix work hardening, two cases must be distinguished: (a) For high fiber volume fractions, the composite breaks when the fibers break: the ultimate tensile strength can be differentiated from the ROM:

$$\sigma_c^{UTS} = V_f\sigma_f^{UTS} + (1-V_f)\sigma_m^{ff} \quad (2.8)$$

where σ_m^{ff} is the stress in the matrix when the applied load reaches that of the failure strain of the fiber (Fig. 2.2). (b) For low fiber volume fractions, the fibers fail before the matrix. All the stresses are supported by the matrix, and the fracture strength is

$$\sigma_c^{UTS} = (1-V_f)\sigma_m^{UTS} \quad (2.9)$$

2. Aluminum Matrix Composites: Processing and Properties

The limiting volume fraction between these two cases is found by equalizing (2.8) and (2.9). In general, the aligned continuous fibers composites follow equation (2.8). The ultimate tensile strength of the fiber can be decreased as a consequence of a potential brittle reaction layer at their surface during processing, resulting in a decrease of the ultimate strength of the composite.

For aligned short fibers composites, the shear lag model has been adapted by Kelly and Tyson [28]. Considering that the force which breaks the fibers $F = \sigma_f^{UTS}(\pi d^2/4)$ is linearly supported by the matrix at the interface: $F = 0$ at fiber end and $F(x) = \pi d \tau_i^{USS} x$ at a distance x from the fiber end, it is deduced that the fiber breaks for a length is

$$l_{cr} = 2x_{cr} = d \frac{\sigma_f^{UTS}}{2\tau_i^{USS}} \quad (2.10)$$

where τ_i^{USS} is the matrix-fiber interfacial shear strength which is, in first approximation, close to $\sigma_m^{USS}/2$. A deleterious interfacial reaction can completely change this value (more precise values can be deduced from fiber pushing experiments). For $l < l_{cr}$, the fibers are not loaded to their full capacity (the fibers are not broken, the fracture occurs by matrix cavitation at the interfaces), and for $l > l_{cr}$ the fibers bear their maximum stress σ_f^{UTS} and are broken. The ultimate tensile strength of the composite is therefore [7]

$$\sigma_c^{UTS} = \begin{cases} V_f \sigma_f^{UTS} \left(1 - \frac{l_{cr}}{2l}\right) + (1 - V_f) \sigma_m^{ff} & l \geq l_{cr} \\ V_f \sigma_f^{UTS} \left(\frac{l}{2l_{cr}}\right) + (1 - V_f) \sigma_m^{UTS} & l < l_{cr} \end{cases} \quad \text{for} \quad (2.11)$$

For misoriented fiber and particle composites, some semi-empirical models based on equation (2.11) have been proposed in [17, 19]. They show that a minimum volume fraction of reinforcement is required for strength improvement of the short fiber composites [17] and of the particles composites [26]. Other models also exist on the base of the Tsai-Hill equation which gives the ultimate tensile strength for an aligned short fiber composite in directions differing from the fiber alignment direction [29]. These models require the exact knowledge of the orientation distribution of the reinforcements, which is experimentally difficult to estimate. If the reinforcements are randomly orientated one can estimate that only 1/4 of the reinforcements are orientated in the applied load direction, and the ultimate tensile strength is reduced in the same proportion. In fact, as for the yielding behavior, the prediction of tensile strength is problematic and requires the knowledge of the matrix hardening, interfacial bonding and micro-damage processes such as reinforcement cracking (particularly important for continuous fiber composites $l > l_{cr}$), matrix cavitation and/or interfacial debonding (particularly important for very short fiber or particulate composites $l < l_{cr}$). For example, in Al/SiC/p systems, Lloyd [30] has observed that particle cracking is an important mechanism only for composites containing particles greater than around 20 μm in size.

2.2.4 Conclusions: Influence of the Microstructural Variables

We have seen that the mechanical properties of the particulate or misoriented short fiber composites mainly rely on two microstructural variables: the interfacial bonding and the matrix hardening.

The bonding (mechanical, physical or chemical) is governed by the nature of the interface. The bond strength is linked to the wetting by

$$W_{ad} = \Gamma_{LV}(1 + \cos \Theta) \quad (2.12)$$

where W_{ad} is the work of adhesion, Θ is contact angle between the liquid metal and the solid ceramic, and Γ_{LV} the surface energy between the liquid metal and vacuum [2]. For most of AMCs the bonding strength is associated to a slight interfacial reaction resulting from the affinity between the alloying elements and the reinforcement. For elastic and plastic behavior, any absence of interfacial bonding may be catastrophic since the material can be considered as an alloy with holes (total absence of load transfer). For fatigue behavior, a weak interface may favor the crack deflection by the reinforcements. Moreover, provided there is a reaction, the reaction layer thickness may be considered as the notch for fatigue prediction [33, 34]. In any case, interfacial reaction must be controlled to avoid any possible degradation of the reinforcement and the composites' properties.

The matrix hardening does not influence the stiffness of the alloy and therefore of the discontinuous AMCs, but significantly improves the yielding behavior and tensile properties (equation (2.11)). A fine precipitation homogeneously distributed in the matrix is required to obtain good mechanical properties for the matrix alloy and therefore also for the composite. Moreover, *precipitation free zones* PFZ near the reinforcements must be avoided since they are favorable to crack propagation.

2.3 The AlCuMgAg Based Composites

2.3.1 Materials

The composites studied in the present work are based on a high performance well characterized Al-4Cu-MgAgMnZr wrought alloy firstly developed by Polmear and Couper [35]. The alloy is derived from 2xxx alloys (AlCuMg alloys) by addition of small amounts of Ag (< 1%) and exhibits at present the best tensile properties at high temperatures (up to 200°C) of all the commercial 2xxx alloys due to the precipitation of a thermally stable phase, the Ω phase. Details on the precipitation state are given in chapter 4 and annex B. The AlCuMgAg alloy has been intensively studied and adapted to the spray deposition technology (Osprey process) [5, 6, 36]. It was shown to be a potential good candidate for the fuselage of the new supersonic passenger aircraft that may replace the Concorde; comparing to 2618 alloy (Al-2.2Cu-1.5Mg-1Fe-1Ni-0.2Si) currently used for the Concorde skins, the new alloy exhibits

better creep resistance and damage tolerance [37]. Due to its good mechanical and physical performance, i.e. elevated temperature capability, damage tolerance and outstanding thermal conductivity, this alloy appears to be an interesting candidate matrix alloy for AMC applications such as car motor components or electronic devices. The transition elements Mn and Zr of the original Al-4Cu-MgAgMnZr alloy were omitted for the composite matrix to avoid embrittling intermetallic phases. The Mg content was raised to 1 wt-% to compensate for its apprehended loss from reaction with the reinforcements (see chapter 4), since it has been shown that a precise balance of Cu, Mg and Ag is required for the precipitation of the Ω -phase. The effective chemical composition of the modified Al-4Cu-1Mg-Ag alloy is therefore Al-4Cu-1Mg-0.5Ag-0.03Fe-0.04Si, hereafter called WFA. Based on this alloy, two kinds of composites have been investigated: one with Al_2O_3 short fibers and one with SiC particulates.

WFA/ Al_2O_3 /sf Composites

The short alumina fibers were processed in preforms custom made by Vernaware Ltd, UK. They consist of 10-30 vol.% β - Al_2O_3 based Saffil chopped fibers (96-97 wt.% Al_2O_3 , 3-4 wt.% SiO_2 to stabilize the beta alumina) with a diameter of 3 μm with 5% SiO_2 or Al_2O_3 binder (hereafter noted *s* and *a*). The fibers are produced by ICI Ltd. UK by using an aqueous phase containing an oxide sol and an organic polymer. The sol is extruded as wound filaments on a drum where the shapes gel. The gelled fibers

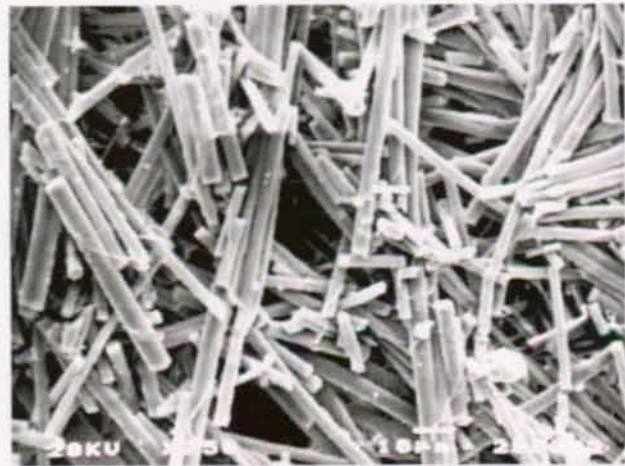


Fig. 2.3 SEM image of a short fiber Al_2O_3 -Saffil preform.

are then dried at about 800°C, this combusts organic material and leaves only a fine grain alumina having 5-10% porosity. They are then calcined (causing about 5% linear shrinkage) at 1400-1500°C to produce the final oxide fibers for reinforcement. A slurry of fibers and binder is made, pressed and cooked to obtain the desirable alumina structure. The fibers are orientated with some preference in the plane of the applied pressure, with a planar random orientation, as shown in Fig. 2.3. The as-received preforms have a parallelepiped form (15 x 80 x 120 mm³). The binder is present on the fibers as a non-uniform thin layer (100 nm), it particularly pins the fibers at contacting points. To fabricate the composites the preform is preheated and pressure-infiltrated with the molten alloy (section 2.3.2).

The composites were fabricated for the assessment of their mechanical performance. For instance, in view of being used for discarding sabots as a substitution of Al-alloy 7075. They were further used in the sub-ordinate PPM-project "High Performance Al-matrix composites" to assess the near net shape capability and the up-scaling ability of the squeeze-casting process for the fabrication of AMCs.

WFA/SiC/p Composites

The SiC particles used as reinforcement are Norton 500HD Green Alpha SiC particles (rounded to obtain a high packing density) with an average dimension of 12 μm (Fig. 2.4). Their chemical composition is: 99.75 wt.% SiC, 0.07 wt.% free C, 0.12 wt.% SiO₂, 0.04 wt.% free Si. The SiC particles are produced from petrol coke and quartz sand in a resistance furnace referred to as the Ascheson Furnace (Ceram Process). The sorted SiC particles are then crushed and milled in several steps. The processing includes chemical cleaning and wet classification [38]. To fabricate the composites, the SiC particles are tap-packed into a steel housing to form a 8 mm x 90 mm x 100 mm particle preform with ~ 60% volume fraction, which is preheated and pressure-infiltrated with the molten alloy (section 2.3.2).

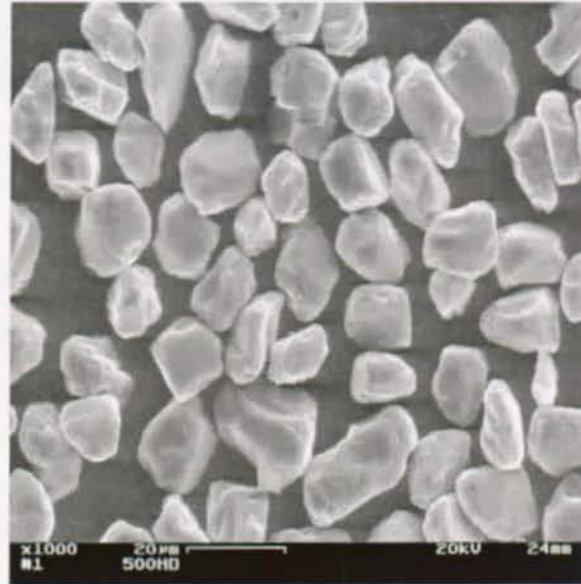


Fig. 2.4 SEM image of SiC 500HD particles.

These high volume fraction SiC_p composites have been evaluated for piston pin applications. The mechanical results are promising and comparable to those of piston pins made from Lanxide composites by reactive infiltration process. Young's modulus of about 200 GPa and 4-points bending strength higher than 700 MPa have been achieved. Another promising application is the fabrication of chip-module carrier plates for electronic packaging. Packaging materials support and protect integrated circuits and other electronic components, and they also play a important role in heat dissipation. The key requirements for electronic packaging materials are: low CTE, possibility of matching the CTE of other electronic materials, high heat conductivity, low weight, low cost and net shape fabrication potential. WFA/SiC/p composites were shown to fulfill these requirements. Samples for evaluation have successfully been produced on an industrial shot control die casting machine (Buhler).

2.3.2 Direct Squeeze-Casting Process

The direct squeeze-casting process (SQC) is a liquid metal forging process, i.e. it combines the advantages of both die casting and forging. Hence, this process offers the opportunity of high production rates at comparatively low costs and allows the processing of both cast and wrought Al and Mg alloys. The elevated process pressure (> 100 MPa) guarantees pore-free castings (making the material weldable and heat treatable) and enables the infiltration of porous preforms for the processing of MMCs. The production rate is quite high (> 5 min / MMC-casting) and, therefore, from an economic point of view, the SQC-

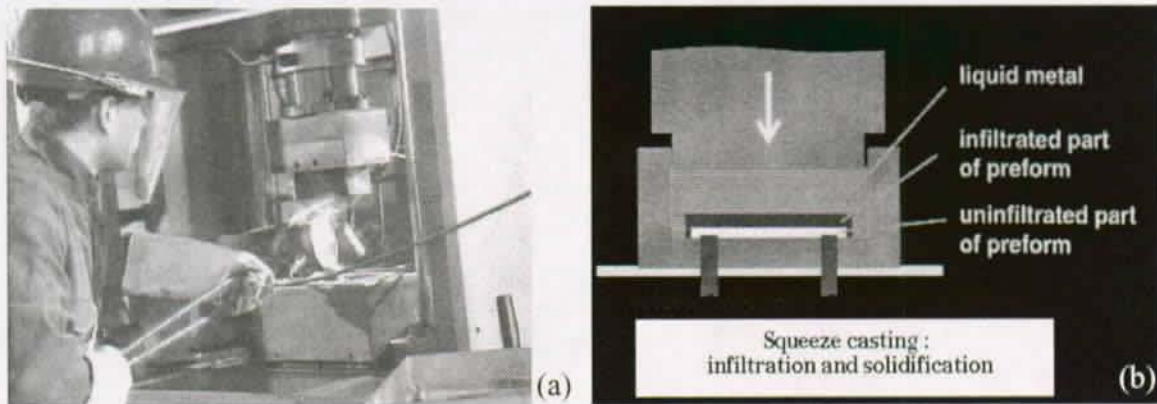


Fig. 2.5 Infiltration by squeeze-casting (a) liquid metal pouring, (b) process scheme

process is superior to reaction or pressure driven infiltration processes that usually feature considerably longer process times. The process for the fabrication of the MMCs is illustrated in Fig. 2.5.

The melt superheat, the preheating temperature of the preform, the preheating temperatures of the squeeze die cavity and the ram, the infiltration speed and the pressurization level and time are parameters that must be controlled and optimized to obtain a sound microstructure and therefore good mechanical properties. The parameter optimization was realized by analyzing, simulating and modeling the complete infiltration and solidification process [4]. For instance, it has been shown that a sufficient preform preheating temperature is required to avoid premature melt solidification that would result in infiltration defects such as porosity, segregation and preform deformation [39, 40]. The infiltration and solidification time is very short (~20 s) and allows to control the extent of the interfacial reaction (with the limitation imposed by the process). Up-scaling of the direct SQC-process from laboratory to industrial scale on a shot control die casting machine was successfully demonstrated particularly suited for the commercial fabrication of "complex" MMC-castings. The WFA/ $\text{Al}_2\text{O}_3/\text{sf}$ and WFA/ SiC/p composites investigated in the present work were fabricated at EMPA-Thun by SQC under identical process conditions. The preform was infiltrated with the Al-4Cu-1Mg-0.5Ag alloy melt with the following processing parameters: melt superheat 730°C, preform preheat 750°C, infiltration speed 10 mm/s, maximum pressure 130 MPa. The composite castings were subsequently solution heat treated at 480°C / 1.2 h + 500°C / 2 h, followed by cold water quenching. After holding at 25°C for 100 hours (T4), the castings were peak-aged at 165°C for 4 h (T6). The hardness responses are presented in section 4.3.1.

2.3.3 Tensile Properties

As illustrated in Fig. 2.6, both WFA/ $\text{Al}_2\text{O}_3/\text{sf}$ and WFA/ SiC/p composites fail during tensile testing by a combination of fiber (or particle) fracture and matrix plastic (micro-shear) deformation. This is an indication that a good interfacial bonding is obtained and that the

critical size of the reinforcement for load transfer is reached (discussion with equation (2.11)). Nevertheless, as, it will be shown in the following sections, this information is not sufficient to predict the mechanical tensile strength due to the high number of microstructural parameters and complex interactions.

WFA/Al₂O₃/sf Composites

The mechanical properties of the WFA/Al₂O₃/sf composites cannot be directly deduced from the micro-mechanistic models presented in section 2.2, since they are highly dependent on the fabrication process, alloy composition and nature of the binder:

(1) The WFA/Al₂O₃/sf composites fabricated by SQC are very close to those fabricated by gas pressure infiltration GPI in the O'Rourke's study [18] (same Saffil fibers and silica binder, similar alloy composition). Nevertheless, since the mechanical properties for the SQC composites are significantly higher (Table 2.1), even with lower fiber content, it is clear that the semi-empirical formulae he developed in [19], which match with his experiments, are not suitable in the present case: we would find for the WFA/Al₂O₃/sf/s composite $E_c = 89$ GPa and $\sigma_c^{UTS} = 410$ MPa. The Young's modulus is close to the experimental one, but the predicted tensile strength is significantly lower (510 MPa).

matrix	% fibers	process	E_c GPa	σ_c^Y MPa	σ_c^{UTS} MPa	δ_c %
Al-4.2Cu-1.4Mg-0.6Ag [19]	25	GPI	97	450	460	0.5
Al-4Cu-1Mg-0.5Ag (WFA)	15	SQC	90	414	510	1.3

Table 2.1 Effect of fabrication process on the properties of AlCuMgAg/Al₂O₃/sf composites

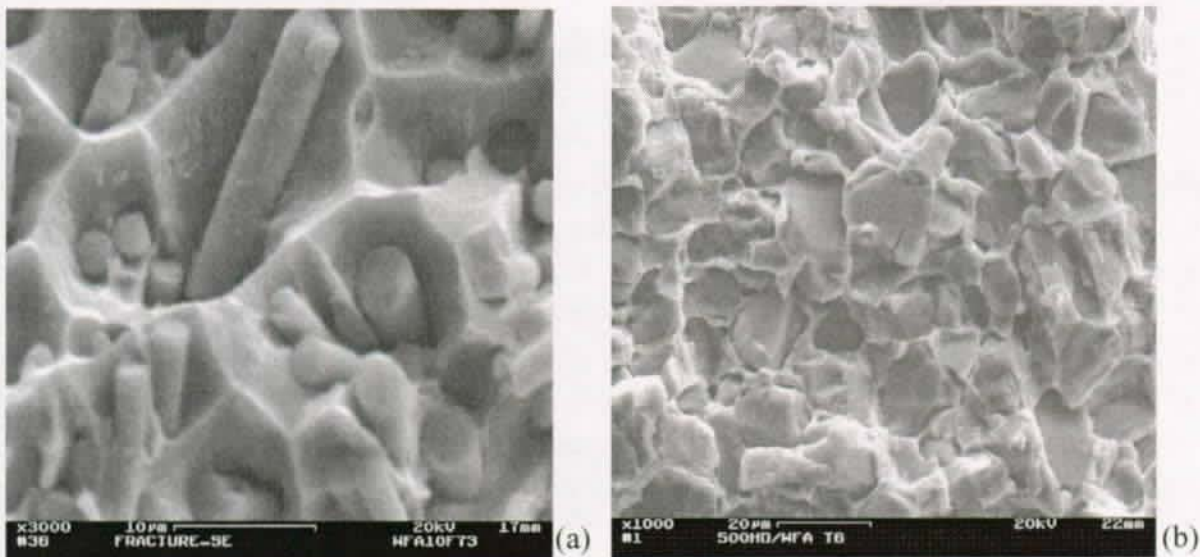


Fig. 2.6 SEM fractographies of the WFA/Al₂O₃/sf/s and WFA/SiC/p composites (T6).

2. Aluminum Matrix Composites: Processing and Properties

(2) The mechanical properties of the Al/Al₂O₃/sf composites are highly dependent on the matrix alloy composition, as illustrated by the test results reported in Table 2.2. A higher Cu content tends to improve the tensile properties of the matrix alloy by age hardening, but does not necessarily improve the composite performances (for instance, composites 2 and 3 have similar tensile strength, although the tensile strength of the unreinforced alloy is 456 MPa and 373 MPa respectively). A probable explanation could be the important segregation of CuAl₂ intermetallics at the interfaces. However, it will be shown in section 4.1.2 that the segregation is highly reduced by the homogenization treatment. Moreover, it will be shown in section 4.5.2 that Cu has not the same primary importance for the precipitation hardening it has in matrix of the composite that it has in the unreinforced alloy (due to the precipitation change produced by chemical reactions between some alloying elements and the reinforcement). The importance of the matrix strength on the mechanical properties of the composites is confirmed by the influence of the aging treatment (T4 and T6 states), as shown in Table 2.3.

matrix	n°	σ_c^Y MPa	σ_c^{UTS} MPa	δ_c (%)
Al-4.5Cu-0.2Mg-AgMnTi	1	337	480	1.8
Al-4Cu-1Mg-0.5Ag (WFA)	2	347	473	1.4
Al-2.8Cu-1Mg-0.5Ag	3	351	477	2.0
Al-1.6Cu-2.4Mg-0.5Ag	4	283	375	1.5
Al-1.4Cu-3.9Mg-0.5Ag	5	264	366	2.2

Table 2.2 Effect of the matrix alloy composition on the properties of composites reinforced with 15 % Al₂O₃ Saffil fibers with an Al₂O₃ binder fabricated by SQC in same conditions [4].

(3) More surprising is the effect of the chemical nature of the binder on the mechanical properties of the WFA/Al₂O₃/sf composites in T6-temper. It was expected that the tensile properties of the WFA/Al₂O₃/sf/a composite would have been superior to those of WFA/Al₂O₃/sf/s since Mg from the WFA matrix was supposed to react with the SiO₂ binder and thus be lost for age hardening. Al₂O₃ being thermodynamically more stable than SiO₂, the alumina binder should withdraw a lesser extent of Mg from the matrix. However, tensile tests presented in Table 2.3 reveal better tensile properties for the AMCs with the SiO₂ binder. Since the only difference is the chemical nature of the binder, no interpretation can be given with the global micro-mechanistic approach detailed in section 2.2. A deeper microstructural study has to be done to better understand what is the structural change between the two composites. The results are presented in section 4.5.3.

binder	temper state	E_c GPa	σ_c^Y MPa	σ_c^{UTS} MP)	δ_c %
SiO ₂	T4	91	260	433	3.5
SiO ₂	T6	90	410	514	1.3
Al ₂ O ₃	T4	86	249	427	4.2
Al ₂ O ₃	T6	95	347	473	1.4

Table 2.3 Effect of the binder on the mechanical properties of the SQC WFA/Al₂O₃/sf composites in T4 and T6 states fabricated under identical conditions.

WFA/SiC/p Composites

Some mechanical properties of the WFA/SiC/p are reported in Table 2.4. The Young's modulus of the composite is high (200 GPa); it obeys the ROM law of equation (2.5) (which predicts a Young's modulus of 204 GPa). From the close results between the as-cast and T6 state, it is supposed that the mechanical properties of these composites are not dominated by the matrix precipitation state [41]. However, tensile strength of similar composites based on pure aluminum alloy are significantly lower ($E_c = 153$ GPa and $\sigma_c^{UTS} \approx 275$ MPa). This leads to the presumption that some alloying elements may affect the interfacial bonding strength, even if an effect of the matrix plasticity or of the matrix ability to accommodate and relax internal stresses during loading is not excluded. Explanations will be given in section 4.2.2.

	E GPa	HB ^a (30)	σ^Y MPa	σ^{UTS} MPa	K_{IC}^b MPa.m ^{1/2}	δ %
WFA alloy as-cast	70	97	164	256	21	5.7
WFA alloy T6	72	170	402	456	24	3.6
WFA/SiC/p as-cast	200	273	-	450	10	-
WFA/SiC/p T6	198	360	-	470	9.5	-

Table 2.4 Mechanical properties of the unreinforced WFA alloy and the SQC WFA/SiC/p composites [4, 41].

a. The Brinell test establishes the relative hardness of a material by pressing a 10 mm steel ball under a known load into the material being tested. The Brinell number is then calculated by dividing the load in kilograms by the curved area in square millimeters of the resulted indentation.

b. The fracture toughness corresponds to the ability of a material to absorb energy before fracture.

2.4 Discussion

It has been shown that the understanding of the mechanical properties of discontinuously reinforced composites is quite complex. Actually, the plastic behavior of discontinuous AMCs is in great part controlled by the load transfer capability (directly linked to the quality of the interface), by the hardening of the matrix and by the stress accommodation ability of the matrix (directly dependent of complex and correlated microstructural parameters such as the dislocation density, the precipitation state, possible precipitation-free zones PFZ...). Therefore, the semi-empirical models presented in section 2.2, although efficient to predict the elastic properties of AMCs, cannot completely describe the plastic behavior of the discontinuous composites such as of the WFA/ Al_2O_3 /sf and WFA/SiC/p composites. Even qualitatively, some results such as the decrease of the mechanical properties of the WFA/ Al_2O_3 /sf composites when an alumina binder is used remain incomprehensible. Therefore, as shown in section 2.3.3, the microstructure of these composites must be studied in detail for a better understanding of their tensile properties. The TEM investigations presented in the chapter 4 will reveal all the important parameters that can be used in a micro-mechanistic model. The aim is to explain qualitatively the mechanical results presented in section 2.3.3, a complete quantitative exploitation of the TEM results would require deeper mechanical studies, far beyond the scope of this work.

Chapter 3

Transmission Electron Microscopy

When electrons are accelerated up to high energy levels (few hundreds keV) and focused on a material, they can scatter or backscatter elastically or inelastically, or produce many interactions, source of different signals such as X-rays, Auger electrons or light (Fig. 3.1). Some of them are used in transmission electron microscopy (TEM).

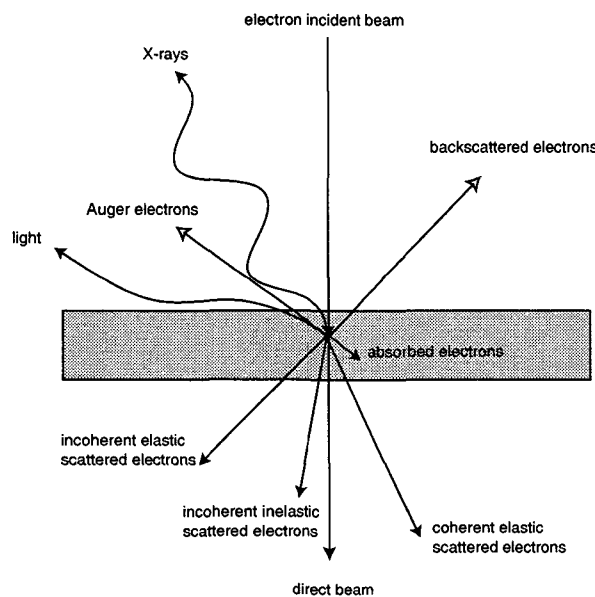


Fig. 3.1 Interactions between electrons and material

The purpose of this chapter is to introduce TEM and the different related techniques used for the microstructural study of the AMCs. The TEM sample preparation of AMCs is described in chapter 3.2. The chemical analyses by energy dispersive spectrometry (EDS) is presented in chapter 3.3. Chapter 3.4 is concerned with the theoretical basis of TEM (diffusion and diffraction). Chapter 3.5 deals with the contrast image formation in a conventional TEM (bright/dark field modes, and diffraction patterns). A brief presentation of high resolution transmission electron microscopy (HREM) with an introduction to electron crystallography is given in chapters 3.6 and 3.7.

3.1 Historical Introduction

The *resolution* ρ of a microscope is defined as the distance between two details just separable from one another. It can be calculated using the Abb theory of images formation for optic systems. For incoherent light or electron beam:

$$\rho = \frac{0.61\lambda}{\sin\alpha} \quad (\text{Rayleigh criterion}) \quad (3.1)$$

where λ is the wavelength of the light, and α the maximum angle between incident and deflected beam in the limit of the lens aberrations.

For optical microscopy, the resolution is therefore limited by the wavelength of light (410-660 nm). The X or γ rays have lower wavelength, but unfortunately, high-performance lenses necessary to focus the beam to form an image do not exist yet (however, X-rays can reveal structural information of materials by diffraction techniques). In 1923, De Broglie showed that all particles have an associated wavelength linked to their momentum: $\lambda = h/mv$ where m and v are the relativist mass and velocity respectively, and h the Plank's constant. In 1927, Hans Bush showed that a magnetic coil can focus an electron beam in the same way that a glass lens for light. Five years later, a first image with a TEM was obtained by Ernst Ruska and Max Knoll [42]. In a TEM, the electrons are accelerated at high voltage (100-1000 kV) to a velocity approaching the speed of light (0.6-0.9 c); they must therefore be considered as relativistic particles. The associated wavelength is five orders of magnitude smaller than the light wavelength (0.04-0.008 Å). Nevertheless, the magnetic lens aberrations limit the convergence angle of the electron beam to 0.5° (instead of 70° for the glass lens used in optics), and reduce the TEM resolution to the Å order. This resolution enables material imaging (section 3.5) and structure determination at the atomic level (section 3.6 and 3.7). In the 1950s, Raymond Castaing developed an electron probe and X-ray detector for the chemical analyses. A modified version of his technique, the energy dispersive spectrometry EDS (section 3.3) is nowadays usually added to the TEM. Many different techniques based on TEM are used in materials science. Some of them will be detailed in the following sections.

3.2 Preparation of the TEM Samples

For TEM observations, thin samples are required due to the important absorption of the electrons in the material. High acceleration voltage reduces the absorption effects but can cause radiation damage (estimated at 170 kV for Al). At these acceleration tensions, a maximum thickness of 60 nm is required for TEM and HREM observations and quantifications. For Al alloys, this thickness can be obtained by electropolishing with a solution of 20% nitric acid and 80% methanol, but this method is not convenient for the

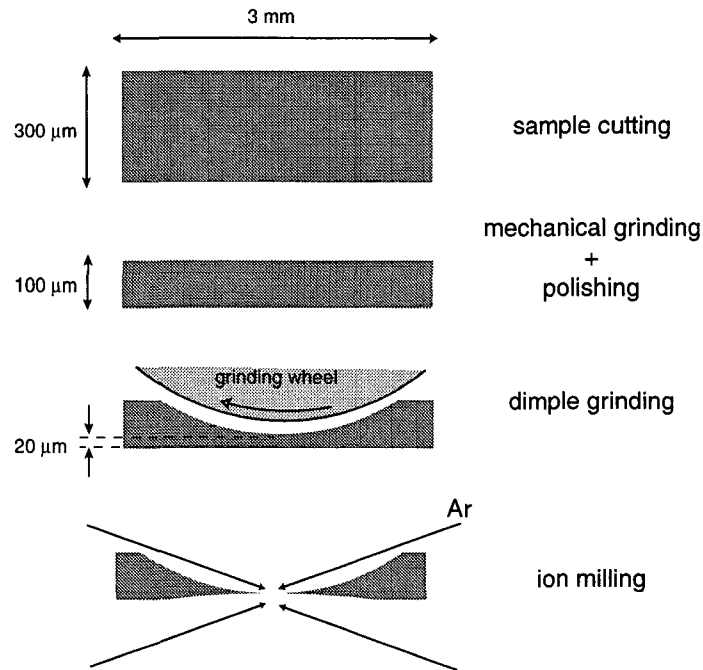


Fig. 3.2 TEM sample preparation of AMCs.

preparation of AMCs due to the low reactivity of the reinforcements in comparison to the unreinforced Al alloys. For AMCs, the following mechanical method was used: TEM foil specimens were prepared by *mechanical dimpling* down to 20 μm , followed by argon ion milling (Fig. 3.2) on a Gatan Duo-Mill machine, operating at an accelerating voltage of 5 kV and 10° incidence angle, with a liquid nitrogen cooling stage to avoid sample heating and microstructural changes associated with the annealing effect. Such effects have been experienced on first samples prepared on an ion mill without cooling stage (PIPS), resulting in an unexpected and substantial coarsening of the precipitation state.

Another preparation method called *focus ion beam* FIB has been tried. A thin slice of the sample was cut by an ion beam on a scanning ion microscope. Unfortunately, the large thickness of the sample ($> 150 \text{ nm}$) impeded good HREM studies. The small observable area (100 nm x 100 nm) permitted to study only one or two grains, which is generally not enough if a special grain orientation is required.

3.3 Chemical Analyses by EDS

The first step in phase identification before the analysis of the diffraction patterns is a chemical analysis that can be done in a TEM microscope by *X-rays energy dispersive spectrometry* EDS, or *electron energy loss spectrometry* EELS. In addition to many other advantages such as the possibility of obtaining information on the chemical bonding and its

3. Transmission Electron Microscopy

good spatial resolution, EELS is particularly appropriated for light elements ($Z < Z_{Al}$), but the identification of the chemical elements and the interpretation of the spectra are not as straightforward as in EDS which remains a quick method for identifying and quantifying the elements thanks to user-friendly software. In this work, EDS has been widely used for the identification and, to a lesser degree, for quantification. Basic knowledge of EDS theory is required to be aware about the limitation and the resolution of this technique [43, 44, 45, 46].

The X-ray microanalyses date from 1950's with the thesis of R. Castaing who built a microprobe on a wave dispersive spectrometre (WDS). This was followed in 1956 by the work of Cosslet and Duncumb who developed it on a scanning electron microscope SEM. EDS is now quasi-systematically associated with TEM to constitute a powerful set called *analytical electron microscopy* AEM [47].

Inelastic interactions between electrons and matter give different kinds of signals: secondary electrons, Auger electrons, X-rays, light and lattice vibrations (Fig. 3.1). The X-ray energy corresponds to a difference between two energy levels of the electron cloud of an atom (K, L...). Since these levels are quantified, the X-ray energy spectrum represents the signature of the atom (Fig. 3.3a). The X-rays are detected by a semi-conductor and processed by a detector protected by an ultrathin window (Fig. 3.3b) and cooled at liquid nitrogen temperature to avoid the thermal noise and the diffusion of the dopant in the semi-conductor. An EDS spectrum is constituted by a background produced by the Bremsstrahlung X-rays and by peaks characteristic to the chemical elements of the material, as shown in Fig. 4.4c.

The identification is quite straightforward for elements beyond C when the peaks do not overlap. For lighter elements, the energy of relaxation of excited atoms is in great part carried off as the kinetics energy of Auger electrons (94% of the relaxation process). Moreover, the potential emitted X-rays are in great part absorbed by the window. If there is an overlapping of the peaks, a deconvolution is required, and gives poor results for close elements, such as Mg

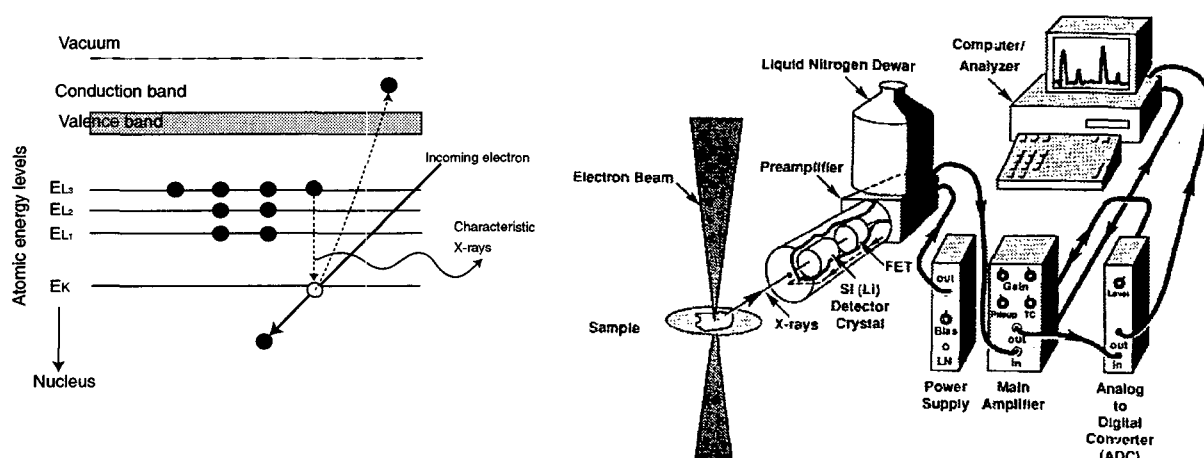


Fig. 3.3 (a) Electronic shell of an atom. The X-rays are emitted by a decrease of one electron from one level to another one, their energies are therefore quantified. (b) X-rays detector in a TEM (modified from [46]).

in an Al matrix. That is the reason why no quantitative results were reported on the Mg content inside the Al matrix of the studied composites. The quantification is more difficult. It takes into account the link between the weight fraction and the generated intensities (ionization cross section) and between the generated intensity and the measured intensity (absorption and fluorescence effects). The measured intensity of an element depends on the other elements present in the sample. For thin samples, where fluorescence and electron absorption are negligible, the weight fraction of the elements are linked by

$$\frac{W_J}{W_A} = k_{JA} \left(\frac{I_J}{I_A} \right)_m \quad (3.2)$$

where W is the weight fraction, I_m the measured intensity and the subscripts represent the element. k_{JA} are the *Cliff-Lorimer ratios*. They can be measured with thin standard specimens of known composition (Cliff-Lorimer method) or calculated for each pair of elements if their ionic cross-sections, fluorescence yields and the detector efficiencies are known (*standardless method*). Then, the ratios are used for other samples containing the corresponding elements. The Cliff-Lorimer method is the most precise one but it imposes a heavy task before obtaining the first results. In this work all the quantifications were done with the standardless method. The thickness of the sample was not taken into account in most of our quantifications on the elements Al, Mg, Si, Cu, Ag because Al, Mg, and Si are very close elements and because the Cu or Ag contents are very low (which reduces the eventual absorption by these elements of X-rays produced by the light atoms). In other cases, for example for the quantification of O, absorption is evaluated after estimating the sample thickness with the thickness fringes observed by TEM in two beam conditions. A precision of 10% can be expected in the quantification (1% with the Cliff-Lorimer method), and of 0.1% for detection threshold in the absence of overlaps. The spatial resolution directly corresponds to the probe size (10 nm for the CM20 microscope and 1 nm for the HF2000 microscope) thanks to the thinness of the TEM samples.

3.4 Electron Scattering: From Diffusion to Diffraction

3.4.1 Diffusion

The electrons are quantum relativistic particles, by consequence their behavior is described by the Dirac equation which time independent Schrödinger equation of classic quantum mechanic (with relativist corrections in the mass of the electron) constitutes a good approximation [48]. Neglecting the interactions between the electrons, the equation for an electron before its interaction with the crystal is

$$\nabla^2 \Psi(r) + 4\pi^2 k^2 \Psi(r) = 0 \quad (3.3)$$

3. Transmission Electron Microscopy

where $\Psi(\mathbf{r})$ is the wave function associated to the electron and \mathbf{k} the wave vector of the electron which is linked to the tension of acceleration U by $k = |\mathbf{k}| = \sqrt{2meU}/h$, where m is the relativist mass of the electron given by $m = m_0(1-\beta^2)^{-1/2}$ where $\beta = v/c$, and e is the absolute value of its charge.

The solution of equation (3.3) is the plane wave function (non-localization plane of the electron) given by $\Psi^{(0)}(\mathbf{r}) = \exp[-2\pi i(\mathbf{k}^{(0)} \cdot \mathbf{r})]$.

During the interaction of the electron with the crystal, the equation is

$$\nabla^2\Psi(\mathbf{r}) + \frac{8\pi^2me}{h^2}[U + V(\mathbf{r})]\Psi(\mathbf{r}) = 0 \quad (3.4)$$

where $V(\mathbf{r})$ is the potential of the crystal. This differential equation can be expressed by an integral form in all the volume of the crystal with the help of the Green function $G(\mathbf{r}, \mathbf{r}') = \frac{\exp[-2\pi ik|\mathbf{r}-\mathbf{r}'|]}{4\pi|\mathbf{r}-\mathbf{r}'|}$. It is called the *diffusion equation*:

$$\Psi(\mathbf{r}) = \exp[-2\pi i(\mathbf{k}^{(0)} \cdot \mathbf{r})] + \frac{8\pi^2me}{h^2} \int_{\Omega} V(\mathbf{r}')\Psi(\mathbf{r}') \frac{\exp[-2\pi ik|\mathbf{r}-\mathbf{r}'|]}{4\pi|\mathbf{r}-\mathbf{r}'|} dv' \quad (3.5)$$

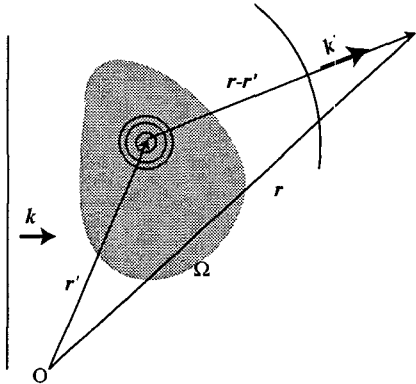


Fig. 3.4 Scattering of an electronic plane wave.

where \mathbf{k} is vector respecting $|\mathbf{k}| = |\mathbf{k}^{(0)}|$. With this equation, one can see that the crystal potential in \mathbf{r}' makes diffuse the electron wave in the \mathbf{k} direction by the intermediate of a spherical wave and a transmission factor given by $(2\pi me/h^2)V(\mathbf{r}')$ (Fig. 3.4). This is closely akin to the optical Huygens approach and its general Kirchhoff's formulation [49]. This equation can be solved with some approximations on the form of the electron wave function under the integral (Born approximations). Details are given in [49, 50, 51].

In all the following work, the problem is simplified with the *first Born approximation*, which supposes that the electrons do not interact or interact only one time with the sample. This condition is obtained for a weak $V(\mathbf{r})$ and a thin sample; this constitute the *kinematical condition*. The wave function can be written as $\Psi(\mathbf{r}) = \Psi^{(0)}(\mathbf{r}) + \Psi^{(1)}(\mathbf{r})$, with $|\Psi^{(1)}| \ll |\Psi^{(0)}|$. We can therefore replace $|\Psi(\mathbf{r}')|$ by $|\Psi^{(0)}(\mathbf{r}')|$ in the integral. Assuming that $|\mathbf{r}| \gg |\mathbf{r}'|$, it follows that $|\mathbf{r}-\mathbf{r}'| = r - (\mathbf{r}' \cdot \mathbf{k})/k$. Equation (3.5) can be written

$$\Psi^{(1)}(\mathbf{r}) = \frac{2\pi me}{h^2} \frac{\exp[2\pi i\mathbf{k} \cdot \mathbf{r}]}{r} \int_{\Omega} V(\mathbf{r}') \exp[2\pi i\mathbf{u} \cdot \mathbf{r}'] dv' \quad (3.6)$$

where $\mathbf{u} = \mathbf{k}^{(0)} - \mathbf{k}$. This expression is very close to that deduced from the general Kirchhoff formula in the *Fraunhofer diffraction* conditions [49]. The integration is done on the volume Ω where the potential is significant; by default the infinity must be taken. It follows that the

amplitude of the scattered wave is

$$A(\mathbf{u}) = K \int_{\Omega} V(\mathbf{r}) \exp[2\pi i \mathbf{u} \cdot \mathbf{r}] d\mathbf{v} \quad (3.7)$$

where $K = 2\pi m e / h^2$. The scattered wave function has the form of a Fourier transform integral of the crystal potential. If we neglect the effects of interatomic binding and interactions of atoms on the diffraction intensities, the total potential corresponds to the sum of the contributions of individual atoms a centered at the positions \mathbf{r}_a :

$$V(\mathbf{r}) = \sum_a V_a(\mathbf{r} - \mathbf{r}_a) \quad (3.8)$$

where V_a is the potential of each individual atom. Equation (3.7) can be written (the atoms being ordered or disordered)

$$A(\mathbf{u}) = K \int \sum_a V_a(\mathbf{r}' - \mathbf{r}_a) \exp[2\pi i \mathbf{u} \cdot \mathbf{r}'] d\mathbf{v}' \quad (3.9)$$

or, by exchanging the sum and the integral:

$$A(\mathbf{u}) = \sum_a f_a^B(\mathbf{u}) \exp[2\pi i \mathbf{u} \cdot \mathbf{r}_a] \quad (3.10)$$

where $f_a^B(\mathbf{u})$ is the *atomic diffusion factor* of the atom a given by

$$f_a^B(\mathbf{u}) = K \int V_a(\mathbf{r}) \exp[2\pi i \mathbf{u} \cdot \mathbf{r}] d\mathbf{v} \quad (3.11)$$

By these two equations, it appears that each atom acts as a diffusion center of spherical waves whose amplitudes are given by the atomic diffusion factor with a phase shift of $2\pi \mathbf{u} \cdot \mathbf{r}_a$. The atomic diffusion factor is proportional to the electron diffusion factor defined by

$$f_a^e(\mathbf{u}) = \int V_a(\mathbf{r}) \exp[2\pi i \mathbf{u} \cdot \mathbf{r}] d\mathbf{v} \quad (3.12)$$

This one is similar to the X-ray diffusion factor (the atomic potential is substituted by the electronic density), even if the interaction processes are different. Both are linked by the Mott formula deduced from the Poisson equation. In general, the atomic diffusion factors are calculated with equation (3.12) as done by Doyle and Turner, the atomic potential being estimated by relativist Hartree-Fock calculi [52, 53]. The very good comparison for Fe, Cu, Al between the calculated and experimental diffusion factors (better than 1% [54]) confirms the validity of equation (3.8). Analytical expressions are given for the diffusion factors in literature [55, 56]. Surprisingly, such analytical expressions do not exist for the radial atomic potential. Therefore, equation (3.12) has been inverted to obtain them. The calculus details are reported in annex A. We found

$$V(r) = -\frac{1}{2\pi r} \frac{d}{dr} \tilde{f}^e(r) \quad (3.13)$$

3. Transmission Electron Microscopy

This formula is used to calculate the radial potential from the analytical expression given by Doyle and Turner of the fitted diffusion factors. Annex A shows that if the diffusion factors are fitted by a sum of Gauss functions, the radial and projected potential is also a sum of Gauss functions. The knowledge of an analytical expression of the radial potentials was used to draw images of disordered materials (section 5.5.3).

3.4.2 Kinematical Diffraction

From equation (3.7), it can be noticed that the amplitude of the diffused spherical wave is proportional to the Fourier Transform (\mathfrak{F}) of the atomic potential of the sample, which is the sum of each atomic potential a situated in r_a . This Fourier Transform can be directly calculated by the Fast Fourier Transform algorithms (FFT) as illustrated with a finite size crystal in Fig. 3.5. The advantage of the FFT is that the amplitude can be calculated even for non-crystalline particles.

Under the conditions of equation (3.7), the appearance of spots in the diffraction pattern comes from the order that can exist in the sample (crystal, quasicrystal, or other type of order). Crystals are characterized by a translational periodic order (base of the crystallography). This crystal potential can be written

$$V_{cryst}(\mathbf{r}) = [V_a(\mathbf{r}) \otimes L(\mathbf{r})] \cdot E(\mathbf{r}) \quad (3.14)$$

where $V_a(\mathbf{r})$ is the atomic potential, $L(\mathbf{r})$ the periodic lattice of the crystal and $E(\mathbf{r})$ the envelope function corresponding to the crystal size. Thus, the amplitude of the diffracted wave (3.7) is proportional to

$$A_{cryst}(\mathbf{u}) \propto V_{cryst}(\mathbf{u}) = [\tilde{V}_a(\mathbf{u})\tilde{L}(\mathbf{u})] \otimes \tilde{E}(\mathbf{u}) \quad (3.15)$$

For a better illustration, let us reduce the problem to 1 dimensional crystal on size l and assume a Gaussian shape of the potential. The envelope function is then a slit function, where slit $(x, l) = 1$ for $|x| < l/2$ and 0 for $|x| > l/2$. Under these conditions, we have

$$V(x) = \exp[-(x/v)^2] \Rightarrow \tilde{V}_a(u) = \sqrt{\pi}v \exp[-(uv)^2] \quad (3.16)$$

$$L(x) = \sum_{n=-\infty}^{\infty} \delta(x - na) \Rightarrow \tilde{L}(u) = \sum_{n=-\infty}^{\infty} \delta(x - n/a) \quad (3.17)$$

$$E(x) = \text{slit}(x, l) \Rightarrow \tilde{E}(u) = \frac{\sin \pi l u}{\pi u} \quad (3.18)$$

This explains the shape of diffraction profiles, as illustrated in Fig. 3.5. The periodicity of the scattering pattern (diffraction) in $1/a$ comes from the periodicity of the lattice a . This corresponds to the *Laue condition* $\mathbf{u} = \mathbf{k}^{(0)} - \mathbf{k} = \mathbf{G}$ detailed in section 3.4.3. The enlargement in $1/l$ of the diffracted peaks comes from the crystal size l . For example, this effect produces the

streaks observed in the electron diffraction patterns acquired on the small θ' plates edge-on (Fig. 4.10c,d and Fig. 4.12a). The decrease of the peak intensity in u is of the order of $1/v$, it comes from the potential shape v . The broadening of the atomic potential can come from thermal vibrations of the atoms or from a mean disorder of the atoms around their lattice positions (due to random vacancies for instance). The scattering is therefore constituted by the Bragg peaks and two contributions significant for $u \ll 1/a$ (crystal size effect) and $u \gg 1/a$ (thermal vibration). Diffuse peaks can appear for u of the order of $1/a$, it reflects the appearance of superordering in the crystal. This point is treated in section 5.5.

For perfect parallelepiped-shaped crystals, another way to write the amplitude of the diffracted wave can be obtained from equation (3.10) by separating the sum on the lattice (with the volume limitation of the sample) and then on the unit cell:

$$\begin{aligned} A_{cryst}(\mathbf{u}) &= \sum_{lattice} \left[\sum_{cell} f_a^B(\mathbf{u}) \exp[2\pi i \mathbf{u} \cdot \mathbf{r}_a] \right] \exp[2\pi i \mathbf{u} \cdot \mathbf{r}_l] \\ &= F^B(\mathbf{u}) \cdot G^B(\mathbf{u}) \end{aligned} \quad (3.19)$$

$$\text{where } F^B(\mathbf{u}) = \sum_{cell} f_a^B(\mathbf{u}) \exp[2\pi i \mathbf{u} \cdot \mathbf{r}_a] \quad (3.20)$$

$$\text{and } G^B(\mathbf{u}) = \sum_{cell} \exp[2\pi i \mathbf{u} \cdot \mathbf{r}_l] \text{ where } |G^B(\mathbf{u})| = \frac{\sin \pi h l N_x}{\sin \pi h} \frac{\sin \pi k N_y}{\sin \pi k} \frac{\sin \pi l N_z}{\sin \pi l} \quad (3.21)$$

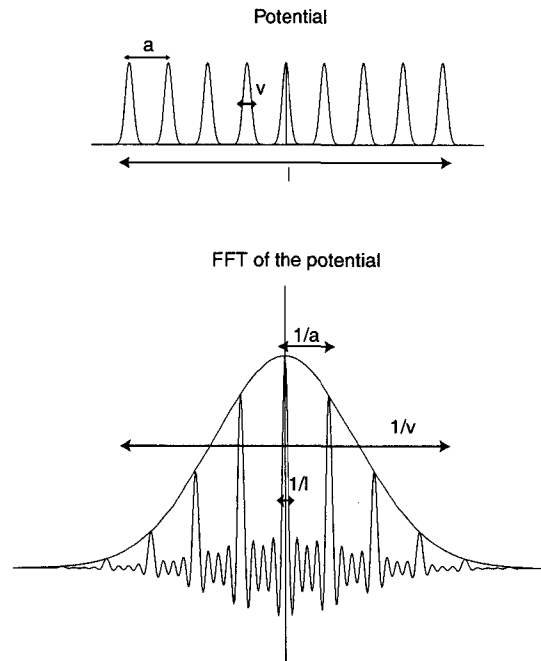


Fig. 3.5 One dimensional view of (a) the potential of a crystal and (b) its Fourier Transform (proportional to the amplitude of the diffused wave)

3. Transmission Electron Microscopy

where $\mathbf{u} = (h, k, l)$ and N_x, N_y, N_z are the numbers of unit cells constituting the lattice in the x, y, z directions. $F^B(\mathbf{u})$ is defined as the *structure factor*, it corresponds to the diffusion factor of the unit cell and includes de atom vibrations (3.16) by the intermediate of the atomic diffusion factor (3.11), and $G^B(\mathbf{u})$ is defined as the *shape factor*, it includes the lattice (3.17) and its envelope (3.18).

3.4.3 Bragg Law

Another way to describe diffraction is to notice that it occurs when the waves diffused by any cell separated by a vector of the lattice \mathbf{r} are in coherence, i.e. when the phase shift is $2\pi.n$ where n is a relative integer. This is written by $\mathbf{u} \cdot \mathbf{r} = n$ where $\mathbf{u} = \mathbf{k}^{(0)} - \mathbf{k}$. This condition is equivalent to impose that \mathbf{u} is vector of the reciprocal space. This is the *Laue law*:

$$\mathbf{u} = \mathbf{G} \quad (3.22)$$

Noting θ_B , the semi-angle between $\mathbf{k}^{(0)}$ and \mathbf{k} , by geometrical considerations, we can notice that $|\mathbf{u}| = 2\sin \theta_B/\lambda$, where λ is the wavelength of the electrons. Moreover, one property of the reciprocal vector is $|\mathbf{G}| = 1/d_{(h,k,l)}$ where $d_{(h,k,l)}$ is the interplanar spacing of the diffracting planes. Therefore, the Laue law $|\mathbf{u}| = |\mathbf{G}|$ gives the *Bragg law*:

$$2d_{(h,k,l)} \sin \theta_B = n\lambda \quad (3.23)$$

3.4.4 Ewald Construction

As illustrated in Fig. 3.5, it can be noticed that the Laue condition $\mathbf{u} = \mathbf{k}^{(0)} - \mathbf{k} = \mathbf{G}$ at the origin of the Bragg peaks is not completely required to obtain an intensity in the SAED pattern: the size effect of the sample or of the observed particle allows a tolerance around the Bragg peaks written by $\mathbf{u} = \mathbf{k}^{(0)} - \mathbf{k} = \mathbf{G} + \mathbf{s}_h$, where \mathbf{s}_h is called *excitation error vector*. The diffraction condition can be reported using the Ewald sphere as illustrated in Fig. 3.6. The diffraction pattern appears to be the intersection between the Ewald sphere and the reciprocal lattice of the crystal convoluted with the shape factor. A symmetric pattern corresponds to large \mathbf{s}_h at large \mathbf{G} vectors (called *Laue condition*) as in Fig. 3.6; a two beam condition corresponds to $\mathbf{s}_h = 0$ (called *Bragg condition*). The *zero order Laue zone* (ZOLZ) pattern corresponds to the intersection of the Ewald sphere with the vectors \mathbf{u} of the reciprocal space normal to a direction of the direct space \mathbf{r} called a *zone axis*: $\mathbf{u} \cdot \mathbf{r} = 0$. The *high order Laue zones* (HOLZ) patterns of index n correspond to the intersection of the Ewald sphere with the vectors \mathbf{u} of the reciprocal space linked to the zone axis by the Laue law: $\mathbf{u} \cdot \mathbf{r} = n$. A small convergence of the electron beam permits a loss of localization of the Ewald sphere which tilts around the $\mathbf{G} = (000)$ point, and favors the appearance of the spots on the diffraction pattern. This is useful for the observations of the HOLZ.

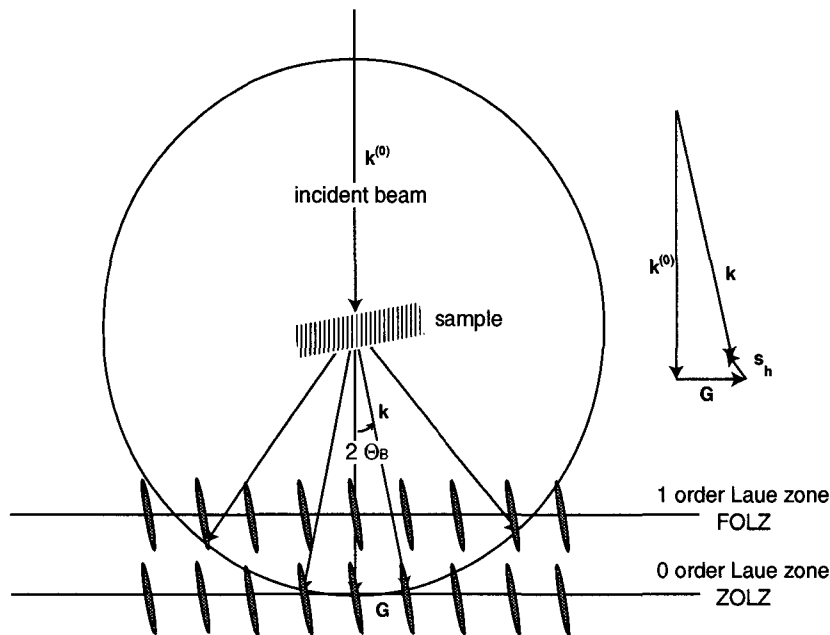


Fig. 3.6 Diffraction conditions $\mathbf{u} = \mathbf{k}^{(0)} - \mathbf{k} = \mathbf{G} + \mathbf{s}_h$ reported on the Ewald sphere $|\mathbf{k}^{(0)}| = |\mathbf{k}|$. Only the ZOLZ planes are represented. The spikes associated to the reciprocal space come from the sample size effect.

3.4.5 Dynamical Diffraction

In the previous part, the electron diffraction has been introduced with the first Born approximation (kinematical diffraction). For strong potentials, for large sample thickness (in comparison with a distance called the extinction distance), or when there are few diffracted beams with low $|\mathbf{s}_h|$ values, the intensity of the diffracted beams is not negligible in comparison to the transmitted beam, and the approximation is no longer valid. The transmitted and diffracted wave functions follow then a system of linear equations called the *Howie-Whelan equations*. They correspond to the coupling between the transmitted and diffracted beams. Details are given in [49, 50, 51].

3.5 Conventional Transmission Electron Microscopy

3.5.1 Imaging Mode

A transmission electron microscope is constituted of: (1) two or three condenser lenses to focus the electron beam on the sample, (2) an objective lens to form the diffraction in the back focal plane and the image of the sample in the image plane, (3) some intermediate lenses to magnify the image or the diffraction pattern on the screen. If the sample is thin (< 200 nm) and constituted of light chemical elements, the image presents a very low contrast when it is

3. Transmission Electron Microscopy

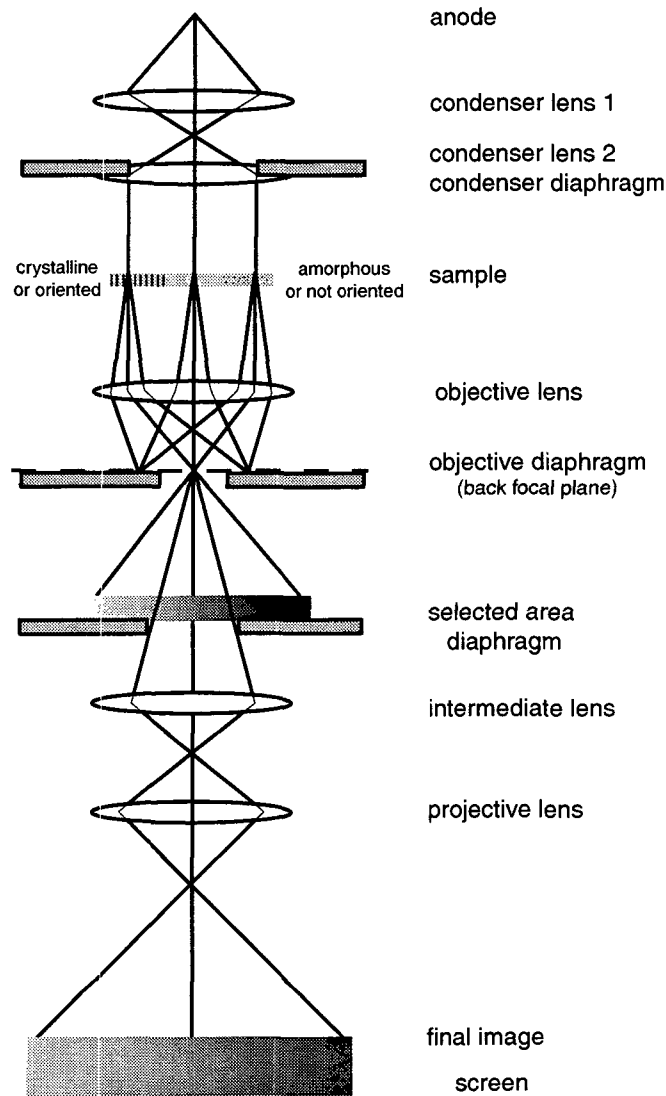


Fig. 3.7 Ray diagram for a transmission electron microscope in image mode. In diffraction mode, an other intermediate lens is inserted to image on the screen the diffraction pattern of the back focal plane.

focused. To obtain an amplitude contrasted image, an objective diaphragm is inserted in the back focal plane to select the transmitted beam (and possibly few diffracted beam): the crystalline parts in Bragg orientation appear dark and the amorphous or not Bragg oriented parts appear bright. This imaging mode is called *bright field* mode BF (Fig. 3.7). If the diffraction is constituted by many diffracting phases, each of them can be differentiated by selecting one of its diffracted beams with the objective diaphragm. To do that, the incident beam must be tilted so that the diffracted beam is put on the objective lens axis to avoid off-axis aberrations (Fig. 3.8). This mode is called *dark field* mode DF. The BF and DF modes are used for imaging materials to nanometer scale.

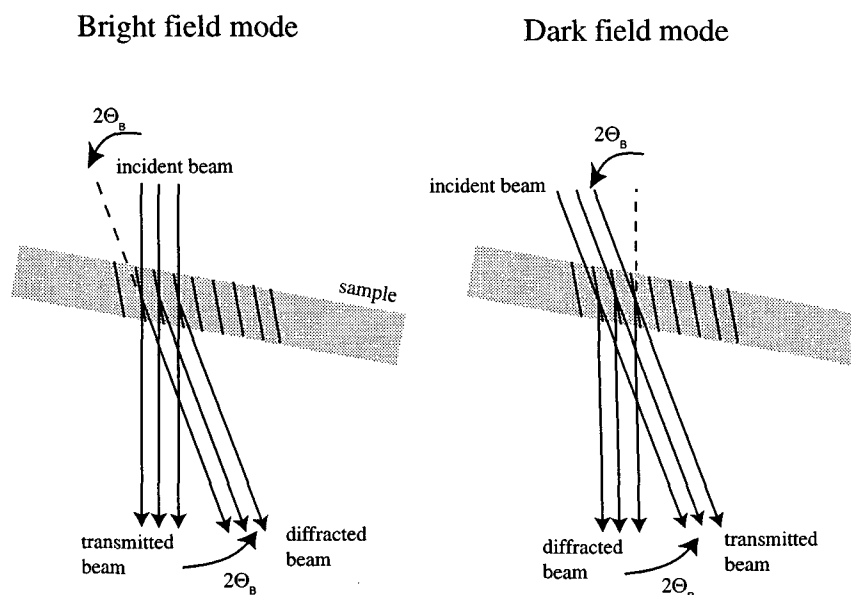


Fig. 3.8 Bright and dark field modes for imaging.

3.5.2 Diffraction Mode

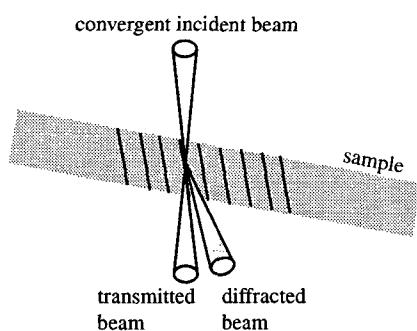


Fig. 3.9 Microdiffraction mode

The selected area diaphragm is used to select only one part of the imaged sample for example a particle or a precipitate. This mode is called *selected area diffraction* SAED. The spherical aberrations of the objective lens limit the area of the selected object to few hundred nanometers. Nevertheless, it is possible to obtain diffraction patterns of a smaller object by focusing the electron beam with the projector lenses to obtain a small spot size on the object surface (2-10 nm). The spots of SAED become disks whose radii depend on the condenser diaphragm. This is called *microdiffraction* (Fig. 3.9).

SAED and microdiffraction patterns of a crystal permit to obtain the symmetry of its lattice and calculate its interplanar distances (with the Bragg law (3.23)). This is useful to confirm the identification of a phase, after assumptions generally based on the literature of the studied system and on chemical analyses (see section 3.3).

These techniques were applied to identify the interfacial reaction products, intermetallic phases and fine precipitation in the AMCs (chapter 4).

3. Transmission Electron Microscopy

3.5.3 Special TEM Techniques

Microdiffraction and Convergent Beam Electron Diffraction CBED

As seen in the previous section, focusing the incident beam favors the acquirement of the HOLZ in the diffraction patterns. The whole pattern WP (ZOLZ + HOLZ patterns) and the bright field pattern BF (deficient HOLZ lines in the 000 disk) bring 3-D information on the observed crystal.

Microdiffraction gives the symmetry of the WP, this allows the determination of the Laue class and in consequence of the crystal system (see annex C.1). Moreover, the possible shift between the ZOLZ and the FOLZ patterns is connected with the Bravais modes, the possible periodicity difference between the ZOLZ and the FOLZ pattern is connected with the presence of glide planes. These pieces of information are a first step to the space group determination. Details are given in [57]. The advantage of this method is that it has few limitations, it allows the study of small particles [58], and the possibility of observing small areas allows quantitative measurements without any thickness or orientational variations.

CBED is more informative than microdiffraction. It uses the symmetry of the WP but also the details inside the diffraction disks in dynamical conditions to break the Friedel's law. The determination of the point group is based on the symmetry of the dynamical HOLZ lines¹ present in the transmitted beam and in the diffracted beam, and on the symmetry between +g/-g beams. Details are given in [59, 60]. In addition, the determination of the space group stands on the Gj_znes and Moodie lines² to assess all the helical axes or glide planes.

Some aspects of microdiffraction and CBED were used for the determination of some polytypic structures of the SiC particles (Fig. 4.8a). A quantitative study based on the intensity of ZOLZ disks obtained by microdiffraction were performed to determine the atomic positions in the precipitates present in the AlCuMgSi and AlMgSi alloys (Fig. 6.12).

Scanning Transmission Electron Microscopy STEM

The basic principle of image formation in the STEM is fundamentally different from static beam TEM: a small spot size is formed on the sample surface with the condenser lenses. This probe is scanned on the sample surface with scan coils, and in parallel, the signal is detected by an electron detector, amplified and synchronously displayed on a cathode-ray tube (CRT) with the scan coils. The detector can be a small disk on the column axis which detects only the transmitted beam (BF STEM image) or a diffracted beam (DF STEM image), or can

1. The HOLZ lines are observed as dark lines in the transmitted beam. They come from a deficit of electron due to an elastic scattering with the HOLZ planes (a bright line is observed in their corresponding spots). The HOLZ lines can be observed outside the transmitted beam when the electron beam has been inelastically scattered before the elastic collision. They are called Kikuchi HOLZ lines.

2. The Gj_znes and Moodie lines appear as dark lines in disks lighten in dynamical condition but which should have been extinguished in kinematical condition. They come from the presence of helicoidal axes or glide planes [61].

be an annular detector (a plate with a hole) which detects all the diffracted beams except the transmitted one (ADF STEM). The resolution of the image is only limited by the spot size (quality of the condenser lenses) since the objective lens is not used. In general, STEM images have poorer resolution but better contrast than TEM images. ADF STEM with high angle (>50 mrad) can be used to make chemical images¹, but in general the contrast in ADF STEM images is determined by the diffraction. This technique was used for the observation of the fine Si precipitates in the matrix of a WFA/Al₂O₃ composite (Fig. 4.16a).

3.6 High Resolution Transmission Microscopy

Conventional TEM uses only the transmitted beams *or* some of the forward scattered beams to create a diffraction contrast image. HREM uses the transmitted *and* the scattered beams to create an interference image. As it will be detailed in the following parts, the TEM microscope must have a high performance (low spherical aberrations and high stability of the high tension, of the lens currents and of the energy of the electron beam). The understanding of the image formation must take into account the two following steps: (1) the propagation of the incident wave through the object, (2) the transfer of the scattered wave by an optical system of the microscope (the objective lens).

3.6.1 Propagation through the sample

The propagation of the incident wave through the sample is usually treated with one of these two different methods: the Bloch waves method or the *multislice method*. Both are applicable to perfect crystals, but in addition the multislice method is also applicable to crystals with defects or to non-periodic structures. It is based on the physical optics approach given by Cowley and Moodie [62]. A complete description is given in [50, 51, 63].

The crystal of total thickness z is cut into many slices of small thickness Δz . The difference between the wave vector in vacuum $k_v = \sqrt{2meU}/h$ and the one in each slice $k_m = \sqrt{2me(U + V(r))}/h$ creates a refraction index given by

$$n_r = (k_m/k_v) = \sqrt{(U + V(r))/U} \cong 1 + V(r)/2U \quad (3.24)$$

which introduces a phase shift between the transmitted and the scattered wave

$$d\alpha = (k_m - k_v) \bullet dr = (n_r - 1)k_v dz = \frac{k_v}{2U} V(r) dz \quad (3.25)$$

1. Annular detectors with large holes called high angle ADF detectors can be used to detect the diffused electrons (the incoherence of high angle scattered electrons make the diffraction impossible) and form images with a signal proportional to the diffusion factor and therefore linked to the mass. These images are called *Z-contrast images*. They can reach atomic level resolution on the best TEM with FEG guns.

3. Transmission Electron Microscopy

Therefore, for each slice, the phase shift is given by

$$\Delta\alpha_n = \frac{k_v}{2U} \int_{z_n}^{z_n + \Delta z} V(x, y, z) dz = \frac{k_v}{2U} V_p(x, y, z_n) \quad (3.26)$$

where $V_p(x, y, z_n)$ is the projected potential of the n^{th} slice. When the wave Ψ_n comes through the n^{th} slice, the phase shift can be expressed by multiplying the wave function by a function called the *transmittance function* given by

$$q_n(x, y) = \exp[-2\pi i \Delta\alpha_n] = \exp[-i\sigma V_p(x, y, z_n)] \quad (3.27)$$

where $\sigma = (\pi k_v)/U = \pi/(\lambda U)$ is the relativistic interaction constant.

Then, we can consider that the wave propagates on a distance Δz . The propagation of a wave near an object follows the Fresnel approximation: the wave is convoluted with the Fresnel propagator:

$$p_{n \rightarrow n+1}(x, y) = \frac{\exp[-2\pi i \Delta z]}{i\lambda \Delta z} \exp\left[-\frac{i\pi}{\lambda \Delta z}(x^2 + y^2)\right] \quad (3.28)$$

In consequence, the multislice interaction cycle can be written

$$\Psi_{n+1} = (\Psi_n \bullet q_n) \otimes p_{n \rightarrow n+1} \quad (3.29)$$

which permits to calculate the wave after its propagation through the sample, called the *exit wave function* Ψ_e .

For a thin area constituted of light atoms, the exit wave function is given directly by equation (3.27) (only half an iteration), which can be developed to the first order:

$$\Psi_e(x, y) \cong 1 - i\sigma V_p(x, y) \quad (3.30)$$

This approximation is called *weak phase object* approximation. In this equation, the unity corresponds to the transmitted beam and the other term to the scattered beam. Since the diffracted beam is out of phase by $\pi/2$ with the transmitted one, it cannot interfere with the transmitted beam! Fortunately, as shown in the following section, the objective lens of the microscope additionally introduces another phase shift which makes the interference possible. Since the mean projected potential is about 200 V.Å for an Al atom (see annex A), σV_p is about 0.1 and the weak phase object approximation is restricted to one or two Al monolayers.

3.6.2 Transfer by the optical system

As usual in transfer theory, the wave transferred through the optical system (the image

wave) is the convolution between the object wave (exit wave) and a *transfer function* $T(\mathbf{r})$:

$$\Psi_i(\mathbf{r}) = \Psi_e(\mathbf{r}) \otimes T(\mathbf{r}) \quad (3.31)$$

which is equivalent to
$$\tilde{\Psi}_i(\mathbf{u}) = \tilde{\Psi}_e(\mathbf{u}) \bullet \tilde{T}(\mathbf{u}) \quad (3.32)$$

In coherent illumination, and without astigmatism, the transfer function T is given by

$$\tilde{T}(\mathbf{u}) = a(\mathbf{u}) \exp 2\pi i \chi(\mathbf{u}) \quad (3.33)$$

where
$$\chi(\mathbf{u}) = \frac{1}{4} C_s \lambda u^4 + \frac{1}{2} \Delta f \lambda u^2 \quad (3.34)$$

where $a(\mathbf{u})$ represents an optional diaphragm of size d in the back focal plane of the objective lens ($a(\mathbf{u}) = 1$ for $|\mathbf{u}| < d$ and 0 for $|\mathbf{u}| > d$), C_s is the spherical aberration coefficient of the objective lens and Δf a defocus value. In fact, the fluctuations of the incident electron energy, of the acceleration voltage and of the objective lens current added to an possible convergent beam effect, damp the CTF for the high spatial frequencies. All the terms of equation (3.34) can be written as envelope functions which limit the information of the HREM images.

In the case of a weak phase object, the image wave deduced by equations (3.30) and (3.31) is

$$\Psi_i(x, y) = [1 - i\sigma V_p(x, y)] \otimes T(x, y) = 1 + \sigma V_p \otimes \text{Re}T - i\sigma V_p \otimes \text{Im}T \quad (3.35)$$

Since $\sigma V_p \ll 1$, the image intensity is given by

$$I(x, y) = |\Psi_i|^2 = 1 + 2\sigma V_p \otimes \text{Im}T \quad (3.36)$$

Therefore, in the weak phase object approximation, only the imaginary part of the transfer function $\text{Im}T$ contributes to the intensity of the image by transmitting the phase information (the amplitude information, negligible for weak phase object, is transferred by $\text{Re}T$). $\text{Im}T$ is represented in Fig. 3.10 with two different defocus values.

Resolution and interpretation

As shown in Fig. 3.10, $\text{Im}T$ is an oscillating function whose shape depends on the defocus value. Each zero implies a loss of the phase information at the corresponding frequency. The “best” transfer function is the one close to 1 for the larger frequency scale. Scherzer has shown [64] that it can be obtained for a particular defocus value:

$$\Delta f_{Sch} = -\sqrt{\frac{4}{3} C_s \lambda} \quad (3.37)$$

At Scherzer defocus $\text{Im}T(\mathbf{u}) \approx -1$ in a large range of \mathbf{u} , therefore $\text{Im}T(x, y) \approx \delta_{x, y}$ and equation

3. Transmission Electron Microscopy

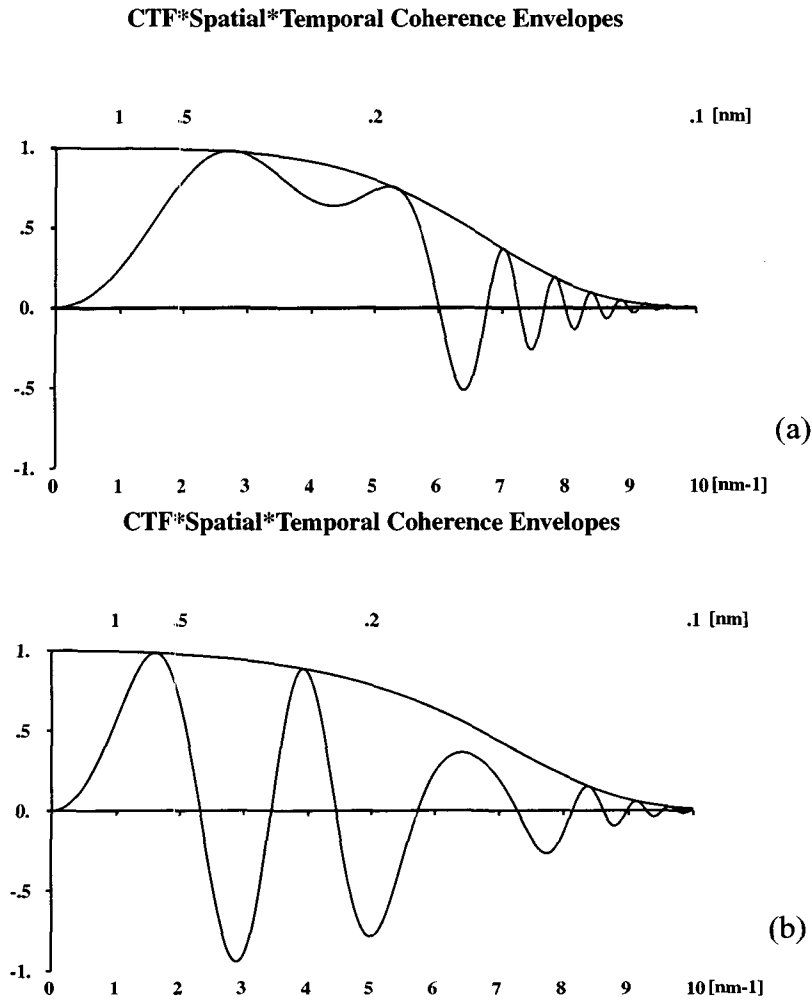


Fig. 3.10 Negative imaginary part of the effective transfer function $\tilde{T}(\mathbf{u})$ of the CM300UT-FEG microscope with their spatial and temporal damping envelopes at (a) $\Delta f = -48$ nm Scherzer defocus and (b) $\Delta f = -100$ nm

(3.36) gives

$$I(x, y) = 1 - 2\sigma V_p(x, y) \quad (3.38)$$

Under these conditions, the image is a direct representation of the projected atomic potential. Nevertheless, at Scherzer defocus $\text{Im}T(\mathbf{u}) \approx -1$ is valid only for frequencies smaller than the first zero of $\text{Im}T(\mathbf{u})$ noted h_{Sch} . This frequency defines the *point resolution* ρ of the microscope (also called Scherzer resolution):

$$h_{Sch} = 1.51 C_s^{-1/4} \lambda^{-3/4} \quad (3.39)$$

$$\rho = 1/h_{Sch} = 0.66 C_s^{1/4} \lambda^{3/4} \quad (3.40)$$

In fact, as shown in Fig. 3.10, information is transmitted at higher frequencies, but due to the oscillations, this information cannot be directly interpreted and simulations are required. The transmission is yet limited by the envelope damping functions and imposes an *information limit*.

3.7 Quantitative Electron Crystallography

3.7.1 Phase Loss Problem in Diffraction

All the information concerning the nature and the positions of the atoms is given by $A(\mathbf{u})$ (3.7) or, for crystalline materials, by the structure factor $F^B(\mathbf{u})$ (3.20). For a unit-cell constituted by many atoms, the atomic positions are in great part given by the phases of the structure factor [65, 66]. The diffraction intensities give only $|F^B(\mathbf{u})|^2$ and the phases are lost. This is the well-known phase problem of X-ray crystallography. Even if in general the number of relationships given by the link between $F^B(\mathbf{u})$ and the acquired intensities greatly exceeds the number of unknown atomic positions, no analytical solution exists. The only information on the direct space is given by the inverse Fourier Transform of $A(\mathbf{u})$:

$$P(\mathbf{r}) = \mathfrak{F}^{-1}(|A(\mathbf{u})|^2) = V(\mathbf{r}) \otimes V(-\mathbf{r}) = \int V(\mathbf{r})V(\mathbf{r} + \mathbf{R})d\mathbf{R} \quad (3.41)$$

where $P(\mathbf{r})$ is the *Patterson function*, which corresponds to the spatial autocorrelation function of the atomic potential. This formula is for example used in X-ray crystallography (replace the atomic potential by the electronic density) in the so-called *heavy atom method*.

Direct methods are also possible and effective thanks to the very good precision in the X-ray intensity measurements on large monocrystals [67]. These methods try to derive the structure factor phases directly from the obtained amplitude through mathematical relationships (Sayre's equations). However, these methods cannot be performed with electron diffraction due to the low precision in the intensities and some potential dynamical effects. The situation is changing with new CCD cameras and imaging plates, even if the curvature of the Ewald sphere remains a problem for the high spatial frequencies. Moreover, electron microscopists are more interested in mixed structures or small particles which are very difficult to study by X-rays.

3.7.2 HREM "Direct" Methods

The direct interpretation of an HREM image is only possible on very thin samples (weak phase object) at Scherzer defocus. In general, these conditions are not fulfilled and the problem remains unsolved: "what is the structure?". Some position parameters of a previous physical structural model can be refined by exploiting the CBED intensities [68]. However, in total absence of any previous physical model, some authors have worked to exploit the HREM images as much as possible to elaborate this crystal model that is further refined using the

3. Transmission Electron Microscopy

diffraction intensities. Indeed, although HREM images contain some phase information characteristic of the atomic positions, the resolution obtained is low due to the CTF functions; on the other hand, diffraction patterns contain information up to higher frequencies due to the absence of any CTF, but only in modulus form. The use of HREM images and/or electron diffraction patterns for structure determination is called *electron crystallography* [69]. This technique dates from the 1950's [70] but has not been widely used until the two last decades due to the complexity of the dynamical effects. Actually, electron crystallography is a complementary technique of X-ray crystallography: the strong interaction between electron and matter (thousands of times stronger than X-rays) enables the structural determination of crystals of a few nanometers size with, in some cases, precisions on the atomic positions comparable to those obtained with X-rays ($\sim 0.02 \text{ \AA}$). Two electron crystallography techniques based on HREM images have recently emerged:

(1) the reconstruction of the exit wave by acquiring HREM images at different defocus values named *through focus exit wave reconstruction* (TF-EWR) [71, 72]. The resulting structure is refined with the diffraction intensities recorded on a CCD camera, with a software which includes the excitation error and the dynamical effects, called *multi-slice least squares* (MSLS) [73]. The atomic position precision is $\sim 0.2 \text{ \AA}$. This method has several drawbacks such as the necessity to know exactly the defocus steps and the heavy task to treat 20 HREM images. Moreover, one fundamental difficulty (but very shortly treated by the authors) is the passage from the exit wave function to the determination of the chemical element and its real position. For example, the structure of the β'' phase in the AlMgSi alloys was claimed to be successfully determined [74] with excellent reliability factors. The determination was, however, based on a composition Mg_5Si_6 determined by chemical X-ray analysis performed on the precipitate embedded in the Al matrix whereas recent X-rays studies on β'' precipitates extracted from the Al matrix reveals the presence of Al (30%-at) [75, annex B2].

(2) the processing of HREM images of thin samples by *crystallographic image processing* (CRISP) [76]. This permits to extract the phase and the amplitudes of the HREM image and correct them by considering the changes introduced by the transfer function, the astigmatism (and possibly the tilt). The second step imposes to this corrected image the "most probable" symmetry (determined by minimizing the sum on each reflection of the phase differences between the image and the "symmetrized" image in which the phases of some reflection are linked by the symmetry). The structure is then refined with the SAED intensities, using a computer program which uses the X-ray refinement methods with the electron diffusion factors. A precision close to the X-rays one ($\sim 0.02 \text{ \AA}$) is obtained [77]. The drawback of the method is the need for very thin samples, so as to be as close as possible to the weak phase object approximation. Moreover, large objects are required to evaluate correctly the validity of the symmetrization since the method relies in great part on the hypothesis of the periodicity of the crystal. Therefore, this method is not well adapted to observations of defects or disorder, but remains a high-performance, crystallographic "filtering" process.

3.7.3 HREM Simulations

Once a structural model is proposed for a crystal, its validity should be checked by HREM image simulations, at least when the sample is not a weak phase object. However, this is rarely done by the users of direct HREM methods. The HREM simulations must take into account the crystal parameters (the model structure to be checked, with the Debye-Waller factors and its structure factor), its thickness, and some TEM parameters such as C_s , Δf , the crystal tilt, the accelerating voltage, the beam divergence and the astigmatism. Simulation programs are available [78].

In this work, the crystallographic structure of the β' phase has been determined (see section 6.3) by the refinement of the atomic positions given by a previous model with the intensities of microdiffraction patterns. HREM simulations were performed to check the refined structure. The two “direct” methods could not be applied due to their major drawbacks.

3.8 TEM Facilities

All the TEM observations have been done at the Interdepartmental Center of Electron Microscopy (CIME, EPFL). Most of the chemical analyses, and all the SAED and microdiffraction patterns and superstructure images were performed on a conventional Philips CM20T-LaB₆ TEM microscope operating at 200 kV and equipped with a EDS Noran Voyager. DSTEM images, some EDS measurements on small rod-shaped precipitates, and HREM images have been performed on an Hitachi HF2000-FEG TEM microscope operating at 200kV. Most of the HREM images have been obtained with a Philips CM300UT-FEG TEM operation at 300kV. All HREM images were acquired on a CCD camera using the Gatan Digital Micrograph software. Their eventual processing has been done with this software. TEM in-situ heating experiments were performed on the CM20 microscope using a Gatan double tilt heating holder. The parameters of the microscopes are presented in Table 3.1.

3. Transmission Electron Microscopy

	Philips CM20T-LaB ₆	Hitachi HF2000-FEG	Philips CM300UT-FEG
E_0 [kV]	200	200	300
C_s [mm]	2.0	1.2	0.6
ρ [nm]	0.28	0.23	0.17
s [nm]	10	5	6
α [mrad]	1	0.25	0.25
d [nm]	10	1.5	2.2

Table 3.1 Parameters of the TEM microscopes used in this work. E_0 accelerating voltage, C_s spherical aberration coefficient, ρ point resolution, s focus spread, α semi-angle of convergence, d smallest probe size.

Chapter 4

Microstructure of the WFA/Al₂O₃/sf and WFA/SiC/p Composites

This chapter gives the main results concerning the microstructures of the WFA/Al₂O₃/sf/s, WFA/Al₂O₃/sf/a and WFA/SiC/p composites. The grain size and microsegregations are observed by SEM and reported in section 4.1. The interfacial reactions between the matrix alloy and the reinforcements during the processing are characterized by TEM and thermodynamically discussed in section 4.2. The Mg present in the alloy will be shown to have a primary role (direct or indirect) on the reactions. The precipitation states in the matrices of the composites are determined by TEM in section 4.3. It will be shown that for all the studied composites the interfacial reactions lead to release of Si in the matrices, which completely modifies their precipitation state. Section 4.4 deals with the identification of nanosized plates and rod-shaped precipitates. The influence of the microstructural parameters on the mechanical properties is discussed in section 4.5. Perspectives for the improvements of the mechanical properties in terms of microstructural design by modification of the chemical composition of the alloy or by change of some of the processing parameters are proposed.

4.1 Grains and Microsegregation

4.1.1 Grain Sizes and Morphologies

WFA/Al₂O₃/sf Composites

The grains in the composite have different morphologies depending on their positions in the infiltrated preform. Their microstructure exhibits chill/columnar/equiaxed zones (Fig. 4.1) corresponding to the classical ingot structure [79]. The chill zone (1 mm layer) is constituted by small equiaxed grains at the edges, at the top and at the bottom of the infiltrated material because these zones are a high nucleation and multiplication area (maintained at 300°C). The columnar zone (1 cm layer) is constituted by columnar grains which grow in the liquid temperature gradient. The equiaxed zone (3 mm layer) is constituted by equiaxed grains which have grown ahead of the columnar grains in sufficient quantity and size to impede the advance of the columnar front. This microstructure is in agreement a centripetal solidification deduced from the temperature gradient simulations performed by CALCOM [4] (the final solidification occurs in the junction part, it lasts ~20 s).

Other differences can be observed in the morphologies and sizes of the grains: they are thin and columnar in the reinforced preform and larger and more equiaxed in the unreinforced part (Fig. 4.1). Moreover, as shown in the optical views of the micro-grain structures reported in Fig. 4.2*a,b*, the dendritic solidification of the alloy is no longer observed when it is reinforced. Without detailing, it can be said that two combined effects are at the origin of such changes [1, 2, 80]: (1) the liquid in areas close to the fibers is more slowly cooled and solidified than in the others areas due to the high calorific capacity of the ceramic fibers (in comparison to the alloy), and (2) the reinforcements act as a barrier to the mass transfer.

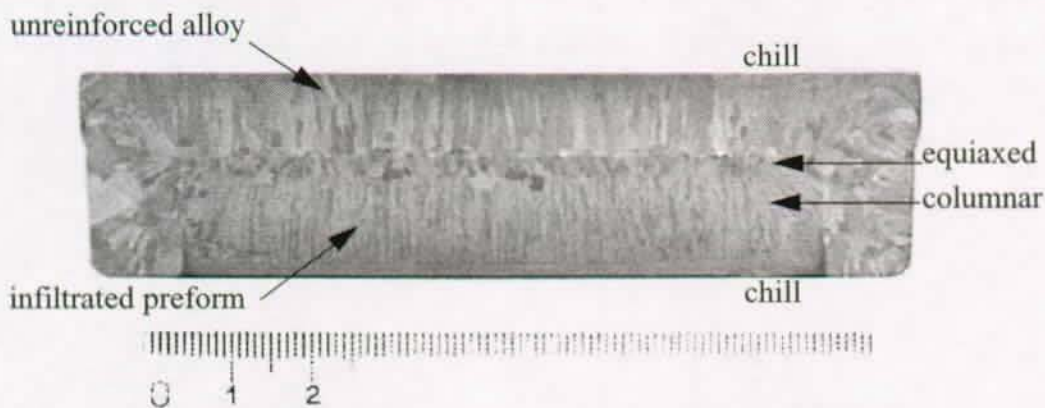


Fig. 4.1 Optical view of the grain morphologies and sizes of the WFA/Al₂O₃/sf/s composite (from EMPA-Thun)

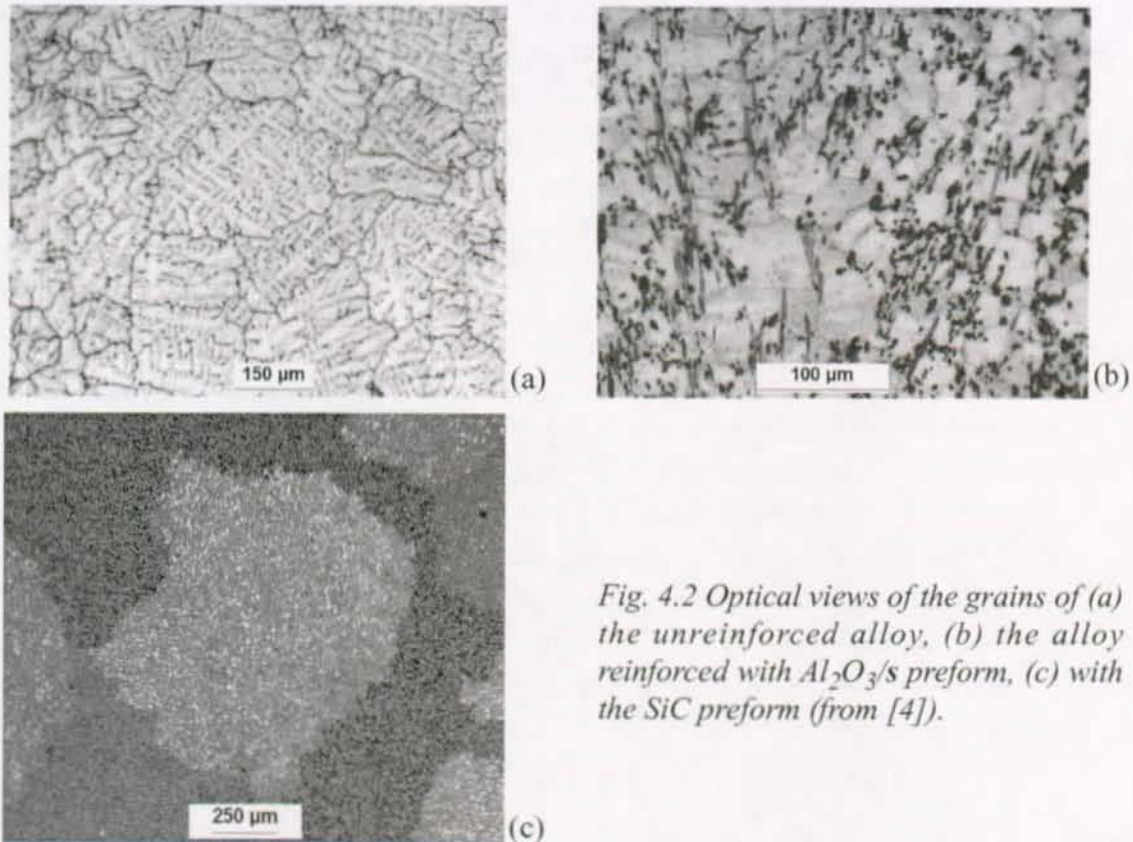


Fig. 4.2 Optical views of the grains of (a) the unreinforced alloy, (b) the alloy reinforced with Al_2O_3/s preform, (c) with the SiC preform (from [4]).

WFA/SiC/p Composites

The grain morphologies and sizes in the WFA/SiC/p composites cannot be observed by optical microscopy at the magnification used in Fig. 4.1 because of the high volume fraction of SiC particles (50%). Nevertheless, as shown in Fig. 4.2a,c, contrarily to the WFA/ Al_2O_3/sf composites, the sub-grains in the infiltrated SiC preform are larger than in the unreinforced matrix alloy. They are equiaxed and here again the dendritic grow pattern can no longer be observed. This sub-grain enlargement is quite unusual in AMCs, but can be understood considering that the average distance between dendrites in the unreinforced alloy is larger than the average distance between the SiC particles, i.e. the SiC impedes the formation of the dendrites. An confirmation was given by Gungor [81], who observed that the dendritic growth can no longer be observed and that the microsegregation is significantly reduced when the solidification time is increased so that the average distance between dendrites is larger than the one between particles (unfortunately he did not directly study the grain sizes).

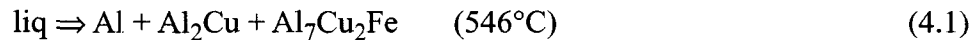
4.1.2 Primary Intermetallics Compounds

This section reports the coarse intermetallic compounds, i.e. those formed in the alloy during the solidification. The reaction products are reported in section 4.2.

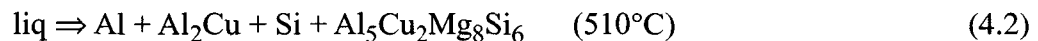
In the unreinforced T6 alloy, an important segregation at grain boundaries of $\theta-Al_2Cu$ was observed by SEM (Fig. 4.3a). Al_7Cu_2Fe phase could also be identified by TEM; it comes

4. Microstructure of the WFA/Al₂O₃/sf and WFA/SiC/p Composites

from Fe-impurities of the alloy. Both compounds are formed during the solidification, they have a globular shape (~5 μm) and are not completely dissolved during the heat treatment. Due to their temperatures of formation (>510°C), these coarse intermetallic phases appear in the mushy state (before the final solidification) from the enrichment of the solute elements and impurities ahead the solidification front, and then migrate during solidification in interdendritic areas. The low temperature ternary eutectic reaction [82] is:



In the as cast WFA/Al₂O₃/sf and WFA/SiC/p composites, the same segregation of θ-Al₂Cu and Al₇Cu₂Fe phases (~1 μm) was observed by SEM (Fig. 4.3b,d). These phases appear at the fiber-matrix interfaces (< 2 μm) or at the grain boundaries (< 0.5 μm). Both generally have a globular shape, but the Al₇Cu₂Fe compounds were also often observed at fiber-matrix interfaces with an elongated shape (> 5 μm). Two other types of coarse insoluble intermetallic phases were observed and identified by TEM: Q-Al₅Cu₂Mg₈Si₆ and Al_xCuSi₂Fe₃. The two phases contain Si and were not observed in the unreinforced alloy. The Q-Al₅Cu₂Mg₈Si₆ phase usually appears at the fiber-matrix interface with a globular or hexagonal shape (~1 μm). In the present situation, the Q-phase was probably formed during the following reaction [82]:



The Al_xCuSi₂Fe₃ compounds were observed in the matrix or at interfaces between two reinforcements. Their composition was determined by EDS. The Al concentration is quoted by *x* because the obtained result *x* = 18 may be over-estimated due the aluminum present in the surrounding matrix and excited by the back scattered electrons spiralling in the objective lens magnetic field. Our TEM observations are in good agreement with a BCC structure with lattice parameter *a* = 1.248 nm ± 0.005 nm. A similar phase has also been reported in a recent study on 6xxx/SiC composites [83]: Al₁₅(Mn,Fe,Cu)₃Si₂ BCC with *a* = 1.28 nm. In addition, Mg₂Si (~1 μm) compounds were clearly identified by SEM and TEM in the WFA/SiC/p composites but no in the WFA/Al₂O₃/sf composite.

This microsegregation appears in all the studied composites at the reinforcement/matrix interfaces. It was proposed by Rohatgi [84] that the microsegregation comes from a nucleation process on the reinforcements. Nevertheless, as previously said for the change of the grain sizes and morphologies, and according to Fig. 4.3c,d, the microsegregation morphology of the studied composites stands on other mechanisms: (1) the interfacial areas are more slowly cooled and (2) the reinforcements act as a barrier to the mass transfer.

In the T6 WFA/Al₂O₃/sf and WFA/SiC/p composites, i.e. after solution heat treatment at 500°C and peak aging (T6-temper), the θ-Al₂Cu, Q-Al₅Cu₂Mg₈Si₆ and Mg₂Si phases are found smaller (~0.2 μm). Hence, these compounds were dissolved to some extent by the heat treatment, even if coarse ones remain in some parts of the samples as observed by SEM (Fig. 4.3c,e). The Al₇Cu₂Fe and Al_xCuSi₂Fe₃ phases have the same size as in the as-cast state because they are insoluble during the heat treatment at 500°C.

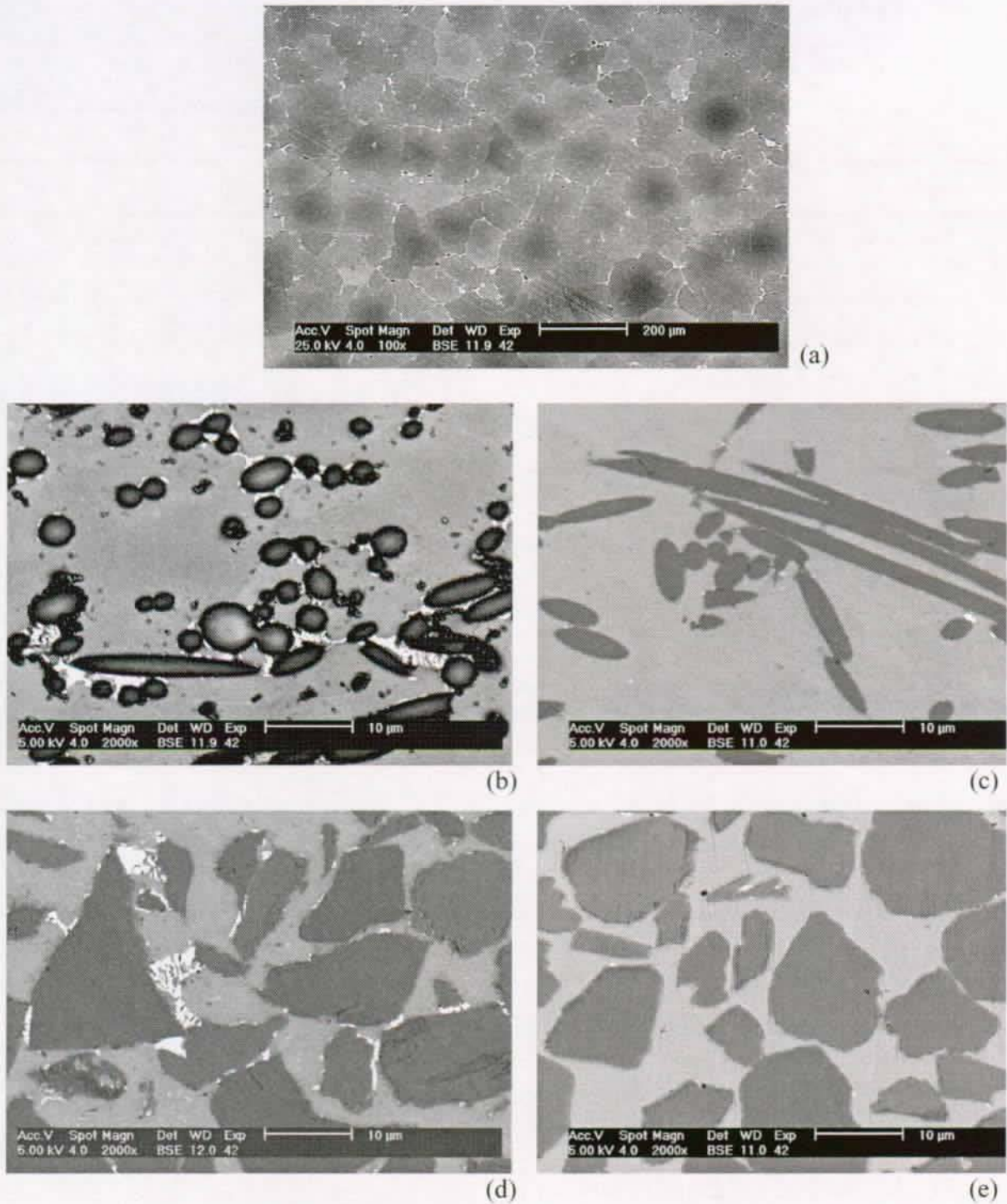


Fig. 4.3 BSE SEM observations of the microsegregation (mainly θ - Al_2Cu) in
 (a) WFA unreinforced alloy (T6),
 (b) WFA/ Al_2O_3 /sf composite (as-cast),
 (c) WFA/ Al_2O_3 /sf composite (T6),
 (d) WFA/SiC/p composite (as-cast),
 (e) WFA/SiC/p composite (T6).

4. Microstructure of the WFA/Al₂O₃/sf and WFA/SiC/p Composites

4.1.3 Chemical Composition of the Matrices

The effective chemical composition of the WFA matrix alloy is given in Table 4.1.

Al	Cu	Mg	Ag	Fe	Si
bal	4.03	1.04	0.53	0.03	0.043

Table 4.1 Effective chemical composition of the unreinforced matrix alloy in wt. %

The EDS measurements of the composition of the matrices of the WFA/Al₂O₃/sf and WFA/SiC/p composites in the T6-temper are provided in Table 4.2 for comparison with the unreinforced matrix alloy.

material	Cu	Mg	Ag	Si
unreinforced alloy	2.9	2.0 (imprecise)	0.5	0.0
WFA /Al ₂ O ₃ a	2.4	0.05 (imprecise)	0.4	0.3
WFA /Al ₂ O ₃ s	3	0.1 (imprecise)	0.7	0.6
WFA /SiC	2.3	0.6 (imprecise)	0.7	3.2 (artifact)

Table 4.2 Chemical composition of the unreinforced matrix alloy and of the composite matrices in the T6-temper in wt. % (EDS analyses in the middle of the grains)

The presence of Si in the matrix of the WFA/Al₂O₃/sf composite is evident, but the high signal of Si measured in the WFA/SiC/p composite was certainly over-estimated because of the large content of SiC particles present around the matrix. No reliable results for Mg concentration could be obtained by this method because of the proximity of the small Mg peak to the large Al K_α peak, which results in a very poor deconvolution quality with standard analyses. Since the reference alloy is virtually free of Si (0.043%), it was thought that Si was released into the matrix of the composites, probably as a consequence of interfacial reactions between the reinforcements and the matrix alloy during the processing. To confirm this point, these interfacial reactions were studied and described in the following section.

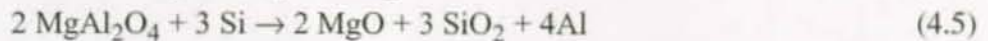
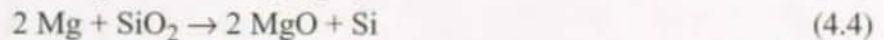
4.2 Interfacial Reactions

4.2.1 WFA/Al₂O₃/sf/s Composites

In the as-cast WFA/Al₂O₃/sf/s composites, EDS measurements and SAED patterns revealed that most of the SiO₂ binder has reacted with Mg to form a spinel MgAl₂O₄ (FCC structure with $a = 0.8045$ nm) as shown in Fig. 4.4.

In the WFA/ Al_2O_3 /sf/s composites (T6), EDS measurements and SAED patterns revealed that the core of this modified binder has been transformed into nanocrystalline MgO as shown in Fig. 4.5a,b. Small precipitates (10-100 nm) were also observed at the edges of the reacted binder or at fiber crossing points. They correspond to θ - Al_2Cu and $MgAl_2O_4$ spinel, as identified by EDS and SAED (Fig. 4.5).

Hence, the possible reactions associated with the release of Si and the depletion of Mg in the matrix are:



The presence of large $MgAl_2O_4$ spinel crystals substituting the SiO_2 binder in the as-cast composite proves that the reduction of the binder occurred during the composite processing according to equation (4.3). The MgO observed in the T6 composite in the core part of the binder indicates that during the heat treatment the $MgAl_2O_4$ spinel crystals may have been transformed by reaction (4.4), or more probably, that the remaining SiO_2 reacted with Mg according to reaction (4.5). It is reported that reaction (4.3) occurs at low Mg content (1-4 at%), and reaction (4.4) at higher Mg content [85, 86]. The observations can therefore be explained considering that during the cooling from the liquid state, part of Mg was also trapped in the coarse Q and Mg_2Si intermetallic particles allowing only reaction (4.3), and that during the homogenization heat treatment that trapped Mg was released and available for reaction (4.4). Since reaction (4.3) is accompanied by a greater volumetric contraction than reaction

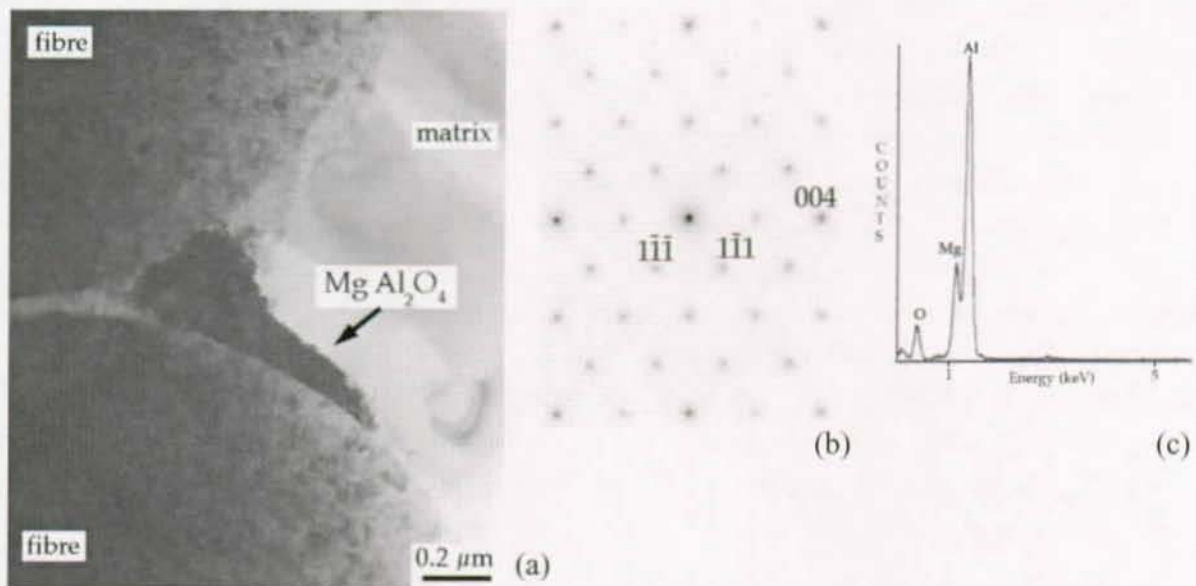


Fig. 4.4 Reacted binder in the WFA/ Al_2O_3 s composite (as cast): $MgAl_2O_4$ -spinel precipitates in the reacted binder. (a) Bright field image, (b) diffraction pattern in $[110]_{spinel}$ and (c) EDS spectrum.

4. Microstructure of the WFA/Al₂O₃/sf and WFA/SiC/p Composites

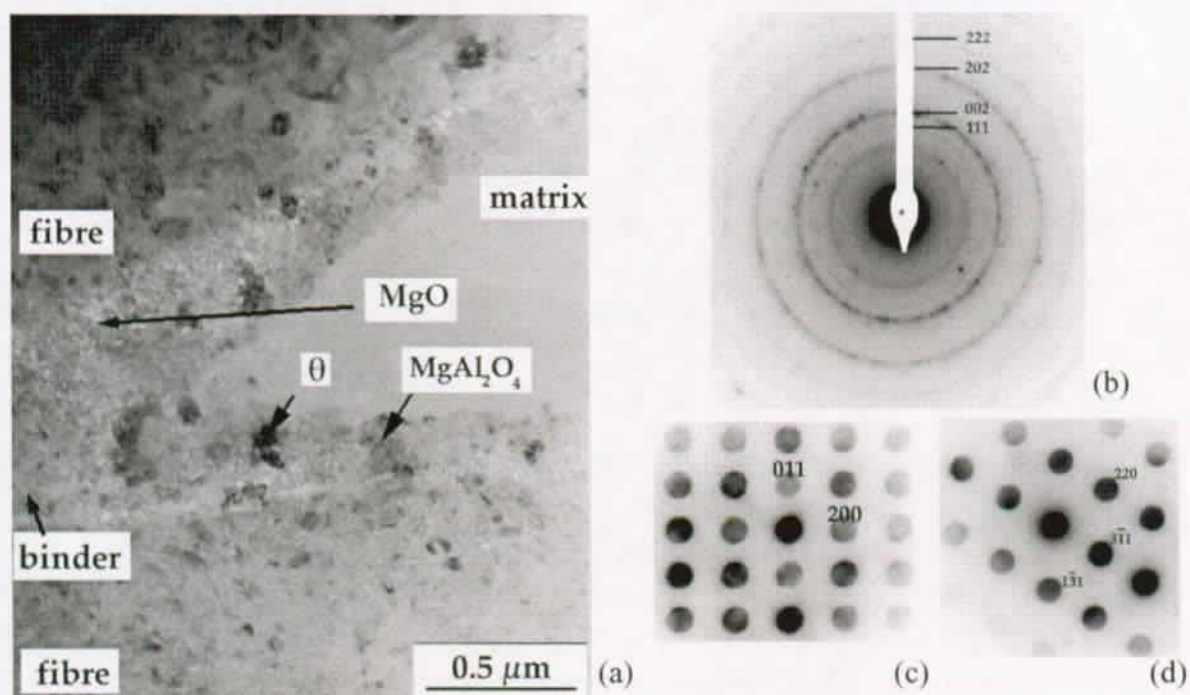


Fig. 4.5 Reacted binder in the WFA/Al₂O₃/sf/s composite (T6): polycrystalline MgO in the core of the binder, θ-CuAl₂, and MgAl₂O₄-spinel precipitates around the binder. (a) BF image, (b) diffraction rings of polycrystalline MgO, (c) θ-CuAl₂ diffraction pattern in [0 1]_θ zone axis and (d) MgAl₂O₄ diffraction pattern in [1 14]_{spinel} zone axis.

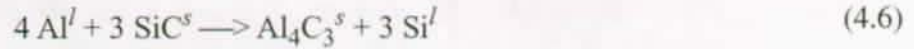
(4.4) the spinel is permeable to Al, whereas MgO can provide an effective barrier to the Al permeation and reaction with the Al₂O₃ fibers [86]. MgO and MgAl₂O₄ have been reported in many other studies on similar composites [87-90].

Part of the silicon released from the reaction was trapped in coarse insoluble compounds such as Q and Mg₂Si phase during the cooling after the infiltration and diffuses into the matrix during the heat treatment to form rod-shaped precipitates (section 4.2.4). According to the SiO₂ binder content, complete reaction of the SiO₂ in the binder could only provide about 0.3 %wt of Si to the matrix (the binder represents 5 wt.% of the fibers and the fibers 15%.vol of the material); this is considerably lower than the 0.6%.wt found in the matrix by EDS analyses (Table 4.2). Considering that SiO₂ is present inside the Saffil fibers (3-4 wt.% of fibers), a small amount of this fiber-SiO₂ may have also reacted with Mg and provide ~ 0.3%.wt of Si to the matrix. This figure was confirmed by EDS analysis on the WFA/Al₂O₃/sf/a composites (Table 4.2). It can be concluded that Si not only came from the SiO₂ binder but also from the SiO₂ contained in the δ-Al₂O₃ fibers.

4.2.2 WFA/SiC/p Composites

Thermodynamically, three reactions are possible, two between the Mg contained in the alloy and a potential SiO₂ oxidation layer at the surface of the SiC particles corresponding to

equations (4.3) and (4.4), and one directly between liquid Al and SiC:



In spite of careful TEM observations in the as-cast composite, neither MgO nor MgAl_2O_4 could be detected whereas small hexagonal plates of Al_4C_3 precipitate were observed in the as-cast composite (Fig. 4.6a,b). This proves that the oxide layer was very thin (in agreement with the figure of 0.12% wt of SiO_2 given by Norton [38]), and that reaction (4.6) occurred during the infiltration of the tap-packed SiC particles. The Al_4C_3 carbides were not dissolved by the heat treatment as confirmed by the TEM observations of the composite in T6-temper (Fig. 4.6c). It is reported that the formation of Al_4C_3 , even if limited, enhances the wettability with the Al matrix [91]. A larger amount of Al_4C_3 usually forms during heat treatments above 650°C [92-94] or also during very long heat treatments (several days) at 610°C when Al is its solid state [95]. This reaction is undesirable because of the high sensitivity of the carbides to water [94]; and the fabrication of Al/SiC AMCs devoid of large Al_4C_3 formation is one of the major concerns.

According to Iseki [92] or Lin [93], the standard free energy associated to reaction (4.6) can be expressed in the form $\Delta G_{Lin}^0 = 103900 - 16.5T$ in J/mol, and takes positive values (+81.2 kJ/mol at 1100°C), suggesting that the formation of Al_4C_3 is not very strong. According to Lee's annexes in [96], the standard free energy associated to reaction (4.6) is $\Delta G_{Lee}^0 = -40500 + 73T$ (after correction of a printing inversion error made in Table A.2 of [96]). This expression seems to be in contradiction with the ones given by Iseki [92] or Lin [93]. Nevertheless, Lee refers to equation (4.6) with Si in liquid state, whereas Iseki and Lin

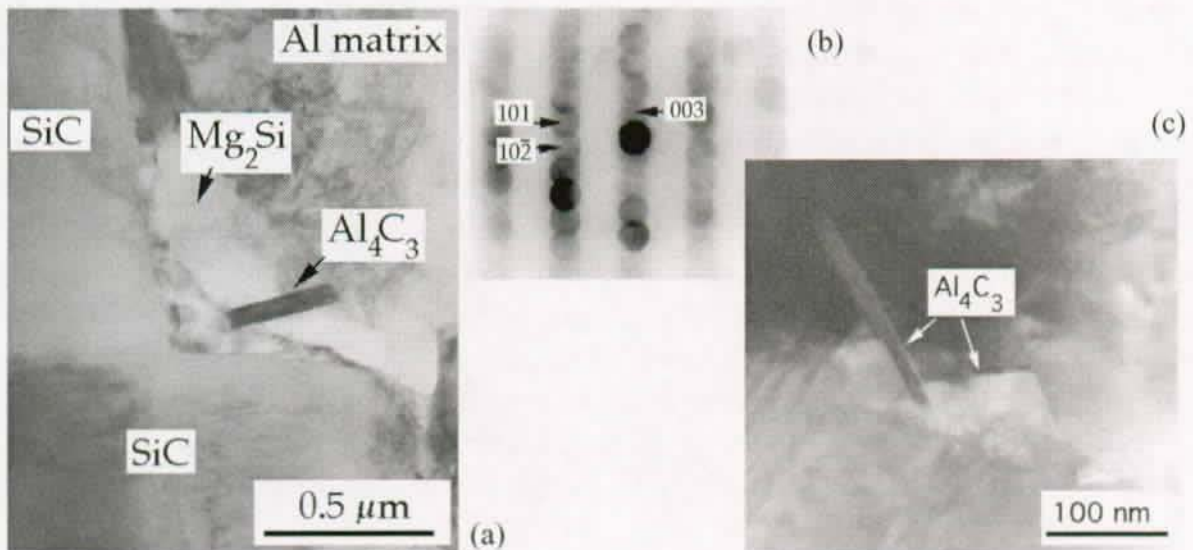


Fig. 4.6 Al_4C_3 hexagonal plate-shaped carbide produced by the interfacial reaction (4.6) (a) in the as-cast WFA/SiC/p composite with (b) its corresponding diffraction pattern; (c) in the composite (T6).

4. Microstructure of the WFA/Al₂O₃/sf and WFA/SiC/p Composites

refer to Si in solid state (which is not realistic for the studied reaction, the change of reference between Si^l and Si^s must be taken into account). Anyway, even with the Lee's expression, the standard free energy remains positive when Al is liquid, its value is +61 kJ/mol at 1100°C and +26 kJ/mol at 640°C, confirming the limited character of reaction (4.6).

Despite $\Delta G^0 > 0$, reaction (4.6) is thermodynamically possible provided that the Si content in the molten Al is low. This can be explained by the chemical activity of Si in Al (mainly representative of the mixing entropy) which makes strongly decrease the Gibbs free energy [92]. On this base, Kannikesaran [97] proposed a stability domain diagram in the Al/SiC system (another one set up from X-ray experiments is given by Viala [98]). Complete expressions of the Gibbs free energy of the reaction are reported by Iseki [92], or Lee [96]. Lee gave the following expression:

$$\Delta G = \Delta G_{Lee}^0 + 3RT \ln x - 4RT \ln(1 - x) + P_{Si}(x) + P_{Al}(x) \quad (4.7)$$

where P(x) are polynomials of degree 3 representative of the excess free energy of Si and Al, and $\Delta G_{Lee}^0 = \Delta G_{Al_4C_3}^0 - 3\Delta G_{SiC}^0$, where $\Delta G_{Al_4C_3}^0$ and ΔG_{SiC}^0 are the Gibbs free energies of formation of Al₄C₃ and SiC respectively by reference to the liquid Al. Lee calculated them on the base of Barin thermodynamic data [99] and took for references the liquid state of Al and Si. Lee used expression (4.7) to calculate the Si content required to prevent the formation of Al₄C₃ carbides, and reported approximately a content of 1%-at for Al solid and at least 7%-at for Al liquid (with a step at the Al melting temperature), in agreement with his experiments [96].

TEM studies on as-cast pure Al reinforced with non-oxidized SiC particles and produced by rapid processes such as squeeze-casting [100] or spray casting [101, 102] report that no Al₄C₃ could be detected and concluded to the absence of any interfacial reaction. Therefore, considering the speed of the SQC elaboration process (the infiltration of the preform lasts less than 1s and solidification is completed after less than 20 s), the formation of the Al₄C₃ carbides in the present study, even if limited, appears surprising. Nevertheless, it was noticed that Mg₂Si compounds are often associated to the Al₄C₃ formation as shown in Fig. 4.6a. Could Mg possibly favor the kinetics of reaction (4.6)? To clearly understand the role of Mg on the interfacial reaction between the liquid Al and SiC, three different composites based on Al(Mg) alloys and reinforced by SiC particles have been elaborated by SQC under identical conditions than the WFA/SiC/p composites and studied by TEM. The SiC particles were infiltrated with three alloys constituted by mixing Mg with high purity Al (99.99%): Al-4Mg, Al-1Mg and pure Al. As it will shown in the following section, the results clearly confirm the important role of Mg on the kinetics of the interfacial reaction (4.6).

4.2.3 Al(Mg)/SiC/p Composites

Effect of the Mg Content

Fig. 4.7 shows that when Mg is added to pure Al matrix, reaction (4.6) is accelerated so that Al_4C_3 formation becomes detectable by TEM for $\text{Mg} > 1\%$. The images also confirm that carbide formation is associated with Mg_2Si formation:

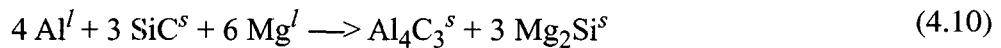


The Al-Mg-Si ternary diagram shows that high Mg and Si concentrations are required to allow the precipitation of Mg_2Si at temperatures higher than 640°C (for example at least 7% Mg and 15 % Si at 640°C). Hence, reaction (4.8) can occur only at the end of the solidification, when some liquid enriched in Si and Mg after diffusion of these elements (see section 4.2.4) remains at the particle interfaces, i.e for $560^\circ\text{C} < T < 640^\circ\text{C}$. Then, reaction (4.8) appears as a coupling reaction that lowers the Si content in liquid Al (and its corresponding activity), and therefore allows the enriched liquid Al and the SiC particles to react according to (4.6). The free energy of reaction (4.8) is given by

$$\Delta G_{\text{Mg}_2\text{Si}}^0 = \Delta G^{0i} + 2(\mu_{\text{Mg}}^s - \mu_{\text{Mg}}^l) + (\mu_{\text{Si}}^s - \mu_{\text{Si}}^l) \quad (4.9)$$

where ΔG^{0i} is the standard free energy for the reaction $\text{Si}^s + 2 \text{Mg}^s \rightarrow \text{Mg}_2\text{Si}^s$, and μ_i the chemical potentials of the pure elements i in their corresponding states.

ΔG^{0i} is given by $\Delta G^{0i} = -77750 + 9.2T$ in J/mol [103], equalling -72 kJ/mol at 640°C . The difference between the chemical potentials is approximated by $\mu_i^s - \mu_i^l \approx (T - T_i^f)\Delta S_i^f$ where ΔS_i^f is the molar entropy of melting of element i , and T_i^f its melting temperature. Considering that reactions (4.6) and (4.8) occur at $T < 640^\circ\text{C}$, the chemical potential difference is negligible for Mg because of the low value of $\Delta S_{\text{Mg}}^f \approx 9.8 \text{ J}/(\text{Kmol})$ and $T - T_{\text{Mg}}^f < 100^\circ\text{C}$, but is important for Si because $\Delta S_{\text{Si}}^f = 29.8 \text{ J}/(\text{K.mol})$ and $T_{\text{Si}}^f = 1412^\circ\text{C}$. Taking this term into account, the free energy of reaction (4.8) can be approximated by $\Delta G_{\text{Mg}_2\text{Si}}^0 \approx -128000 + 39T$, equalling -92 kJ/mol at 640°C . The "pumping" reaction (4.8) allows the following global reaction



where $\Delta G^0 = \Delta G_{\text{Lee}}^0 + 3\Delta G_{\text{Mg}_2\text{Si}}^0 = -254 \text{ kJ/mol}$ at 640°C ; the reaction is thermodynamically strong.

The fact that both Al_4C_3 and Mg_2Si were observed in the as-cast AlMg/SiC composites despite the short time of solidification proves that the kinetics of the reactions (4.6) and (4.8) is rapid and that the reactions are coupled [104].

For $640^\circ\text{C} < T < 750^\circ\text{C}$, as shown by J. Hertz [105], although no Mg_2Si formation is possible, the affinity between Mg and Si in the liquid Al is also sufficient to favor the reactivity of the Al with the SiC particles. The thermodynamical calculations are quite complex and are not presented in this work.

4. Microstructure of the WFA/Al₂O₃/sf and WFA/SiC/p Composites

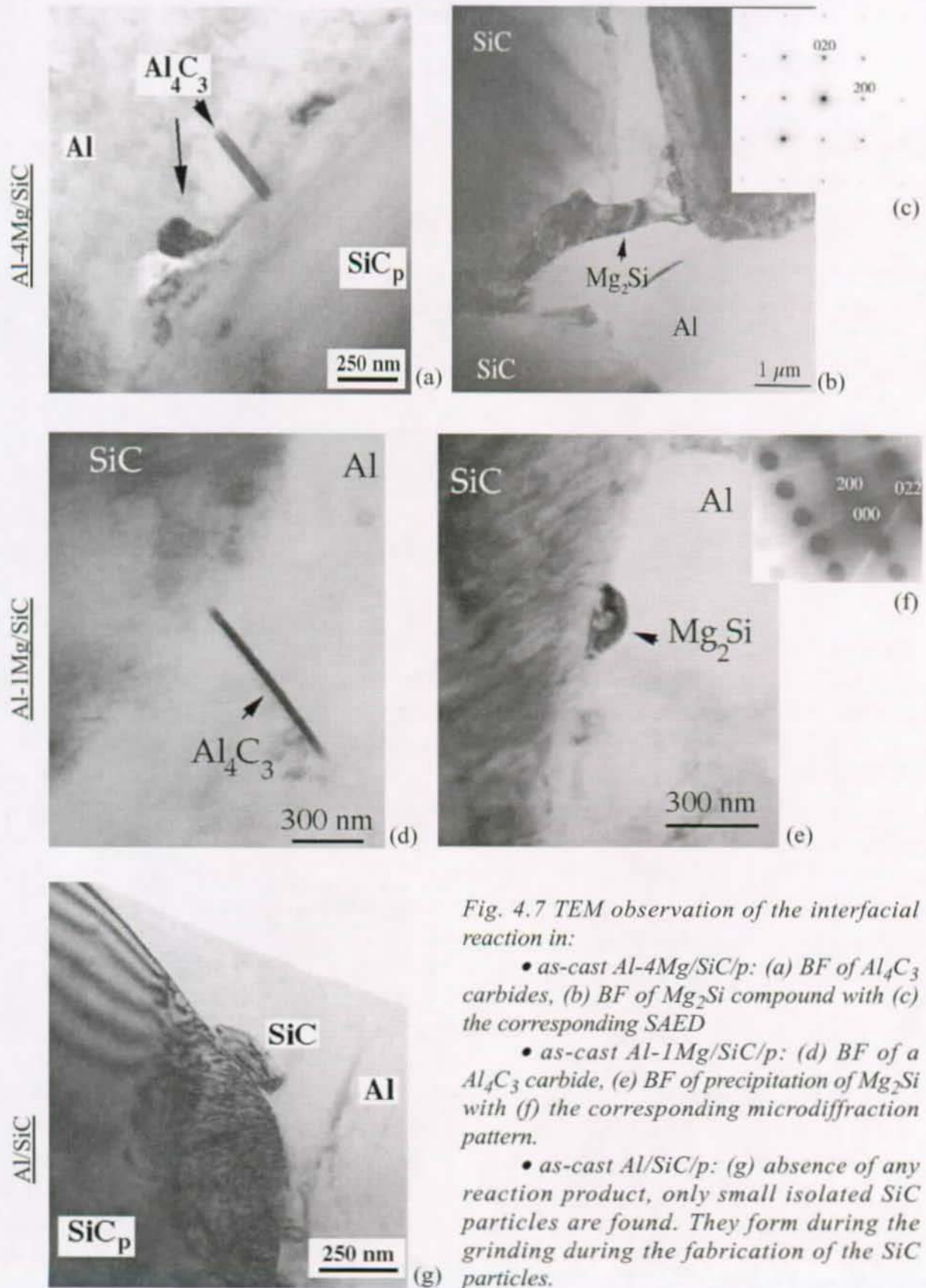


Fig. 4.7 TEM observation of the interfacial reaction in:

- as-cast Al-4Mg/SiC/p: (a) BF of Al₄C₃ carbides, (b) BF of Mg₂Si compound with (c) the corresponding SAED

- as-cast Al-1Mg/SiC/p: (d) BF of a Al₄C₃ carbide, (e) BF of precipitation of Mg₂Si with (f) the corresponding microdiffraction pattern.

- as-cast Al/SiC/p: (g) absence of any reaction product, only small isolated SiC particles are found. They form during the grinding during the fabrication of the SiC particles.

Absence of Reprecipitation of SiC

Small SiC particles such as the one observed in Fig. 4.7g are present in all the studied Al(Mg)/SiC/p composites. Moreover, strange contrasts are observed by TEM at the edges of the SiC reinforcement particles (Fig. 4.8d). Since it has been suggested that the SiC reinforcements particles can react with the molten Al to dissolve from active sites and reprecipitate at lower energy sites [97], which has been apparently confirmed by Romero [107], we have investigated this possibility by studying the structure of the small SiC particles and of the edges of the SiC reinforcement particles.

The SiC reinforcement particles have a 6H structure corresponding to the stacking order of the $\text{SiC}_4/\text{Si}_4\text{C}$ octahedra layers in the ABCB'A'C' sequence (also noted 33) [108]. This structure has been confirmed by CBED (WP+BF patterns) and SAED on the [001] axis (respectively in Fig. 4.8a,b) and SAED on the [010] axis (Fig. 4.8f). We found that the small SiC particles have the same structure. The stacking sequence of the 6H-SiC forbids the {100} reflections. However, these reflections clearly appear in the SAED patterns acquired on the edges of the SiC reinforcement particles (Fig. 4.8c). We interpret these observations by a high density of stacking faults producing locally AB stacking sequences (2H), as confirmed by the HREM image and the streaks in the SAED pattern in the [010] axis (respectively in Fig. 4.8e and f). The high stacking density areas can therefore be easily imaged in DF mode by choosing a (100) reflection as shown in Fig. 4.8d. We believe that these stacking faults are neither due to the interfacial reaction (4.6) nor to the possible SiC reprecipitation, but to the crushing and milling of the SiC during their fabrication process (section 2.3.1). This assumption was confirmed by the TEM observations of these areas on non-infiltrated SiC particles prepared by a slight manual crushing in a mortar (a soft operation compared to the fabrication process), and deposited on an amorphous carbon substrate (Fig. 4.8g).

The high stacking fault density areas do not inevitably correspond to the asperities observed by Johnson [102], and no relation could be observed between them and the nucleation sites for the Al_4C_3 carbides. Moreover, even if clearly shown with an aluminum drop on a SiC substrate [109], no orientation relationship could be found in our composites between the Al grains and the SiC particles, and this certainly because the grain size is far larger than the SiC particles (section 4.1.1). No special orientation relation relationship was found between the SiC particles and the Al_4C_3 carbides.

Han reported wetting results of AlMg/SiC/p systems [91] and showed an increase of the wettability between Al and the non-oxidized SiC particles for any temperature between 580°C and 1000°C when Mg is added to Al. Han had attributed this effect to a reduced surface tension of the liquid Al and possibly to a chemical reaction between Mg and the native SiO_2 oxide layer, but had noticed that this assumption was weak since the SiC particles were not artificially oxidized. It could be interesting to study if there is a link between the effect of Mg on the interfacial reaction and the effect of Mg on the wettability.

4. Microstructure of the WFA/Al₂O₃/sf and WFA/SiC/p Composites

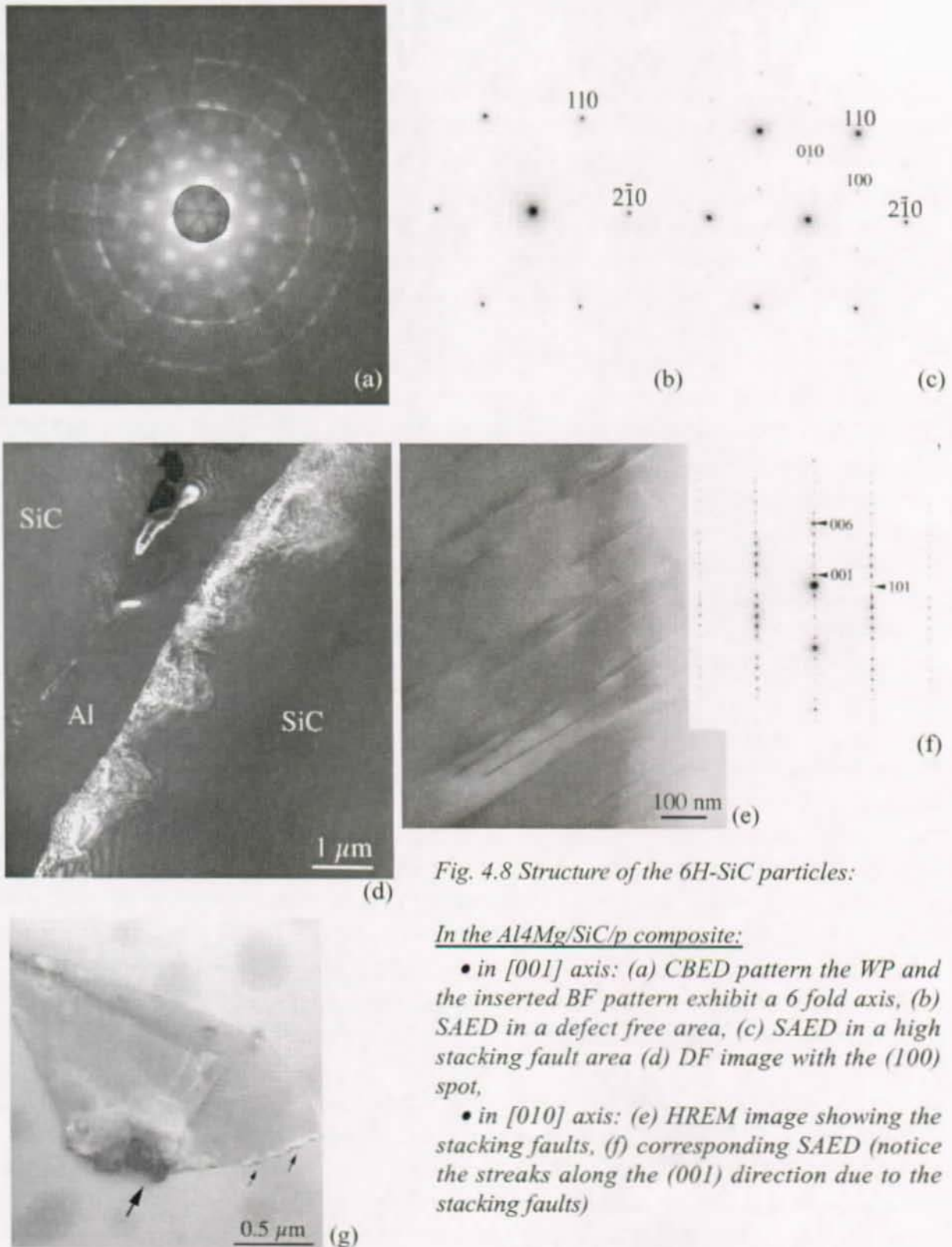


Fig. 4.8 Structure of the 6H-SiC particles:

In the Al₄Mg/SiC/p composite:

- in [001] axis: (a) CBED pattern the WP and the inserted BF pattern exhibit a 6 fold axis, (b) SAED in a defect free area, (c) SAED in a high stacking fault area (d) DF image with the (100) spot,

- in [010] axis: (e) HREM image showing the stacking faults, (f) corresponding SAED (notice the streaks along the (001) direction due to the stacking faults)

A crushed as-received SiC particle:

- (g) DF image in [001] axis acquired with the (100) spot.

4.2.4 Diffusion of Si, Mg and Cu

In the as-cast composites, no Si could be detected by EDS in the matrix outside the coarse precipitates. It is assumed that the Si released from the reactions (4.5), (4.5) or (4.6) was entirely incorporated in compounds present at the reinforcement interfaces such as Mg_2Si or $Q-Al_5Cu_2Mg_8Si_6$, or in rod-shaped precipitates present in the matrix (described in section 6.2.1.). The simulation of the infiltration process performed by CALCOM [4] showed that the solidification process lasted about 20s, and the cooling to 450°C about 30 s. The diffusion coefficients of Si, Cu and Mg in the liquid Al ($T > 630^\circ C$) are quite independent of species concentrations and have a value between $\sim 10^{-4} \text{ cm}^2/\text{s}$, which is more than three order higher than the Si diffusion coefficient in solid Al at $T = 600^\circ C$ ($D_{Si} = 150 \cdot 10^{-10} \text{ cm}^2/\text{s}$). For instance, the characteristic diffusion length of Si during the 20 s of the solidification $l = \sqrt{D_{Si}t}$ is more than 140 μm . This value is far higher than half of the average reinforcement distance, estimated from the reinforcement volume V and the reinforcement volume fraction f by $d \approx (V/f)^{1/3}$, which is $\sim 25 \mu\text{m}$ for the WFA/ Al_2O_3 /sf composite and $\sim 15 \mu\text{m}$ for the WFA/SiC/p composite. Therefore, the diffusion of Si, Cu and Mg through the matrix during solidification process is complete for both composites. These elements are not homogeneously spread in the matrix, but trapped in the coarse intermetallic compounds at the matrix/reinforcement interfaces or in the rod-shaped precipitates in the matrix.

In the T6 composites, Si was clearly detected. As expected, the solution heat treatment ($480^\circ C/1.2 \text{ h} + 500^\circ C/2\text{h}$) dissolved the coarse intermetallic phases, and was sufficiently long to homogeneously spread Si, Mg and Cu in the matrix. Indeed, if we examine the Si diffusion, although the diffusion coefficient is low ($D_{Si} = 10 \cdot 10^{-10} \text{ cm}^2/\text{s}$ at $500^\circ C$), the characteristic diffusion length $l \approx 20 \mu\text{m}$, which is sufficiently high to allow the Si diffusion throughout the matrix.

4.3 Precipitation States

As previously shown, the interfacial reactions of the AlCuMgSi-matrix with the silica present in the Saffil fibers (and from the binder of the WFA/ Al_2O_3 /sf/s composite) or directly with the SiC particles, led to a release of Si in the matrix and to a decrease of the Mg content; this has modified the chemical composition of the alloy (section 4.1.3). The resulting new matrix alloy has a composition of a complex AlCuMgSiAg alloy. Since the T6 condition of the composites is far from the thermodynamical equilibrium condition, the number of different phases is generally higher than the number given by the phase rule: $\phi = m + 2$ where ϕ is the number of possible stable phases and m the number of components (at fixed pressure and temperature). The expected metastable and stable phases of the new AlCuMgSiAg alloy can be derived from better known aluminum alloys, i.e. AlCu (θ'' , θ' , θ), AlCuMg (S'' , S' , S), AlCuMgAg (σ , Ω), AlMgSi (β'' , β' , β and type -A, -B, -C, pure Si at high Si contents), AlCuMgSi (σ , precursors of Q, Q). Their chemistry, crystallography and orientation

4. Microstructure of the WFA/Al₂O₃/sf and WFA/SiC/p Composites

relationships ORs (when they are known) are reported in Annex B.

In all the following part, the precipitation states of the composites will be observed in the T6 state, possibly overaged at 170°C/600h to make the precipitates coarser (section 4.3). The precipitation states will also be observed after an overaging at 300°C/24h to have an idea about the structural evolution and stability of the phases (section 4.4.3). The precipitation in the as-cast state of the composites, although less interesting for the understanding of the mechanical properties, are reported in chapter 6 to better understand the precipitation mechanisms inside the AlCuMgSi alloys. The precipitation in the overaged as-cast composites will also be presented to propose a modification of the processing of the composites (section 4.5.4).

4.3.1 Hardness Curves

After the solution heat treatment at 480°C/2h + 500°C/2h followed by water quenching, the age hardening response at 170°C of the composites and of the unreinforced alloy have been determined by Brinell HB30 hardness measurements. They are presented in Fig. 4.9. The mean level of the curves (about 100 for the WFA alloy, 200 for WFA/Al₂O₃/sf composites and 350 for the WFA/SiC/p composite) reflects in great part the volume fraction of the reinforcements (respectively 0, 15% Al₂O₃ and 60% SiC) and their nature. These curves are used to determine the T6 state of the materials i.e. the aging time corresponding to the maximum hardness.

The required time to obtain the hardness peak is 20 h for the unreinforced WFA alloy, 10 h for the WFA/SiC/p composite, 8 h for WFA/Al₂O₃/sf/a composite and only 6 h for the WFA/Al₂O₃/sf/s composite. Usually, the acceleration of the precipitation kinetics is attributed

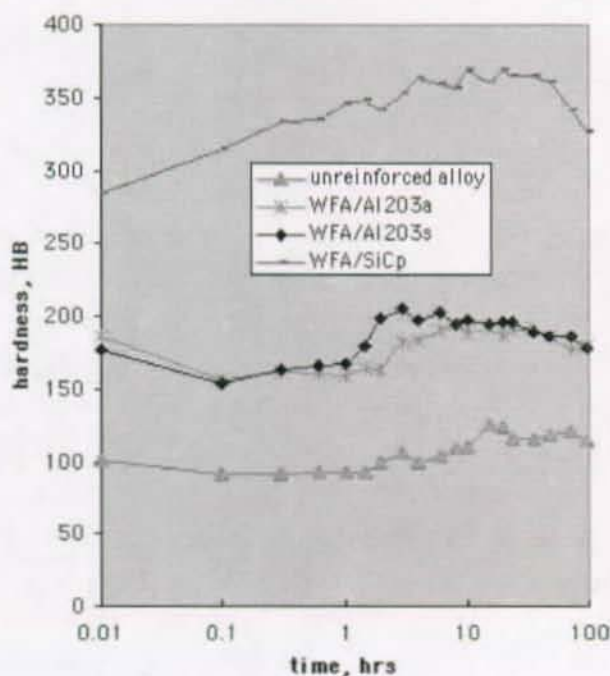


Fig. 4.9 Brinell hardness curves of the WFA alloy and its WFA/Al₂O₃/sf/s, WFA/Al₂O₃/sf/a and WFA/SiC/p composites during aging at T = 170°C.

to the increase of the dislocation density (coming from the CTE mismatch with equation (2.6)) which increases the solute diffusivity and act as nucleation sites for heterogeneous precipitation. Nevertheless, this idea is a consequence of results obtained on composites reinforced with Al_2O_3 fibers or SiC particles based on 2xxx or 6xxx alloys which are respectively hardened by θ' and β' precipitates known to favorably nucleate on dislocations [2]. A generalization to our composites could be a misinterpretation for three reasons: (1) the main hardening precipitation in the WFA alloy is constituted by Ω precipitates which are only reported to nucleate homogeneously from GP zones, (2) the acceleration is far more marked for the WFA/ Al_2O_3 /sf composites than for the WFA/SiC/p composites despite their low reinforcements content, even if it can be argued that the aspect ratio is larger for the fibers and that the Al_2O_3 's CTE is double the SiC's CTE (8.3 and $4.5 \cdot 10^{-6}\text{K}^{-1}$ respectively), and (3) the slight but real difference in the WFA/ Al_2O_3 /sf composites hardness responses depending on the chemical nature of the binder cannot be explained with any dislocation model. Therefore, deeper microstructural TEM investigations are required to clearly understand the role of the reinforcements in the precipitation kinetics.

4.3.2 Modification of the Precipitation State

The precipitation state of the unreinforced alloy in T6-condition is characterized by the presence of Ω plates in the $\{111\}_\alpha$ planes and of S' rods along the $\langle 100 \rangle_\alpha$ directions, as evidenced by the identification of the diffraction pattern in the $[001]_\alpha$ axis (Fig. 4.10a) and by the DF image (Fig. 4.10b). θ' phase could not be traced.

The small addition of Si to the WFA alloy resulting from the interfacial reactions in the composites dramatically affected the precipitation state, as shown in Fig. 4.10. The dominant Ω and S' phases observed in the monolithic alloy could not be detected in the composite matrices anymore. The absence of Ω was evidenced by the lack of its characteristic spots in the $1/4$ (220) positions and confirmed by the absence of streaks in $\{111\}_\alpha$ directions in the $\langle 110 \rangle_\alpha$ diffraction patterns. The S' phase was not observed: either the complex $[210]_\alpha$ diffraction pattern which is often used for S' identification is explained by double diffraction of θ' , and no S phase could be observed in the overaged samples. Actually, the new precipitation state exhibits two kind of fine morphologies: plates and rods; the phases are identified in the following section.

4. Microstructure of the WFA/Al₂O₃/sf and WFA/SiC/p Composites

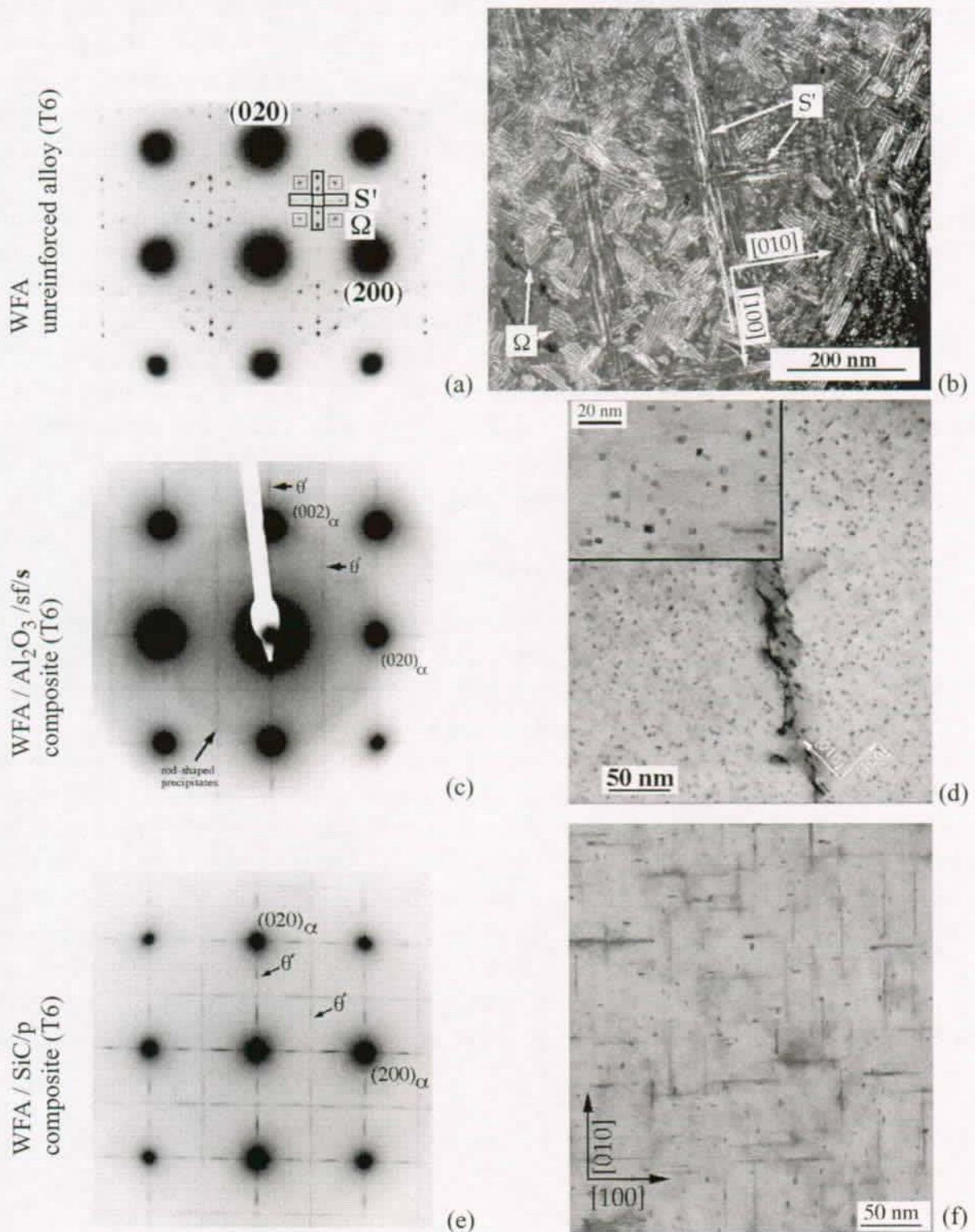


Fig. 4.10 Precipitation state of (a,b) the unreinforced WFA alloy, (c,d) of the matrix of the WFA/Al₂O₃/sf/s composite and (e,f) of the matrix of the WFA/SiC/p composite. The SAED patterns in [001]_α axis are presented in (a,c,e) and the TEM images in (b, d: BF and f: DF). An enlargement of the rod-shaped precipitates is in the top left corner of (d).

4.4 Identification of the Precipitates

4.4.1 θ' Plate-Shaped Precipitates

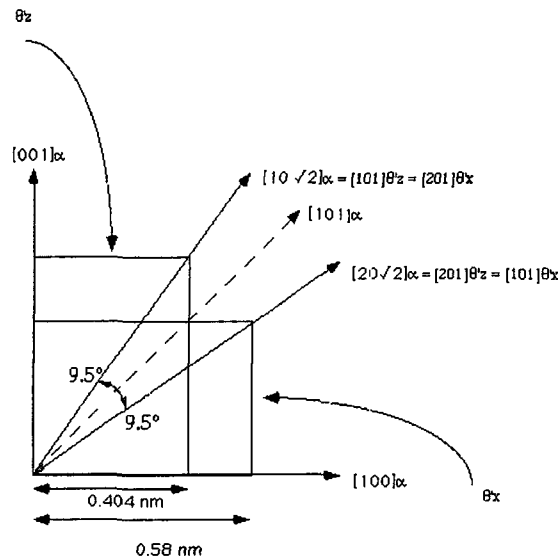


Fig. 4.11 Scheme of the OR between the θ' plates and the Al matrix in projection along $[001]$.

As shown in Fig. 4.10*c,d,e,f*, the composite's matrices feature a fine and dense dispersion of plate- and rod-shaped precipitates. The plate precipitates were identified as θ' plates. Even if they are hardly visible in the background of Fig. 4.10*d,f*, their presence became evident by orientating the sample in the $[10\sqrt{2}]_\alpha$ direction. Indeed, as shown in Fig. 4.11, because of the tetragonal structure of θ' with $a = 0.404$ nm, $c = 0.58$ nm $= \sqrt{2}a_\alpha$ and because of the OR of the precipitates with Al.

$[100]_{\theta'} // [100]_\alpha$ and $(001)_{\theta'} // (001)_\alpha$
the $[10\sqrt{2}]_\alpha$ direction corresponds to $[101]_{\theta'}$ and $[201]_{\theta'}$ directions of the θ' plates oriented in $(100)_\alpha$ and $(001)_\alpha$ planes respectively, and designated as θ'_x and θ'_z accordingly. Therefore, a SAED in $[10\sqrt{2}]_\alpha$ direction permitted to obtain the zone axes of two of the three θ' variants and made diffract the (002) planes of the third variant, as confirmed by the diffraction simulation¹ in Fig. 4.12*b*. The DF image in $[10\sqrt{2}]_\alpha$ direction acquired with the spot $(1\bar{1}1)_\alpha$ which includes the θ'_x spot revealed the θ'_x precipitates (Fig. 4.12*c,d,e*). The rhombus shape of the θ' precipitates on the DF image of Fig. 4.12*c,e* corresponds to the square shape with sides along $\{110\}_\alpha$ and projected on the plane perpendicular to the $[10\sqrt{2}]_\alpha$ direction (electron beam direction) as illustrated for θ'_z in Fig. 4.13*a*. The measured acute angle of the rhombus (62°) is in agreement with the predicted α_{shape} given by:

$$\alpha_{\text{shape}} = 2 \cdot \text{Arctan}[\text{Cos}(\alpha_{\text{tilt}})] \approx 60^\circ \quad (4.11)$$

for $\alpha_{\text{tilt}} = 45^\circ + 9.5^\circ$ for θ'_x

This kind of observation brings interesting information about the growth of the θ' phase. Indeed, we can conclude that during the beginning of precipitation this phase grows in the $\langle 011 \rangle_\alpha$ directions as represented in Fig. 4.13*b*, and in the $\langle 001 \rangle_\alpha$ directions when its size is sufficiently large (>100 nm) as proven by the rectangular shape in Fig. 4.12*d* (projection of a square shape with edges along the $\langle 001 \rangle_\alpha$ directions). To our knowledge, this is the first time

1. See annex C for the details of the SAED simulation program.

4. Microstructure of the WFA/Al₂O₃/sf and WFA/SiC/p Composites

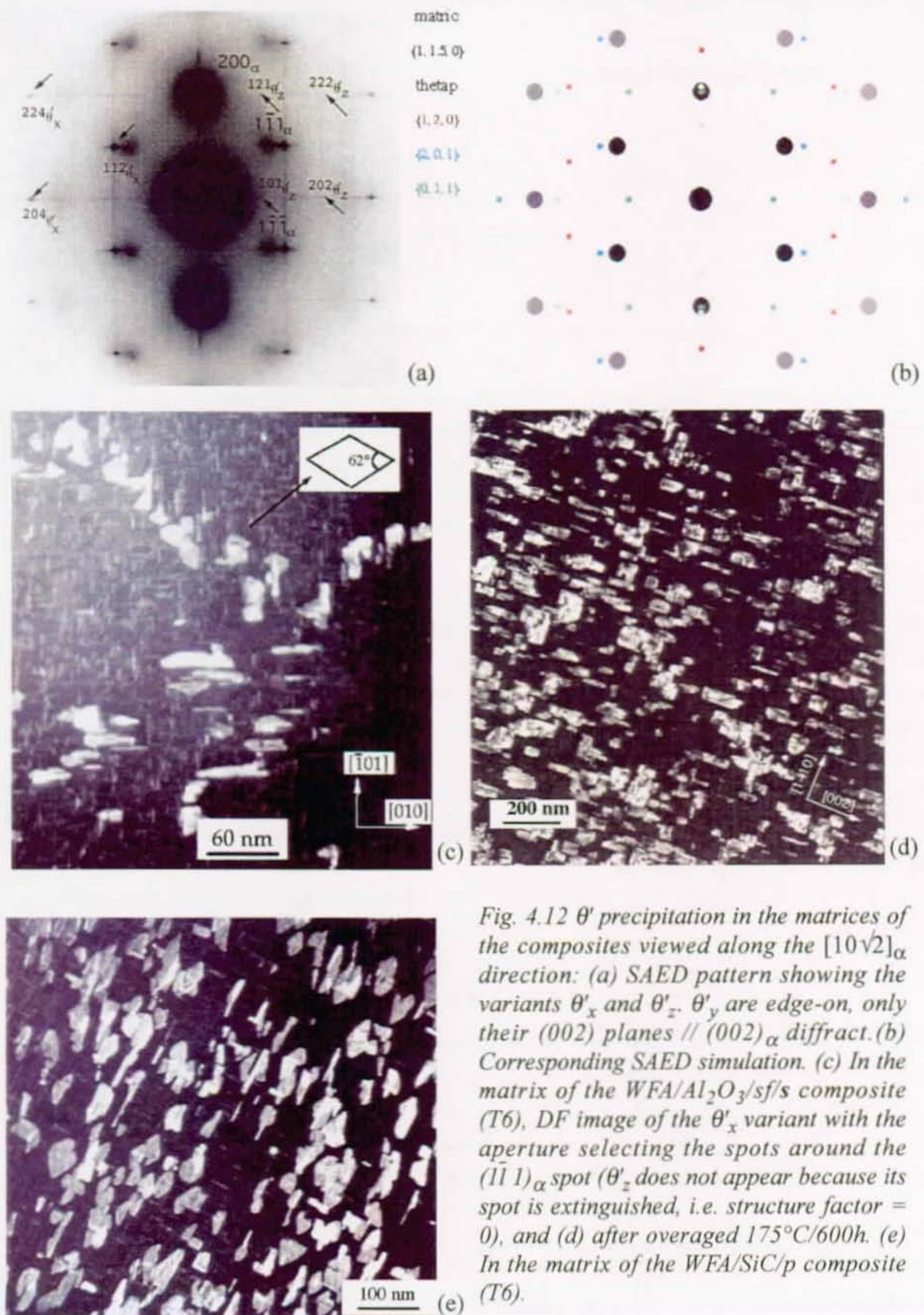


Fig. 4.12 θ' precipitation in the matrices of the composites viewed along the $[10\sqrt{2}]_\alpha$ direction: (a) SAED pattern showing the variants θ'_x and θ'_z . θ'_y are edge-on, only their (002) planes // $(002)_\alpha$ diffract. (b) Corresponding SAED simulation. (c) In the matrix of the WFA/Al₂O₃/sf/s composite (T6), DF image of the θ'_x variant with the aperture selecting the spots around the $(1\bar{1}1)_\alpha$ spot (θ'_z does not appear because its spot is extinguished, i.e. structure factor = 0), and (d) after overaged 175°C/600h. (e) In the matrix of the WFA/SiC/p composite (T6).

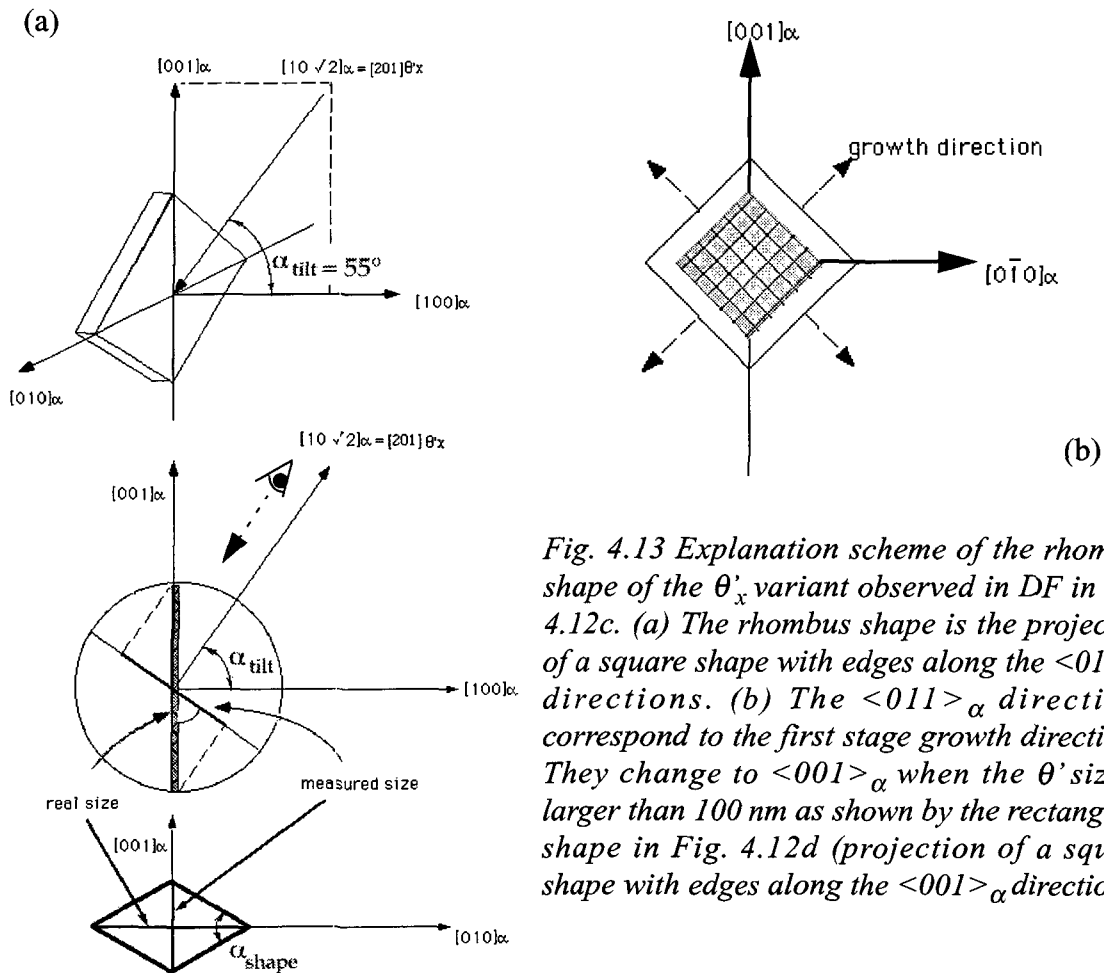


Fig. 4.13 Explanation scheme of the rhombus shape of the θ'_x variant observed in DF in Fig. 4.12c. (a) The rhombus shape is the projection of a square shape with edges along the $\langle 011 \rangle_\alpha$ directions. (b) The $\langle 011 \rangle_\alpha$ directions correspond to the first stage growth directions. They change to $\langle 001 \rangle_\alpha$ when the θ' size is larger than 100 nm as shown by the rectangular shape in Fig. 4.12d (projection of a square shape with edges along the $\langle 001 \rangle_\alpha$ directions).

that this growing transition is put in evidence; in literature only octagonal or square shapes are reported during growing ([110] or annex B).

Furthermore, contrarily to the classical points of view, neither high dislocation densities, nor abnormal high densities of θ' precipitates nucleated on dislocations in the vicinity of the fibers-matrix interfaces (Fig. 4.14a) were observed in the present TEM investigations. This can be explained by the presence of Si, released by the interfacial reactions during the processing and kept in solid-solution in the matrix alloy forming Si-vacancies pairs. These pairs favored a homogeneous nucleation of the θ' precipitates, as shown in the next section, and led to the formation of the dislocation loops necessary for growth of the θ' plates [110]. These dislocation loops formed during the cooling could join to form helical dislocations with the axis along the $\langle 100 \rangle_\alpha$ directions, as observed in the matrices of the composites (Fig. 4.14b), thus confirming the excess of vacancies (they are generally characteristic of quenched Al alloys containing an excess of vacancies [111]). The helical dislocations were not observed in the unreinforced alloy which proves that they were not introduced during the TEM sample preparation.

4. Microstructure of the WFA/Al₂O₃/sf and WFA/SiC/p Composites

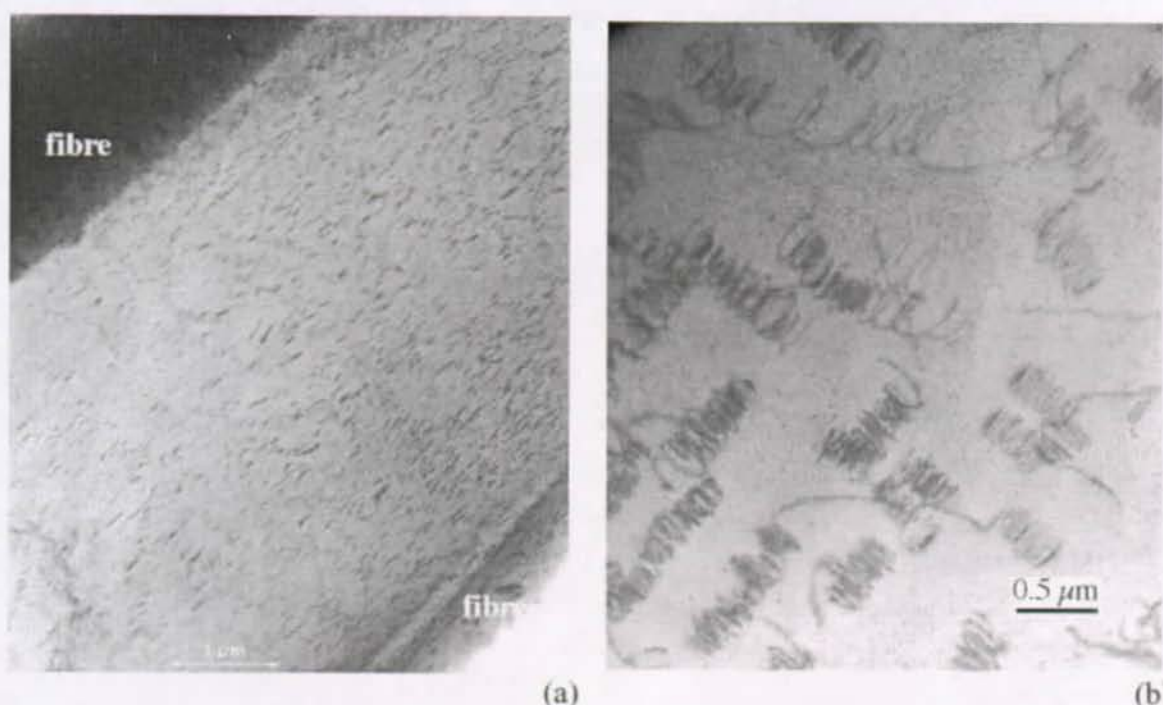


Fig. 4.14 (a) Homogeneous distribution of θ' precipitates in the matrix of the WFA/Al₂O₃/sf/s composite (T6+overaging at 175°C/600h). No abnormal high density due to the pretended higher dislocation density at the fiber/matrix interface can be observed. (b) Helical dislocations in $\langle 100 \rangle_{\alpha}$ directions in the matrix of the WFA/Al₂O₃/sf/s composite (T6).

4.4.2 Rod-Shaped Precipitates

The fine and dense precipitation of rods along the $\langle 100 \rangle_{\alpha}$ directions with a square cross-section ($1-4 \text{ nm}^2$) are shown in Fig. 4.10d,e and in the background of the DF images of Fig. 4.12c,e. Some of them seem to lay on θ' plates. Their length was estimated to 20 nm. After thickness determination of the observation zone thanks to the thickness fringes, their density was estimated to $10^{16}-10^{17} \text{ cm}^{-3}$ for the WFA/Al₂O₃/sf/s composite and $10^{15}-10^{16} \text{ cm}^{-3}$ for the WFA/SiC/p composite. Their fine size and shape made difficult the determination of their crystallographic structure and chemical composition by classical TEM methods. Therefore, HREM, DSTEM and EDS analyses with nanoprobe were used to identify them. Two different types of rods were distinguished: (1) those not lying on the θ' plates and "isolated" in the Al matrix and (2) those lying on the θ' plates (their nature was shown to depend on the composite type).

QP Rod-Shaped Precipitates

The "isolated" rod shaped precipitates in the matrices of the WFA/Al₂O₃/sf/s and WFA/SiC/p composites in the T6 condition have been studied by HREM on the CM300 microscope. They have a section of 1-2 nm as shown in Fig. 4.15. Their EDS analyses with an electron

probe of 1 nm size on the HF2000 microscope revealed the presence of Al, Mg, Si and Cu. The Mg/Cu and Si/Cu ratios measured on 4 precipitates of this type range between 3.5-4.5 and 2-4, respectively, close to those of the stable Q-Al₅Cu₂Mg₈Si₆ phase (4 and 3 respectively).

The HREM images of these precipitates do not exhibit clear patterns as shown in Fig. 4.15, whatever the precision on the rod orientation, defocus and astigmatism correction. Nevertheless, the *power spectra* PS of the HREM images (modulus part of the FFT of the image) clearly exhibit a hexagonal arrangement with $a = 0.395 \text{ nm} \pm 0.005 \text{ nm}$. This phase is very stable at temperatures up to 175°C, as proved by its unchanged size during overaging at 175°C/600h (compare Fig. 4.15a and c). Its OR with α -Al is:

$$(100)_{QP} // (100)_{\alpha} \text{ and } [001]_{QP} // [001]_{\alpha} \quad (4.12)$$

In addition to its composition close to that of Q, it will be shown in section 4.4.3 that these rods are transformed into the Q-phase by overaging at 300°C. Therefore, we have called this phase QP (for precursor of the Q-phase). One can notice that $a_Q/a_{QP} = 2.63 \approx \sqrt{7}$. It will be shown in chapter 6 that a structural phase transition exist between QP and Q.

The blurred aspect of the HREM images is only observed for the very small rod-shaped precipitates, whereas clear patterns appear for the small θ' plates of 1-2 nm thickness, which proves that this aspect is intrinsically linked to the nanosized rod shape of these precipitates. Moreover, the PS proves that the QP phase is neither random nor amorphous, but that it is crystalline, although disordered. The filtered HREM image Fig. 4.15e shown in f reveals the mean positions of the atoms (see section 5.5.3 for more explanations).

Si Rod-Shaped Precipitates

In the matrix of the WFA/Al₂O₃/sf/s composites (T6), in addition to the isolated QP rod-shaped precipitates, pure Si rods have been observed lying on the θ' plates. The Si precipitates appeared in the first stages of the precipitation. Some of them ($1 \times 2 \times 10 \text{ nm}^3$) have been observed by HREM. They have been grown by overaging at 175°C/600h to form rods or rectangular plates ($4 \times 10 \times 60 \text{ nm}^3$), permitting clear DSTEM images with precise EDS measurements (Fig. 4.16a), HREM images (Fig. 4.16b) and BF TEM images (Fig. 4.16c). These Si precipitates are coherent with the aluminum matrix, with an OR as follows:

$$[001]_{\alpha} // [\bar{1}\bar{1}0]_{Si}, [010]_{\alpha} // [111]_{Si}, [100]_{\alpha} // [\bar{1}\bar{1}\bar{2}]_{Si} \quad (4.13)$$

The $[100]_{\alpha} // [\bar{1}\bar{1}\bar{2}]_{Si}$ direction was deduced from the two first ones; it represents the Al and Si zone axes of Fig. 4.16c,d. One can notice that the direct HREM image of Fig. 4.16d is hardly directly interpretable due to the double diffraction with the Al matrix which makes triplicate the interplanar distance between the $(111)_{Si}$ planes as shown in Fig. 4.16e. The small misfit associated to the $(002)_{\alpha}$ and the $(220)_{Si}$ planes are at the origin of the moiré fringes observed in the Fig. 4.16c,d. Indeed, the distance between the moiré fringes calculated by

$$D_{moire} = \frac{d_{200\alpha} \cdot d_{220Si}}{d_{200\alpha} - d_{220Si}} = 3.6 \text{ nm} \quad (4.14)$$

4. Microstructure of the WFA/Al₂O₃/sf and WFA/SiC/p Composites

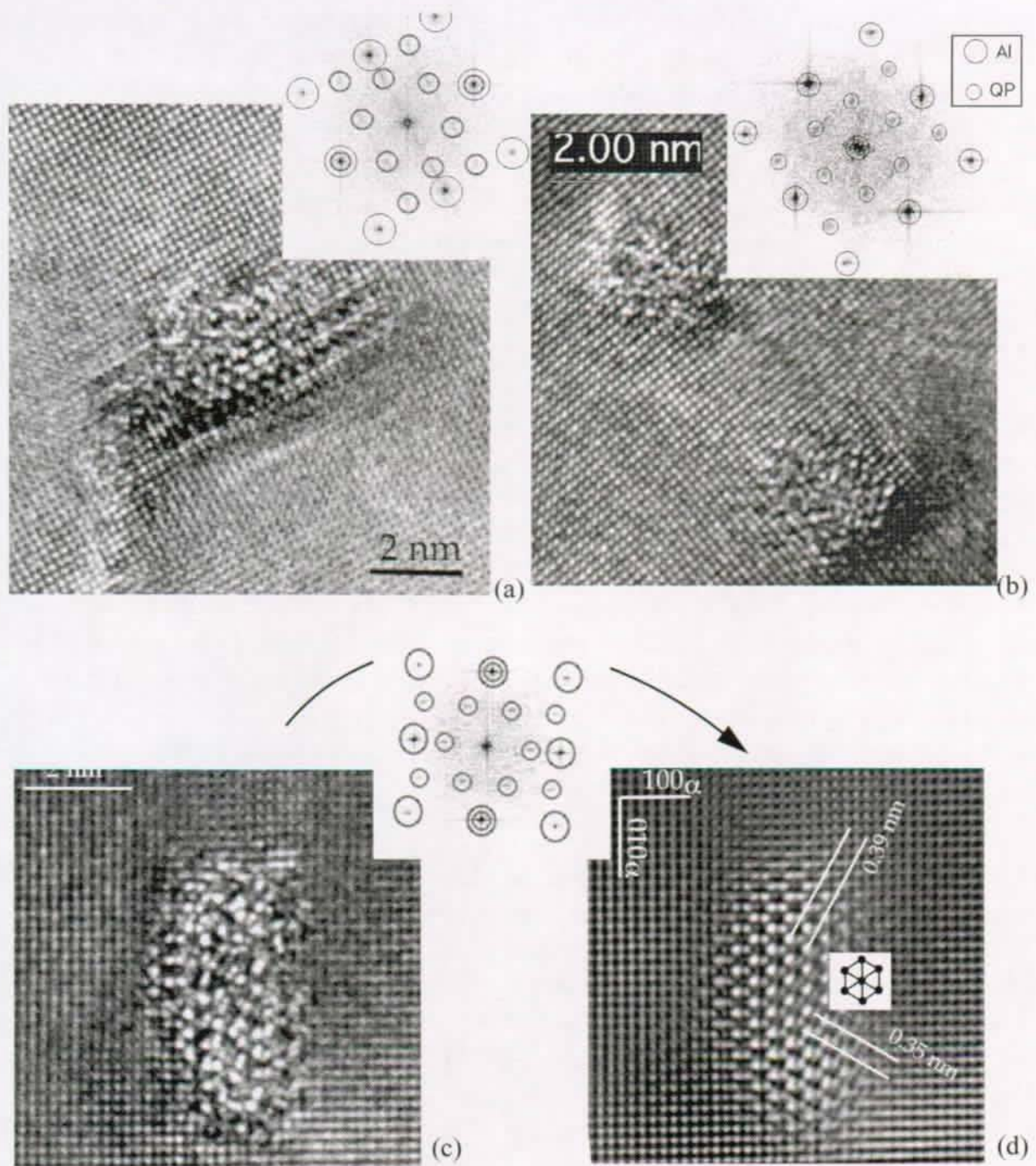


Fig. 4.15 HREM images of QP rod-shaped precipitates in $[001]_{\alpha}$ direction: (a) in the matrix of the WFA/Al₂O₃/sf/s composite (T6) and (b) in the matrix of the WFA/SiC/p composite (T6). Their respective PS are reported in the top right corners. Notice that although no clear pattern is visible in the HREM images of the precipitates, the PS clearly exhibit a hexagonal arrangement of the spots at 0.395 nm in addition to the Al spots. (c) In the matrix of the WFA/Al₂O₃/sf/s composite (T6 + overaging 175°C/600h), a HREM image with (d) its corresponding filtering with the QP and Al spots. The sizes of the masks approximately correspond to the sizes of the circles added in the PS.

4.4. Identification of the Precipitates

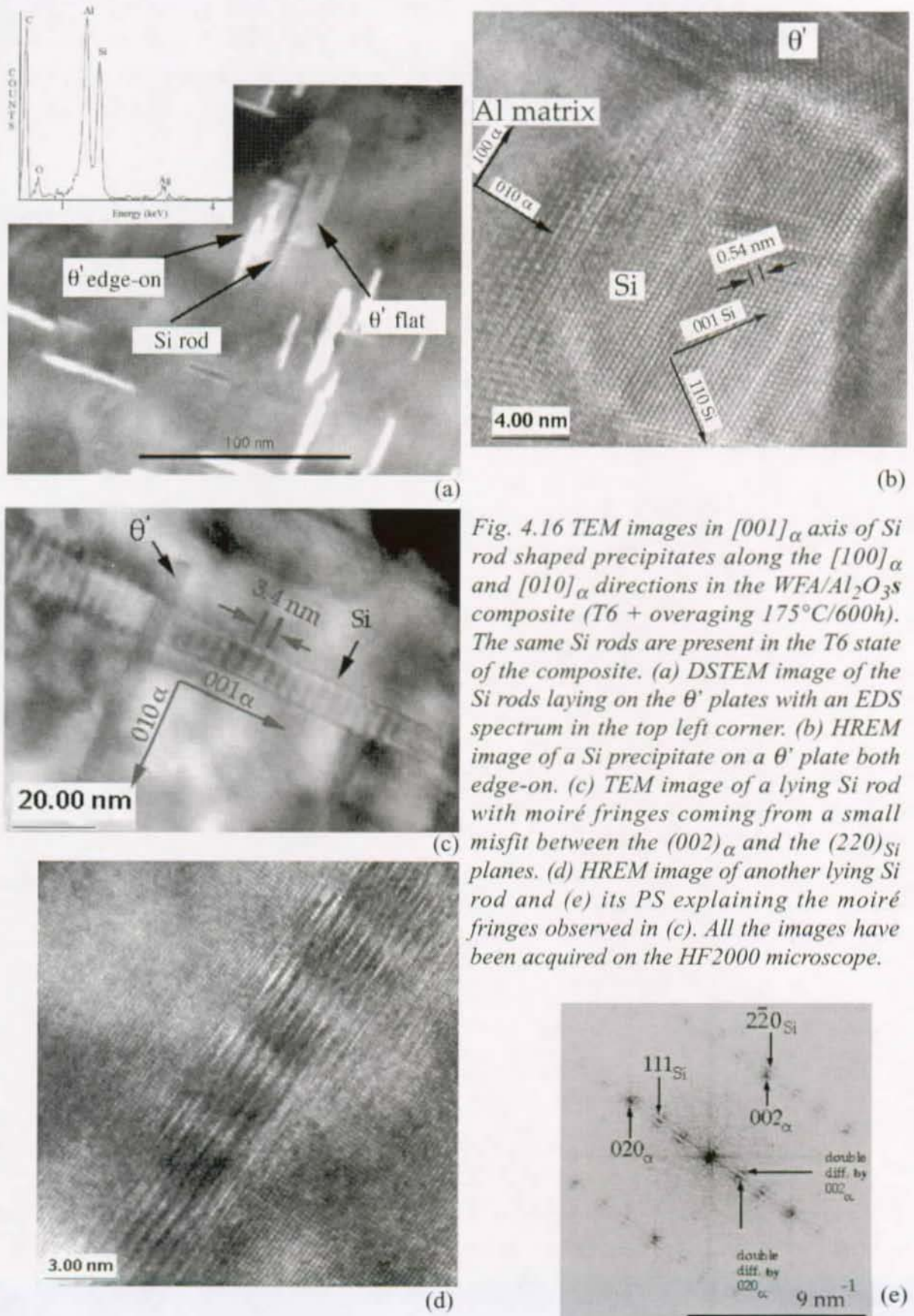


Fig. 4.16 TEM images in $[001]_\alpha$ axis of Si rod shaped precipitates along the $[100]_\alpha$ and $[010]_\alpha$ directions in the WFA/ $\text{Al}_2\text{O}_3/\text{Si}$ composite (T6 + overaging $175^\circ\text{C}/600\text{h}$). The same Si rods are present in the T6 state of the composite. (a) DSTEM image of the Si rods laying on the θ' plates with an EDS spectrum in the top left corner. (b) HREM image of a Si precipitate on a θ' plate both edge-on. (c) TEM image of a lying Si rod with moiré fringes coming from a small misfit between the $(002)_\alpha$ and the $(220)_{Si}$ planes. (d) HREM image of another lying Si rod and (e) its PS explaining the moiré fringes observed in (c). All the images have been acquired on the HF2000 microscope.

4. Microstructure of the WFA/Al₂O₃/sf and WFA/SiC/p Composites

is in agreement with Fig. 4.16c. The smallest misfit corresponding to the $(001)_{\alpha} // (2\bar{2}0)_{\text{Si}}$ planes (5.2%) is associated to the rod orientation in $[1\bar{1}0]_{\text{Si}}$ direction. The OR (4.14) is one of those reported by Rosenbaum in his study of the precipitation of Si plate-like particles in Al-Si alloys [112].

QC Rod-Shaped Precipitates

In the WFA/SiC/p composites (T6), rod-shaped precipitates are joined to the θ' plates. Similarly to the Si rod-shaped precipitates in the WFA/Al₂O₃/sf/s composite, these rods are too small ($2 \times 2 \times 30 \text{ nm}^3$) to get structural information by conventional TEM or nanodiffraction techniques, but they could be identified by EDS analyses and HREM. The EDS measurements indicated that these precipitates contain Mg, Cu and Si (and possibly Al), the Mg/Cu and Si/Cu ratios, close to 7 and 3.5 respectively, being higher than those of the stable Q-Al₅Cu₂Mg₈Si₆ phase (4 and 3 respectively). An HREM image of one of these precipitates, with its corresponding PS and filtered image, is shown in Fig. 4.17. Even if the effect is not as marked as for the QP precipitates, no clear pattern can be observed in the HREM image of Fig. 4.17a, whereas a clear hexagonal pattern appears in the PS and in the filtered image of Fig. 4.17b. The measured hexagonal parameter is $a_{\text{QC}} = 0.675 \text{ nm} \pm 0.01^{\circ} \text{ nm}$.

For the moment its c parameter is assumed to be the same as the parameter of Al a_{α} (= 0.405 nm) because these precipitates form rods in $\langle 100 \rangle_{\alpha}$ directions without moiré fringes (but it may be a multiple of a_{α}). Their OR with the matrix was found to be

$$(100)_{\text{QC}} // (110)_{\alpha} \text{ and } [001]_{\text{QC}} // [001]_{\alpha} \quad (4.15)$$

One can notice that the $\{100\}_{\text{QC}}$ spots are very weak and diffuse, but the $\{110\}_{\text{QC}}$ spots are very strong and sharp. One can also notice that these $\{110\}_{\text{QC}}$ spots correspond to the $\{100\}_{\text{QP}}$ spots observed in Fig. 4.15, as confirmed by the fact that $a_{\text{QC}}/a_{\text{QP}} = 1.71 \approx \sqrt{3}$. Therefore, since this phase is very close to the QP- and Q-phases, we have called it QC (for phase close to the Q-phase, or Cayron's phase as one prefers). The OR of the "virtual" QP phase associated to QC is

$$(100)_{\text{QP}} // (110)_{\alpha} \text{ and } [001]_{\text{QP}} // [001]_{\alpha} \quad (4.16)$$

More crystallographic details about the QP/QC/Q phases are given in chapter 6.

4.4.3 Evolution of the Precipitation by Overaging at 300°C/24h

Overaging at 175°C/600h has only led to an increase in the size of the Si rod-shaped precipitates and θ' plates, but not the size of the QP precipitates (compare Fig. 4.15a and c). Therefore, to have an idea about the stability of all the phases present in the T6 state of the composites and more particularly to determine the stable phases related to the QP or QC phases, the WFA/Al₂O₃/sf/s and WFA/SiC/p composites were subjected to an overaging

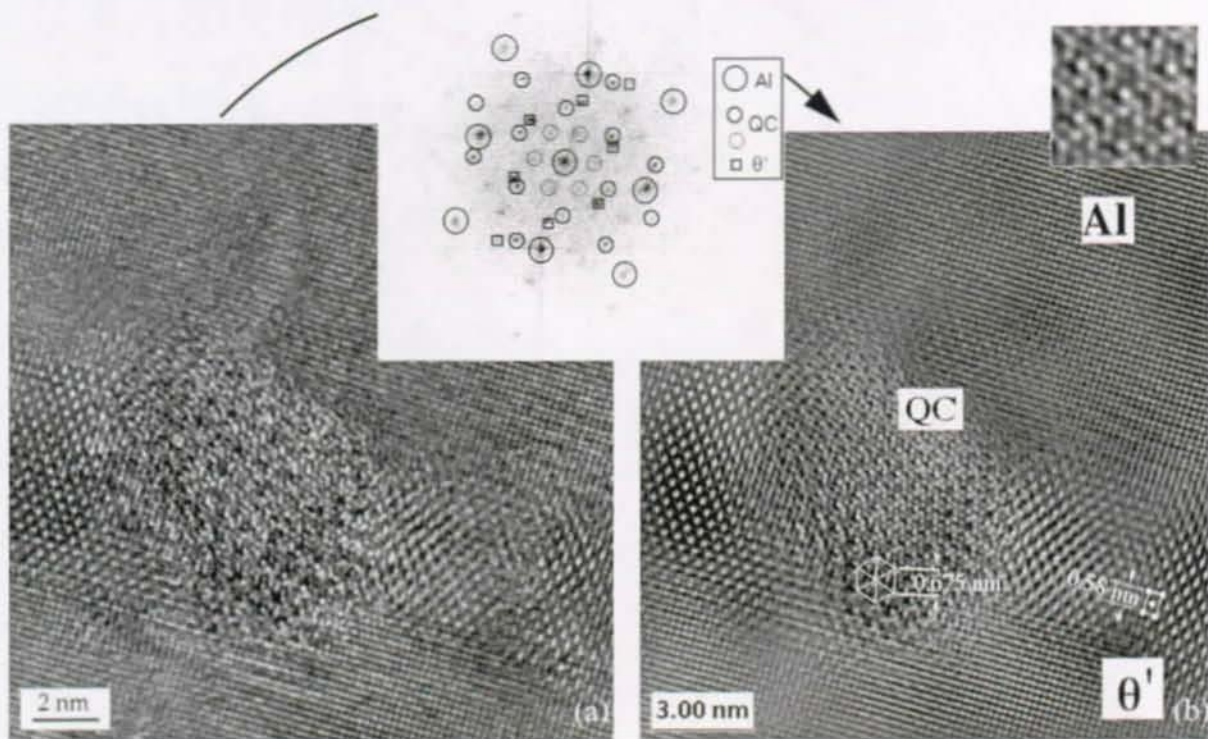


Fig. 4.17 QC rod-shaped precipitate along a $[001]_{\alpha}$ direction in the WFA/SiC/p composite (T6): (a) HREM image of a QC rod on a θ' plate both edge-on, with the PS at top right corner and (b) the corresponding image filtered on the QC, Al and θ' spots. The masks have approximately the size of the Al circles added in the PS. An enlargement of the QC filtered part is at the top right corner

treatment at $300^{\circ}\text{C}/24\text{h}$. After the overaging, both composites feature the same precipitation state, with the presence of θ' , θ plates and Q rod-shaped precipitates as shown in Fig. 4.18a. The Q precipitates were found with two different cross-sections: rectangular and cylindrical (average size 25 nm). They were observed as isolated precipitates as shown in Fig. 4.18a,c, or sometimes lying along θ' precipitates as shown in Fig. 4.18b. By SAED and HREM images, two ORs with the aluminum matrix have been determined for these Q precipitates.

The first OR deduced from Fig. 4.18f is

$$(210)_{\text{Q}} // (100)_{\alpha} \text{ and } [001]_{\text{Q}} // [001]_{\alpha} \quad (4.17)$$

This OR is the most frequent one and was found to be independent of the section shape; it was reported by Dubost [113], and by Sagalowicz for the M-phase (crystallographic structure similar to the Q-phase, but containing only Al, Mg, Si). Sagalowicz wrote OR (4.17) under an equivalent form allowing to understand the rectangular shape by minimization of the interface misfits [114]:

$$[\bar{1}1\bar{2}0]_{\text{Q}} // [510]_{\alpha} \text{ and } (0001)_{\text{Q}} // (100)_{\alpha} \quad (4.18)$$

4. Microstructure of the WFA/Al₂O₃/sf and WFA/SiC/p Composites

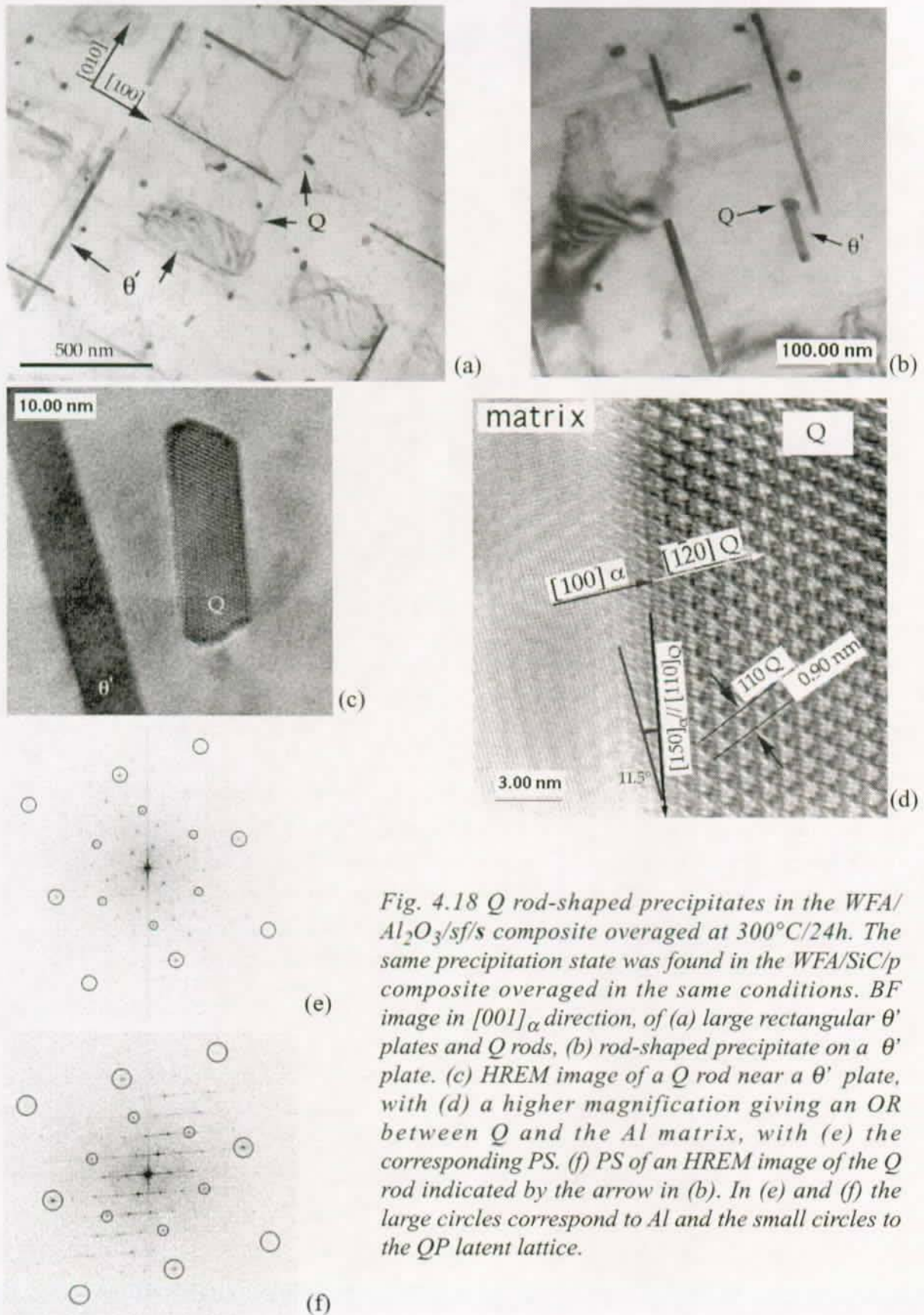


Fig. 4.18 *Q* rod-shaped precipitates in the WFA/Al₂O₃/sf/s composite overaged at 300°C/24h. The same precipitation state was found in the WFA/SiC/p composite overaged in the same conditions. BF image in [001]_α direction, of (a) large rectangular θ' plates and *Q* rods, (b) rod-shaped precipitate on a θ' plate. (c) HREM image of a *Q* rod near a θ' plate, with (d) a higher magnification giving an OR between *Q* and the Al matrix, with (e) the corresponding PS. (f) PS of an HREM image of the *Q* rod indicated by the arrow in (b). In (e) and (f) the large circles correspond to Al and the small circles to the QP latent lattice.

The second OR deduced from Fig. 4.18e is:

$$(100)_Q // (100)_\alpha \text{ and } [001]_Q // [001]_\alpha \quad (4.19)$$

This OR is rare and was found to be generally associated to the rod-shaped precipitates with a cylindrical section. It can be noticed that the $\{210\}_Q$ spots correspond to the $\{100\}_{QP}$ spots shown in Fig. 4.18d,f. This explains that $a_Q/a_{QP} = 2.63 \approx \sqrt{7}$ noticed in section 4.4.2. From the two Q's ORs, one can deduce the ORs of the "virtual" QP precipitate associated to Q:

$$\text{from (4.17): } (100)_{QP} // (100)_\alpha \text{ and } [001]_{QP} // [001]_\alpha \quad (4.20)$$

$$\text{from (4.19): } (100)_{QP} // (110)_\alpha \text{ and } [001]_{QP} // [001]_\alpha \quad (4.21)$$

In conclusion, during the overaging treatment at 300°C/24h, the Si rod-shaped precipitates were dissolved, a part of θ' plates were dissolved to form θ compounds, and it seems that the QP and the QC phases were transformed into the Q-phases. More arguments are given in chapter 6 to confirm this point.

4.5 Conclusions and Prospects

4.5.1 Grains and Microsegregation

In comparison with the unreinforced alloy, the grain sizes and morphologies were strongly affected by the presence of the reinforcements (loss of the dendritic structure), depending on the ratio between the average inter-dendritic distance of the alloy and the average inter-reinforcement distance. Microsegregation of mainly Al_2Cu , $\text{Al}_7\text{Cu}_2\text{Fe}$ and $\text{Q-Al}_5\text{Cu}_2\text{Mg}_8\text{Si}_6$ was clearly visible in the as-cast composites at the interface between the matrix and the reinforcements, and was significantly reduced by the heat treatment at 500°C for 2 hrs. In addition to its presence in the Q-phase intermetallics, Si was detected in the matrices of all the composites.

4.5.2 Chemistry and Precipitation Modification of the Base Alloy

The interfacial reactions between the AlCuMgAg matrix alloy and the Saffil-fiber + SiO_2 -binder or the SiC particle reinforcements released Si in the matrices of the composites during the processing. This slightly modified the composition of the alloy (decrease of the Mg content and appearance of Si), and its precipitation state has been dramatically changed. The expected S' and Ω phases were substituted by a fine precipitation of rod-shaped QP precipitates (precursor of the stable Q phase) and of θ' plates lying on rod-shaped precipitates which are pure Si rods for the WFA/ Al_2O_3 /sf/s composites and QC rods (another phase close to the stable Q phase) for the WFA/SiC/p composites. We believe that in the WFA/ Al_2O_3 /sf/s composites, the Mg content, after the interfacial reaction with the SiO_2 from binder and fibers (section 4.2.1), was not sufficient for the formation of the QC precipitates, and that only Si could precipitate on the θ' plates. In the WFA/SiC/p composites, an indirect reaction between

4. Microstructure of the WFA/Al₂O₃/sf and WFA/SiC/p Composites

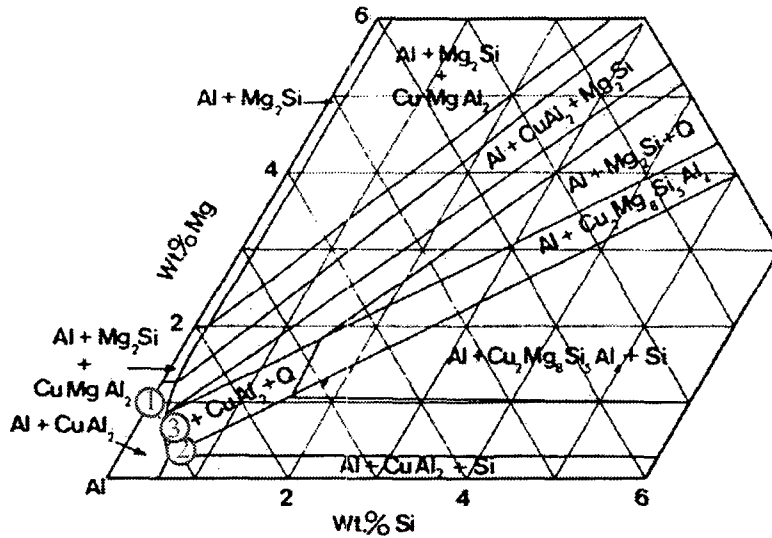


Fig. 4.19 Section of the Al-Cu-Mg-Si diagram at 500°C, 4% Cu from Modolfo [82]. The estimated composition of the alloys is indicated by the circled numbered: (1) for the unreinforced WFA alloy, (2) same alloy reinforced with the Al₂O₃/s fibers and (3) with the SiC particles.

Mg and the SiC particles also occurred (section 4.2.2), but was certainly more limited and less Mg consuming. Even if the microstructure in the T6 states of the two composites is slightly different, the stable phases are the same (θ and Q). The chemical modification of the alloy can be qualitatively summarized in a pseudo-quaternary phase diagram as that reported in Fig. 4.19.

One cannot pretend that the reinforcements accelerate the kinetics of the precipitation, as may be concluded from the hardness curves (section 4.3.1), since the precipitation has been qualitatively modified. It is thought that the most important factor for the rapid kinetics of the new precipitation is the high content of Si-vacancies pairs which act as nucleation site for the θ' plates.

During the study of the precipitation state, two phases not reported before (QP and QC) have been found in the AlMgCuSi matrices of the composites after the modification of the WFA base alloy caused by the interfacial reactions. As detailed in chapter 6, these phases provided us with new ideas about the precipitation mechanisms in the AlCuMgSi and AlMgSi alloys.

4.5.3 Effect of Binder Composition on the WFA/Al₂O₃/sf AMC Tensile Properties

The tensile tests (section 2.3) and the hardness curves (section 4.3.1) tend to show that the mechanical properties of the WFA/Al₂O₃/sf composites are higher with a silica binder than for an alumina binder, whereas the other parameters remain constant (nature and content of the fibers, elaboration process etc...). The TEM study allows a qualitative explanation of these results. Indeed, we have shown that in addition to the silica contained in the alumina fibers, the silica binder also reacted with the Mg of the alloy. This provided an extra source of Si that did not exist when an alumina binder is used (section 4.1.3). Since it has been shown that Si forms Si-vacancies pairs that favor the nucleation of the θ' plates and QP rod-shaped

precipitates, the precipitate density is expected to be higher for the WFA/Al₂O₃/sf/s composite than for the WFA/Al₂O₃/sf/a composite. This is confirmed by the comparison of the BF images of their precipitation density shown in Fig. 4.20: the ratio of the precipitate densities between the two composites is estimated at 1.5.

Vivas has shown by HREM and TEM in-situ straining in a similar alloy (6056-T6) that the rod-shaped precipitates of this alloy (not identified) are sheared by the dislocations [115]. The force corresponding to the shearing was evaluated as $F_m \approx 0.6$ nN. She also estimated the strengthening coming from the precipitation hardening [116], by using the hardening expression given by Gerold [27]. The shear strength $\Delta\tau$ coming from the small sheared obstacles can be written:

$$\Delta\tau = \frac{F_m^{3/2}}{b^2 R \sqrt{\mu}} \sqrt{\frac{f}{2}} \quad (4.22)$$

where μ is the shear modulus ($= 29.3$ GPa), b the modulus of the Burgers vector ($= 0.286$ nm), f the volume fraction of the precipitates ($= 0.05$) and R the radius of small rectangle section ($= 3$ nm). Her results were in agreement with the mechanical properties (she found $\Delta\tau = 95$ MPa and concluded that $\Delta\sigma = 300$ MPa). Using equation (4.22) with the results obtained from section 4.4.2 for the WFA/Al₂O₃/sf/s composite ($f \approx 0.02$, $R = 1.5$ nm) and from Fig. 4.20 for the WFA/Al₂O₃/sf/a composite ($f \approx 0.013$, $R = 1.5$ nm), we find $\Delta\tau = 120$ MPa for the matrix of the WFA/Al₂O₃/sf/s composite and $\Delta\tau \approx 100$ MPa for the matrix of the WFA/Al₂O₃/sf/a composite. The ratio between the $\Delta\tau$ of each matrix is 1.2. The higher $\Delta\tau$ with a SiO₂ binder than with a Al₂O₃ binder is in agreement with the tensile results obtained in section 2.3.3 ($\sigma_c^y = 417$ MPa for the WFA/Al₂O₃/sf/s composite and $\sigma_c^y = 347$ MPa for the WFA/Al₂O₃/sf/a composite).

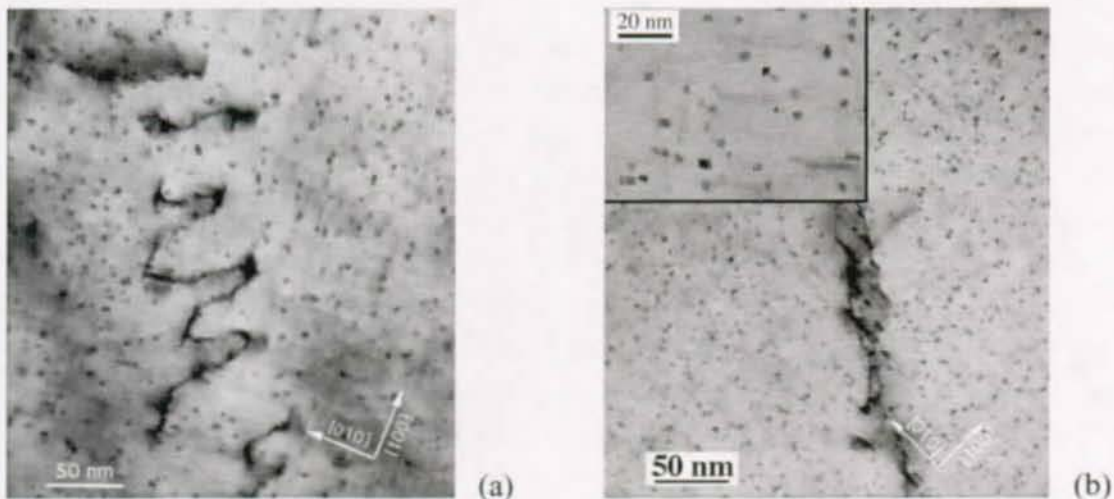


Fig. 4.20 Precipitation state in the matrix of (a) the WFA/Al₂O₃/sf/a and (b) the WFA/Al₂O₃/sf/s composites in their T6 states. The BF images were acquired in two beam condition. The thickness was estimated from the equal thickness fringes (~ 80 - 100 nm).

4.5.4 Prospects for the Improvements of the Tensile Properties

WFA/Al₂O₃/sf Composites

Since the interfacial strength of the WFA/Al₂O₃/sf composites is "good" due to the slight interfacial reaction spread at the surface of the fibers with limited thickness (section 4.2.1), and since the tensile properties of these composites highly depend on their matrix (section 2.3.3), potential improvement of the tensile properties seems to rely on the design of the matrix microstructure. Two approaches are proposed:

(1) *Avoid the precipitation change.* As introduced in section 2.3.1, the WFA base alloy (2xxx series) was chosen for its promising mechanical properties both at room and high temperatures (up to 200°C) given by the precipitation of the Ω plates. It is probable that the mechanical properties of the WFA/Al₂O₃/sf composites would be improved if it was possible to keep unchanged the precipitation sequence of the base alloy. One way to achieve this goal could be to apply a surface coating treatment (for example with TiB₂) to create a diffusion barrier impeding the chemical reaction. However, this solution would be very costly and therefore not compatible with the aim of developing low cost AMCs. Another way could be the modification of the process to impede the formation of the Si-vacancies pairs responsible of the appearance of the θ' plates. This idea is based on the TEM observations of the as-cast WFA/SiC/p composite aged at 175°C/600h (no solution heat treatment). Indeed, it was shown that in this sample, in addition to the large θ' and mixed QP/QC/Q rod-shaped precipitates (30 x 40 x 700 nm³), characteristic for the as-cast state (details are given in section 6.1), the S' and Ω phases appear during aging (with also the σ phase), as shown in Fig. 4.21. We believe that the slow air cooling after the processing has allowed the Si released during the interfacial reaction to diffuse and form the mixed large QP/QC/Q rods and intermetallics, leaving the matrix without the Si-vacancies pairs necessary for θ' nucleation, and thus promoting the Ω and S' precipitation. Therefore, an idea could be to directly age the composite after its infiltration and air cooling. However, the mechanical tests on the as-cast composites are disappointing, embrittlement and loss of strength was observed due to the presence of large non-dissolved intermetallic compounds. A solution could be to adjust the cooling rate of the composite after the heat treatment: no too fast to avoid the Si-vacancies pairs formation, but not too long to control the size of the intermetallic compounds.

(2) *Accept the precipitation change but try to adapt the alloy* to its further chemical modification during the elaboration of the composite. After the WFA alloy modification by the chemical interfacial reaction, the chemical composition and precipitation state are close to those of an AlCuMgSi alloy like the 2214 alloy studied by Dubost [113]. This is an alloy which contains the same elements than some of 6xxx alloys such as the 6061 or 6013 alloys, but with a higher Cu content. Its Cu, Mg and Si contents have been optimized to obtain the best mechanical properties, higher than those of the 6061, 6013 and Al-4Cu-1Mg-0.5Ag alloys (Table 4.3). The main problem of this alloy remains is its poor corrosion resistance,

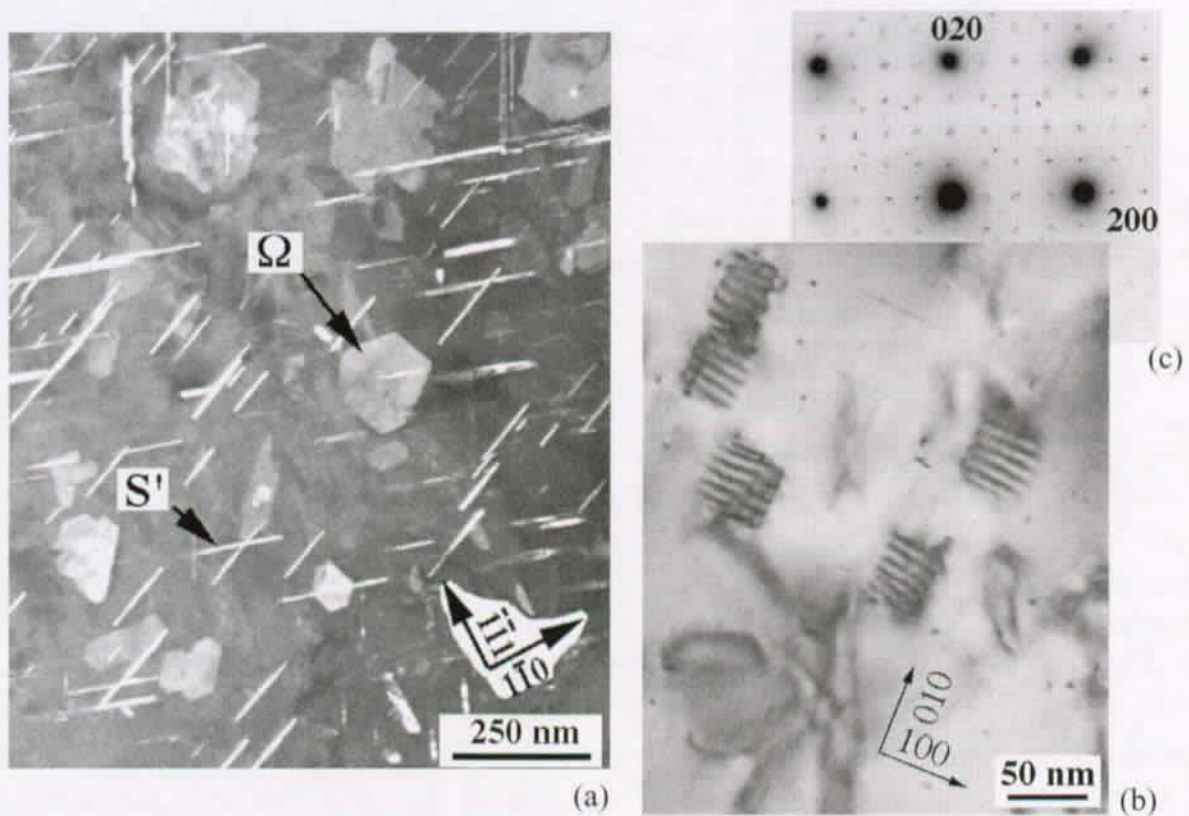


Fig. 4.21 Precipitation in the as-cast WFA/SiC/p composite overaged at 175°C/600h: (a) DF image of Ω plates and S' rods-shaped precipitates in $[112]_{\alpha}$ direction. (b) BF of the σ cubic precipitates in $[001]_{\alpha}$ direction with (c) their corresponding SAED. The small misfits between the $(400)_{\sigma}$ and $(200)_{\alpha}$ produced the moiré fringes in (b). The Ω , S' and σ phases appeared during aging.

which can nevertheless be improved by an appropriate heat treatment [113].

alloy	σ^e MPa	σ^{UTS} MPa	δ %	K_{IC} MPa.m ^{1/2}
Al-5Cu-0.4Mg-0.4Ag [6] (cast alloy)	463	520	10	35
Al-4Cu-1Mg-0.5Ag [4] (cast alloy)	402	456	3.6	24
Al-4Cu-0.8Si-0.6Mg-0.6Mn (2214) [113] (wrought alloy)	429	481	12.8	25.6
Al-1Mg-0.8-Si-0.25Cu-0.35Mn (6061) [117] (wrought alloy)	275	310	12	-
Al-1Mg-0.8-Si-0.8Cu-0.35Mn (6013) [117] (wrought alloy)	330	415	8	-

Table 4.3 Mechanical properties of some 2xxx and 6xxx alloys

For all the studied composites (WFA alloy reinforced with Al_2O_3 or SiC), the Mg content decreased and Si appeared (0.3-0.6%). It seems possible to quantitatively take these changes into account to obtain, after the elaboration, a matrix as close as possible to the optimized 2214 alloy. For example one can propose a Al-4Cu-0.2Si-1Mg alloy composition for the composite with the Al_2O_3 s fibers, Al-4Cu-0.5Si-0.8Mg for the composite with the Al_2O_3 a fibers, and Al-4Cu-0.5Si-1Mg for the composite with the SiC particles. In any case, Ag, which represent 30-50% the price of the WFA alloy, is not required to obtain the new expected precipitation state.

WFA/SiC/p Composites

As shown in section 2.3.3, the good mechanical properties of the WFA/SiC/p composites mainly rely on good interfacial particle/matrix bonding. This is linked to the wetting by (2.12). Therefore, the lower tensile properties of the Al/SiC AMC ($\sigma^{\text{UTS}} = 434$ MPa) compared to those of the as-cast WFA/SiC/p composite ($\sigma_c^{\text{UTS}} = 703$ MPa) given in section 2.3.3, can be explained by the absence of Mg which, as shown in section 4.2.3 could promote adhesion between the SiC and the alloy. However, the interfacial reaction extent must be controlled to avoid excessive formation of Al_4C_3 carbides. Consequently, it could be interesting to adjust the Mg content to obtain a good compromise between adhesion and interfacial reaction extent, keeping a good precipitation hardening for the matrix. One way to regulate the Mg content could be to add Zn in the alloy to form T-(Al,Zn)₄₉Mg₃₂ compounds which incorporate Mg, as proved for the AlMgZn/ Al_2O_3 -Altex/cf composites [106].

Chapter 5

Introduction to Order-Disorder Transitions

In the previous chapter, two new types of nanometer rod-shaped precipitates were observed; they were named QP and QC and seemed to be precursors of the stable Q- $\text{Al}_5\text{Cu}_2\text{Mg}_8\text{Si}_7$. Before a complete TEM and HREM study of these phases, subject of the next chapter, an introduction to ordering mechanisms is required. Order-disorder transitions will be introduced in the global framework of phase transitions (solid-liquid-gas, ferro-para magnetic, ferro-para electric, superfluids, polymers), without enlarging the presentation to critical phenomena.

Most of the approach presented in this chapter is based on the simple following thermodynamic concept: for a closed system in thermal equilibrium, the transition is a consequence of a compromise: the energy tends to order and the entropy associated to the temperature tends to break the order. Different classifications of phase transitions will be presented in section 5.1. Phenomenological Landau's approach by thermodynamics will be treated in section 5.2. A more general approach by using statistical mechanics on an Ising model, as well as Monte Carlo simulations, will be treated in section 5.3. It will help us to introduce the order parameters and approximate methods such as the Bragg-Williams method. Since we are interested in disordered nano-precipitates present in a matrix, the most appropriate observation means, i.e. TEM diffraction and HREM will be treated in section 5.5 to show their potential applications for the study of ordering mechanisms.

5.1 Classification of the Phase Transitions

5.1.1 Chemistry

A microscopic approach by crystal chemistry can provide a basis for the classification of the phase transitions [118]. If a solid undergoes a phase transition at a critical temperature T_c by absorbing thermal energy, the transformed phase possesses higher internal energy, the bonding between neighboring atoms or units are weaker than in the low-temperature phase. This results in a change in the nature of the first and second-nearest neighbor bonds. Phase transition in solids may be classified into three categories:

(1) Displacive transitions [119] proceed through a small distortion of the bonds (dilatational or rotational). The atomic displacements are reduced to 0.01-0.1Å and the specific heat is low (few J/g). The main characteristic is the group-subgroup relationship between the phases. This permits for example to clearly define an order parameter used for the thermodynamical description of the transition. These transitions can be of the first or second order (these terms will be explained in the next section).

(2) Reconstructive transitions [120] proceed through the breaking of the primary or secondary bonds. These transitions were firstly described by Buerger [121]. They imply large atomic displacements with 10-20% of distortion of the lattice, the specific heat is important (~kJ/g). These transformations are sluggish since the barrier of energy is high. The main characteristic is the absence of any group-subgroup relationship between the phases contrarily to the case of Landau transitions (section 5.2). The transitions can even increase the symmetry of the high temperature phase. This transition occurs in many materials such as ZnS, C, H₂O, Am, C, SiO₂, TiO₂. Bain transitions (BCC-FCC) and Buerger transitions (BCC-HCP) can be described as reconstructive.

(3) Order-disorder transitions proceed through substitution between atoms possibly followed by small atomic displacements. They are commonly found in metals and alloys but also in some ceramics. Some of them keep a group-subgroup relationship, as for the CuZn transition (between BCC and simple cubic SC structure), others are also reconstructive as for Am, Fe, Co, ZnS or SiC (FCC-HCP). These transitions can be described with the help of a latent lattice common to the phases [120].

5.1.2 Thermodynamics

Let us consider a closed, isochore and diathermic system in thermal contact with a heat bath. This system is characterized by its free energy F (minimum at equilibrium), given by

$$F = E - T.S \quad (5.1)$$

E is the internal energy and depends on the bonding between the atoms. S is the entropy, characteristic of the disorder by $S = k_B \cdot \text{Log } \Omega(E)$, where Ω is the complexion number, i.e. number of configurations of the system for a given energy E . At low temperatures, the

entropic term is negligible and the system is driven by E (negative) which has its maximum absolute value when the bonds of highest energy are formed (the system is ordered). At high temperatures, the system is driven by $T.S$ which is maximum for a disordered system. Therefore, it appears that T is the balancing coefficient between order and disorder: a phase transition must exist at a critical temperature T_c . In this first approach we have voluntarily neglected the fact that the internal energy of the system can fluctuate. Actually the system must be considered as a canonical ensemble (section 5.3.1).

Closed, expansible and diathermic systems are characterized by their free energy G which remains continuous during the phase transition. However, thermodynamic quantities like entropy S , volume V , heat capacity C_p , the volume thermal expansivity α or the compressibility β can undergo discontinuity. Ehrenfest classified the phase transitions in function of the thermodynamic quantities that present a discontinuity. The order of the transition is the same than the order of the derivation of G required to obtain a discontinuity:

If $V = \left(\frac{\partial G}{\partial p}\right)_T$ or $-S = \left(\frac{\partial G}{\partial T}\right)_p$ has a discontinuity, the transition is of first order.

If $\left(\frac{\partial^2 G}{\partial p^2}\right)_T = \left(\frac{\partial V}{\partial p}\right)_T = -V\beta$, $\left(\frac{\partial^2 G}{\partial T \partial p}\right) = \left(\frac{\partial V}{\partial T}\right)_p = V\alpha$ or $\left(\frac{\partial^2 G}{\partial T^2}\right)_p = -\left(\frac{\partial S}{\partial T}\right)_p = -\frac{C_p}{T}$ has a discontinuity, the transition is of second order. Higher order transitions would involve further differential quantities.

5.2 Landau's Phenomenological Approach

A phenomenological treatment of phase transitions has been given by Landau in 1937 [122]. The theory is based on the assumption that the free energy of the system is a continuous function that can be developed in a Taylor series near the critical temperature T_c , depending on a parameter called the *order parameter*, and noted ξ . This parameter is characteristic of the degree of order. It can be the magnetization for ferro-paramagnetic transition, the polarization for ferro-paraelectric transition, or the percentage of atoms that are on their right sublattice for an order-disorder transition (for this type of transition, details will be given in section 5.4.2).

The main property of the free energy is to remain unchanged by the symmetry operations of the highest symmetric phase implied in the transition. The development of the free energy keeps therefore only the even exponents of ξ

$$F(T, \xi) = F_0(T) + \frac{\alpha(T)}{2}\xi^2 + \frac{\beta(T)}{4}\xi^4 + \frac{\gamma(T)}{6}\xi^6 \quad (5.2)$$

Let us assume that β and γ do not depend on the temperature. Since F is an increasing function with ξ at high temperatures (preponderance of the $T.S$ component in F), we must have $\gamma > 0$. If $\beta > 0$, the exponent 6 term can be ignored, if $\beta \leq 0$, all the terms must be taken into

5. Introduction to Order-Disorder Transitions

consideration. These two cases are the conditions of a second and a first order transition respectively.

5.2.1 Second Order Transitions

Case $\beta > 0$. Since F is minimum for $\xi = 0$ when $T \geq T_c$, and for $\xi > 0$ when $T < T_c$, the sign of α must change at T_c . In first approximation $\alpha = \alpha_0(T - T_c)$ with $\alpha_0 > 0$, and the expression of F is

$$F(T, \xi) = F_0(T) + \frac{\alpha_0(T - T_c)}{2}\xi^2 + \frac{\beta}{4}\xi^4 \quad (5.3)$$

The stable states are given by

$$\left(\frac{\partial F}{\partial \xi}\right)_T = \xi(\alpha + \beta\xi^2) = 0 \quad (5.4)$$

$$\left(\frac{\partial^2 F}{\partial \xi^2}\right)_T = \alpha + 3\beta\xi^2 \geq 0 \quad (5.5)$$

As shown in Fig. 5.1a, for $T \geq T_c$, the system has one minimum at $\xi = 0$, and for $T < T_c$, two minima represented in Fig. 5.1b given by

$$\xi = \pm \sqrt{\frac{\alpha_0(T - T_c)}{\beta}} \quad (5.6)$$

The specific heat $L = T_c \cdot \Delta S_{(T_c)}$ can be calculated by

$$S = -\left(\frac{\partial F}{\partial T}\right)_\xi = -\frac{\alpha}{2}\xi^2 - \left(\frac{\partial F_0}{\partial T}\right)_\xi \quad (5.7)$$

It can be noticed that S and ξ are continuous at $T = T_c$. This transition is a second order transition in the Ehrenfest classification.

5.2.2 First Order Transitions

Case $\gamma > 0$ and $\beta < 0$. Similarly to the precedent case, the sign of α changes at T_c and in first approximation $\alpha = \alpha_0(T - T_c)$. The stable states are given by

$$\left(\frac{\partial F}{\partial \xi}\right)_T = \xi(\alpha + \beta\xi^2 + \gamma\xi^4) = 0 \quad (5.8)$$

$$\left(\frac{\partial^2 F}{\partial \xi^2}\right)_T = \alpha + 3\beta\xi^2 + 5\gamma\xi^4 > 0 \quad (5.9)$$

As shown in Fig. 5.1c, it can be noticed that for $T > T_2 = T_c + \beta^2/(4\gamma\alpha_0)$, it exists only one

phase, which corresponds to $\xi = 0$ (phase I). Just below T_2 , it appears another metastable phase corresponding to $\xi > 0$ (phase II). This phase becomes stable as soon as $F - F_0 = 0$ obtained for $T = T_1 = T_c + 3\beta^2 / (16\gamma\alpha_0)$. Below T_1 , the phase I becomes metastable until T_c is reached for $T < T_c$, only phase II exists. The order parameter corresponding to the metastability ($T_1 < T < T_2$) or to the stability ($T < T_1$) of phase II is represented in Fig. 5.1d

$$\xi = \pm \sqrt{\frac{-\beta + (\beta^2 - 4\alpha_0(T - T_c))^{1/2}}{2\gamma}} \quad (5.10)$$

It can be noticed that a temperature range $\Delta T = T_2 - T_c$ exists where the two phases can coexist. Each of them are successively stable, metastable and unstable. This situation is generally observed with a thermal hysteresis. The order parameter ξ , as well as the specific heat L (equation (5.7)) are discontinuous at T_1 . This transition is a first order transition in the Ehrenfest classification.

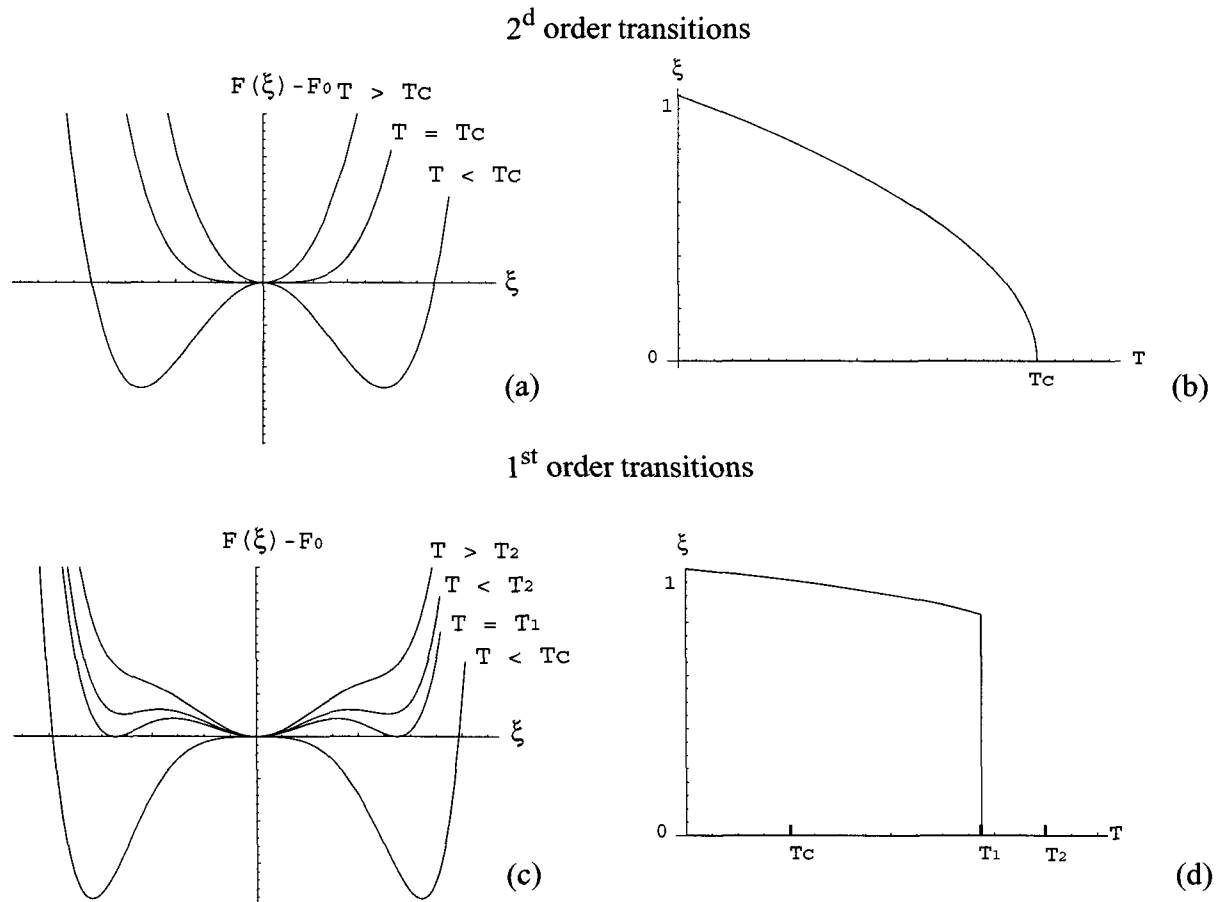


Fig. 5.1 Landau's treatment of phase transitions: (a,b) and (c,d) second and first order transitions respectively: (a,c) the free energy curves in function of the order parameter and (b,d) the order parameter curves in function of temperature.

5.3 Statistical Mechanics Approach

5.3.1 Canonical Ensembles

A closed isochore ($N, V = \text{cst}$) and diathermic system in thermal contact with a heat bath is in equilibrium when its free energy F is minimum. Its internal energy can fluctuate and actually the system must be considered as a set of all the microstates, defined as a *canonical ensemble* [125]. The probability P_x that the system has the energy E_x (and is in a configuration x) is given by the Boltzmann distribution law

$$P_x = \frac{1}{Z} \exp\left(-\frac{E_x}{k_B T}\right) \quad (5.11)$$

The constant of proportionality Z is called the *canonical partition function*, it does not depend on the specific state of the system and is determined by the normalization requirement

$$Z(T, N, V) = \sum_x \exp\left(-\frac{E_x}{k_B T}\right) \quad (5.12)$$

This partition function is characteristic of the thermodynamics of the system since the free energy and the average energy can be deduced from it by

$$F = -k_B T \log Z \quad (5.13)$$

$$\langle E \rangle = \sum_x P_x E_x = -\left(\frac{\partial}{\partial \beta} \ln Z\right)_{N, V} \quad (5.14)$$

where $\beta = 1/(k_B T)$. The $\langle \rangle$ denote the thermal average, i.e. the average on all the configurations with their respective probability.

5.3.2 The Ising Model

The Ising model is probably the simplest statistical model whose solution is not trivial. It was introduced by Lenz and Ising in 1925 [123]. Let us consider a simple lattice and suppose that there is a magnetic moment at each lattice site which can only have two orientations along a given direction, up and down, further noted 1 and $\bar{1}$ respectively. The simplest coupling is then introduced by considering that the nearest neighbor spins interact: a pair of parallel spins has an energy $-J$ and a pair of antiparallel spins has an energy J . Of course it is quite easy to calculate the energy of each configuration for a finite system, but the high number of configuration impedes the calculations of an explicit expression of the partition function when the dimension of the system is $d \geq 3$. However this model is very interesting because it brings most of the important and basic ideas about phase transitions.

For $d = 1$, one can easily show that there is no phase transition in the absence of any external field. Indeed, let us imagine a long chain of N ordered spins. The free energy required to create a simple antiphase boundary, i.e. the free energy difference between two possible

kinds of configurations: $(1,1,\dots,1,1,\dots,1,1)$ and $(1,1,\dots,1,\bar{1},\dots,\bar{1},\bar{1})$ is J . Since, there are N simple states in antiphase boundary configuration, the free energy change is

$$\Delta F = J - k_B T \ln N \quad (5.15)$$

which is always negative for any reasonable value of N and T . This implies that the disordering occurs spontaneously in 1-D system.

For the case $d = 2$, the energy required to create an antiphase boundary is of the order of $\sqrt{N} \cdot J$ and the entropy of the order of $\ln(3^{\sqrt{N}} \cdot \sqrt{N})$. A phase transition is therefore possible at $k_B T_c$ of the order of J [118]. The exact rigorous solution is far more difficult to obtain and was given only in 1944 by Onsager: $k_B T_c = 2.2692 |J|$ [124].

The usual Ising model can be generalized by considering the n^{th} nearest interaction. Let us denote $H(\{\sigma_n\})$ the energy of a configuration characterized by the spin numbers σ_n in the presence of a magnetic field h

$$H(\{\sigma_n\}) = -\frac{1}{2} \sum_{n,m} J_{nm} \sigma_n \sigma_m - h \sum_n \sigma_n \quad (5.16)$$

where J_{nm} is the pair energy of the $(n - m)$ nearest neighbors.

5.3.3 Monte Carlo Simulations

There are two general classes of simulation. One is called the *molecular dynamics* method. Here, one considers a classical dynamical model for atoms and molecules, and the trajectory is formed by integrating Newton's equations of motion. The procedure provides dynamical information as well as equilibrium statistical properties. The other, subject of this section, is called the *Monte Carlo* method¹. This procedure is more generally applicable than molecular dynamics in that it can be used to study quantum systems and lattice models as well as classical assemblies of molecules. For more simplicity, the Monte Carlo method will be discussed on the base of the magnetic Ising model [125, 126].

A trajectory is a chronological sequence of configurations for a system. A configuration of a lattice Ising magnet is the list of spin variables $\sigma_1, \sigma_2, \sigma_3, \dots, \sigma_N$. Let us call x a point in the N -dimensional configurational space (also called phases space) obtained along the trajectory at time t : $x(t) = (\sigma_1, \sigma_2, \sigma_3, \dots, \sigma_N)$, for example, $x(t) = (1, \bar{1}, \bar{1}, 1, \dots, 1, 1)$. The aim of the Monte Carlo method is to simulate trajectories representative of the thermal equilibrium state of the system, so that the thermal average value of a property P follows

$$\langle P \rangle = \lim_T \frac{1}{T} \sum_{t=1}^T P_{x(t)} \quad (5.17)$$

This means that trajectories should be ergodic and constructed in such a way that the Boltzmann distribution law is in agreement with the relative frequencies with which the

1. The origin of the name comes from the city in south of France well known for its roulette and other hazard games.

5. Introduction to Order-Disorder Transitions

different configurations are visited. Let us consider a trajectory going through two states $x = (\dots, \bar{1}, 1, 1, \dots)$ and $x' = (\dots, \bar{1}, \bar{1}, 1, \dots)$, produced by flipping a spin in the x state. The two states x and x' have a probability of existence, respectively p_x and $p_{x'}$, given by the Boltzmann's law (5.11). The energy associated to a possible change of state $\Delta E_{xx'} = E_{x'} - E_x$ governs the relative probability of this change through the Boltzmann distribution law. Lets call $w_{xx'}$ this probability of change per unit time. The evolution of the states probabilities follows the *Master equation*

$$\frac{dp_x}{dt} = \sum_{x'} [-w_{xx'}p_x + w_{x'x}p_{x'}] \quad (5.18)$$

At equilibrium in the canonical ensemble, $\frac{dp_x}{dt} = 0$, which associated to (5.11) results in

$$\frac{w_{xx'}}{w_{x'x}} = \frac{p_x}{p_{x'}} = \exp\left(\frac{-\Delta E_{xx'}}{k_B T}\right) \quad (5.19)$$

Provided a trajectory obeys this condition, the statistics acquired from this trajectory will coincide with those obtained from a canonical ensemble. In the *Metropolis algorithm* [127], the following particular values of $w_{xx'}$ have been chosen

$$w_{xx'} = \begin{cases} 1, & \Delta E_{xx'} \leq 0 \\ \exp\left(\frac{-\Delta E_{xx'}}{k_B T}\right), & \Delta E_{xx'} > 0 \end{cases} \quad (5.20)$$

That is if $\Delta E_{xx'} \leq 0$, the move is accepted and if $\Delta E_{xx'} > 0$, the move is accepted only with an exponential probability which depends on both temperature and difference of energy.

Unfortunately, a certain degree of experimentation is always required to indicate whether the statistical results are reliable. And while the indications can be convincing, they can never be definitive. Indeed, some problems may arise when the system is sluggish such as in substitutional transitions, because the trajectory can be blocked in a local minimum surrounded by large energy barriers.

5.3.4 Phase Diagrams

Let us chose the generalized multi-body Ising model. Usually the variation of energy produced by a spin flipping or by an exchange of atoms is calculated with the multiple interaction energies between the spins with equation (5.16) or between the atoms (as detailed in the next section) with equation (5.26). Depending on the resulted values, Monte Carlo method makes possible to predict the different kinds of thermodynamically stable structures in function of temperature.

At $T = 0K$, the problem is reduced to the minimization of the internal energy (*ground state*) and can be treated analytically. Details are given by Ducastelle [128]. Let us define a given cluster $\alpha_i = \{n_1, \dots, n_{r_i}\}$ a given set of lattice sites (the index i to specify the type of the

cluster: pair, triangle, ...). Let us define its occupation number $\sigma_\alpha = \sigma_{n_1} \dots \sigma_{n_{r_i}}$. The Hamiltonian (5.16) can be written in a generalized way by

$$H(\{\sigma_n\}) = \sum_i v_i \sigma_{\alpha_i} \quad (5.21)$$

where v_i only depends on the bonding energies $\{V_{nm}\}_i$ limited to the size of the type- i cluster. Noting x_i the correlation function $x_i = \langle \sigma_{\alpha_i} \rangle$, the energy of the system is

$$\langle E \rangle = \langle H \rangle = \sum_i X_i x_i \quad (5.22)$$

where $X_i = r_i v_i$, where r_i is the number of type- i clusters in the system. Some relationships exist between the x_i . These ones were given by Kanamori [129]. Let us note p_n the number equalling 1 if $\sigma_n = 1$ and 0 if $\sigma_n = 0$. p_n and σ_n are linked by equation (5.28). The relationships between the x_i can be obtained by expressing the fact that $\langle p_n p_m \rangle$, $\langle p_n (1-p_m) \rangle$, $\langle (1-p_n) p_m \rangle$, $\langle (1-p_n)(1-p_m) \rangle$, and $\langle p_n p_m p_l \rangle$, $\langle p_n p_m (1-p_l) \rangle$, etc., being probabilities, should be positive and lower than 1. A general expression of the relationships was given by Ducastelle [128] who exprimed the probability of finding a type- i cluster ρ_i by

$$\rho_i = \frac{1}{2^{|\alpha|}} \left(1 + \sum_{j \neq \emptyset} x_j \sum_{\beta_j \subset \alpha_i} \sigma_{\beta_j} \right) \quad (5.23)$$

where $|\alpha|$ is the number of sites in the cluster α . Equation (5.23) looks complicated but its application is easy and direct. For example, for triangular clusters, it takes the form

$$\rho_{\{n, m, p\}} = \frac{1}{8} [1 + x_1(\sigma_n + \sigma_m + \sigma_p) + x_2(\sigma_n \sigma_m + \sigma_m \sigma_p + \sigma_n \sigma_p) + x_3 \sigma_n \sigma_m \sigma_p] \quad (5.24)$$

We must minimize the energy given by equation (5.22) respecting the linear inequalities given by $0 \leq \rho_i \leq 1$ with ρ_i given in equation (5.23). The problem can be solved by linear programming. A simple geometrical solution was given by Kudo and Katsura in 1976 [130]: the inequalities given by (5.23) define a polyhedra in the x_i space, and the minimization of the energy, which is a linear form of the x_i , is obtained for one of the vertices of the polyhedra. The solutions $\{x_i\}_0$ give a configuration of the clusters that constitute the phases, and depend on the X_i values (linked to the bonding energies $\{V_{nm}\}_i$). It will be seen in section 6.4.2 that an important and interesting problem which occurs for some lattices is the construction of periodic structures with some of the cluster solution $\{x_i\}_0$. These lattices are called *frustrated*. The construction may be impossible and may imply a degeneration of the solution in infinite approximate solutions.

5.4 Ordering in Binary Alloys

5.4.1 Equivalence with the Ising Model

For a AB binary alloy which features an order-disorder phase transition, the Ising lattice is the Bravais lattice of the highest symmetry phase. Let us define the parameter p_n

$$p_n = p_n^A = \begin{cases} 1 & \text{if the site } n \text{ is occupied by the atom A} \\ 0 & \text{if the site } n \text{ is occupied by the atom B} \end{cases} \quad (5.25)$$

The expression of the Hamiltonian is (apart from an irrelevant constant) [128]

$$H(\{p_n\}) = \frac{1}{2} \sum_{n,m} V_{nm} p_n p_m - \mu \sum_n p_n \quad (5.26)$$

where $V_{nm} = V(n-m)$ represents the energy of the creation of an A-B pair separated by $(n - m)$

$$V_{nm} = V_{nm}^{AA} + V_{nm}^{BB} - 2V_{nm}^{AB} \quad (5.27)$$

where $V_{nm}^{ij} = V^{ij}(n-m)$ is the energy of the $(n - m)$ nearest neighbors occupied by i and j atoms, $\mu = \mu^A - \mu^B + V^{BB} - V^{AB}$. μ^i is the chemical potential of the element i , and $V^{ij} = \sum_n V^{ij}(n)$. The two expressions (5.16) and (5.26) are formally equivalent, with

$$\sigma_n = 2p_n - 1 \quad (5.28)$$

$$h = \frac{1}{2}\mu - \frac{1}{4} \sum_n V(n) \quad (5.29)$$

$$J_{nm} = -\frac{1}{4} V_{nm} \quad (5.30)$$

It can be noticed that an order-disorder transition in a binary AB alloy is equivalent to a magnetic transition where $h > 0$ (because the number of atom A and B must remain constant, which is not the case for the number of up or down spins). An A-B change corresponds to a spin flip. This equivalence can be generalized to many physical phenomena called *critical phenomena*¹.

5.4.2 Order Parameters

During an order-disorder transition in an alloy, one of the symmetry or translational

1. *Critical phenomena is certainly one of the most interesting branches of modern physics. It gives the same fundamental base of a priori many different phenomena, such as superconductivity, transitions in polymers, ferroelectrics, superfluids. It can even be applied to the quarks bond in protons and neutrons [131, 132]. It plays a central role in the unification quest (grand unified theory, superstring theory): our actual universe with 4 forces would come from a hot and condensed universe governed by one force, which would have been subject to a symmetry breaking during its expansion and cooling after the Big Bang [133].*

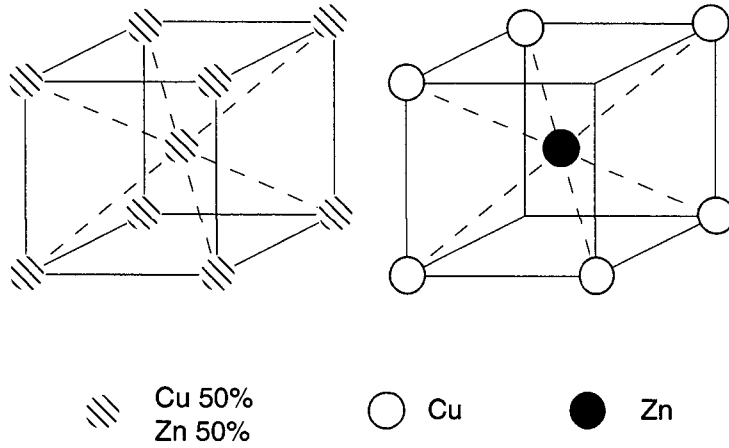


Fig. 5.2 Disordered (high temperature) and ordered structure (low temperature) of CuZn. The broken symmetry corresponds to a change between the BCC and the SC structures.

elements of the high temperature phase is broken and the Bravais lattice is separated into two sublattices. Let us illustrate the concepts of short and long order parameters with the example of an AB alloy (50%, 50%) with the same number of sites in each sublattice, such as the CuZn transition illustrated in Fig. 5.2. At $T = 0\text{K}$, all the A atoms are on one of the sublattices, that will be noted α . For $0 < T \leq T_c$, most of the A atoms remain on their right α sublattice, and other A atoms can change the sublattice to go on the wrong sublattice (noted β). Let us call c_A and c_B the fractional portions of A and B atoms ($c_A = c_B = 1/2$). For the magnetic Ising model, the order parameter is the normalized magnetization $M/N = \langle \frac{1}{N} \sum \sigma_n \rangle$. For the order-disorder transition, a similar parameter is not relevant because $h > 0$. Indeed, it can be deduced from equation (5.28) that its value would be always $c_A - c_B = 0$. Therefore, let us introduce the new parameters

$$r_A = \frac{1}{N_A} \sum_{n \in \alpha} p_n^A \quad (5.31)$$

$$w_A = \frac{1}{N_A} \sum_{n \in \beta} p_n^A \quad (5.32)$$

where r_A denotes the number of A atoms on the right α sublattice divided by the total number of A atoms N_A , and w_A the number of A atoms on the wrong β sublattice divided by N_A . By definition, $r_A + w_A = 1$. At $T = 0\text{K}$, $r_A = 1$, at $T = \infty$, $r_A = w_A$. Moreover, $c_A = c_B = 1/2$, and the number of sites of each sublattice are equal ($N_\alpha = N_\beta = N/2$); it follows that $r_A = r_B + c_B - N_\alpha/N = r_B = r$ and $w_A = w_B = w$. Therefore, these two parameters can be used to create an order parameter similar to the magnetization

$$\xi = \frac{r - w}{r + w} = 2r - 1 \quad (5.33)$$

ξ is called the *long range order* LRO parameter, it is a measure of the fraction of atoms A

5. Introduction to Order-Disorder Transitions

sitting on their right sublattice site. Its value is $\xi = 1$ at $T = 0$ K, $0 < \xi < 1$ for $0 < T \leq T_c$, and 0 for $T > T_c$.

Similarly to equation (5.31), let us introduce the parameter

$$r_n = \frac{1}{2Nz_n} \sum_{\substack{(j \in \alpha)(j+n \in \beta) \\ (j \in \beta)(j+n \in \alpha)}} P_j^A P_{j+n}^B \quad (5.34)$$

which corresponds to the number of right n^{th} nearest neighbors divided by $2Nz_n$ the number of pairs formed by the nearest neighbors of the system (independently whether A is in the right or wrong position). Here again $r_n + w_n = 1$. Similarly to equation (5.33), let us define

$$\xi_n = \frac{r_n - w_n}{r_n + w_n} = 2r_n - 1 \quad (5.35)$$

ξ_n is a *short range order* SRO parameter. It corresponds to the pair correlation coefficient between the n^{th} nearest neighbors. Since the atoms always tend to have for nearest neighbors the right ones, we have $\xi_1 \geq \xi_2 \geq \dots \geq \xi_n$. Moreover, for very large distances between sites $n \rightarrow \infty$, the probability of finding a right pair r_n becomes independent of n and can be expressed in function of the probability of finding a pair of atoms both on their right site or both on their wrong site. Equation (5.34) therefore becomes

$$r_\infty = r^2 + w^2, \quad (5.36)$$

which, with equation (5.33), becomes

$$\xi_\infty = 2r_\infty - 1 = \xi^2 \quad (5.37)$$

The long range order parameter corresponds to the square of the limit of the short range order parameter series.

5.4.3 Approximate Methods

There exist many methods for treating the phase transitions on an Ising lattice. The first one was introduced by Bragg and Williams in 1934 for the order-disorder transition [134], and is usually referred to as the B-W method. This is similar to the Weiss's method for the treatment of ferro-paramagnetic transitions [135]. Let us illustrate this method with the CuZn phase transition. The model is based on the simplification provided by the assumption that $\xi_1 = \xi_2 = \dots = \xi$. It means that all the sites of a sublattice α or β have the same probability to be occupied by A or B independently of their neighbors. There is absolutely no *correlation length* (in magnetic terms it is the maximum distance over which the flip of a spin has no more influence on the other spin). This method neglects all the fluctuations of the system. The mean number of the 1st nearest neighbor A-B bonds is by definition $N_{AB} = (N/2) z r_1$, where z is the

number of nearest neighbors (its value is 8 for the CuZn phases). Under these conditions

$$N_{AB} = (N/2) z r = Nz (\xi^2 + 1) / 4 \quad (5.38)$$

Calling $V = V(1)/2$ the mean energy to form an A-B bond, with $V(1)$ defined in (5.27), the mixing energy becomes

$$E = -N V z (\xi^2 + 1) / 4 \quad (5.39)$$

Additionally, the complexion number in the B-W approximation is

$$\Omega = \frac{N_A!}{N_A r_A! N_A (1-r_A)!} \cdot \frac{N_B!}{N_B r_B! N_B (1-r_B)!} \quad (5.40)$$

and therefore, using the Stirling approximation and the fact that $N_A = N_B = N/2$, the entropy of configuration can be simplified

$$S = \left(-\frac{kN}{2} \right) \cdot [r_A \ln r_A + (1-r_A) \ln(1-r_A) + r_B \ln r_B + (1-r_B) \ln(1-r_B)] \quad (5.41)$$

With equation (5.33) and the fact that $r_A = r_B = r$, it becomes

$$S = \left(-\frac{k_B N}{2} \right) \cdot [(1+\xi) \ln(1+\xi) + (1-\xi) \ln(1-\xi) - 2 \ln 2] \quad (5.42)$$

Therefore, the free energy of mixing is given by

$$\frac{F}{N} = \left(-\frac{Vz}{4} \right) (\xi^2 + 1) + \frac{k_B T}{2} \cdot [(1+\xi) \ln(1+\xi) + (1-\xi) \ln(1-\xi) - 2 \ln 2] \quad (5.43)$$

To find the order parameter for the equilibrium state, we are looking for the minimum of the $F(\xi)$ obtained for

$$\left(\frac{\partial F}{\partial \xi} \right)_T = 0 \Leftrightarrow \ln \left(\frac{1+\xi}{1-\xi} \right) = 2 \frac{T}{T_c} \xi \Leftrightarrow \xi = \tanh \left(\frac{T_c \xi}{T} \right) \quad (5.44)$$

where

$$T_c = \frac{Vz}{2k_B} \quad (5.45)$$

Equation (5.44) does not have any analytical solution but can be solved numerically. As shown in Fig. 5.3, it has always the solution $\xi = 0$, and when $T < T_c$, it has also a second distinct solution. For $T < T_c$ the solution $\xi = 0$ is unstable and the other solution is stable: the alloy is ordered, even if not completely ordered. For $T \geq T_c$, the solution $\xi = 0$ is stable: the alloy is disordered. There is no discontinuity of the order parameter when T goes through T_c : it is a second order transition.

The B-W model is also called the *mean-field* approximation, generally used for the magnetic Ising model. Indeed, the B-W approximation is equivalent to consider that only $V(1) > 0$, and the other $V(n) = 0$, which, by considering equation (5.29), is the same as to replace a fluctuating field by a mean field. Apart from a constant term corresponding to the mean field of

5. Introduction to Order-Disorder Transitions

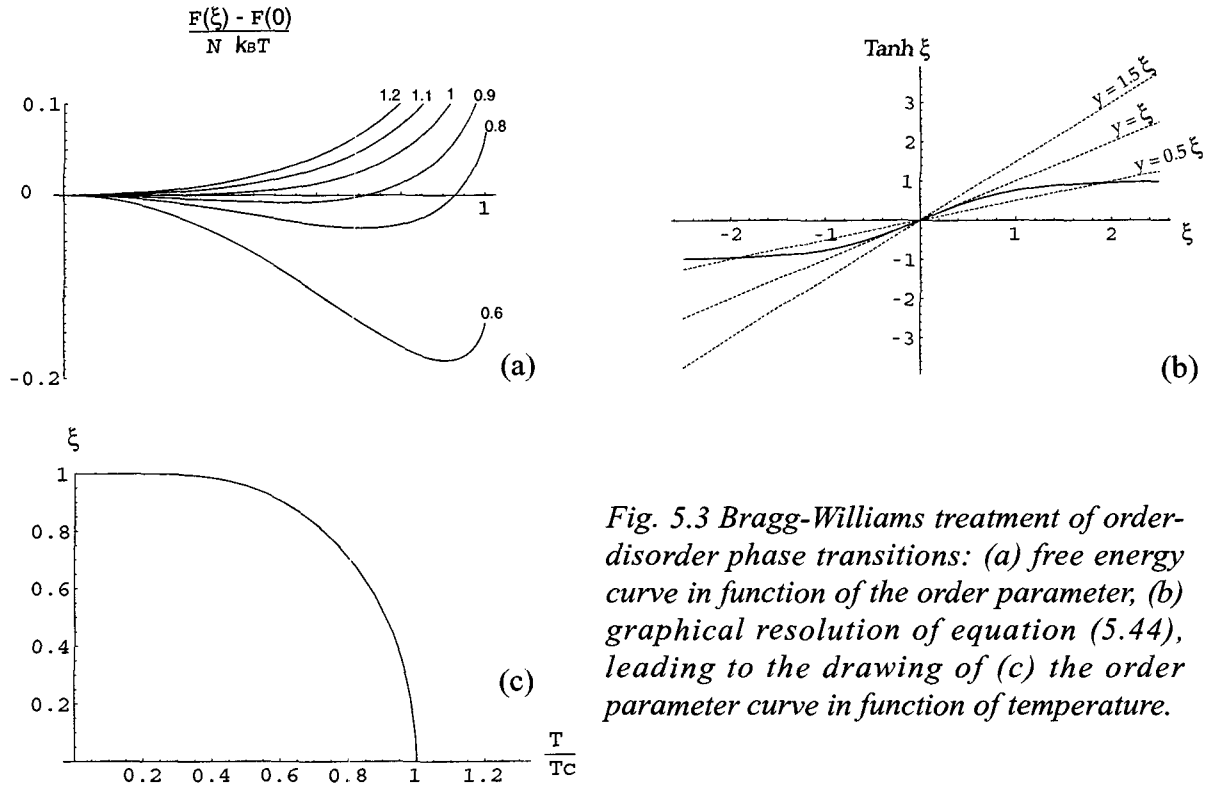


Fig. 5.3 Bragg-Williams treatment of order-disorder phase transitions: (a) free energy curve in function of the order parameter, (b) graphical resolution of equation (5.44), leading to the drawing of (c) the order parameter curve in function of temperature.

the completely disordered state, the expression of the equivalent mean field is

$$h_0 = \frac{zV\xi}{2} \quad (5.46)$$

This can also be obtained by the differentiation of (5.39). Considering that the proportion r/w obeys the Boltzmann law, the result (5.44) can be found again

$$\frac{r}{w} = \exp\left(\frac{2h_0}{k_B T}\right) = \exp\left(\frac{zV\xi}{k_B T}\right) = \frac{1 + \xi}{1 - \xi} \quad (5.47)$$

We have introduced the B-W in the example of AB (50%, 50%) alloy with a transition between CC and SC structures. Actually, the model can be generalized to any AB (c_A , c_B) alloy. The B-W model can also be applied to transitions between FCC and SC structures. In this case, the model is more complex and must take into account the 1st-antiliberals the α - α and β - β bonds in addition to the α - β bonds. Its results in a prevision of a first order transition¹. The B-W model is generally in good agreement with the observations of order-disorder phase transition. For instance, the CuZn BCC-SC transition is of second order whereas the AuCu₃ FCC-SC transition is of first order. No metastable CuZn structure phase exists at room

1. The first order character of the transition of FCC alloy can also be understood by the fact that the FCC lattice is a very constrained or frustrated lattice, i.e. not easily ordered [128].

temperature after quenching, in contrary to the AuCu₃ system. Nevertheless, there are many inadequacies in the B-W approximation. The *critical exponents* (representative of the variation with T near T_c of parameters such as the order parameters, the correlation length or the heat capacity) are not correct. A better approximate model has been given by Bethe which considers not only the point correlation function (as the B-W method), but also the pair correlation functions [136]. This method has been generalized by considering the polyhedra interactions, this has been done mainly by Kikuchi (1951) with its *Cluster Variation* method (CV) [137, 138]. It gives very good approximations for the critical exponents.

Another very performing method is based on the renormalization group theory developed by Wilson in 1972 [139] (he was award the 1982 Nobel Prize in Physics for his contribution). Wilson's method is very general and has wide applicability extending well beyond the field of phase transitions. The method is based on finding a link between the coupling parameters (such as J in the simple Ising model) so that the problem remains invariant, i.e. the partition function must be unchanged during the scaling steps (for example when a group of 4 spins is replaced by one spin according to a certain averaging law). The method can predict with a very high degree of accuracy the critical exponent (behavior close to T_c).

5.5 Scattering and HREM Images of Disordered Particles

This section is dedicated to the diffraction, HREM observations and simulations of disordered particles. Other methods usually more effective for ordering characterization [140], like X-ray and neutron diffraction will not be presented because they are not appropriate to our study of the nanosized precipitates present with many other phases in a matrix. Many disordered structures can be generated along a trajectory during Monte Carlo simulations of an ordering mechanism. Their representations are not easily comparable in the direct space, but if large enough, they exhibit the same diffraction patterns. Nevertheless, as it will be shown, this diffraction pattern is not enough to completely characterize the ordering mechanisms.

5.5.1 Diffuse Scattering and Disorder

As introduced in section 3.4.2, the diffuse scattering comes from a potential disorder in a crystal: the finite size of a particle breaks the translational and infinite order and makes the spots broader, the thermal motions (Debye-Waller) or small displacements of atoms around their mean positions lower the spot intensities for high G vectors. The diffraction generally comes from the order, which, for a binary substitutional alloy, depends on the correlations that exist between the substitutions (as shown in section 5.4.2). Cowley [141] has expressed the total diffracted intensity by

$$I(u) = N(f_A c_A + f_B c_B)^2 \sum_n \exp[2\pi i u \cdot \mathbf{R}_n] + N(f_A^2 - f_B^2) \sum_n \langle s_0 s_n \rangle \exp[2\pi i u \cdot \mathbf{R}_n] \quad (5.48)$$

5. Introduction to Order-Disorder Transitions

where N is the number of atoms, \mathbf{R}_n the vectors between the lattice points n , f_A and f_B their atomic diffusion factors, and $\langle s_0 s_n \rangle$ the correlation between the site 0 and n . s_n represents the difference between the real occupation of the site n and the mean occupation

$$s_n = p_n^A - c_A = c_B - p_n^B \quad (5.49)$$

with p_n^A defined in (5.25). Here the brackets $\langle \rangle$ represent the spatial average over all sites¹. $\langle s_n s_m \rangle$ is linked to the probability $\langle P_n^A P_m^B \rangle$ noted P_{nm}^{AB} to find the A and B atoms separated by a vector $m - n$ given by

$$P_{nm}^{AB} = \langle p_n^A p_m^B \rangle = c_A c_B + \langle s_n s_m \rangle. \quad (5.50)$$

$\langle s_n s_m \rangle$ are other SRO parameters. They are more often used than the ξ_n SRO parameters defined in 5.4.2 because their one-point and two-point correlations can directly be obtained by inversion of the second term of equation (5.48) noted $I_d(\mathbf{u})$

$$\langle s_0 s_n \rangle = \frac{1}{N(f_A - f_B)^2} \mathfrak{F}^{-1}[I_d(\mathbf{u})] \quad (5.51)$$

The parameter $\alpha_{nm} = \langle s_n s_m \rangle / c_A c_B$ is called the *Warren-Cowley parameter*. It is also often used. Similarly to ξ_n , it tends to the square of the long range order ξ when the modulus of $m-n$ tends to ∞ , with m and n respectively on α and β .

The other multiple-point correlations $\langle s_n s_m s_l \dots \rangle$ cannot be obtained by diffraction experiments. However, they are essential to unambiguously define the complete arrangement of the atoms, and thus to completely determine the order. Indeed, Welberry [142] has shown that substantial differences in the multi-point lattice averages can exist without affecting the two-point correlations, and thus proving that very different kinds of ordering clearly distinguishable in direct space can exhibit the same diffraction patterns with the same intensities. Therefore, equation (5.48) cannot be used to prove the unicity of a model, but can only be used to simulate diffractions when strong physical and chemical arguments govern the model and only when few parameters -in general the interaction constants of the Monte-Carlo process- are fitted by the program; for example for 1,3-dibromo-2,5-diethyl-4,6-dimethylbenzene and for mullite [142].

In equation (5.48), the first term gives the Bragg peaks and the second term gives the diffuse scattering. It can be noticed that this diffuse intensity part produces sharp superstructure Bragg spots when the perfect superstructure is obtained ($\xi = 1$), diffuse peaks or streaks if the structure just exhibits a 'tendency towards ordering' ($0 < \xi < 1$), and a uniform background for disordered structure ($\xi = 0$). The superstructure peaks for $0 < \xi < 1$ are diffuse due to the small size of the ordered clusters (linked to SRO parameter). Their intensities decrease rapidly with u because the order is only partially obtained inside of each cluster (similar to a Debye-Waller effect). This description is a simplified presentation, more

1. In a large system in thermal equilibrium, this spatial averaging is equivalent to a temporal averaging or to an averaging on all the configurations with their respective probability.

details are given in [141, 142, 143, 144].

5.5.2 Diffuse Scattering Simulations

In chapter 6, diffuse scattering simulations will be performed to confirm the validity of an ordering model developed for the precipitation in the Al-Cu-Mg-Si alloys. We will study an order-disorder transition inside a precipitate family containing four elements (Al, Mg, Si, and Cu), with substitutions and atomic displacements. Since this transition is more complicated than the substitution ordering with two species, it will not be possible to apply equation (5.48). To simulate diffuse scattering, we have preferred to build an image of the total projected potential of the disordered structure to perform its FFT. Indeed, from equation (3.7), noting n the zone axis, one can notice that the intensity of the diffraction pattern is proportional to the square of the modulus of the FFT of the projected potential

$$\begin{aligned} I(\mathbf{u}) &= |A(\mathbf{u})|^2 = K^2 \left| \int_{\Omega} V(\mathbf{r}) \exp[2\pi i \mathbf{u} \cdot \mathbf{r}] d\mathbf{v} \right|^2 \\ &= K^2 \left| \int_{\mathbf{r} \perp \mathbf{n}} \int_{\mathbf{r} \parallel \mathbf{n}} V(\mathbf{r}) \exp[2\pi i \mathbf{u} \cdot \mathbf{r}] d\mathbf{v} \right|^2 = K^2 \left| \int_S V_p(\mathbf{r}) \exp[2\pi i \mathbf{u} \cdot \mathbf{r}] ds \right|^2 \end{aligned} \quad (5.52)$$

The projected potentials are calculated for the atomic species using the method described in annex A and integrated along the observation direction (which can be different from a zone axis). Such potential images are represented in Fig. 5.4. Diffraction and HREM simulations usually require periodic conditions to perform Discrete Fourier Transforms. These conditions are obvious for translational periodic structures (perfect crystals), but are arbitrary and require large supercell sizes for quasicrystals, structures containing defects and disordered structures. The advantage of the method presented here is that no periodic conditions are required due to the use of Continuous Fourier Transform to calculate the atomic potential of a single atom. Moreover, projected potential simulations can be performed for comparisons with the experimental HREM images (if the weak phase object approximation is obtained), permitting to distinguish two potential disordering processes producing the same point and pair correlation parameters.

5.5.3 Filtered HREM Images

In the weak phase object approximation at Scherzer defocus a HREM image is nearly the representation of the projected potential of the object. If the observed area of the crystal is large enough, it is possible to calculate from the HREM images the multiple point correlations and thus completely define the order. Even if the weak phase object approximation is not obtained, for simple A-B substitutional transformations, with a large difference between the A and B diffusion factors, a direct interpretation of the atomic position remains possible [145].

However, at least for the precipitates studied in this work, the thin parts of the samples

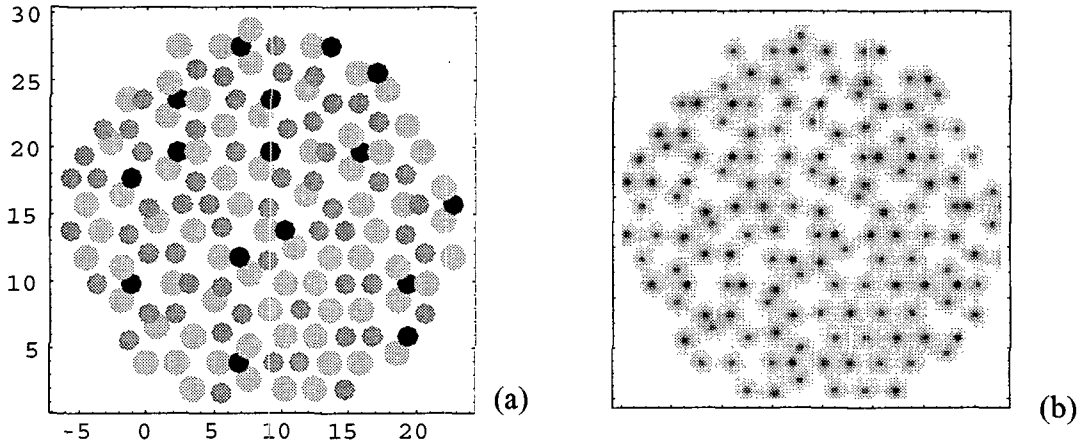


Fig. 5.4 Disordered structure represented in (a) illustrative model: \bullet Si, \circ Mg, \bullet Cu, and (b) projected potential calculated with annex A.

are too amorphous to be observed. Thus, the HREM images were acquired in thicker parts which impeded the weak phase object approximation. Moreover, the transformation is more complex than a simple A-B substitutional transformation since it involves four elements (Al, Mg, Si and Cu) with substitutions and atomic displacements (see chapter 6). In addition, no clear pattern can be identified in the observed precipitates due to the slight disorder between each atomic plane normal to the electron beam. Nevertheless, as usual in ordering phenomena, the atoms are disordered around the lattice of the final ordered phase. Applying a mask filter in the reciprocal space of the HREM images allows to show an image of the mean atomic positions, i.e. the latent lattice. Indeed, the filtering corresponds to apply to the FFT of the image (noted $\mathfrak{I} I(u)$) a Gaussian mask (size noted $1/m$ [nm^{-1}]) with the periodicity (noted $1/a$ [nm^{-1}]). The filtered image $I_f(u)$ can be written in one dimension by

$$\begin{aligned}
 I_f(x) &= \mathfrak{I}^{-1} \left[\mathfrak{I} I(u) \bullet \sum_{n=-\infty}^{\infty} \delta(u - n/a) \otimes \exp[-u^2/m] \right] \\
 &= I(x) \otimes \mathfrak{I}^{-1} \left[\sum_{n=-\infty}^{\infty} \delta(u - n/a) \otimes \exp[-u^2/m] \right] \\
 &= I(x) \otimes \left[\sqrt{\pi m a} \sum_{h=-\infty}^{\infty} \delta(x - ha) \bullet \exp[-m\pi^2 x^2] \right] \quad (5.53)
 \end{aligned}$$

Equation (5.53) shows that applying a mask filter in the reciprocal space corresponds to average each pattern separated by the periodicity a of the direct space image with the neighboring other patterns on a distance m . Thus, this makes appear a pattern (of size a) only if mean positions (with random disorder around these positions) exist inside this pattern. The size of the mask ($1/m$) must be chosen to contain the diffuse intensity, which means that the

average must be performed on the correlation length distance. Therefore, this method is effective only for slightly disordered structures (largely below the critical transition temperature). This method was used for comparisons between experimental and simulated HREM images based on a refined model of the crystal structure (section 6.3.5).

5.5.4 Dark Field Superstructure Images

Some slightly disordered structures can be mixed, i.e. constituted with two or more phases corresponding to superstructures. *Dark field superstructure images* consist in acquiring dark field images with two diffracted spots (single plane stacking information) or, if it is possible, with 3 non-colinear spots (atomic column arrangement information) of each superstructure phase. If the information limit is sufficient to transfer the spatial frequencies, the lattices of each structure appear by interference. Therefore, these images can be used to observe the ordered parts of a disordered precipitate, and possibly to determine the correlation length. To obtain such images, the disordering must occur two—dimensionally so that the crystal remains perfectly periodic in the third direction (direction of the electron beam) and so that superposition effects are eliminated. This method can be applied to thick regions with a relatively low resolution microscope. For example, a conventional electron microscope not necessarily dedicated to HREM is sufficient for periodicities higher than 0.4 nm. This type of images is widely used for ordered-disordered structures [146, 147] such as Cu-Zn, Cu-Al or Ni-Mo[148], Au₄Mg, AuCd, AuMn [149, 150]. In this work, DF superstructure images will be used to show different superordered parts in the AlCuMgSi rod-shaped precipitates (section 6.1.3).

5.5. Scattering and HREM Images of Disordered Particles

Chapter 6

Order-Disorder Transition in the AlCuMgSi and AlMgSi Alloys

This chapter deals with the precipitation of the QP and QC rod-shaped precipitates identified in the WFA alloy reinforced with the Al₂O₃ fibers or SiC particles (section 4.4). More generally, it brings a simple and new approach to the understanding of the precipitation mechanisms in the 6xxx aluminum alloys and in some 2xxx aluminum alloys. Section 6.1 shows by superstructure DF images and in-situ TEM aging that a structural phase transition exists between the QP, QC and Q phases. Section 6.2 proposes an order-disorder model implying the existence of a latent lattice to describe the transition. The model is generalized to the metastable phases in the 6xxx alloys. One of the direct application given in section 6.3 is the determination by microdiffraction simulations of the crystallographic structures of the QC and β' phases. The ordering processes (kinetics and size effects) are discussed in section 6.4 and illustrated with Monte Carlo simulations. Eventually, the complete phase transition model is summarized and discussed in section 6.5.

6.1 Structural Phase Transition in the AlCuMgSi Alloys

6.1.1 TEM Observations of the QP, QC and Q Phases

QP/QC/Q Precipitates in the T6 State Matrix

As shown in section 4.4.2, except for the pure Si precipitates, all the observed rod-shaped precipitates in the T6 reinforced WFA alloy contain Cu, Mg, Si and probably Al. They have a hexagonal structure with $a = 0.395$ nm (QP) or with $a = 0.675$ nm (QC). By overaging at 300°C , they seem to transform into the stable Q- $\text{Al}_5\text{Cu}_2\text{Mg}_8\text{Si}_6$ phase. Their c parameter was supposed to be $c = a_\alpha = 0.405$ nm. Moreover, we noticed that the PS of the HREM images of the QP, QC and Q phases acquired in their rod direction $[001]$ have some common spots which correspond to the $\{100\}_{\text{QP}}$ spots. This property appears in the direct space by the fact that $a_Q/a_{QP} \approx \sqrt{7}$ and $a_{QC}/a_{QP} \approx \sqrt{3}$. One can assume that the QP, QC and Q phases are deeply structurally linked, and these observations call to mind the order-disorder transitions introduced in chapter 5. However, the small size of the QP and QC precipitates (section ≈ 2 nm) impedes for the moment further quantitative measurements or qualitative confirmation of this idea.

QP/QC/Q Precipitates in the As-Cast State Matrix

The rod-shaped precipitates present in the as-cast reinforced alloy are shown in Fig. 6.1a. They are coarser (section ≈ 20 nm) than in T6 condition due to the slow air cooling of the material. Some of them are constituted of θ' and mixed QC/Q phases. The rod shape of θ' - CuAl_2 precipitates is rather unusual because normally they appear as plates due to their tetragonal structure with $a_{\theta'} = 0.405$ nm $= a_\alpha$ ($c_{\theta'} = 0.58$ nm) and their OR $[100]_{\theta'} // [001]_\alpha$ and $(001)_{\theta'} // (100)_\alpha$. Here, their unusual shape is due to a new OR:

$$[100]_{\theta'} // [001]_\alpha \text{ and } ((001)_{\theta'}, (100)_\alpha) = 16^\circ \pm 0.5^\circ \quad (6.1)$$

as shown in Fig. 6.1b. This OR was found for all the observed θ' precipitates, isolated or joined to other phases.

The size of the precipitates allowed valuable EDS measurements that confirmed the close composition of QC and Q phases (compare Fig. 6.1e and f). The important observation in agreement with our idea about a possible phase transition between the Q family phases is given in Fig. 6.2. The BF image of Fig. 6.2a acquired on the CM20 microscope clearly shows a mixed QP/Q precipitate. Some parts appear ordered with a large lattice corresponding to the Q structure and other parts appear disordered. The corresponding SAED pattern given in Fig. 6.2b exhibits sharp spots in agreement with the QP hexagonal structure ($a = 0.395$ nm ± 0.005 nm). The OR with the matrix is:

$$(100)_{\text{QP}} // (100)_\alpha \text{ and } [001]_{\text{QP}} // [001]_\alpha \quad (6.2)$$

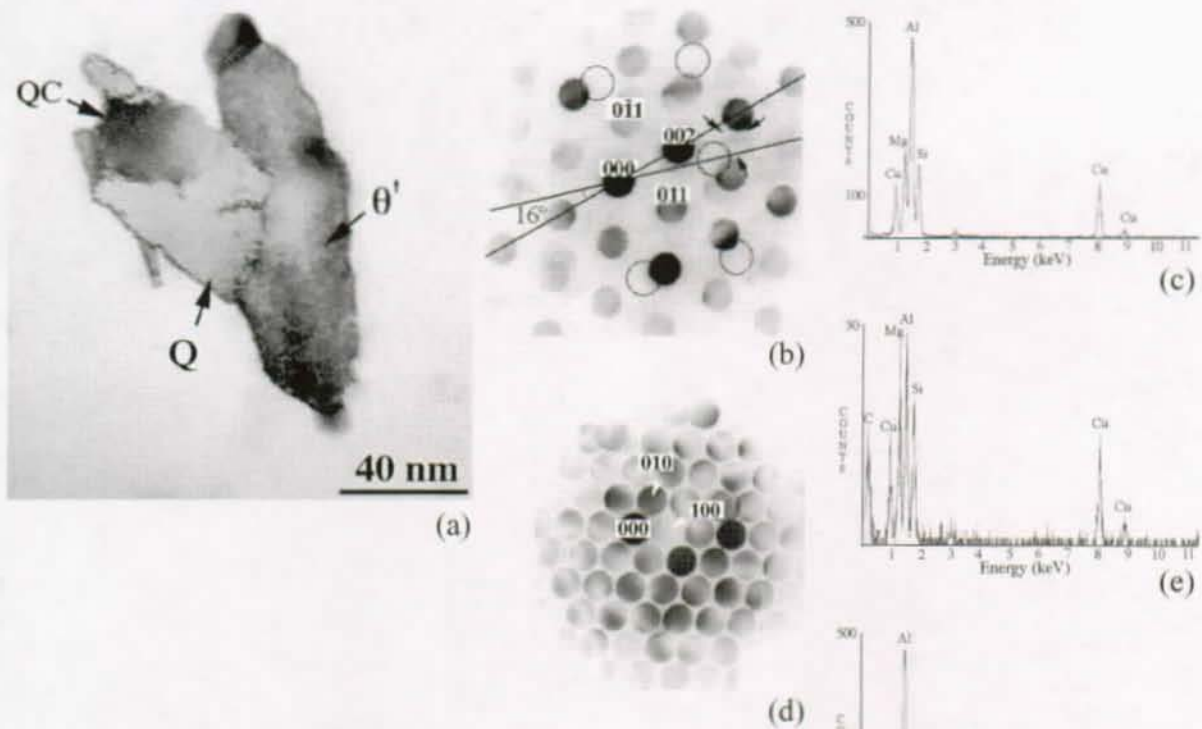


Fig. 6.1 Rod-shaped precipitates of θ' , QC and Q phases in the matrix of the as-cast WFA/SiC/p composite: (a) BF image in $[001]_{\alpha}$ direction, with microdiffraction patterns and EDS spectra of the θ' part (in b and c), QC part (in d and e) and Q part (f).

which is the same that OR (4.12) or (4.20). The Q spots appear as diffuse spots around the QP spots in the SAED. The maxima are formed at the same positions than the Q phase observed in Fig. 4.18e.

6.1.2 Link between the QP/QC/Q Lattices

Fig. 6.2 confirms that QP and Q phases, which coexist in the same precipitate, have common spots in their SAED. Other observations confirm this fact for the QP and QC phases (see Fig. 6.11e and Fig. 6.19b for example). It is therefore concluded that Q and QC are based on the same QP latent lattice. For all the observed precipitates in the as-cast or T6 reinforced alloys, the ORs of this QP lattice (really observed as in Fig. 6.2b or Fig. 6.2d, or deduced from the common Q and QC spots) are:

$$\text{OR1} \quad (100)_{\text{QP}} // (100)_{\alpha} \text{ and } [001]_{\text{QP}} // [001]_{\alpha} \quad (6.3)$$

$$\text{OR2} \quad (100)_{\text{QP}} // (110)_{\alpha} \text{ and } [001]_{\text{QP}} // [001]_{\alpha} \quad (6.4)$$

The link between the Q family structures is represented in the direct-space in Fig. 6.3. The parameters of the Q and QC phases deduced from this model and based on the QP lattice

6. Order-Disorder Transition in the AlCuMgSi and AlMgSi Alloys

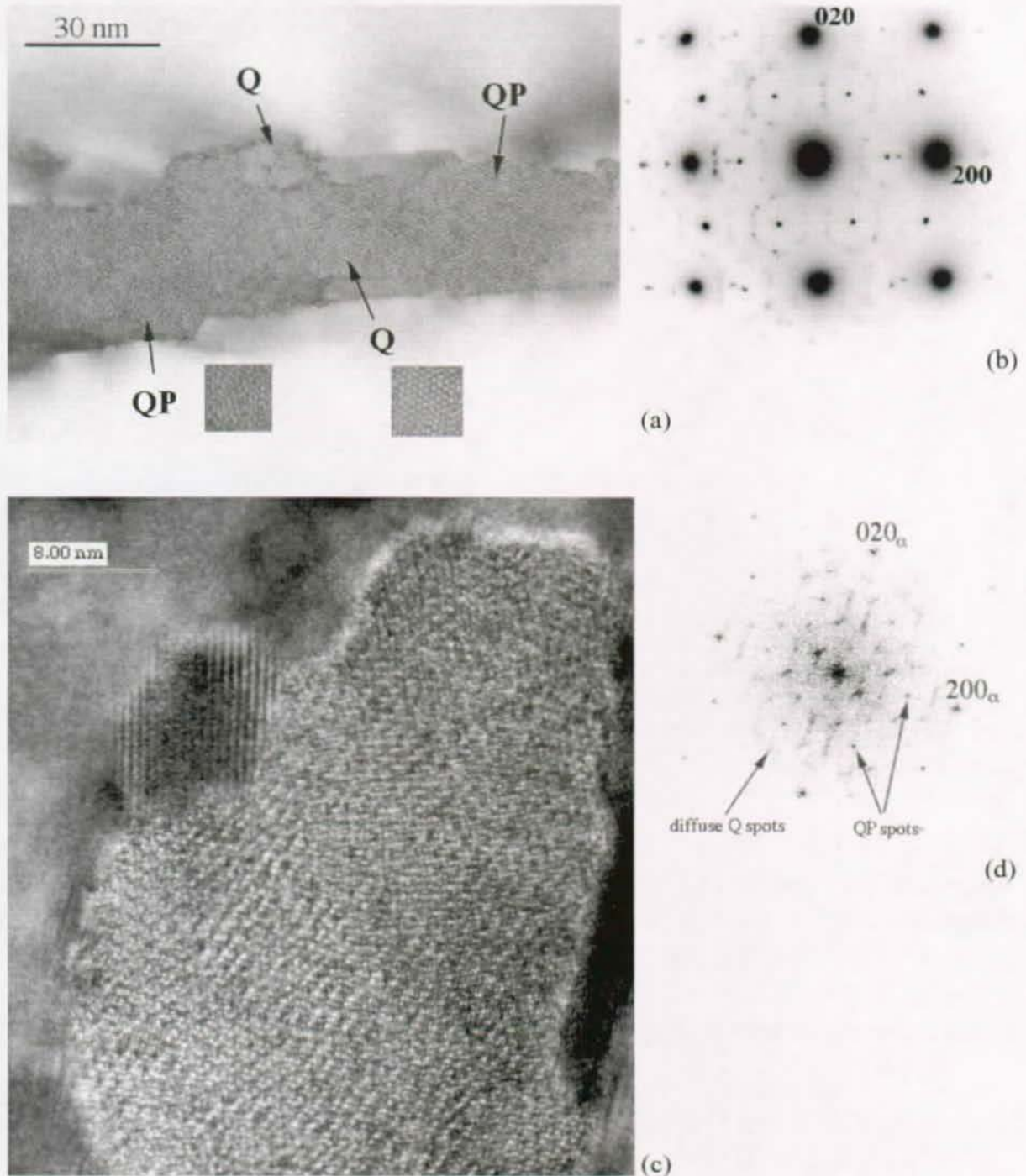


Fig. 6.2 Mixed QP/Q rod-shaped precipitates in $[001]_{\alpha}$ direction in the matrix of the as-cast WFA/SiC/p composite. (a) BF image acquired with the CM20 microscope showing the ordered Q parts and disordered QP parts (enlargements at the bottom), with (b) its SAED pattern, the sharp spots correspond to the QP phase and the diffuse spots around them correspond to the Q phase. (c) HREM image obtained with the CM300 microscope (no periodic pattern is visible), (d) its PS is similar to the SAED presented in (b).

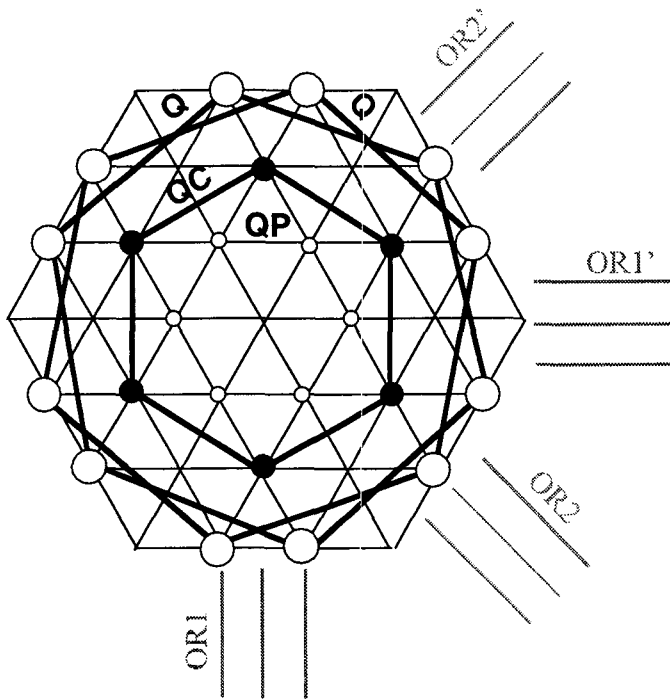


Fig. 6.3 Representation in the direct space along the $[001]_{\alpha}$ direction of the link between the QP, QC and Q lattices. All are based on the QP latent lattice. The two ORs with the Al matrix are indicated.

($a = 0.393$ nm) are:

$$a_{QC} = \sqrt{3} a_{QP} = 0.680 \text{ nm (instead of the observed } 0.675 \text{ nm)}$$

$$a_Q = \sqrt{7} a_{QP} = 1.040 \text{ nm (instead of the observed } 1.035 \text{ nm).}$$

Most of the QC precipitates are based on the QP lattice in OR2, which can be explained by the small misfit of 0.84% associated to the $(400)_{QC} // (220)_{\alpha}$ planes. Most of the Q precipitates are based on the QP sublattice in OR1 as explained by the small misfits between the Al and Q lattices [151]. The nanosized isolated QP precipitates observed in the T6-temper composite are found in the OR1, which can be explained by the small misfit of 2.9% associated to the $(110)_{QP} // (200)_{\alpha}$ planes.

The maximum number of variants generated for each OR (1 or 2) is given by the symmetries of the matrix along the $[001]_{\alpha}$ projection: 4-fold axis and mirror plane \Rightarrow multiplicity = 8. If we only consider the Laue groups of the phases (which are centrosymmetric, see annex C1), the multiplicity for each OR is reduced to 4. Therefore, combining the two possible ORs, we obtain 8 variants generated along the $[001]_{\alpha}$ axis for the Q precipitates, and only 4 for QC or QP because of their common mirror plane with the matrix. Some of the Q variants are represented in Fig. 6.4. The two $[100]_Q$ directions of the two Q variants generated from QP in OR1 make an angle with the $[100]_{\alpha}$ direction of $-\text{Arctan}(1/3\sqrt{3}) = -10.9^{\circ}$ (Fig. 6.3) and are respectively numbered 1 and 2. The two other Q variants generated from 1 and 2 by the 4-fold symmetry of Al (in OR1') are rotated by 90° (one is numbered 3 in Fig. 6.4). The 4 variants in OR2 and OR2' are deduced from all the previous variants by a rotation of 45° (one is numbered 4 in Fig. 6.4). Considering the three equivalent $\langle 100 \rangle_{\alpha}$ directions, the number of variants is 24 for Q, and 12 for QP or QC.

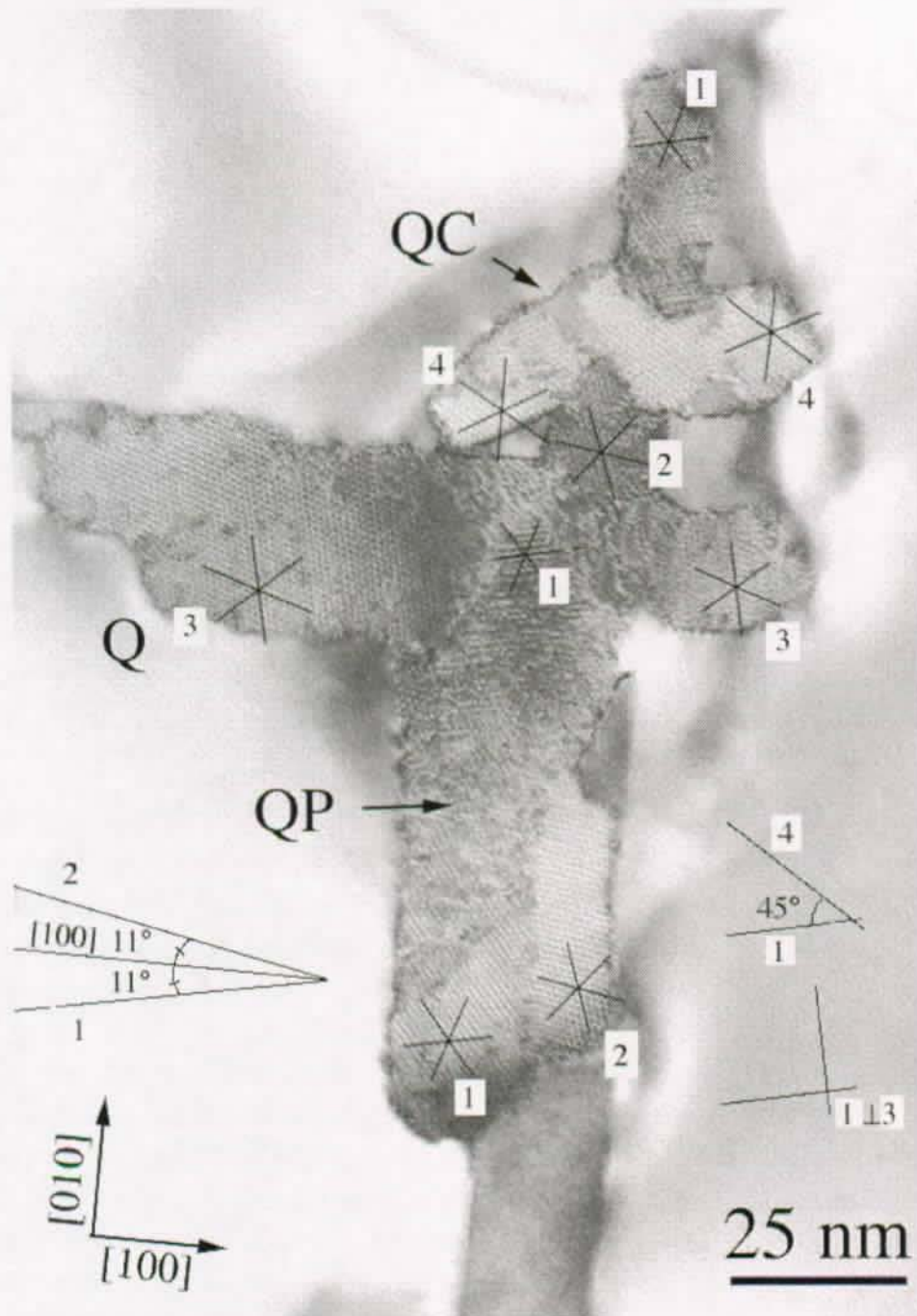


Fig. 6.4 In the matrix of the WFA/Al₂O₃/sf/s composite, BF image in [001]_α axis of a rod-shaped precipitate constituted of QP/QC parts and different Q variants: 1 and 2 correspond to OR1, 3 to OR1' (deduced from 1 by a rotation of 90°), and 4 to OR2 (deduced from 1 by a rotation of 45°).

6.1.3 Confirmation of the Structural Transition between the QP/QC/Q Phases

The diffuse spots in Fig. 6.2*b* or Fig. 6.2*d* can be attributed to a SRO (section 5.5). The Q parts of the precipitate in Fig. 6.2*a* can be interpreted as an ordering of the QP phase toward the Q phase. A continuous transformation between QP and Q by ordering appears to be the most suitable interpretation of our results as confirmed by the absence of clear pattern in the HREM image of Fig. 6.2*c*. A similar transformation between QP and QC seems to be possible since QP and QC phases also have common reflections. Since the QP phase has the smaller hexagonal parameter of the Q family phases, we think by an analogy with the classical phase transitions described in chapter 5 that this phase corresponds to the disordered phase (high temperature) of the QP/QC/Q transition. The QC and Q phase would correspond to ordered phases obtained from QP by a symmetry breaking during the cooling. To confirm this idea: (i) DF superstructure imaging, a special TEM technique to study order-disorder structures (section 5.5.4), was checked to be effective to observe the Q family precipitates, and (ii) in-situ TEM experiments using this technique were performed:

DF Superstructure Images

DF superstructure images of the QP/QC/Q precipitates in the as-cast reinforced alloys have been acquired with the CM20 microscope on a CCD camera after orientating the precipitates along their [001] rod direction and selecting the (110), (210) and (120) spots with the objective diaphragm as indicated in Fig. 6.5*a*. This technique reveals itself to be very effective to observe the QP/QC/Q mixed structures as presented in Fig. 6.5*b,c*. The Q phase is clearly visible in these superstructure images because its spots in the SAED are included in the objective diaphragm as evidenced in Fig. 6.5*a*. These images prove that the precipitates are ordered along their [001] directions and two—dimensionally disordered in the (001) plane.

In-Situ TEM Observations of the Transition

To confirm the transition between $QP \rightarrow QC \rightarrow Q$, the as-cast WFA/Al₂O₃/sf/s composite, has been heated up to 250°C, and in-situ TEM observations on a mixed QP/QC/Q precipitate similar to the ones of Fig. 6.5 have been performed. A video movie of this experiment has been recorded and superstructure images have been acquired on a CCD camera at intermediate temperatures; here only the beginning and final stages are reported. Fig. 6.6*a* is a superstructure image of a mixed precipitate in the matrix at 30°C. The precipitate is mainly ordered with the QC structure, but two separated areas with the Q structure are clearly visible. At 230°C, the QC part begins to dissolve. At 250°C, the dissolution is accelerated. After 15 min at 250°C, most of the QC part is dissolved. After 1 hr at 250°C followed by a rapid cooling until 30°C to stabilize the heating holder, one can notice on Fig. 6.6*b* that a small QC part between the two initial Q parts, and the surrounding disordered QP parts, are totally transformed into Q phase.

6. Order-Disorder Transition in the AlCuMgSi and AlMgSi Alloys

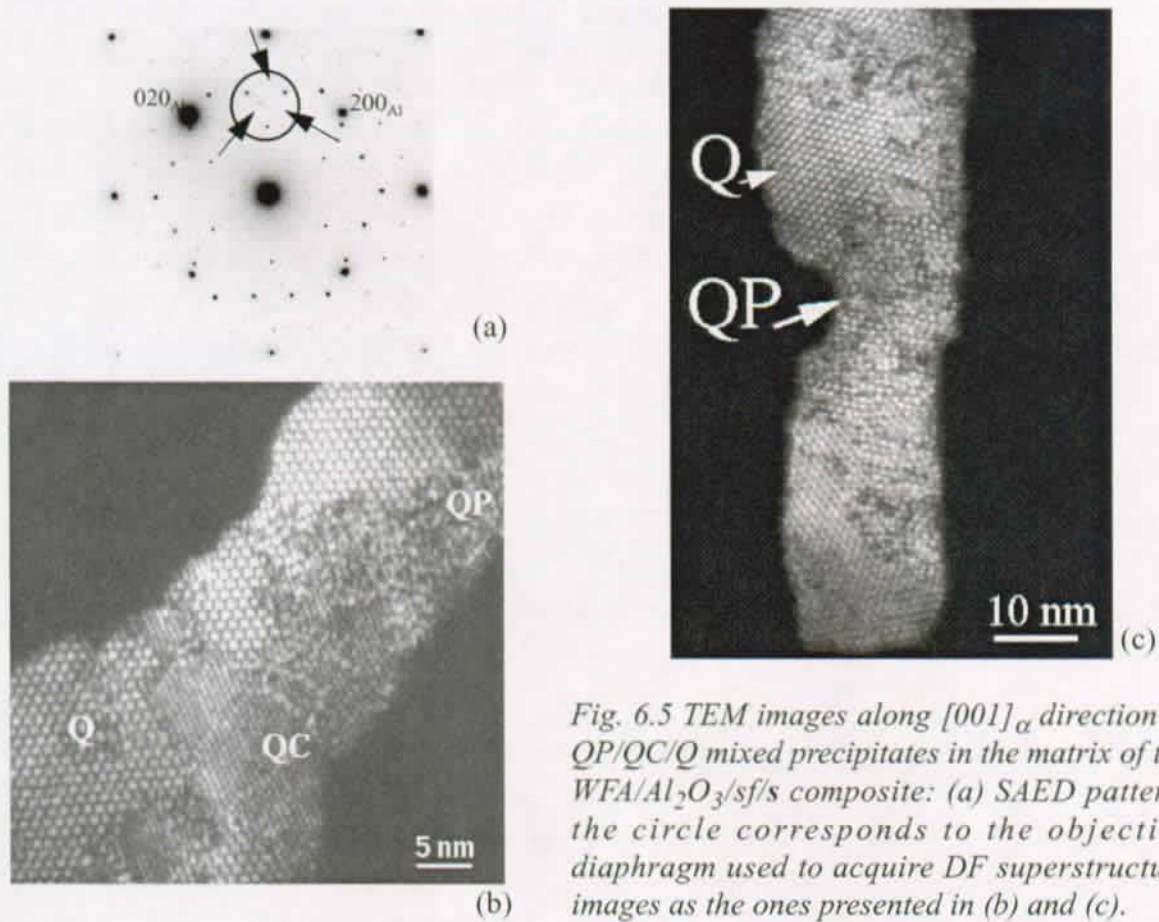


Fig. 6.5 TEM images along $[001]_{\alpha}$ direction of QP/QC/Q mixed precipitates in the matrix of the WFA/ Al_2O_3 /sf/s composite: (a) SAED pattern, the circle corresponds to the objective diaphragm used to acquire DF superstructure images as the ones presented in (b) and (c).

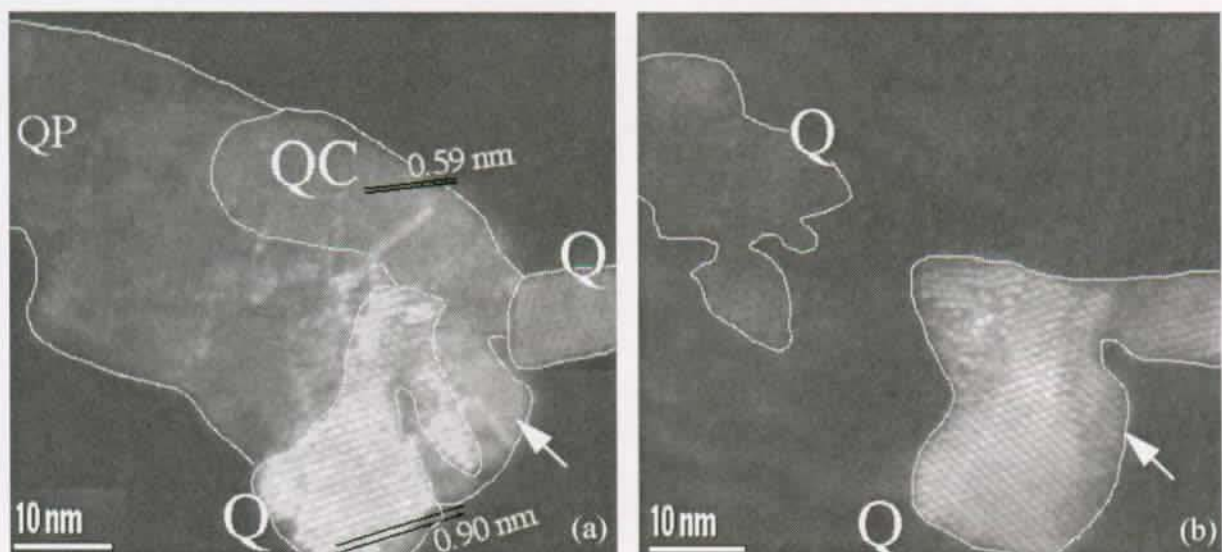


Fig. 6.6 In-situ heating TEM observations in the matrix of the WFA/ Al_2O_3 /sf/s composite of a QP/QC/Q mixed precipitate imaged in DF superstructure in the $[001]_{\alpha}$ axis: (a) 25°C, (b) 250°C for 1h, followed by a cooling down to 30°C to stabilize the sample holder. Notice the transformation of the QC and disordered QP parts into the Q phase.

6.2 Structural Transition Model

6.2.1 Q structure: Sub-Unit Clusters and qh-Lattice

The X-ray determination of the crystal structure of the Q-phase made by Arnberg and Aurivillius [152] allowed us to refine our model of QP/QC/Q structural transition. The Q-phase crystal was found by these authors to have a hexagonal structure with $a = 1.0393$ nm and $c = 0.4017$ nm (space group $P\bar{6}$). The projection down the c -axis is represented in Fig. 6.7a, and the atomic positions are given in Table 6.1 (second column).

As shown in Fig. 6.7b, it can be noticed that the positions of the (Al,Mg), Si and Cu atoms in the Q cell are very close to the positions of the nodes of a lattice constituted by the vertices and the barycentres of the QP lattice (subsequently named the qh-lattice), hexagonal with

$$a_{qh} = \frac{a_{QP}}{\sqrt{3}} = 0.227 \text{ nm} \quad (6.5)$$

The positions of the qh-lattice columns are given in Table 6.1, they were calculated with the

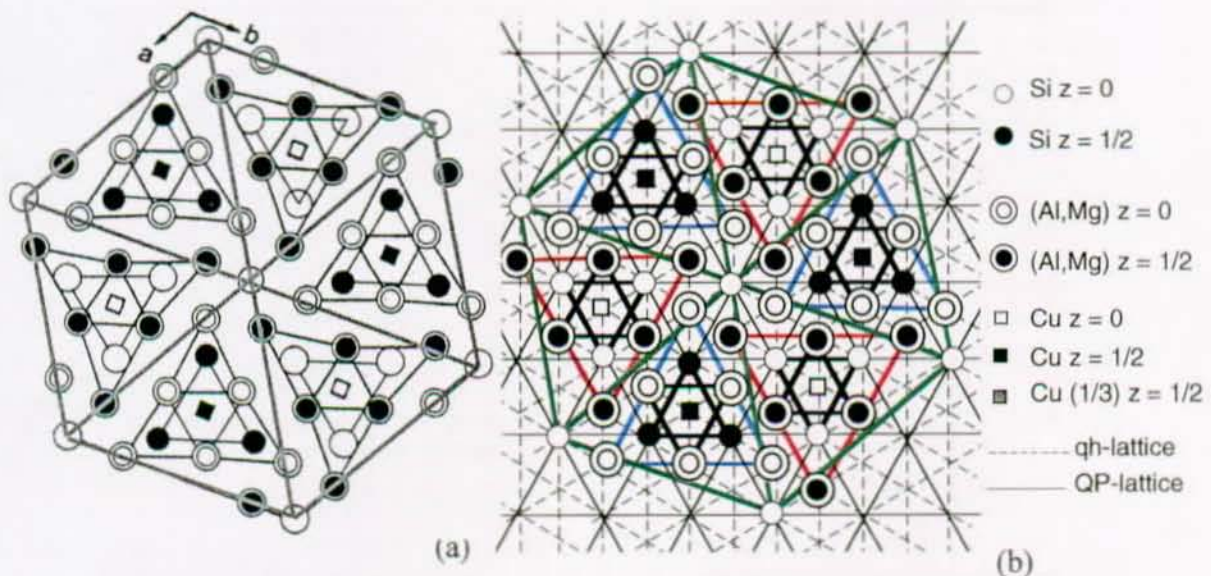


Fig. 6.7 Atomistic model of the structural link between Q and QP: (a) Projection down the c axis of the Q crystal structure from Arnberg and Aurivillius [152]. These authors have already noticed and marked the quasi-hexagonal clusters. (b) Schematic Q structure matching with the QP lattice. The projections of the atoms are situated on the qh-lattice built with the nodes and the barycentres of the QP lattice. The sub-unit clusters are represented by the stars of David. The displacements between (a) and (b) are given Table 6.1

6. Order-Disorder Transition in the AlCuMgSi and AlMgSi Alloys

help of the inverse of the transfer matrix between the Q/qh lattices

$$\begin{bmatrix} 1 & 4 \\ -4 & 5 \end{bmatrix}^{-1} = \frac{1}{21} \begin{bmatrix} 4 & 1 \\ 5 & -4 \end{bmatrix} \quad (6.6)$$

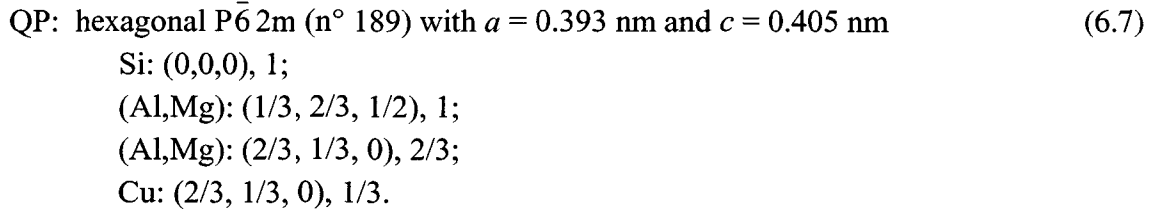
It can also be noticed that the Arnberg's cell is constituted of clusters' of (Al,Mg) and Si atoms distributed around the Cu atoms that can be viewed in projection as a triangle containing a star of David of 3.83 Å (distance between the Si atoms). The modified structure the Q-phase would have if the atoms were placed on the qh-lattice is constituted of similar clusters (represented by the red and blue stars in Fig. 6.7b) containing a star of David of 3.93 Å (QP lattice parameter). The clusters of atoms with the star of David shape are hereafter named QP *sub-unit clusters*. According to our model, the transformation would imply a substitution between atoms followed by small atomic displacements (< 0.5 Å), the (Al,Mg) atoms coming closer without any rotation of the clusters¹. This schematic Q structure is as compact as the Q structure, and has the advantage to introduce the QP lattice found experimentally.

atom	Q atomic positions (X-rays, L. Arnberg)			qh-lattice site positions (calculated)		
	x	y	z	x	y	z
Cu(1)	1/3	2/3	1/2	1/3	2/3	1/2
Cu(2)	2/3	1/3	0	2/3	1/3	0
Si(1)	0	0	0	0	0	0
Si(2)	0.5822	0.8621	1/2	4/7=0.571	6/7=0.857	1/2
Si(3)	0.4157	0.1325	0	3/7=0.428	1/7=0.143	0
(Al,Mg)(4)	0.2426	0.0020	1/2	4/21=0.190	-1/21=-0.047	1/2
(Al,Mg)(5)	0.7878	-0.008	0	17/21=0.810	1/21=0.047	0
(Al,Mg)(6)	0.6332	0.1405	1/2	13/21=0.619	2/21=0.095	1/2
(Al,Mg)(7)	0.3790	0.8587	0	8/21=0.380	19/21=0.905	0

Table 6.1 Atomic positions in the Q crystal determined by Arnberg [152], and in the qh-lattice calculated with equation (6.6), given in Q unit-cell %. The highest displacement is $0.05.a_Q \approx 0.5 \text{ \AA}$.

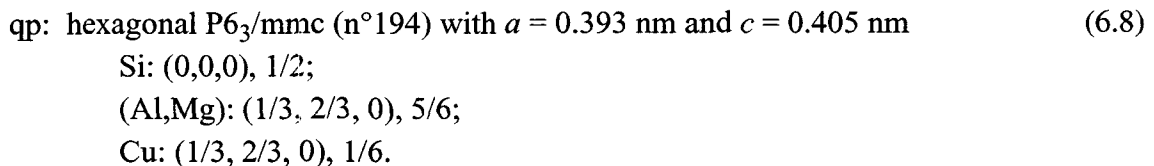
1. In a previous publication [153], we based our model on a figure equivalent to Fig. 6.7, but with a wrong choice of the QP lattice deduced from the Q lattice. Therefore, the table equivalent to Table 6.1 was also far less convincing. We had to invoke a large rotation of the clusters, which is actually absolutely not required. Eventually, the transition does not appear reconstructive as previously supposed, but simply order/disorder.

As a consequence, it seems plausible that the QP phase corresponds to the structure of these modified clusters present in each part of the modified Q structure. We can therefore propose a model for the QP structure by periodically arranging these clusters on the qh-lattice as represented in Fig. 6.8a:



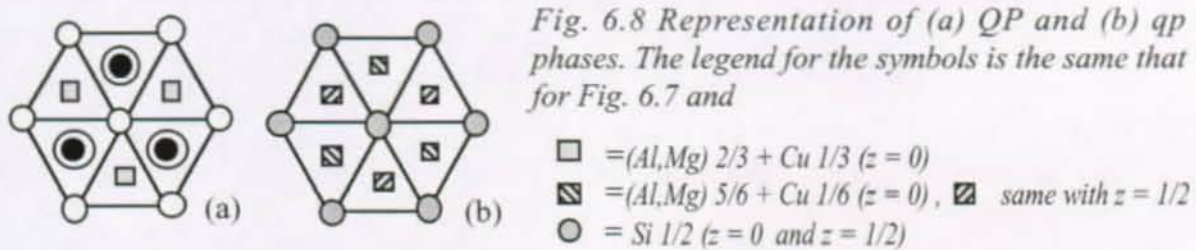
The occupancy probabilities of 1/3 for Cu and 2/3 for (Al,Mg) atoms are necessary to respect as well as possible the [Si]/[Cu] and [Si]/[(Al,Mg)] ratios of the Q-phase. The QP \rightarrow Q transition could be obtained by a substitution on the qh-lattice between the Cu and the (Al,Mg) atoms in half of the clusters (red or blue). The QP phase corresponds to the disordered phase because it has the smallest cell parameters of the Q-family phases. Its disorder character can be explained by the substitutions between the (Al,Mg) and Cu atoms accompanied by the related displacements of the atoms due to the difference between their sizes (Cu, Al and Mg atoms have radii of respectively 1.3, 1.4 and 1.6 Å). This spacial disorder has the same effect for the diffraction that the thermal vibration of atoms (Debye-Waller factor). The atoms are randomly displaced around mean positions (qh-lattice), visible on the filtered HREM image of Fig. 4.15d. The continuous transformation between Q and QP observed in Fig. 6.2a is explained by the beginning of an ordering of the atoms situated on the qh-lattice with the Q-order.

Moreover, it can also be noticed that in the modified Q structure of Fig. 6.7b only the Si atoms are in their right position on the QP lattice, and that the Cu and (Al,Mg) atoms exchange their sites in function of their cluster type (red or blue) on the qh-lattice. The (Al,Mg) and Cu atoms are on an honeycomb lattice corresponding to the qh-lattice without the QP nodes (also called hereafter the qh-lattice). We can therefore imagine a more primitive latent phase, qp, without any distinction between (Al,Mg) or Cu atoms sites, represented in Fig. 6.8b:



The qp \rightarrow QP transition is obtained by a substitution on the honeycomb qh-lattice between the Cu and the (Al,Mg) atoms. We think that the qp phase is the primitive latent phase at the origin of all the transformations since it has the highest hexagonal symmetry group.

Since the distinction between the QP and qp structures is far beyond the actual TEM possibilities we will continue to call the rod-shaped precipitates that exhibit a hexagonal arrangement with $a = 0.393$ nm with the name QP, although their crystallographic structure could probably be the qp phase one.



The proposed model for structural transformation $qp \rightarrow QP \rightarrow Q$ implies the existence of a common latent lattice and atom substitutions on the qh-lattice producing displacements by atomic size effects less than 0.5 \AA . These notions are characteristic of an *order-disorder phase transitions* (chapter 5).

6.2.2 Difference between Q and Q'

The microdiffraction patterns acquired on the rod-shaped Q precipitates (Fig. 6.9a) are not in total agreement with the stable Q structure proposed by Arnberg. Actually, they probably correspond to an intermediate state between the structure of the stable phase of Fig. 6.7a (simulated diffraction in Fig. 6.9b) and the schematic Q structure proposed in Fig. 6.7b (simulated diffraction in Fig. 6.9c). Indeed, the experimental diffraction presents strong $\{140\}$ and $\{310\}$ spots as for the stable Q phase, but also strong $\{210\}$ spots which do not appear in the simulation of the stable Q phase diffraction. These $\{210\}$ spots correspond to the $\{100\}$ spots of the QP phase and clearly appear in the diffraction of the schematic Q phase. It can also noticed that for all the diffractions, the $\{140\}$ spots are the strongest: they correspond to the $\{100\}$ spots of the qh lattice. In consequence, it seems now legitimate to call these rods Q' or λ' [154], even if we will continue in this study to call them Q (we will specify "stable Q phase" to refer to the structure found by Arnberg [152]). A quantitative analysis of the

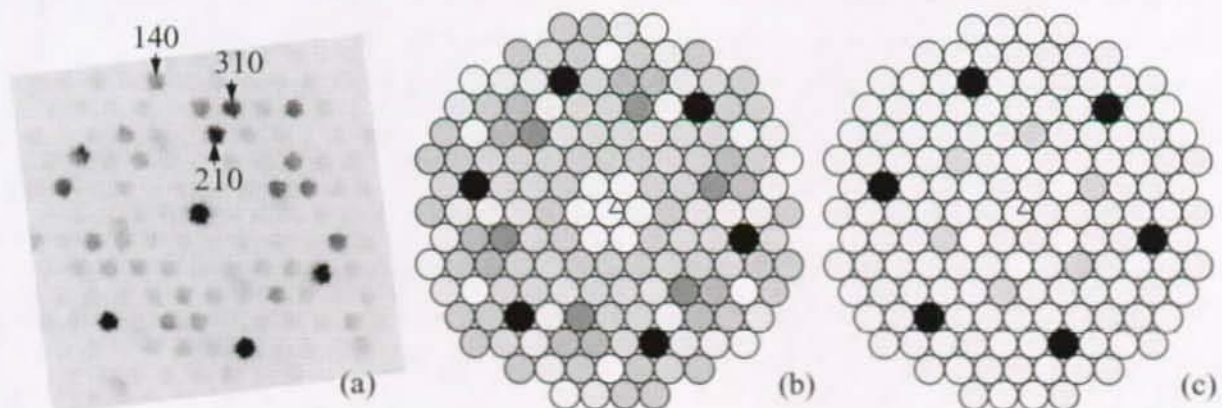


Fig. 6.9 Difference between the structures of the Q' phase and the stable Q phase: (a) experimental microdiffraction acquired on a Q' rod-shaped precipitate (named also Q in this work). (b) Simulated microdiffraction patterns of the stable Q phase presented in Fig. 6.7a and (c) of the schematic Q phase presented in Fig. 6.7b.

microdiffraction patterns, similar to the one that will be presented for QC in section 6.3, could be done to determine the crystallographic structure of this Q' phase.

6.2.3 Application of the Structural Model to the AlMgSi Alloys

Another interesting point is the presence of Cu in the Q-phase crystal. According to Arnberg [152], the Q structure is close to the Th_7S_{12} structure, the positions of the Si atoms being nearly the same as those of the Th atoms, and the positions of (Al,Mg) atoms being nearly the same as those of the S atoms. The only difference is that the $(2/3, 1/3, 1/2)$ and $(1/3, 2/3, 0)$ positions in the clusters are occupied by Cu atoms in the Q structure and empty in the Th_7S_{12} structure. Thus, by this observation, the existence of a Q structure without Cu (but possibly empty or occupied by Si atoms) seems to be possible. Actually, the Q structure is reported without Cu from EDS measurements in AlMgSi alloys and named M [151], type-C [156] or B' [155] (hereafter, we will call it B' since it is the oldest one). The Q and B' phases have the same hexagonal parameters. Consequently, it was checked if the structural model could be applied to the AlMgSi alloys.

The $[(\text{Al,Mg})]/[\text{Si}]$ ratio of the sub-unit QP clusters is 1 in our model, which is consistent with the low $[\text{Mg}]/[\text{Si}]$ ratio (close to 1) found by atom probe field ion microscopy (APFIM) in the clusters present in the early stages of precipitation in AlMgSi alloys [157]. Moreover, Mg and Al are regarded as one element by Arnberg [152], but the author, after the refinement of the Q-phase, made the assumption that $[\text{Al}]/[\text{Mg}] = 4/8$ or $5/7$, with the $[(\text{Al,Mg})]/[\text{Si}]$ ratio unchanged ($12/7$). Thus, if our model would apply to the AlMgSi alloys¹, the presence of Al in β'' or β' precipitates could be realistic. Actually, Al was recently detected in β'' precipitates after a matrix dissolution [158] and in general the $[\text{Mg}]/[\text{Si}]$ ratios are reported to be less than 1 [157]. Thus, it was examined if the structures in the AlMgSi alloys are also based on a common lattice. The sub-unit clusters would be similar to the QP sub-unit clusters, but without Cu. They are hereafter named βP sub-unit clusters. The primitive phase was named βp .

Subsequently, the structures of the precipitates in AlMgSi alloys was investigated. Considering that Si can occupy the same position in the sub-unit cluster than Cu, the AlMgSi alloys with excess of Si are probably closer to the AlCuMgSi alloys than the AlMgSi alloys without Si excess ($a_{\beta\text{P}} = a_{\text{QP}} = 0.393$ nm). These kinds of alloys have been extensively studied by Matsuda [159]. Three different precipitates have been reported:

- type A: hexagonal lattice with $a = 0.405$ nm, $c = 0.67$ nm.
- type B: orthorhombic lattice with $a = 0.684$ nm, $b = 0.793$ nm, $c = 0.405$ nm
- type C (B' or M): hexagonal lattice with $a = 1.04$ nm, $c = 0.405$ nm.

Of course the type-C which corresponds to the Q-phase is in agreement with the model of the βP sublattice. Type-B is also in agreement with this model: the phase based in the βP lattice with $a = [1,2,0]_{\beta\text{P}}$, $b = [200]_{\beta\text{P}}$ and $c = [001]_{\beta\text{P}}$ (Fig. 6.10) would be orthorhombic with $a = 0.670$ nm, $b = 0.786$ nm, $c = 0.405$ nm. For the type-A phase, it can only be noticed that its

1. The reader could report to annex B2 for the chemical and crystallographical information about the metastable phases present in the AlMgSi alloys.

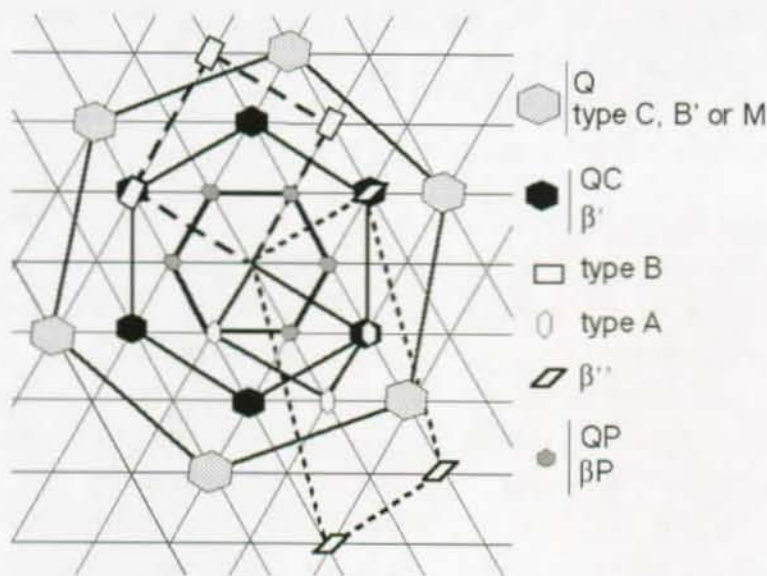


Fig. 6.10 Possible extension of the structural model to the AlMgSiCu alloys in general:
 - AlCuMgSi alloys: QP, QC and Q based on the QP latent lattice ($a_{QP} = 0.393$ nm).
 - AlMgSi alloys with Si in excess: type A, B and C based on the βP lattice ($a_{\beta P} = 0.393$ nm)
 - AlMgSi alloys without Si in excess: β' and β'' based on the βP lattice ($a_{\beta P} = 0.407$ nm)

parameter c is also close to the QC hexagonal parameter and its parameter a close to $a_{\beta P}$. The capability for Si to replace Cu in the QP sub-unit clusters for the type-A, -B, -C phases seems to be confirmed by the high [Si]/[Mg] ratio (respectively 3.6, 2.5 and 1.2) reported by Matsuda [159].

For the AlMgSi alloys without excess of Si the two main phases are β'' and β' . The QC and β' phases are probably very close ($a = 0.675$ nm and 0.705 nm respectively). We have considered that the only difference between the two phases is the presence (or absence) of the Cu in the unit cell. The smaller unit cell of QC could come from an attractive effect of Cu on the Si atoms. The hexagonal parameter of the latent lattice was deduced from the β' one:

$$a_{\beta P} = a_{\beta'} / \sqrt{3} = 0.407 \text{ nm.} \quad (6.9)$$

For β'' phase, a lattice based on this latent lattice with $a = [3\bar{1}0]_{\beta P}$, $b = [001]_{\beta P}$ and $c = [120]_{\beta P}$ (see Fig. 6.10) would be monoclinic with $a = 1.467$ nm, $b = 0.405$ nm, $c = 0.705$ nm and $\beta = 104^\circ$, which are close to the lattice parameters reported for β'' by Andersen [160]. Nevertheless, the difference between the calculated and the experimental parameters (5 %) did not allow us to conclude definitely for this kind of alloy.

In conclusion, the phase transition approach we have proposed to explain the QP, QC, Q structures in AlCuMgSi alloys seems to apply to the AlMgSi alloys [153]. The existence of the Q-phase without Cu (B'), the similarity of the QC and β' lattice, the possibility to include the type-B phase, and nearly the β'' phase, as summarized in Fig. 6.10 and Table 6.2, was judged very encouraging. A first and direct application given in the following section confirmed this opinion.

6.3. Crystallographic Structures of the QC and β Phases

alloy	phase type	parameters (literature and this work)	parameters (calculated)
Al-Cu-Mg-Si $a_{QP} = 0.393$ nm	QP	hexagonal $a = 0.393$ nm, $c = 0.405$ nm	(parameter a_{QP} deduced from QP)
	QC	hexagonal $a = 0.67$ nm, $c = 0.405$ nm	hexagonal $a = 0.68$ nm, $c = 0.405$ nm
	Q	hexagonal $a = 1.04$ nm, $c = 0.401$ nm	hexagonal $a = 1.04$ nm, $c = 0.405$ nm
Al-Mg-Si Si in excess $a_{\beta P} = 0.393$ nm	type-A	hexagonal $a = 0.405$ nm, $c = 0.67$ nm	hexagonal $a = 0.39$ nm, $c = 0.67$ nm
	type-B	orthorhombic $a = 0.68$ nm, $b = 0.79$ nm, $c = 0.405$ nm	orthorhombic $a = 0.67$ nm, $b = 0.79$ nm, $c = 0.405$ nm
	type-C, M or B'	hexagonal $a = 1.04$ nm, $c = 0.401$ nm	hexagonal $a = 1.04$ nm, $c = 0.405$ nm
Al-Mg-Si $a_{\beta P} = 0.407$ nm	β''	monoclinic $a = 1.52$ nm, $b = 0.405$ nm $c = 0.67$ nm, $\beta = 105^\circ$	monoclinic $a = 1.46$ nm, $b = 0.405$ nm $c = 0.67$ nm, $\beta = 104^\circ$
	β'	hexagonal $a = 0.705$ nm, $c = 0.405$ nm	(parameter $a_{\beta P}$ deduced from β')

Table 6.2 Comparison between the parameters of the phase cells obtained from literature (annex B2) and from simple calculi with the QP (or βP) latent lattice. For the AlCuMgSi and AlMgSi alloys with Si in excess, the hexagonal parameter of the latent lattice is $a = 0.393$ nm, and for the AlMgSi alloys $a = 0.407$ nm.

6.3 Crystallographic Structures of the QC and β' Phases

The structural model we proposed seems to explain the different kinds of phases found in the AlMgSi(Cu) alloys by unifying them as a same family of phases based on the same latent lattice. It has been shown in the previous section that the transition from the latent phase qp and βp toward the Q and B' phases respectively implies atomic substitutions and displacements. The mechanisms of the transition toward the other ordered phases like QC and β' phases have not been identified yet. Therefore, we confronted the model to experimental TEM data about the QC and β' structures in the aim to (i) confirm the similarities between the QC and β' phases, (ii) detail the qp (or QP) \rightarrow QC and βp (or βP) \rightarrow β' transitions at atomic level, and eventually (iii) give the crystallographic structure of the QC and β' phases. Let us recall that up to the present work, the QC phase was not known yet, and only that the lattice

parameters of the β' phase were known [161] (no realistic structure could be proposed for this phase due to the difficulty to study such very small precipitates, as reported in annex B2).

6.3.1 Similarities between the QC and β' Phases

In 1993, Epicier has reported a hexagonal phase with $a = 0.683$ nm in an AlMgSi alloy containing Cu and thought that this phase was β' (the absence of any EDS measurements impeded the possible detection of Cu) [162]. Nevertheless, in the case of the present work, the differences in the lattice parameters and chemical compositions are sufficiently significant to use the different QC and β' names. Actually, we assumed that in addition to the small (but not negligible) difference in their a lattice parameters, the only difference between the QC and β' phases is the presence of Cu in the sub-unit clusters.

To check this assumption, a 6061 alloy (0.65% Si, 1% Mg, 0.25% Cu, 0.5% Cr) has been studied. The alloy was solutionized at 550°C, water quenched and then aged at 185°C for 600 h to coarsen the precipitates in the aim to facilitate the TEM observations. Even if this alloy contains a small amount of Cu, it was checked by EDS that the analyzed β' precipitates do not contain any Cu, or only in negligible amounts, as reported for this kind of alloy by an APFIM study [163]. Actually, it was observed that the alloying Cu was incorporated in Q precipitates at the grain boundaries (this is the origin of the corrosion problem of such alloys). The TEM observations clearly confirmed and detailed the hypothesis about the similarities between the QC and β' phases:

(1) Both have close hexagonal parameters ($a_{QC} = 0.675$ nm and $a_{\beta'} = 0.705$ nm) and precipitate in the Al matrix with the same two possible ORs that are

$$\text{OR1} \quad (100)_{\beta',QC} // (100)_{\alpha} \text{ and } [001]_{\beta',QC} // [001]_{\alpha} \quad (6.10)$$

$$\text{OR2} \quad (100)_{\beta',QC} // (110)_{\alpha} \text{ and } [001]_{\beta',QC} // [001]_{\alpha} \quad (6.11)$$

For the QC phase, the two ORs could have been deduced from the QP's ORs given in (6.3) and (6.4) respectively. For the β P phase, the two ORs were reported in literature (annex B2).

(2) Both can coexist with respectively Q and B' which are both hexagonal with $a = 1.04$ nm, with and without Cu respectively (see annex B2) (Fig. 6.11a,b).

(3) Their SAED patterns exhibit the same very particular features, with very weak $\{100\}$ and $\{200\}$ spots and intense $\{300\}$ spots (Fig. 6.11e,f).

(4) Their [Mg]/[Si] ratios are both close to 1.3 (results from EDS spectra presented in Fig. 6.11c,d), which is close to the [Mg]/[Si] ratio of the stable Q phase. Cu is present in large amount in the QC phase ($[Cu]/[Mg] \approx 0.28$, which is close to the $[Cu]/[Mg]$ ratio of the stable Q phase), whereas it is in negligible amount in the β' phase ($[Cu]/[Mg] < 0.05$).

As detailed in the following sections, microdiffraction patterns and HREM images on isolated QC and β' precipitates along their [001] zone axis were acquired. The comparison with microdiffraction patterns simulated on the base of the structural model permitted to propose a crystallographic structure for QC and β' . Then, HREM simulations of the deduced crystallographic structures were compared with experimental ones.

6.3. Crystallographic Structures of the QC and β Phases

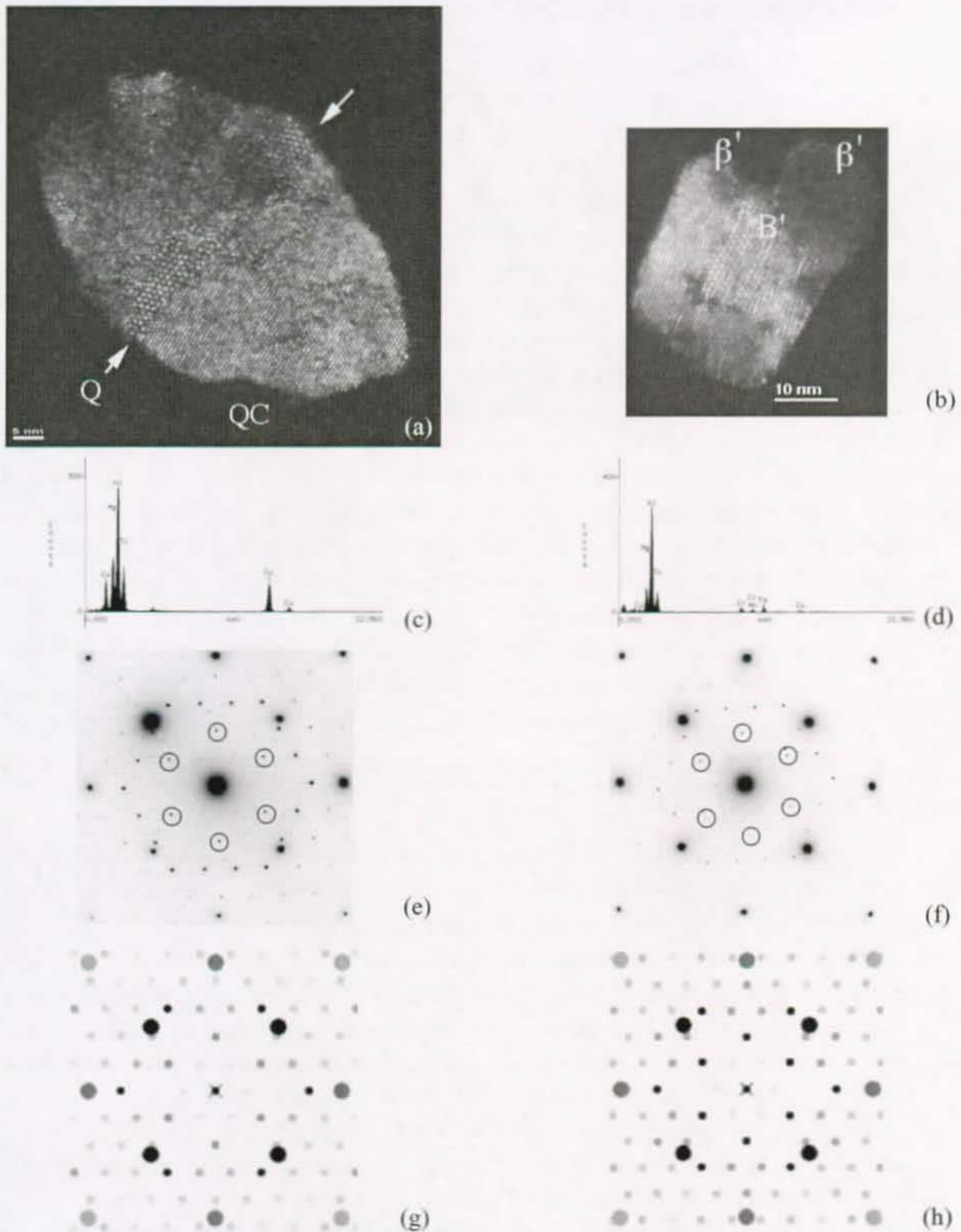


Fig. 6.11 Similarities between the QC (AlCuMgSi alloys) and β' phases (AlMgSi alloys) respectively in (a,c,e,g) and (b,d,f,h): (a,b) DF superstructure images, (c,d) EDS spectra, (e,f) SAED patterns (the spots corresponding to the QP and β P latent lattices are indicated by the circles), (g,h) simulated SAED (with a crystallography detailed in section 6.3.4).

6.3.2 Microdiffraction and Computing Details

The microdiffraction patterns were acquired on the CM20 microscope with the smallest condenser aperture (semi-convergence angle of 0.03°) and with the smallest spot size (10 nm) on a Gatan CCD Slow Scan camera for a good linearity of the intensities. The beam was focused in the aim to reduce the size of the analyzed area and to enlarge the spots to improve the signal/noise ratios while impeding a possible CCD camera saturation. Therefore, the term "microdiffraction" was preferred to the term "convergent beam electron diffraction" (CBED) which corresponds to larger beam convergence angles in order to explore the reciprocal space [57]. Only the zero order Laue zone (ZOLZ) could be analyzed because the higher ones do not appear in the diffraction patterns, even by tilting the sample (probably due to the partial disordering state of the precipitates which reduces the intensities of associated to the high G reciprocal vectors). The HREM images were acquired on isolated QC and precipitates along their [001] axis with the Philips CM300UT-FEG microscope. The integration of the intensities on the microdiffraction disk areas and the filtering of the HREM images were performed using the Gatan Digital Micrograph software. A Mathematica program linked to EMS [78] was written to refine the crystallographic structures of the QC and β' phases. The structures were built with EMS varying the atomic positions and the occupancy of some atoms, the intensities of the corresponding microdiffraction patterns were then calculated with EMS (I^{calc}) and compared to the experimental ones (I^{obs}). Similarly to conventional X-ray structure analysis, a comparison value was given by the reliability factor .

$$R = \frac{\sum_i (I_i^{obs} - I_i^{calc})^2}{\sum_i (I_i^{calc})^2} \quad (6.12)$$

The refinement is then computed by minimizing the R factor. This TEM approach is close to the one applied for the SrTiO₃ phase study [164]. In our work, the R factor must be considered only as a least-squares figure-of-merit factor without statistical meaning. Indeed, the least-squares fitting is a maximum likelihood estimation (chi-square minimization) of the fitted parameters if the measurement errors are independent and normally distributed with a constant standard deviation [165]. In our work, one microdiffraction pattern by structure was acquired on the CCD camera, integrated and analyzed (more were acquired on negatives as the ones presented in Fig. 6.11*e,f* and checked to be qualitatively in agreement with these ones), which was not sufficient to calculate the standard deviation errors and check if they were normally distributed. Therefore, the experimental data were fitted to propose a refined model of the structures, but not to give a statistical validity of this model.

Microdiffraction patterns of QC and β' phases along their [001] zone axis were obtained at the very thin parts of the samples. They are reported in Fig. 6.12*a* and *b*, respectively. Both exhibit very particular features: the {200} spots are nearly extinguished, the intensities of the {100} spots are very low, the most intense spots are the {300} ones. As expected, the two microdiffraction patterns are close, but a slight difference can be noticed: the {110} spots are

more intense (relatively to the $\{210\}$ spots) for β' than for QC. For a quantitative study, the intensities were integrated on the spot areas, without considering those partly superposed to the Al spots. Each $\{300\}$ spot contains more than one million counts. The β' microdiffraction pattern is slightly tilted as it can be measured by the relative intensity difference between two opposite spots (40%), but this tilt is sufficiently low to be corrected by applying a central symmetry¹, making the difference between the intensities of $\{300\}$ spots decrease down to 12%. The QC microdiffraction pattern is well orientated (the difference is less than 15%). Fig. 6.12c,d represent the corresponding simulated microdiffraction patterns after refinement of the structures detailed in the following sections.

6.3.3 Basic Ideas about the Structures

To simplify the problem, we have begun to search the QC and β' structures on the base of the QP phase proposed in (6.7). We have simplified the sub-unit clusters used in our structural model by considering them as two triangles rotated by 60° , one of Mg atoms and the other of Si atoms, with Cu atom present in the barycenter with an occupancy less than 1 (and possibly Si or (Al,Mg) atoms). These sub-unit clusters are represented in the right part of Fig. 6.13. When the sizes of all the triangles are equal, these clusters are supposed to build the QP phase. Two different ways exist to build the QC phase (with a periodicity of 0.675 nm) on the base of the QP phase ($a = 0.393$ nm):

- (1) change the size of the triangles, which corresponds to a displacive transition,
- (2) suppose that Cu is present only in the clusters that build a hexagonal pattern with a periodicity of 0.67 nm, which corresponds to a substitutional order-disorder transition.

The hypothesis (2) can be excluded by considering the QC diffraction pattern. Indeed, the structure corresponding to the case (2) would not have its $\{300\}$ planes equivalent, and consequently the $\{100\}$ and $\{200\}$ spots in the experimental microdiffraction pattern would be significantly brighter (confirmed by the simulations), which is not the case. Therefore, only the case (1) has to be analyzed. The QC structure was built from the QP substructure by changing the size of the cluster triangles (compactness of the atoms). Moreover, the occupancy of the Cu atoms in the triangular sites was changed, and Si was inserted. A small rotation of the clusters around their center along the $[001]$ axis has also been tried². The structure of β' was supposed similar, the only difference being that the triangular sites can only be filled with Si atoms. To summarize, four parameters were fitted: the two sizes of the triangles r_{Mg} and r_{Si} (radii of the circumscribed circles divided by the hexagonal parameter a_{QC} or $a_{\beta'}$), the Cu (or/and Si) occupancy p_{Cu} and p_{Si} , and the angle of rotation of the clusters α . The structural model is illustrated in Fig. 6.13. The space group of this structure is $P\bar{6}2m$ ($n^\circ 189$) if the clusters are not rotated, and $P\bar{6}$ ($n^\circ 174$) otherwise.

1. Assuming a linear approximation of the shape factor (3.21).

2. In the first approach given in [153], we thought that the transition would imply a rotation of the sub-unit clusters.

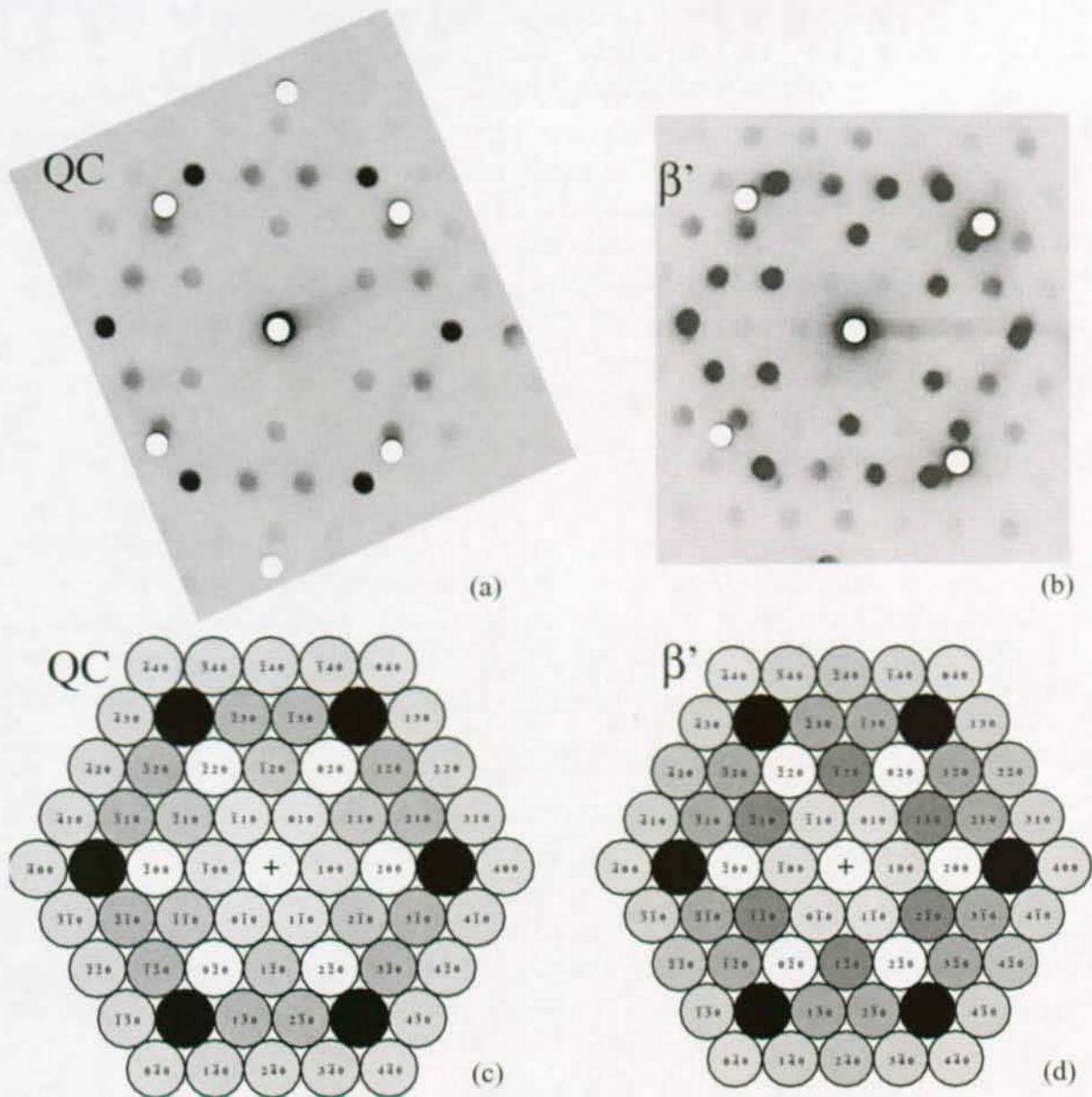


Fig. 6.12 Microdiffraction patterns in $[001]$ zone axis of (a) QC and (b) β' precipitate present in the matrix of the as-cast WFA/ Al_2O_3 /sf composite and in the 6061 alloy (T6 + overaging) respectively. The Al spots are indicated by the white disks. For comparison, corresponding microdiffraction patterns of (c) QC and (d) β' phases, simulated by EMS after the refinement of the structural model proposed in section 6.2.

6.3.4 Structural Refinements

The refinements were computed by simulating the microdiffraction patterns in kinematical condition. Indeed, the $\{200\}$ spots are nearly extinguished in the experimental microdiffraction patterns of Fig. 6.13, whereas they would be brighter in dynamical

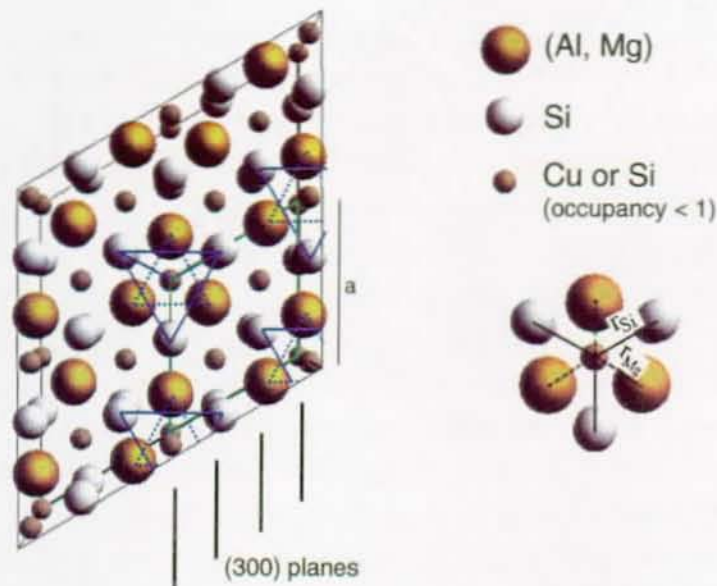


Fig. 6.13 Structural model of the QC or β' phase down the $[001]$ direction, 2×2 unit-cells are represented. The sub-unit triangular clusters are indicated by the triangles. Their barycenter can be filled with only Si atoms (β') or with Cu and Si atoms (QC), with a total occupancy less than 1.

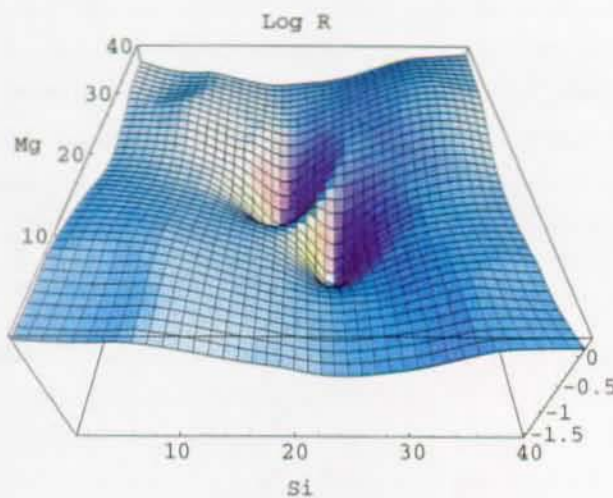


Fig. 6.14 Refinement of the β' structure with $\alpha = 0^\circ$ and $p_{Si} = 1/3$: the reliability factor R (in Log scale) is mapped in function of the size of the two triangles r_{Mg} and r_{Si} both varying from 0.1 to 0.5. The two minima correspond to an exchange of the Mg by Si atoms.

conditions due to the dynamic way that exists between them and the bright $\{300\}$ spots. The Debye-Waller factors have been set to 0.005 for all the atoms¹, and the deviation error to 0.5 nm^{-1} for all the microdiffraction patterns. For the β' structure with $p_{Si} = 0.33$ and $\alpha = 0$, the reliability factor R surface in function of r_{Mg} and r_{Si} , both varying from $1/3 - 0.2$ to $1/3 + 0.2$ with a step of 0.01, is represented in Fig. 6.14. It exhibits two quasi-symmetric minima. They correspond to an exchange of the Mg by the Si atoms in the sub-unit clusters and give very similar results due to the fact that the atomic scattering factors of these elements are very close.

1. Higher values should probably be more appropriate due to the slight disorder present in the observed precipitates, as shown in the next section.

6. Order-Disorder Transition in the AlCuMgSi and AlMgSi Alloys

For the β' structure determination, (1) the effect of changing the Si occupancy with α fixed to 0, and a p_{Si} step of 0.05 is shown in Fig. 6.15a with three p_{Si} represented ($p_{\text{Si}} = 0, 0.3$ and 1). The R surfaces in function of r_{Mg} and r_{Si} varying from $(1/3-0.1)$ to $(1/3+0.1)$ with a step of 0.01 are represented with their related simulated microdiffraction patterns corresponding to the minimum. The minimal R has been found to be 21% for $p_{\text{Si}} = 0.35$, $r_{\text{Mg}} = 0.29$ and $r_{\text{Si}} = 0.36$. (2) The effect of tilting the clusters with p_{Si} fixed to 0.35, and a α step of 1° is shown in Fig. 6.15b with three α represented ($\alpha = 2^\circ, 5^\circ$ and 8°). The minimal R has been found for $\alpha = 0$ with the same parameters r_{Mg} and r_{Si} that we found in (1). This can be understood by the fact that the simulated microdiffraction patterns loose their mirror symmetry when the sub-unit clusters are tilted, whereas the experimental microdiffraction patterns are nearly symmetric (after imposing the central symmetry). Actually, it can be noticed that the case $\alpha = 5^\circ$ gives also good results ($R = 22\%$) with different r_{Mg} and r_{Si} parameters (0.35 and 0.32 respectively). In fact, as illustrated in Fig. 6.16, the calculations showed that the symmetry $P\bar{6}2m$ ($r_o, \alpha = 0^\circ$) is equivalent to the symmetry $P\bar{6}$ with the special values $r_p = \sqrt{r_o^2 - r_o + 1/3}$ and $\alpha = 30^\circ - \text{Arcos}(1/2\sqrt{3}r_p)$, so that the case ($r_{\text{Mg}} = 0.29$, $r_{\text{Si}} = 0.36$, $\alpha = 0^\circ$) is equivalent to the case ($r_{\text{Mg}} = 0.35$, $r_{\text{Si}} = 0.32$, $\alpha = 4.5^\circ$). Eventually, the microdiffraction pattern corresponding to the best fit is reported in Fig. 6.12d for comparison with Fig. 6.12b.

For the QC structure determination, the same method has been applied with different ways to fill the triangular sites¹: (1) fill with only Cu atoms, (2) fill with Cu and Si atoms so that the total occupancy per site equals 1 and (3) fill with Cu atoms to complete the β' structure found previously. All these cases give good results ($R < 23\%$), and the best one was found for the case (3): $R = 19\%$ with $p_{\text{Cu}} = p_{\text{Si}} = 0.35$, $r_{\text{Mg}} = 0.28$, $r_{\text{Si}} = 0.36$ and $\alpha = 0^\circ$. The corresponding microdiffraction pattern is reported in Fig. 6.12c for comparison with Fig. 6.12d.

Since the occupancy of the Si and Cu atoms in β' and QC structures are close to 1/3, and since Jacobs suggested that the c parameter of β' could be 3×0.405 nm [161], an ordering of Cu and Si atoms along the [001] direction was considered. Nevertheless, in the studied alloys, no diffraction patterns along the [100] or [010] axis exhibits a tripling of the c parameter and all could be explained with the proposed structures as shown in Fig. 6.17. Therefore, no evidence of an ordering along the [001] direction could be found: the triangular sites are filled randomly on the (001) planes and along the [001] direction.

1. When the present study was done and published in [167], I did not think about filling the interstitial sites with (Al,Mg) and Cu atoms, which should have been done to respect the Q chemical composition. This would also have been equivalent to determine the QC phase not from the QP phase given (6.7) as proposed in [153]. Results close to: (Al,Mg) 2/3 and Cu 1/3 for QC and (Al,Mg) 2/3 and Si 1/3 for β' could be expected.

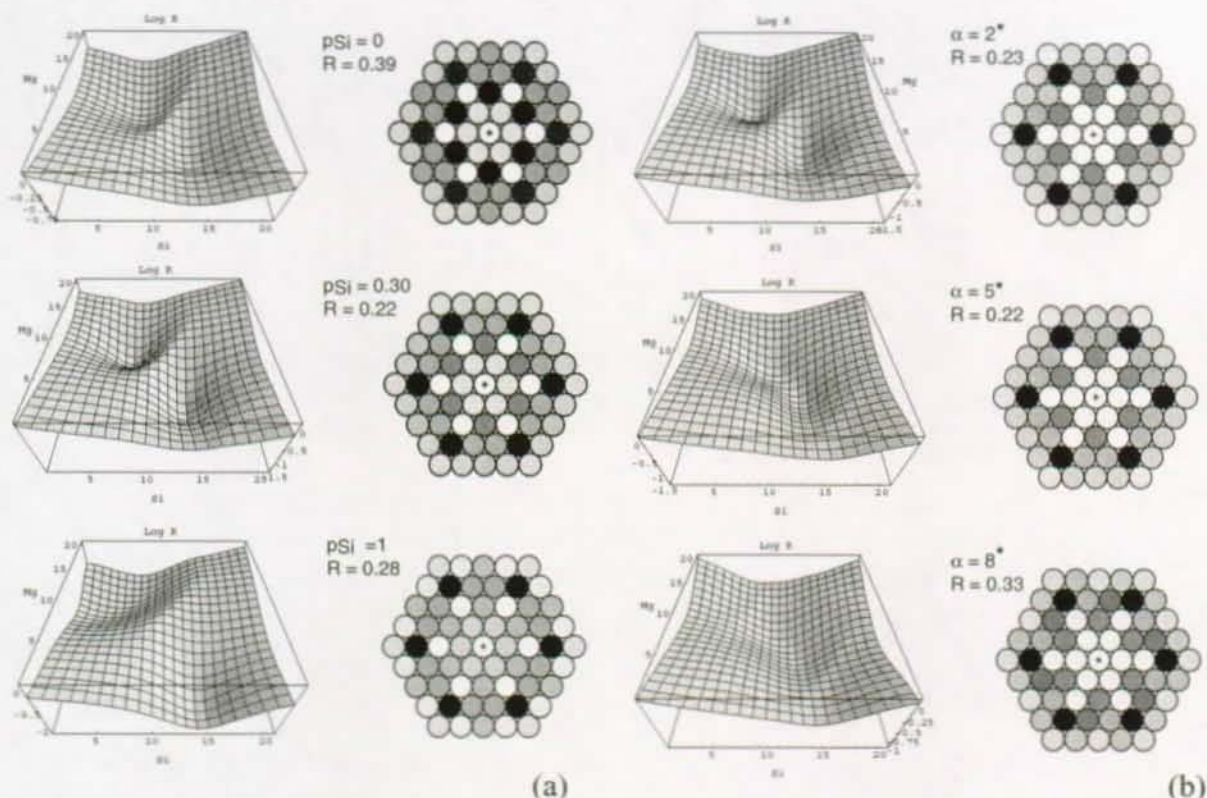


Fig. 6.15 Refinement of the β' structure, R is mapped in function of the size of the two triangles r_{Mg} and r_{Si} both varying from 0.2 to 0.4:

(a) by varying the Si occupancy in the triangular site of the clusters with $\alpha = 0^\circ$: $p_{Si} = 0$, $p_{Si} = 0.3$ and $p_{Si} = 1$ with their simulated microdiffraction patterns corresponding to the values r_{Mg} and r_{Si} which give the R minimum. The hollows of these reliability factor R surfaces have their minimum ($R = 21\%$) for $p_{Si} = 0.35$, with $r_{Mg} = 0.29$ and $r_{Si} = 0.36$.

(b) by rotating the clusters with $p_{Si} = 0.35$ (the symmetry is then $P\bar{6}$): $\alpha = 2^\circ$, $\alpha = 5^\circ$ and $\alpha = 8^\circ$, and their simulated microdiffraction patterns corresponding to the values r_{Mg} and r_{Si} which give the R minimum. The hollows of these reliability factor R surfaces have their minimum ($R \approx 21\%$) for $\alpha = 0^\circ$ and $\alpha = 5^\circ$, which are equivalent and correspond to a recovered symmetry $P\bar{6}2m$.

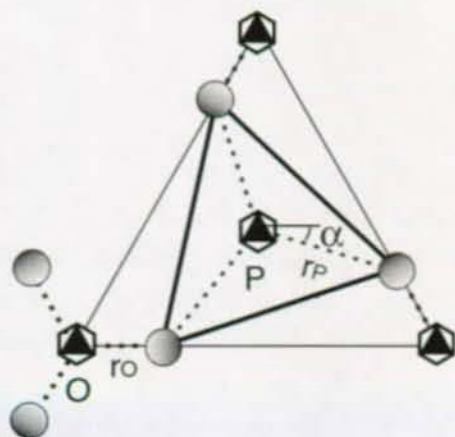


Fig. 6.16 Scheme showing the equivalence between a $P62m$ structure (r_o , $\alpha = 0^\circ$) and a $P\bar{6}$ structure with the special values

$$r_p = \sqrt{r_o^2 - r_o + 1/3} \text{ and } \alpha = 30^\circ - \text{Arcos}[1/(2\sqrt{3}r_p)].$$

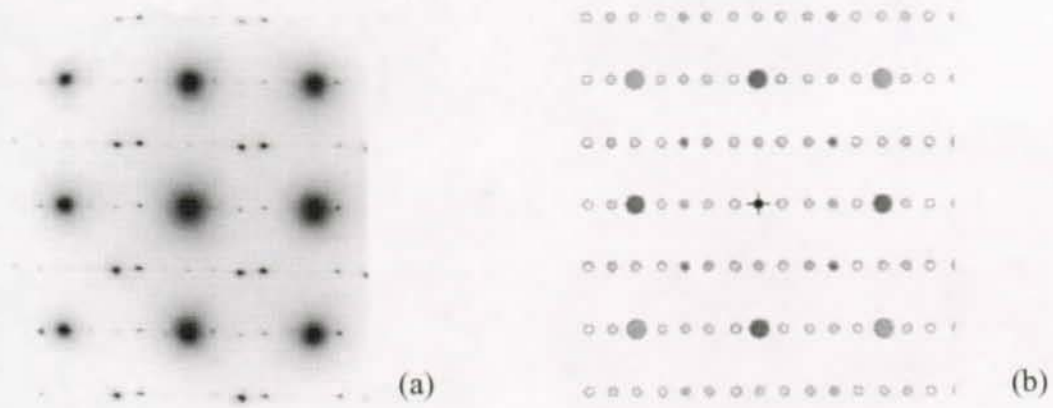


Fig. 6.17 In a as-cast WFA/SiC/p composite, SAED pattern of a QC precipitate in ORI (6.10) in the $[010]_{QC} // [010]_{\alpha}$ axis. (a) Experimental and (b) simulated with double diffraction. The slight misalignment between the simple and double diffracted spots is due a small misalignment in the OR ($\sim 1.2^\circ$).

To summarize, the refined structures (with atomic positions and occupancies) are:

$$\beta' : \text{hexagonal } P\bar{6}2m \text{ with } a = 0.71 \text{ nm, } c = 0.405 \text{ nm,} \quad (6.13)$$

Mg: (0.29, 0, 1/2), 1;

Si: (0.36, 0.36, 0), 1;

Si: (0, 0, 0), 1/3; (*)

Si: (1/3, 2/3), 0, 1/3. (*)

$$QC : \text{hexagonal } P\bar{6}2m \text{ with } a = 0.67 \text{ nm, } c = 0.405 \text{ nm,} \quad (6.14)$$

Mg: 0.28, 0, 1/2, 1;

Si: 0.36, 0.36, 0, 1;

Si: 0, 0, 0, 1/3; (*)

Cu: 0, 0, 0, 1/3;

Si: 1/3, 2/3, 0, 1/3. (*)

Cu: 1/3, 2/3, 0, 1/3.

(*) see previous footnote p. 118.

6.3.5 Verification of the Structures by HREM

HREM images of the β' precipitates found in the 6061 alloy averaged at $185^\circ\text{C} / 600 \text{ h}$ were acquired. One of them is reported in Fig. 6.18. A simulated image in agreement with the experimental pattern is inserted in the image. Since the atomic diffusion factors of Mg, Si and Cu with an occupancy of 1/3 are very close, the simulations showed that the complex hexagonal patterns formed in HREM can appear with a periodicity of 0.407 nm at certain defocus and thickness values, and when the precipitates are perfectly oriented along their

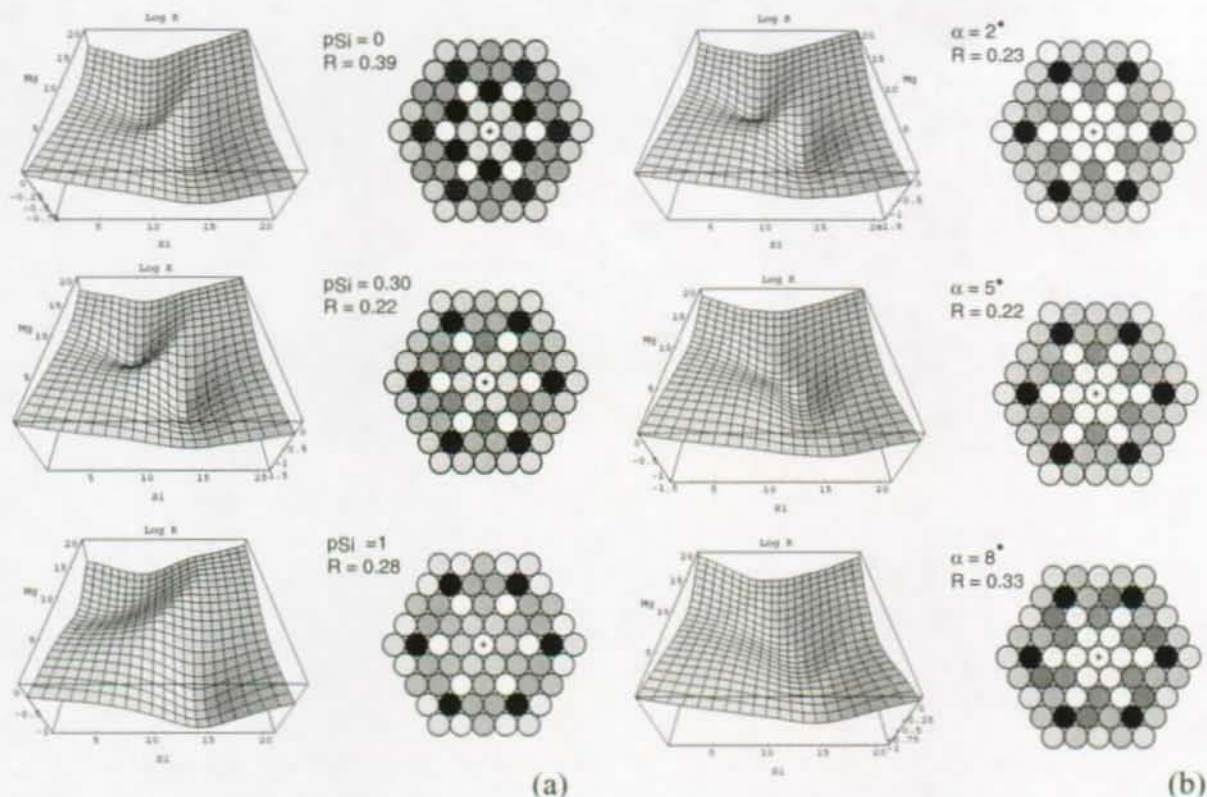


Fig. 6.15 Refinement of the β' structure, R is mapped in function of the size of the two triangles r_{Mg} and r_{Si} both varying from 0.2 to 0.4:

(a) by varying the Si occupancy in the triangular site of the clusters with $\alpha = 0^\circ$: $p_{Si} = 0$, $p_{Si} = 0.3$ and $p_{Si} = 1$ with their simulated microdiffraction patterns corresponding to the values r_{Mg} and r_{Si} which give the R minimum. The hollows of these reliability factor R surfaces have their minimum ($R = 21\%$) for $p_{Si} = 0.35$, with $r_{Mg} = 0.29$ and $r_{Si} = 0.36$.

(b) by rotating the clusters with $p_{Si} = 0.35$ (the symmetry is then $P\bar{6}$): $\alpha = 2^\circ$, $\alpha = 5^\circ$ and $\alpha = 8^\circ$, and their simulated microdiffraction patterns corresponding to the values r_{Mg} and r_{Si} which give the R minimum. The hollows of these reliability factor R surfaces have their minimum ($R = 21\%$) for $\alpha = 0^\circ$ and $\alpha = 5^\circ$, which are equivalent and correspond to a recovered symmetry $P\bar{6}2m$.

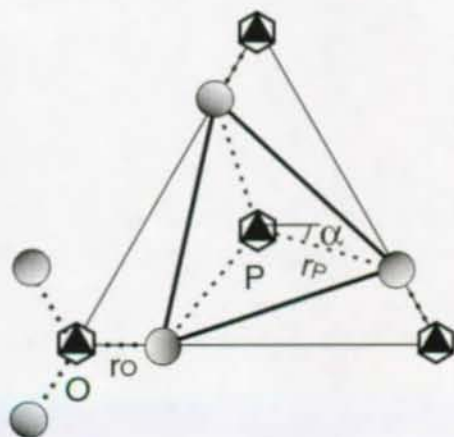


Fig. 6.16 Scheme showing the equivalence between a $P62m$ structure (r_o , $\alpha = 0^\circ$) and a $P\bar{6}$ structure with the special values

$$r_p = \sqrt{r_o^2 - r_o + 1/3} \text{ and } \alpha = 30^\circ - \text{Arcos}[1/(2\sqrt{3}r_p)].$$

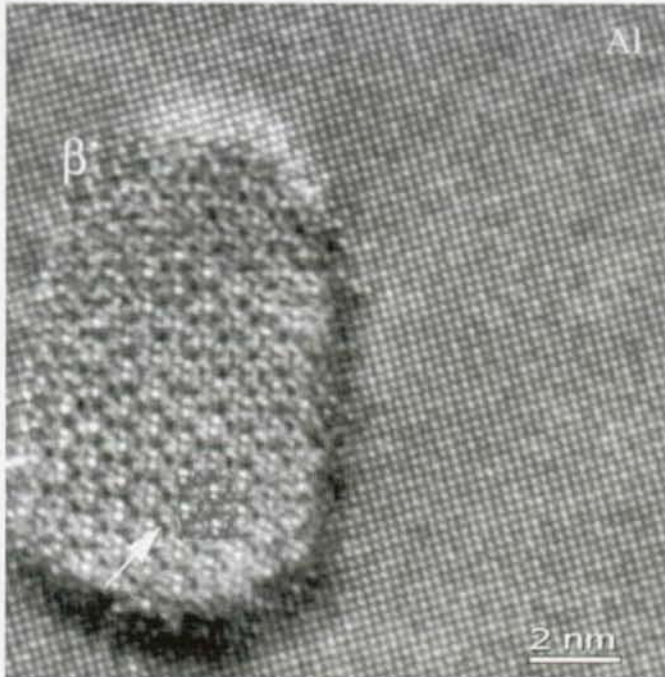


Fig. 6.18 In the 6061 alloy (T6+ aging 185°C/600h): HREM unfiltered image on the CM300 microscope of a β' rod-shaped precipitate along its [001] direction. A simulation is inserted and indicated by the white arrow; its parameters are: thickness 90 nm, defocus -140 nm, crystal tilt corresponding to the center of the Laue circle on the (200) spot ($\approx 0.5^\circ$).

[001] axis. This is not the case for Fig. 6.18 due to the slight crystal tilt.

HREM images of the QC precipitates present in the as-cast matrix and in the T6 matrix of the composites have also been acquired; some of them are reported in Fig. 6.19a and Fig. 6.20a, respectively. In each image, contrarily to the β' precipitates, no clear unique pattern could be identified. Moreover, it can be noticed in the PS of the images that the spots corresponding to the QP lattice are sharp, and that the other ones appear more diffuse as indicated by the arrows in Fig. 6.19b and Fig. 6.20b. This can be interpreted by a partial disordering in the QC structures, as introduced in section 5.5.1. This slight disordering made the comparison with HREM simulations more difficult. Nevertheless, after filtering, some parts of the images are in agreement with images computed with the EMS program [78] as shown in Fig. 6.19c and Fig. 6.20c. It was shown in section 5.5.3 that the Fourier filtering corresponds to average each pattern of the image separated by the periodicity a of the structure with the neighboring other patterns on a distance m . Here, the filtering revealed details in the pattern of size a_{QC} , because mean positions exist in the pattern (with random disorder around these positions). This explains the efficiency of filtering the HREM images to analyze such slightly disordered structures.

6.3.6 Discussion

The QC and β' structures were characterized by comparison between experimental and simulated microdiffraction patterns (Fig. 6.12). As represented in Fig. 6.7, the QC and β' structures ($a = 0.67$ nm and $a = 0.71$ nm, respectively) are based on sub-unit triangular clusters (respectively $a_{QP} = 0.393$ nm and $a_{\beta P} = 0.407$ nm). This arrangement is very close to the one characterizing the nepheline structures, as for example the $BaAl_2O_4$ structure [168], the sub-

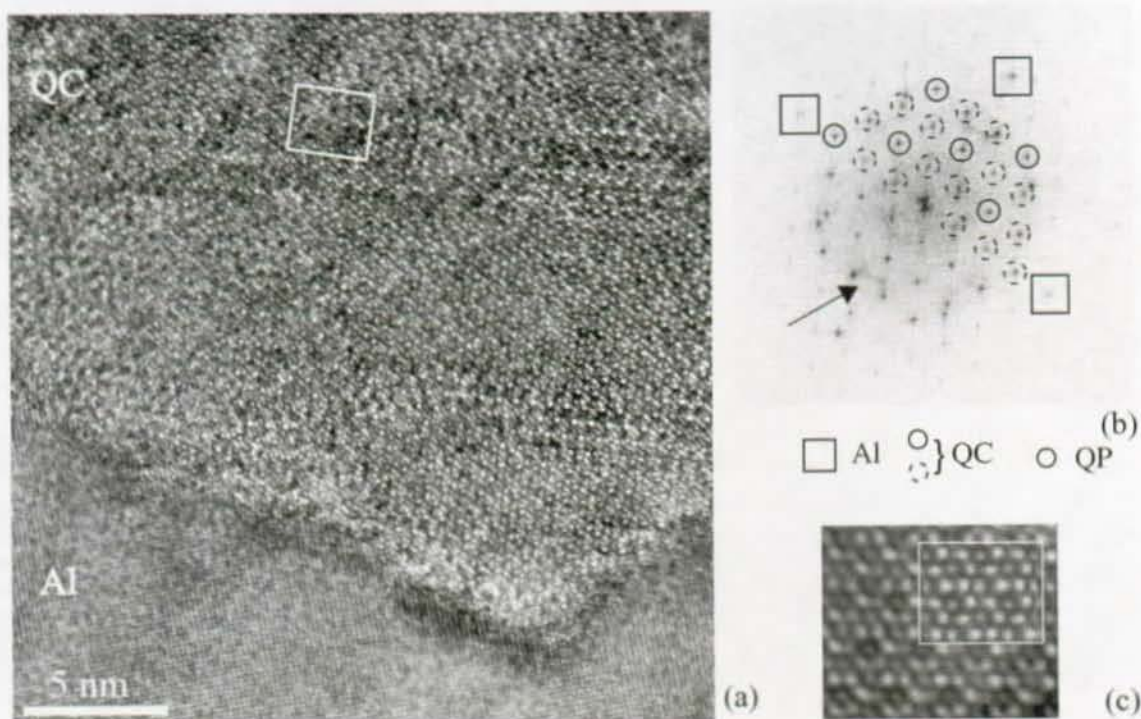


Fig. 6.19 QC precipitate in the matrix of the as-cast WFA/Al₂O₃/sf composite, (a) HREM image on the CM300 microscope of a QC rod-shaped precipitate along its [001] direction, (b) corresponding FFT, the Al spots are indicated by the squares, the QP sublattice spots by the solid circles, the other QC spots by the dashed circles (they are diffuse as indicated by the arrow). (c) Image corresponding to the part delimited by the white rectangle represented in (a), filtered with the QC and Al spot with a mask size close to the size of the QC circles reported in (b). A simulation is inserted on the right top corner with the following parameters: thickness 32 nm, defocus -80 nm (Scherzer at -48 nm), crystal tilt corresponding to the center of the Laue circle on the (200) spot ($\approx 0.5^\circ$).

unit triangular MgSiCu_{1/3} cluster corresponding to the AlO₆ octahedra. It was found that the Mg atoms are separated by 0.34 nm, which is close to the interatomic distance in the compact hexagonal Mg structure (0.32 nm).

Very recently, another phase named u-phase, was reported in the AlMgSi alloys containing Mn and Cr [166]. This phase has a needle shape (section ≈ 5 nm) along [001]_α direction, it nucleates during heating at 580°C on the β' needles, and has a hexagonal structure with $a = 0.670$ nm and $c = 0.808$ nm. The EDS measurements have shown that this phase contains Mg and Si ([Mg]/[Si] ≈ 0.8), and small amount of Mn and Fe. We strongly believe that this u-phase is QC-type structured i.e. built with the same sub-unit clusters, but with Si, Mn and Fe in the triangular site of the clusters.

The TEM method used to refine the structures is well adapted to this kind of small precipitates, but the precision on the atomic positions is low (0.7 Å) and the real nature of atom could not be established with absolute certainty due to the very close scattering factors of Al, Mg and Si. Thus, Mg atoms can be replaced by mixed (Al, Mg) atoms as proposed by

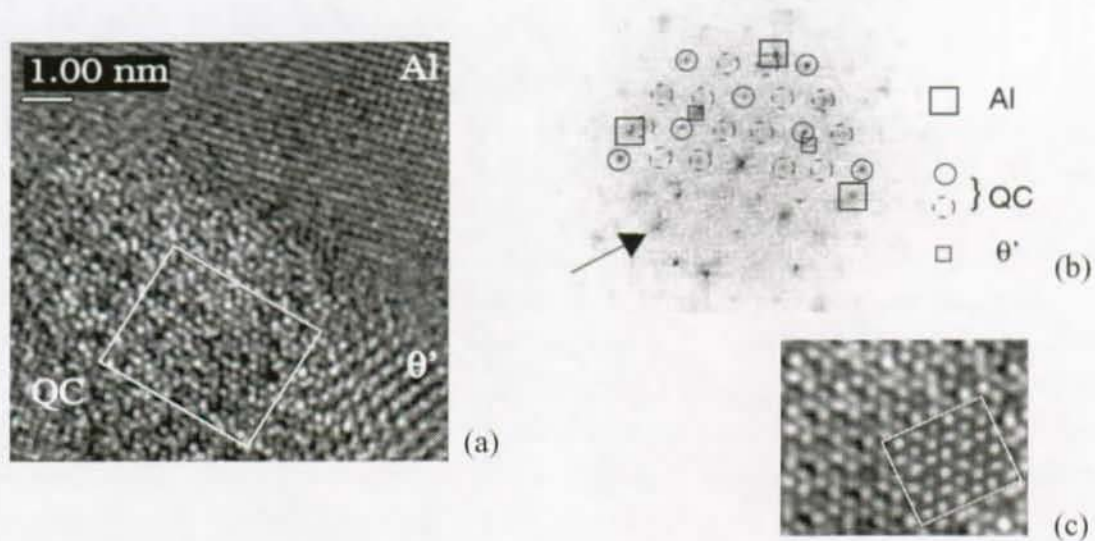


Fig. 6.20 A QC rod-shaped precipitate (situated on a θ' - CuAl_2 plate) in the matrix of a T6 WFA/SiC/p composite: (a) HREM image at 300 kV of a precipitate along its [001] direction (b) corresponding FFT, the Al spots are indicated by the large squares, the θ' spots by the small squares, the QC sublattice spots by the solid circles, the other QC spots by the dashed circles (they are diffuse as indicated by the arrow), and (c) image corresponding to the white rectangle part, represented in (a), filtered with the QC and Al spot with a mask size close to the size of the circles reported in (b), a simulation is inserted on the right corner with the following parameters: thickness 26 nm, defocus -105 nm, crystal tilt corresponding to the center of the Laue circle on the (110) spot ($\approx 0.4^\circ$)

X-ray for the stable Q structure [152], an exchange between (Al,Mg) and Si atoms in the clusters is not excluded, and the exact nature and occupancy of the atoms in the triangular sites of the sub-unit clusters are not obtained.

The coming closer of the (Al,Mg) atoms and the taking away of the Si atoms seems difficult to understand if we only consider the QP \rightarrow QC transition (found purely displacive). It is probable that the primitive latent qp phase is at the origin of the transition. In the qp phase, all the atoms are situated on the qh-lattice: the Si atoms are on the hexagonal QP lattice and the (Al,Mg) and Cu atoms are on the honeycomb qh-lattice with a respective occupancy of 5/6 and 1/6. The transition qp \rightarrow QP is produced by substitutions between the (Al,Mg) and the Cu atoms (see Fig. 6.8); but due to the difference between the (Al,Mg) and Cu sizes, the resulted QP phase could be only an imaginary intermediate state, which would immediately be transformed into QC by the displacement of the atoms.

Complementary observations should be done to validate the qp \rightarrow (QP) \rightarrow QC sequence. However, this section has clearly confirmed the model of structural phase transition in the AlMgSiCu alloys and its extension to the AlMgSi alloys proposed in section 6.2.

6.3.7 First conclusions

In summary, the structural phase transition we have discovered between the rod-shaped precipitates in the AlMgSiCu alloys has the following properties: (i) the 3 lattices of Q ($P\bar{6}$), QC ($P\bar{6}2m$), and QP ($P\bar{6}m2$) or qp ($P6_3/mmc$) are based on the same lattice, the QP lattice, (ii) the QP, QC and Q structures are constituted of atoms positioned on a latent lattice, the qh-lattice, and (iii) the QP, QC and Q superstructures come from ordering of the atoms on the honeycomb qh-lattice, producing sub-unit triangular clusters by atomic size effects.

The model seems to be applicable to all the rod-shaped precipitates in the AlMgSi alloys (i) with Si in excess such as the B' phase and type-A and -B phases, and (ii) without Si in excess such as the β'' and β' phases. This assumption is confirmed by the similarities between the β' and the QC phases which can be respectively mixed with B' or Q phases in the same precipitate. The only difference between QC and β' and between Q and B' is the presence of Cu in the sub-unit clusters of the Q-family phases. For the AlMgSi alloys, the sub-unit clusters have been named βP ($P\bar{6}m2$) and the most primitive phase βp ($P6_3/mmc$).

The model has permitted to propose a crystallographic structure for the β' and QC phases in qualitative and quantitative agreement with microdiffraction patterns. It has been concluded that the QC and β' phases are formed by a displacive transition from the QP and βP phases. Actually, it is thought that the primitive qp and βp phases produced QP and βP by an order-disorder transition with only substitutions between the (Al, Mg) and Cu atoms on the honeycomb qh lattice, immediately transformed into QC and β' phases by atomic size effects.

Some observations remain unclear for the moment. Why some large precipitates (cross section ≈ 20 nm) present a slight disordering (such as in Fig. 4.17, Fig. 6.19 and Fig. 6.20) and not others (such as in Fig. 6.18)? Why the small rod-shaped QP precipitates (section ≈ 1.5 nm) order themselves toward the Q structure during their growing? The next section will give some elements of response.

6.4 Ordering Processes during the Precipitation

This section describes how the ordering mechanisms, and some of the interesting properties such as kinetics and size effects, can be simulated by Monte Carlo method. It will be shown that the apparent complex phase transition can be reduced to an Ising model on an honeycomb lattice. By this approach, the phase transition will be shown to rely on fundamental physical theory (complex problem of ground state introduced in section 5.3.4).

6.4.1 Monte Carlo Simulations

From our observations and the model proposed in section 6.2, we consider that the phase transition keeps constant the number of each chemical element. We also make the

assumption that the volume is kept constant. Therefore, the phase transition could be simulated by Monte Carlo method with the Metropolis algorithm described in section 5.3.3. Before, the model was reduced to its simplest expression:

The QC and Q phases are supposed to be superstructure phases of the primitive qp phase, their ordering is produced by substitutions of the atoms followed by displacements due to atomic size effects. The displacements are limited to the first neighbors for QC and to the first and the second neighbors for Q; they form clusters, which are QP sub-unit clusters for the QC phase and unit clusters for Q (limited by the red or blue triangles in Fig. 6.7b). It was noticed that

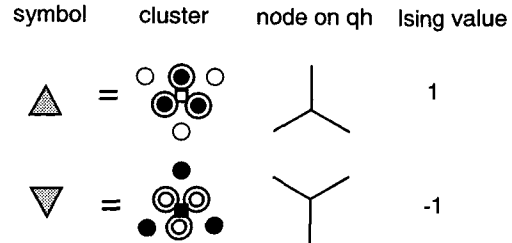


Fig. 6.21 Representation of the two kinds of sub-unit clusters, (up and down) with their Ising value associated (1 and -1).

the Si atoms remain on a QP lattice and that the substitutions of the atoms can only occur on the honeycomb qh-lattice. In our simulations, only the first neighbors displacements were taken into account, thus only the sub-unit clusters were considered. There are two kind of sub-unit clusters, one up and the other down as represented and symbolized in Fig. 6.21. Each of this sub-unit cluster is associated to one of the two QP sublattices constituting the honeycomb qh-lattice. By consequence, we will naturally create an Ising model constituted of two kinds of spins (1 and -1) for the two cluster types but also with the possibility to have a spin value of zero if no cluster is formed. These three values are positioned on the honeycomb qh-hexagonal lattice, with the following rule: $\sigma_i = (1 \text{ or } 0)$ on one QP sublattice, and $\sigma_i = (-1 \text{ or } 0)$ on the other QP sublattice¹. To illustrate this model, each phase is represented by an atomic scheme in Fig. 6.22a,b,c, or by equivalent up/no/down and 1/0/-1 schemes in Fig. 6.22d,e,f and Fig. 6.22g,h,i respectively.

The positions of the nodes of the three QP lattices that constitute the qh-lattice were calculated with the transfer matrix qh/Q:

$$\begin{bmatrix} X_{QP} \\ Y_{QP} \end{bmatrix} = \frac{1}{3} \begin{bmatrix} 2 & -1 \\ 1 & 1 \end{bmatrix} \begin{bmatrix} x_{qh} \\ y_{qh} \end{bmatrix}, \quad (6.15)$$

which gave

$$\begin{cases} [2x_{qh} - y_{qh}]_3 = 0 \\ [x_{qh} + y_{qh}]_3 = 0 \end{cases} \quad \text{for QP without spin value (0)} \quad (6.16)$$

1. This 0/(1/-1) formulation could also have been reduced to a classical 0/1 formulation of order-disorder since the sign of the spin depends only of the choice of one of the QP sublattice constituting the qh honeycomb lattice.

6. Order-Disorder Transition in the AlCuMgSi and AlMgSi Alloys

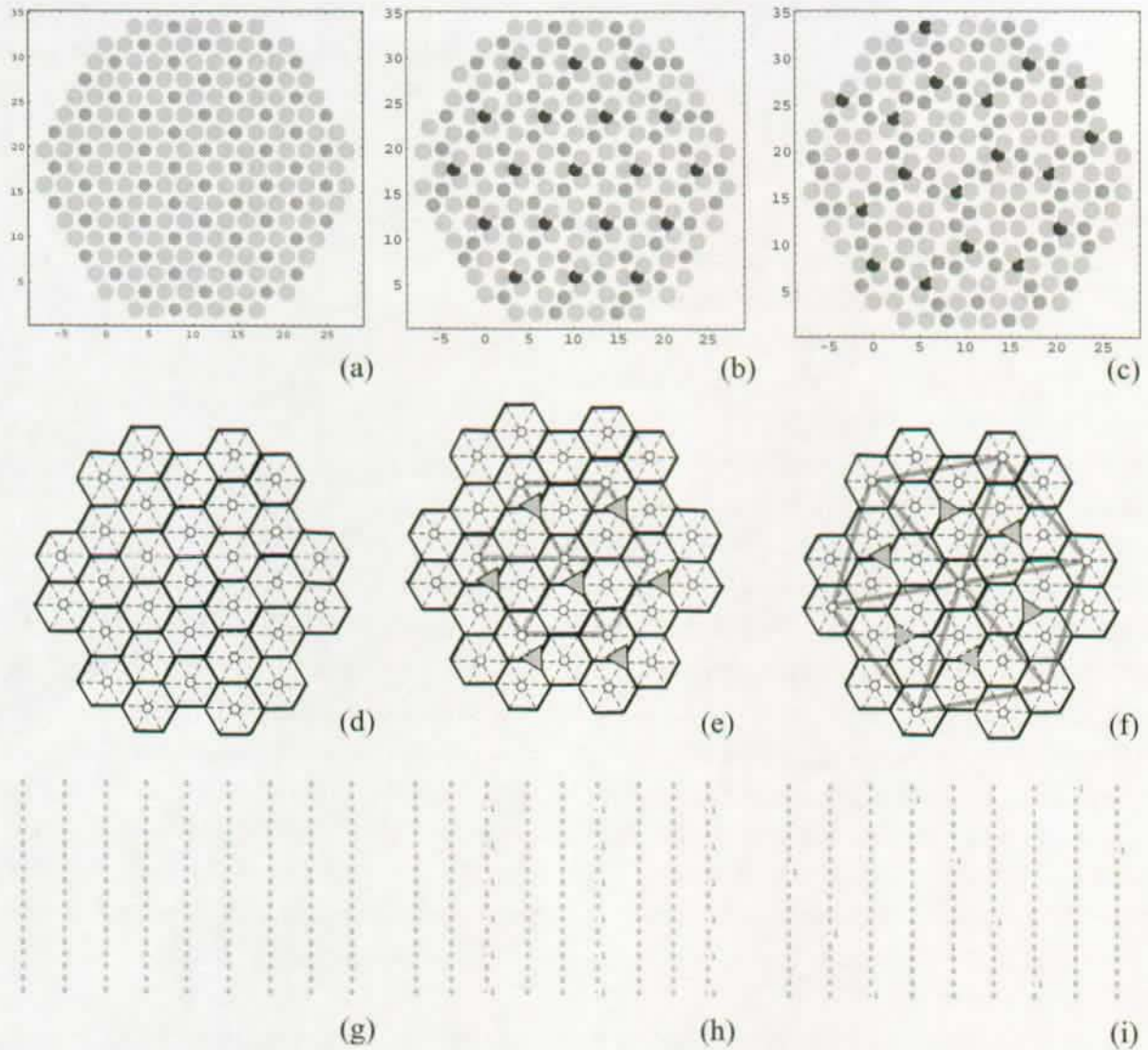


Fig. 6.22 Models of the structures, with a constant volume and composition:

- (a) qp, ● Si 1/2, ● (Al,Mg) 5/6 + Cu 1/6
 (b) QC, ● Si 1, ● (Al,Mg) 1, ● (Al,Mg) 2/3 + Cu 1/3
 (c) Q, ● Si 1, ● (Al,Mg) 1, ● Cu 1

(the scale is in Å), and their representation in spin up/down model respectively in (d), (e) and (f), and with their representation in spins 1/0/-1 model used for the calculus of Hamiltonian of the configuration respectively in (g), (h) and (i).

$$\begin{cases} [2x_{qh} - y_{qh}]_3 = 0 \\ [x_{qh} + y_{qh}]_3 = 0 \end{cases} \quad \text{for QP with spin 0 or 1} \quad (6.17)$$

$$\begin{cases} [2x_{qh} - y_{qh} - 1]_3 = 0 \\ [x_{qh} + y_{qh} - 2]_3 = 0 \end{cases} \quad \text{for QP with spin 0 or -1} \quad (6.18)$$

At each step of the program, the variation of the energy produced by a change of a spin value ($1 \Leftrightarrow 0$) for one QP sublattice or ($-1 \Leftrightarrow 0$) for the other was calculated by taking into account the pair interactions up to the 7 neighbors as shown in Fig. 6.23. The Hamiltonian of the system that was considered to calculate an energy change depends on the type of the QP sub-lattice. Its expression is given on right part of Fig. 6.23. Only the pair interactions were considered, as it is generally done by the other researchers [142], even if, as pointed out in section 5.5.1, the multiple-points interactions may have a great influence on the geometrical aspect of the atomic arrangement. Moreover, boundary conditions were imposed so that a cluster formation was possible only for sites farther than the 7th neighbor of any boundary sites. The Metropolis algorithm used for the simulation has been described in section 5.3.3: if the difference of energy between two configurations, x (old) and x' (possibly new), is $\Delta E_{xx'} = E_{x'} - E_x \leq 0$, the new spin value is accepted; otherwise, the new value is accepted with a probability

$$p = \exp\left(\frac{-\Delta E_{xx'}}{k_B T}\right) \quad (6.19)$$

This process was repeated for each spin of the system; calling N the number of atoms along a a_{QP} direction, only $2/3 \cdot N$ sites were visited per line (the QP sub-lattice with Si atoms was excluded), which represents $4/9 (N \times N)$ sites. This defines what is called a *Monte Carlo cycle*. In our program, all the variables such as N_{cy} , the number of Monte Carlo cycles, N the size of the system and T the temperature could be chosen, and $(e_1, e_2, \dots, e_n, \dots, e_7)$ the set of pair interaction energies could be adjusted.

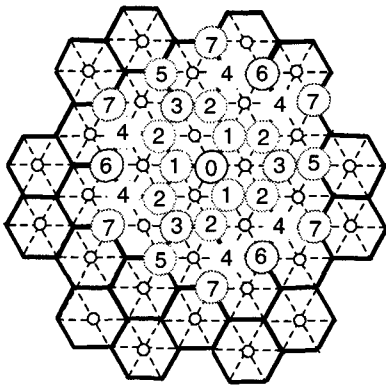


Fig. 6.23 Representation of the n^{th} neighbors on the qh honeycomb lattice.

Expression of the part of the Hamiltonian used to calculate the energy change by flipping a spin.

```
If [(ConditionClust [l,m]=="Down") ,
```

```
H=Isg [ [l,m] ] *
(e1* (Isg [ [l+1,m] ]+Isg [ [l,m+1] ]+Isg [ [l-1,m-1] ])+
e2* (Isg [ [l+1,m+2] ]+Isg [ [l+2,m+1] ]+Isg [ [l+1,m-1] ]+
Isg [ [l-1,m-2] ]+Isg [ [l-2,m-1] ]+Isg [ [l-1,m+1] ])+
e3* (Isg [ [l+2,m+2] ]+Isg [ [l,m-2] ]+Isg [ [l-2,m] ])+
e4* (Isg [ [l+3,m+1] ]+Isg [ [l+2,m-1] ]+Isg [ [l+1,m+3] ]+
Isg [ [l-1,m+2] ]+Isg [ [l-3,m-2] ]+Isg [ [l-2,m-3] ])+
e5* (Isg [ [l+3,m] ]+Isg [ [l,m+3] ]+Isg [ [l-3,m-3] ])+
e7* (Isg [ [l+3,m+3] ]+Isg [ [l,m-3] ]+Isg [ [l-3,m] ])) ;
```

```
If [(ConditionClust [l,m]=="Up") ,
```

```
H=Isg [ [l,m] ] *
(e1* (Isg [ [l+1,m+1] ]+Isg [ [l,m-1] ]+Isg [ [l-1,m] ])+
e2* (Isg [ [l+1,m+2] ]+Isg [ [l+2,m+1] ]+Isg [ [l+1,m-1] ]+
Isg [ [l-1,m-2] ]+Isg [ [l-2,m-1] ]+Isg [ [l-1,m+1] ])+
e3* (Isg [ [l+2,m] ]+Isg [ [l,m+2] ]+Isg [ [l-2,m-2] ])+
e4* (Isg [ [l+3,m+2] ]+Isg [ [l+2,m+3] ]+Isg [ [l+1,m-2] ]+
Isg [ [l-1,m-3] ]+Isg [ [l-3,m-1] ]+Isg [ [l-2,m+1] ])+
e5* (Isg [ [l+3,m+3] ]+Isg [ [l,m-3] ]+Isg [ [l-3,m] ])+
e7* (Isg [ [l+3,m] ]+Isg [ [l,m+3] ]+Isg [ [l-3,m-3] ])) ;
```

6.4.2 Ground State Problem

Before processing the simulations to adjust the $(e_1, e_2, \dots, e_n, \dots)$ pair interaction energies to the n^{th} neighbors, one needs to find their range of values. Since the Q phase is the stable phase at room temperature, it was assumed that this phase is also the stable phase at $T = 0$ K, i.e. the *ground state* of our Ising model. The question was: what must be the pair interaction energies to obtain the Q structure as the ground state result? Inversely, the question was: what are the ground state structures in function of the pair interaction energies? It is a general complex problem linked to the prediction of the phase diagrams, introduced in section 5.3.4. Our model was treated on the base of a honeycomb lattice with three spin values (1/0/-1) but could have been reduced to a two spin values problem (0/1) (see previous footnote). This kind of honeycomb Ising lattice problem has been partially treated by Kudo and Katsura. By considering only the interactions up to the 3rd neighbors, they found the ground state ordered structures represented in Fig. 6.24 [130]. They identified most of the vertices of the configuration polyhedra, except two, the missing numbers IV and XIV of Fig. 6.24. These ones correspond to an impossibility of building periodic ground state structures with the cluster types given by the vertex value solutions. These missing numbers are the representation of an interesting and intrinsic problem linked to frustrated lattices. Kanamori [169] has proved that these missing structures are in fact structures degenerated in an infinite series of regularly ordered ground state structures constructed of periodic zigzagging antiphase boundaries. He noted them T_n and R_n (n corresponding to the amplitude of the zigzag). Such series constitute what is called a devil's stair [128]. Ducastelle has shown that this effect also appears even if only the interactions up to the second neighbors are considered [128]. He graphically represented the modification of the configuration polyhedra due to the frustration effect, as reported in Fig. 6.25.

It can be noticed that $n^\circ\text{I}$, $n^\circ\text{II}$, $n^\circ\text{VII}$, $n^\circ\text{V}$ and $n^\circ\text{IX}$ correspond to the qp, QP, QC, type-A and type-B ordering, respectively. Nevertheless, the Q structure has not his equivalent

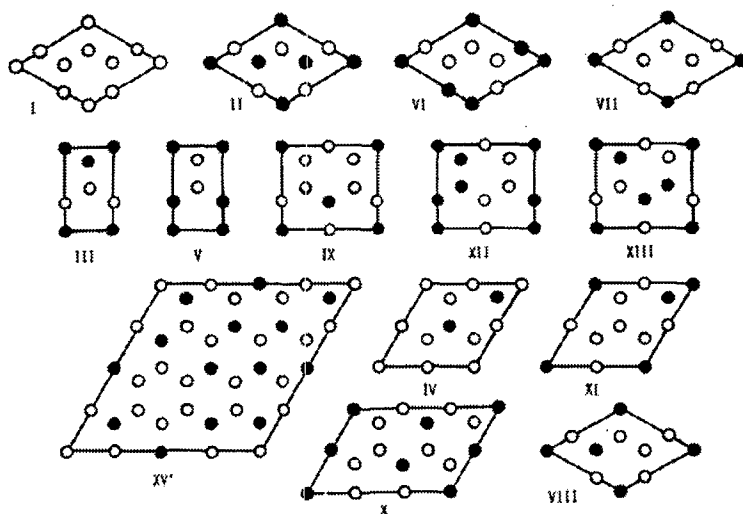


Fig. 6.24 Ground state structures on a honeycomb lattice found by Kudo and Katsura by finding the vertices values of the configuration polyhedron. From [130]. $n^\circ\text{I}$, $n^\circ\text{II}$, $n^\circ\text{VII}$, $n^\circ\text{V}$ and $n^\circ\text{IX}$ correspond respectively to the qp, QP, QC, type-A and type-B ordering

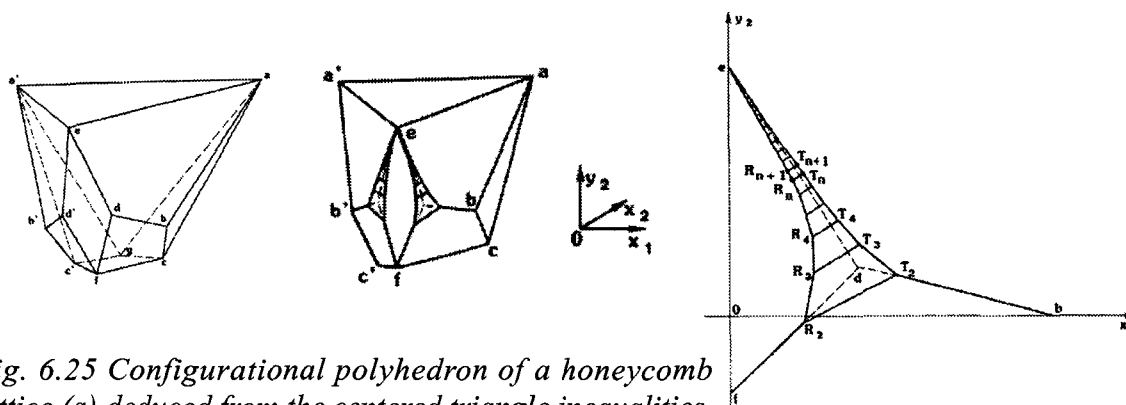


Fig. 6.25 Configurational polyhedron of a honeycomb lattice (a) deduced from the centered triangle inequalities, (b) after the degeneracy of the vertex d and (c) projection along the x_2 axis. x_1, x_2, y_2 denote the point, nearest-neighbor and second-nearest neighbors correlation function, respectively. From [128].

neither in vertices identified by Kudo and Katsura [130] nor in the zigzag structures T_n or R_n determined by Kanamori [169]. Thus it was concluded that the resolution of our ground state problem requires at least the pair interaction energies up to the 4th neighbors (or perhaps three-body interactions). Table 6.3 gives the signs of the pair interactions required to form clusters between the n -nearest neighbors sites and then those required to form the QC and Q ordering¹ (a very first approximation of a phase diagram).

neighbors	cluster formation	QC ordering	Q ordering
e1	+	-	-
e2	-	+	+
e3	+	-	-
e4	+	-	+
e5	-	-	+
e6	-	-	+
e7	-	-	+

Table 6.3 Sign of the pair interaction required to form a cluster with the 0/1 formulation.

We have begun to explore some regions in the (e_1, e_2, \dots, e_4) space without succeeding in finding good values for the Q ordering. We had to go up to the 5th nearest-neighbors for the QC ordering and to 7th nearest-neighbors for the Q ordering.

The final aim of such a Monte Carlo study was to find, by comparison between diffractions of experimental and simulated structures, the appropriate pair interaction values

1. With the reduced (0/1) problem, the sign must be always negative. With the (1/0/-1) formulation, the sign depends whether the two considered sites are on the same QP sublattice.

(e_1, e_2, \dots, e_7) to determine the multiple-point correlations $\langle \sigma_i \sigma_j \sigma_k \dots \rangle$ and then characterize the ordering process of the transformation. Since the experimental diffraction patterns can only lead to the pair correlation $\langle \sigma_i \sigma_j \rangle$ as said in section 5.5.2, the problem could be solved in theory by comparison between HREM images and simulated projected potentials (in the approximation of the weak phase object), or by comparison between the complete FFT images (with modulus and phases). In this aim, a general form of the projected potential of a disorder cell has been calculated as detailed in annex A and illustrated in Fig. 5.4. Unfortunately, the algorithm remains slow and did not allow to explore too many variables. Therefore, the FFTs were calculated by reducing the atomic potential to one pixel with a gray level proportional to Z ; only qualitative comparisons were realized and discussed.

6.4.3 As-Cast State: Kinetics Effect

The presence of mixed (QP or qp) / QC / Q and (βp / β / B') precipitates (Fig. 6.1, Fig. 6.19) in the slowly air-cooled as-cast composites may appear in contradiction with the metastable character of the phases (the unique reported stable phase is the Q phase [82]). In fact, these observations can be explained if we consider that the $qp \rightarrow QC \rightarrow Q$ or $\beta p \rightarrow \beta' \rightarrow B'$ transformations are order/disorder and hence are sluggish (section 5.1.1). The sluggish kinetics of $qp \rightarrow QC$ or $\beta p \rightarrow \beta'$ is less marked than the one of the $qp \rightarrow Q$ or $\beta p \rightarrow B'$ transformations because only substitutions between first neighbors are involved. Therefore, the QC and β' phases can be considered as intermediate metastable phases coming from the high temperature disordered qp and βp phases and appearing before the more complex Q or B' phases in the as-cast state during the cooling of the material from its liquid state because of the kinetics of the transition.

The sluggish character of the transition could not be directly simulated by Monte Carlo method (which is not straightforward to obtain time dependent dynamical information, contrarily to molecular dynamics). Nevertheless, it is clear that the frustrated character of the honeycomb lattice reduces the dynamics of the transitions. For instance, it has been noticed that about $N_{cy} = 20$ was required to create the QC structure and more than $N_{cy} = 50$ to create the Q structure (with stacking faults and twins), which gives a qualitative idea of their respective dynamics of transition. Moreover, the low dynamics of the Q ordering was obtained for a large range of (e_1, e_2, \dots, e_7) values. It produced PS images similar to those observed for the mixed QP/Q precipitates, as shown in Fig. 6.26.

6.4.4 T6 State: Size Effect

In the AlMgSiCu matrices in T6 state, small QP (or qp) and not perfectly ordered QC rod-shaped precipitates were observed (Fig. 4.15, Fig. 6.17). Their presence looks in contradiction with the metastable character of these phases: why Q or B' phase does not firstly and definitively precipitates? Since the misfits associated to the precipitates coherent with the Al matrix are low whatever their structure (QP, QC or Q) or (βp , β' or B') and whatever their

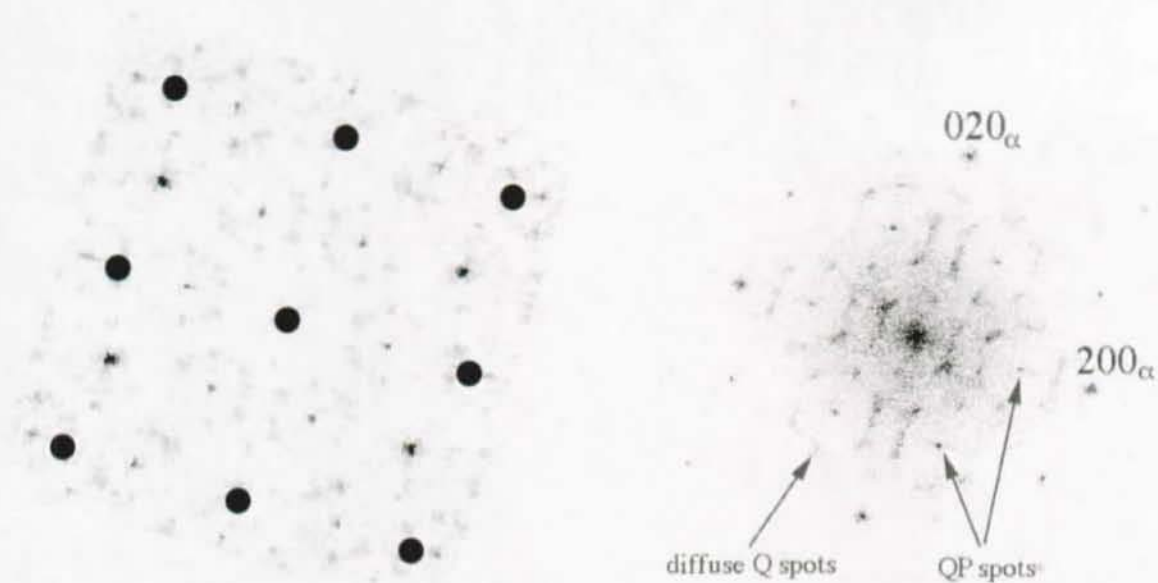


Fig. 6.26 Kinetics effect simulated by Monte Carlo with $N_{cy} = 50$, $(e1, e2, e3, e4, e5, e6, e7) = (-0.1, 0.1, -0.06, 0.1, 0.1, 0, 0.1)$ at $T = 100K$ (for indication) (a) PS of the simulated cell, the Al spots are indicated by the filled circles. For comparison (b) the PS of the mixed QP/Q precipitate of Fig. 6.2d.

OR (1 or 2), a matrix effect does not seem to bring an answer. In fact, the observations can be explained by considering a physical property well known for small particles: the particle size effect on the critical temperature. This effect has been observed for first order transition (melting temperature of gold particles [170]) or for second order transition (critical temperature of ferroelectrics particles [171, 172]). Indeed, the critical transition temperature decreases when the particle size decreases, and a critical particle size can appear under which only the "high temperature" (disordered) phase exists whatever the temperature. There are two different ways to understand such effect:

The first way consists in considering that the solid particle of size r_s has a surface energy γ_s which makes increase its internal pressure:

$$P_{int} = P_{ext} + \frac{2\gamma_s}{r_s} \quad (6.20)$$

Due to its higher internal pressure, the particle has the tendency to explode, i.e. to melt. From thermodynamical considerations [170], by neglecting the surface energy of the liquid ($\gamma_s \gg \gamma_l(\rho_s/\rho_l)^{2/3}$), one can show that the melting temperature is given by the expression

$$\theta = 1 - \frac{2\gamma_s}{L\rho_s r_s} \quad (6.21)$$

where ρ is the density and $1 - \theta = (T - T_0)/T_0$, where T_0 is the melting temperature of the

6. Order-Disorder Transition in the AlCuMgSi and AlMgSi Alloys

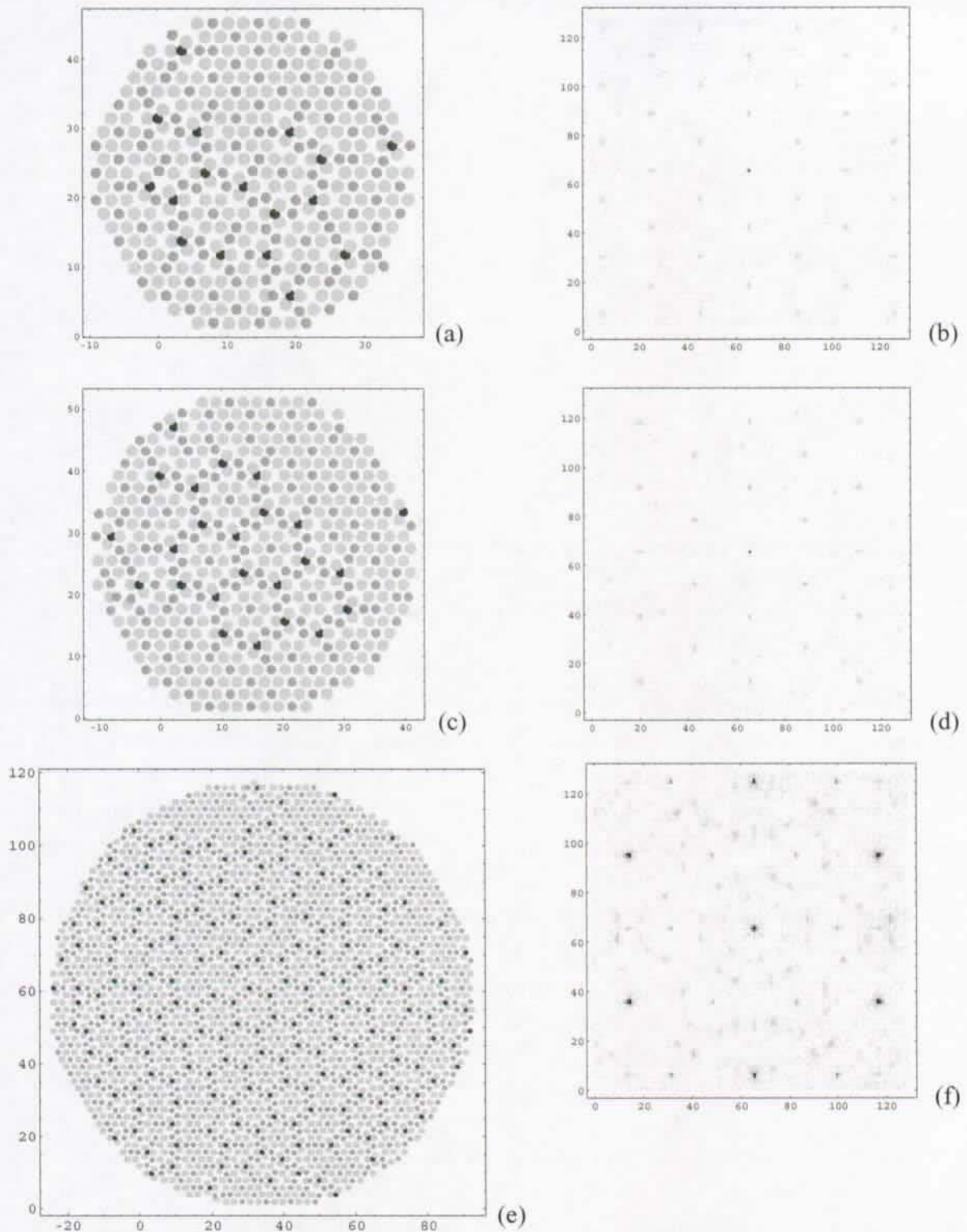


Fig. 6.27 Size effect simulated by Monte Carlo with $N_{cy} = 150$, $(e_1, e_2, e_3, e_4, e_5, e_6, e_7) = (-0.1, 0.1, -0.06, 0.05, 0.05, 0, 0.05)$ at $T = 100K$. After applying a circle mask, the sizes are, in (a) 48 Å, in (c) 54 Å and in (e) 120 Å. Their FFT are reported in (b), (d) and (f) respectively. The size sufficient for the Q -ordering is about 50 Å. For sizes > 100 Å, the Q precipitate is a mixture of two variants.

bulk and L the latent heat of fusion. The corresponding figure is given in Fig. 6.28c. This approach has its limits since it is based on thermodynamics which usually applies to systems with large numbers of entities.

The second way of understanding the size effect relies on the main ideas of phase transitions. Physically, the solidification of a gold particle or the superordering from the qp or βp phases comes from a cooperative effect of all the atoms in the structure; if the particle is too small this effect cannot occur impeding LRO, and only SRO appears by formation of clusters ordered on few lattice distances (which is visible on the diffraction patterns by the diffusion of the intensities). Therefore, this effect is easily simulated by Monte Carlo methods, as it was done for the determination of percolation threshold, magnetization or susceptibility [126] (even if it is often considered as an artifact problem that one must avoid to find the exact critical temperature of a bulk material by computing). In our simulations, this effect is obvious for sizes smaller than 7 interatomic distances (boundary conditions), but also appears at larger distances as shown in Fig. 6.27.

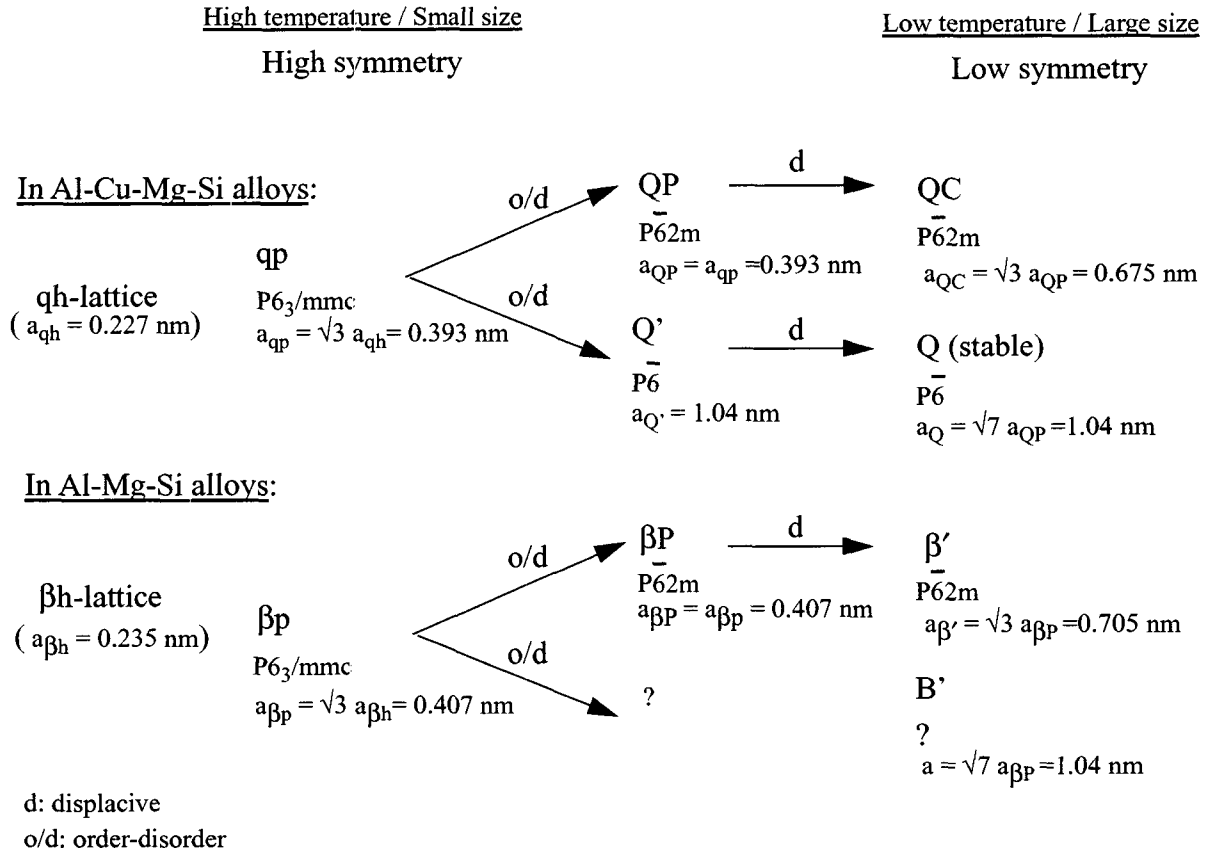
6.5 Conclusion and Prospects

Section 6.2 revealed by TEM observations of the precipitation state in the AlCuMgSi matrices of WFA/Al₂O₃/sf and WFA/SiC/p composites that a phase transition exists between the stable Q phase and two others metastable noted QC and QP. The consideration of the crystallography of the Q phase made us suppose that the QC (AlCuMgSi alloys) and the β' (AlMgSi alloys) phases have very close structures, based on latent lattices (respectively noted QP and βP), and constituted by triangular sub-unit clusters.

Section 6.3 confirmed the model: the QC and β' precipitates (both hexagonal with $a = 0.67$ nm, and $a = 0.71$ nm respectively) exhibit similar superstructures and diffraction patterns. Their structures come from to a slight displacement of the atoms from their positions on the QP and βP structures, these latter being probably only intermediate structures coming from the qp and βp structures by an order-disorder transition. After refinement by comparison between the experimental and computed microdiffraction patterns, their crystallography was found hexagonal $P\bar{6}2m$. The difference was explained by the fact that QC contains Cu in addition to Si in the triangular sites of the clusters.

6. Order-Disorder Transition in the AlCuMgSi and AlMgSi Alloys

The model of phase transition that we propose can be summarized in this way:



During the cooling step of the processing, the $qp \rightarrow (QP \rightarrow) QC \rightarrow Q$ transition is sluggish (due to its order-disorder character): all the coarse rod-shaped precipitates formed in the as-cast material are not Q phase structured, but mixed with QC phase (Fig. 6.28a).

After the solution heat treatment and during the aging, the stable Q phase does not firstly appear, but respects the $qp \rightarrow (QP \rightarrow) QC \rightarrow Q$ sequence: it is supposed that this is the growing of the precipitates which makes them structurally change, the critical temperature of transition being an increasing function of the particle size (Fig. 6.28b,c).

Further experiments should be done to confirm and specify the model:

(1) to make in-situ X-rays measurements on large Q crystals. If the model is correct, the $Q \rightarrow QC (\rightarrow QP) \rightarrow qp$ structural sequence should be observed by heating the crystal. At EMPA-Thun, we have tried to elaborate such a crystal by mixing Al, Cu, Si and Mg at 1100°C , without success (large Mg_2Si crystals were formed). Nevertheless, a crystal such the one used by Arnberg for his X-rays study [152] could be sufficient.

(2) to reconsider the precipitation sequence in the AlMgSi alloys. According to our model, all the rod-shaped precipitates already observed in these alloys obey the structural

transition with β_p as primitive phase. It seems then strange that the β'' phase could come from the β' phase whereas its cell parameters are larger and its symmetry lower. Moreover, as discussed in annex B2, the $\beta'' \rightarrow \beta'$ sequence dates from the first observations of the 6xxx alloys when the names were not consistent between the authors. We believe that in-situ HREM observations should be done to check the precipitation sequence and precise the mechanisms: dissolution/reprecipitation or structural change (as we suppose). An in-situ heating sample holder for HREM observations on the CM300 microscope has been designed by A. Sfera at the CIME (initially to study the ferroelectric domain walls) and is under construction. Such an instrument is necessary for further understanding of the precipitation mechanisms in the AlMgSi alloys.

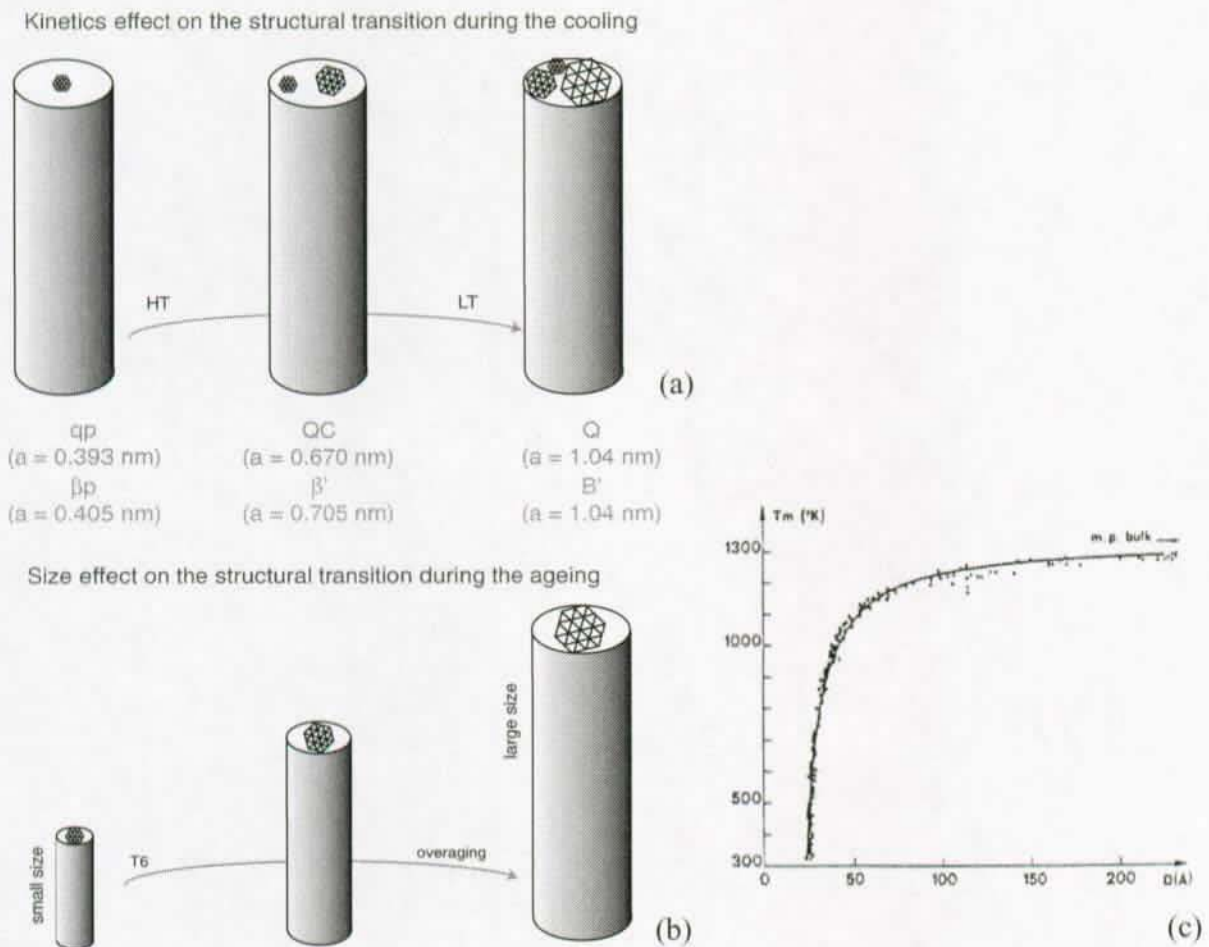


Fig. 6.28 (a) Kinetics effect at the origin of the mixed $QP/QC/Q$ structures observed in the as-cast alloys (such as in Fig. 6.2 and Fig. 6.4). (b) Size effect at the origin of the formation of the disordered QP (or qp) phase in the first step of nucleation, and of the structural change during the growing by overaging. (c) The size effect is similar to those responsible for the decrease of the melting temperature of a gold particle when reducing its size, from [170].

6. Order-Disorder Transition in the AlCuMgSi and AlMgSi Alloys

Chapter 7

Conclusions

Two kinds of aluminum matrix composites (AMCs) based on a precipitation hardened Al-4Cu-1Mg-0.5Ag alloy (denoted WFA) and reinforced with Al₂O₃ Saffil short fibers (15%) and with SiC particles (60%) have been fabricated by squeeze-casting process (SQC) for the assessment of their mechanical performance for potential automotive and electronic applications. The composites were noted WFA/Al₂O₃/sf and WFA/SiC/p, respectively. Toward a better understanding of their mechanical properties, their microstructure has been studied by transmission electron microscopy TEM.

Compared to the unreinforced alloy, the grain sizes and morphologies are strongly affected by the presence of the reinforcements (loss of the dendritic structure). Microsegregation mainly of Al₂Cu, Al₇Cu₂Fe and Q-Al₅Cu₂Mg₈Si₆ is clearly visible in the as-cast composites at the interface between the matrix and the reinforcements, and is significantly reduced by a heat treatment at 500°C for 2 hours. In addition to its presence in the Q-phase intermetallics, Si was detected in the matrices of all the composites. From interface reaction investigations by TEM, it has been deduced that Si was released from two different interfacial reactions:

(1) for the WFA/Al₂O₃/sf composites, a reaction occurs between the Mg from the alloy and the SiO₂ from the Saffil fibers and from the binder of the preform when a silica binder was used. The reaction leads to the formation of MgAl₂O₄ during the infiltration, and MgO during the heat treatment at 500°C.

(2) for the WFA/SiC/p composites, a reaction occurs directly between Al and the SiC particles. The reaction leads to the discontinuous precipitation of Al₄C₃ hexagonal plates. Due to its high affinity to Si, Mg plays an indirect but important role in the kinetics of the reaction.

The chemical composition of the matrix alloy is modified by the appearance of Si and the decrease of the Mg content. In consequence, the precipitation state in the matrices of the composites is significantly changed. The precipitation of the Ω and S' phases, characteristic of the unreinforced WFA alloy, is substituted by a fine and dense precipitation of nano-sized QP rod-shaped precipitates (precursors of the stable Q-Al₅Cu₂Mg₈Si₆ phase) hexagonal with $a = 0.393$ nm and $c = 0.405$ nm and of θ' plates. The θ' plates lie on nano-sized rod-shaped precipitates identified by HREM, DSTEM, EDS and microdiffraction techniques: in the WFA/Al₂O₃/sf composites the precipitates correspond to the Si phase, and in the WFA/SiC/p

composites they correspond to the QC phase (other precursor of the stable Q-Al₅Cu₂Mg₈Si₆ phase, hexagonal with $a = 0.67$ nm and $c = 0.405$ nm). It is assumed that the Si-vacancy pairs act as nucleation sites for the θ' plates. The slight improvement of the tensile properties of the WFA/Al₂O₃/sf composites when a silica binder is used instead of an alumina one can be explained by a higher density of the QP rod-shaped precipitates in the matrix of this composite (due to the higher Si content). The results of these findings allow to propose some pathways for the improvement of the tensile properties of the composites.

The QP and QC rod-shaped precipitates in the matrices of the WFA/Al₂O₃/sf and of the WFA/SiC/p composites are new phases whose detailed investigation by TEM helps to establish new concepts involved in the precipitation mechanisms in the 6xxx alloys in general. Indeed, the TEM study using superstructure DF imaging and in-situ heating experiments on the QP and QC precipitates in the as-cast state of the composites reveals the existence of a structural phase transition. A model has been developed from the crystallographic structure of the stable Q-phase (determined by X-rays). It describes the QP, QC and Q structures as superordered structures built on an order-disorder transition from a primitive phase named qp. Moreover, the model predicts that a similar transition exists between all the metastable phases in the 6xxx alloys (β'' , β' , B', type-A, type-B). For instance, β' is shown to be structurally similar to QC, with Si substituting Cu in the unit-cell. The latent lattices implied in the transitions are noted QP and β P for the matrices of the composites (AlCuMgSi alloys) and for the 6xxx alloys (AlMgSi alloys) respectively.

Microdiffraction patterns and superstructure DF images acquired on a CCD camera confirm that QC and β' are structurally similar. After refinement by comparison between the experimental and computed microdiffraction patterns, their crystallography has been found to be hexagonal $P\bar{6}2m$.

Eventually, according to the model, the structural transitions in the AlCuMgSi and AlMgSi alloys are: $qp \rightarrow (QP \rightarrow) QC \rightarrow Q$ and $\beta p \rightarrow (\beta P \rightarrow) \beta' \rightarrow B'$, respectively. Both follow the breaking symmetry path $P6_3/mmc \rightarrow P\bar{6}2m \rightarrow P\bar{6}$.

This sequence is respected during the cooling of the materials, and structurally mixed precipitates are observed in the as-cast state due to kinetics effects. This sequence also holds during aging of the materials, quite probably due to a precipitate size effect on the critical temperature of transition. Monte Carlo simulations on an Ising lattice have been computed to illustrate those effects.

Bibliography

Chapter 1 Introduction

- 1 Clyne, T. W., and Withers, P. J. (1993), *An Introduction to Metal Matrix Composite*, Cambridge University Press, Cambridge.
- 2 Suresh, S., Mortensen, A., and Needleman, A. (1993), *Fundamental of Metal-Matrix Composites*, Butterworth-Heinemann, Stoneham, MA 02180, USA.
- 3 On the web: <http://mmc-assess.tuwien.ac.at/>
- 4 Official final report on PPM project 2.1B (1995-1998), *High Performance Aluminium Matrix Composites*.
- 5 Beffort, O., Solenthaler, C., and Speidel, M. O., 1995. *Mat. Sci. Engng*, **A191**, 113.
- 6 Beffort, O., Solenthaler, C., Uggowitzner, P. J., and Speidel, M. O., 1995. *Mat. Sci. Engng*, **A191**, 121.
- 7 Taya, M., and Arsenault, R. D., (1989), *Metal Matrix Composites, Thermomechanical Behavior*, Pergamon Press, Oxford.
- 8 Polmear, I. J. (1995). *Light Alloys. Metallurgy of the Light Metals*, Arnold, London.
- 9 Lorimer, G. W., (1978), "Precipitation in aluminum alloys" in *Precipitation processes in Solids*, TMS-AIME Warrendale, PA, pp. 87-119.

Chapter 2 Aluminum Matrix Composites: Processing and Properties

- 10 On the web: <http://bricad.com/aluminium/dur/>
- 11 On the web: http://www.3M.com/market/industrial/mmc/products_page.html
- 12 On the web: <http://www.amc-mmc.co.uk/>
- 13 On the web: <http://207.178.131.112/intro/index.html>
- 14 On the web: <http://www.lanxide.com/mmc.htm>
- 15 Cox, H. L., 1952, *J. Appli. Phys.*, **3**, 72.
- 16 Kelly, A., (1973). *Strong Solids*, 2nd edn, Oxford University Press, Chapter 5.
- 17 Friend, C. M., 1987, *J. Mater. Sci.*, **22**, 3005.
- 18 O'Rourke, J. M., Bushby, R. S. and Scott, V. D., 1996, *Comp. Sci. Tech.*, **56**, 957.
- 19 O'Rourke, J. M., Bushby, R. S. and Scott, V. D., 1996, *Comp. Sci. Tech.*, **56**, 1071.

BIBLIOGRAPHY

- 20 Halpin, J. C. (1984), *Primer on Composite Materials: Analysis*, Rev. edn, 130, Lancaster, PA, Technomic Publ.
- 21 Loyd, D. J., 1994, *Int. Mater. Rev.*, **39**, 1.
- 22 Eshelby, J. D., 1957, *Proc. Roy. Soc.*, **241**, 376.
- 23 Eshelby, J. D., 1959, *Proc. Roy. Soc.*, **A252**, 561.
- 24 Arsenault, R. D., and Fischer, R. M., 1983, *Scripta Metal.*, **17**, 67.
- 25 Arsenault, R. D., and Shi, N., 1986, *Mater. Sci. Engng*, **81**, 175.
- 26 Qin, S. and Gupta, M., 1995, *J. Mater. Sci.*, **30**, 5223.
- 27 Gerold, V., (1979), *Dislocations in Solids Vol.4, Dislocation in Metallurgy*, ed. by F. R. N. Nabarro, Chapt 15.
- 28 Kelly, A., and Tyson, W. R., 1965, *J. Mech. Phys. Solids*, **13**, 329.
- 29 Azzi, V. D., and Tsai, S. W., 1965, *Exp. Mech.*, **5**, 283.
- 30 Lloyd, D., 1991, *Acta Met. Mat.*, **39**, 59.
- 31 Firrao, D., and Roberti, R. (1985), *Proc. 113th AIME Conf.*, edited by J. M. Wells and J. B. Landes, 165-177.
- 32 LeRoy, G., Embury, J. D., Edwards, G., and Ashby, M. F., 1981, *Acta Metal.*, **29**, 1509.
- 33 Metcalfe, A. G., 1967, *J. Comp. Mat.*, **1**, 356.
- 34 Le Petitcorps, Y., Lahaye, M., Paillet, R., and Naslain, R., 1988, *Comp. Sci and Tech.*, **32**, 31.
- 35 Polmear, I. J., 1964, *Trans. AIME*, **230**, 1331.
- 36 Eschbach, L., Solenthaler, C., Uggowitzer, P. J., and Speidel, M. O., 1999, *Mat. Sci. Tech.*, **15**, 836.
- 37 Polmear, I. J., Pons, G., Barbaux, Y., Octor, H., Sanchez, C., Morton, A. J., Borbidge, W. E., and Rogers, S., 1999, *Mat. Sci. Tech.*, **15**, 861.
- 38 Norton AS, Norton-Lillesand, Norway, private communication.
- 39 Zhang, Z., Long, S. and Flower, H. M., 1994, *Composites*, **25**, 380.
- 40 Long, S., Flower, H. M., and Beffort, O. (1997), *Proc. 4th Decennial Inter. Conf. Solidif. Proc.*, edited by J. Beech and H. Jones, Sheffield, U.K., 92-96.
- 41 Long, S., Beffort, O., Cayron, C. and Bonjour, C., 1999, *Mater. Sci, Engng*, 175.

Chapter 3 Transmission Electron Microscopy

- 42 Hawkes, P. (1995) *Electrons et microscopes*, CNRS editions, Paris.
- 43 Budd, P. M. and Goodhew, P. (1988), *Light.Element Analysis in the Transmission Electron Microscope: WEDX and EELS*, Oxford University Press, Royal Microscopical Society.
- 44 Horita, Z., 1998, *Mater. Trans., JIM*, **39**, 947.
- 45 Williams, D. B. and Carter, C. B. (1996), *Transmission Electron Microscopy : a Textbook for Materials Science*, Plenum Press, New York.

BIBLIOGRAPHY

- 46 Goldstein, I. J., Newbury, D. E., Echlin, P., Joy, D. C., Romig, Jr., A. D., Lyman, C. E., Fiori, C. and Lifshin, E. (1992), *Scanning Electron Microscopy and X-ray Microanalysis*, 2^d ed., Plenum Press, New York.
- 47 Williams, D. B. (1984) *Practical Analytical Electron Microscopy in Materials Science*, Philips Electronics Instruments, Inc., USA.
- 48 Fujiwara, K., 1961, *J. Phys. Soc. Japan*, **16**, 2226.
- 49 Cowley, J. M. (1984), *Diffraction Physics*, 2^d ed., Elsevier Science Publishers, North-Holland Physics Publishing, Amsterdam.
- 50 Reimer, L., (1997) *Transmission Electron Microscopy*, 4th ed, Springer, Berlin.
- 51 Stadelmann, P., 1996, *Cours de Microscopie Electronique*.
- 52 Doyle, P. A. and Turner, P. S., 1967, *Acta Cryst.*, **22**, 153.
- 53 *International Tables for X-ray Crystallography, vol. IV* (1974), ed. by J. A. Ibers and W. C. Hamilton, International Union of Crystallography, Kynoch Press, Birmingham.
- 54 Batterman, B. W., Chipman, D. R. and Marco, J. J., 1961, *Phys. Rev.*, **122**, 68.
- 55 Doyle, P. A. and Turner, P. S., 1968, *Acta Cryst.*, **A24**, 390.
- 56 Weickenmeir, A. and Kohl, H., 1991, *Acta Cryst.*, **A47**, 590.
- 57 Morniroli, J. P. and Steeds, J. W., 1992, *Ultramicroscopy*, **45**, 219.
- 58 Redjamaïmia, A., Morniroli, J. P., Metauer, G. and Gantois, M., 1990, *Proc. of the XIIIth Inter. Cong. for Electron Microscopy*, Seattle, 494.
- 59 Buxton, B. F., Eades, J. A., Steeds, J. W. and Rackham, G. M., 1976, *Phil. Trans.*, **281**, 171.
- 60 Tanaka, M., Saito, R. and Sekii, H., 1983, *Acta Cryst.*, **A39**, 357.
- 61 Gjønnnes, J. and Moodie, A. F., 1965, *Acta Cryst.*, **19**, 65.
- 62 Cowley, J. M. and Moodie, A. F., 1957, *Acta Cryst.*, **10**, 609.
- 63 Phillipp, F., 1998, *Mater. Trans., JIM*, **39**, 888.
- 64 Scherzer, O., 1949, *J. Appl. Phys.*, **20**, 20.
- 65 Zou, X., 1999, *5th Electron Crystallography School*, Nantes, Lecture D.
- 66 Zou, X. D. (1995), *Electron Crystallography of Inorganic Structures- Theory and Practice*. Chem. Comm. **5**, Stockholm, Ph. D. thesis.
- 67 Giacobazzo, C., Monaco, H. L., Viterbo, D., Scordari, F., Gilli, G., Zanotti, M. and Catti, M., (1992), *Fundamentals of Crystallography*, edited by C. Giacobazzo, Oxford University Press.
- 68 Tsuda, K. and Tanaka, M., 1999, *Acta Cryst.*, **A55**, 939.
- 69 Dorset, D. L. (1995), *Structural Electron Crystallography*, Plenum Press, New York.
- 70 Vainshtein, B. K., 1964, *Structure Analysis by Electron Diffraction Techniques*, Pergamon Press Ltd., Oxford.
- 71 Van Dick, D. and de Jong, A. F., 1992, *Ultramicroscopy*, **47**, 266.
- 72 Zandbergen, H. W., Bokel, R., Connolly, E. and Jansen, J., 1999, *Micron*, **30**, 395.

BIBLIOGRAPHY

- 73 Zandbergen, H. W., Jansen, J., Cava, R. J., Krajewski, J. J., Peck, W. F., and Gyorgy, E. M., 1994, *Nature*, **372**, 759.
- 74 Zandbergen, H. W., Andersen, S. J. and Jansen J., 1997, *Science*, **277**, 1221.
- 75 Naoi, T., Matsuda, K., Sato, T., Kamio, A. and Ikeno, S., 1998, *Proceedings of the 6th International Conference on Aluminium Alloys ICAA6*, edited by T. Sato and S. Kumai, (Toyohashi: The Japan Institute of Light Metals), **2**, 861.
- 76 Hovmöller, S., 1992, *Ultramicroscopy*, **41**, 121.
- 77 Weirich, T. E., Ramlau, R., Simon, A., Hovmöller, S. and Zou, X., 1996, *Nature*, **382**, 144.
- 78 Stadelmann, P., 1987, *Ultramicroscopy*, **21**, 131.

Chapter 4 Microstructure of the WFA/Al₂O₃/sf and WFA/SiC/p Composites

- 79 Rappaz, M. and Gandin, Ch. A., 1993, *Acta Metall. Mater.*, **41**, 345.
- 80 Mortensen, A. and Jin, I., 1992, *Int. mater. rev.*, **37**, 101.
- 81 Gungor, M. N., Cornie, J. A. and Flemings, M. C. (1986) in *Interfaces in Metal-Matrix Composites*, ed. by A. K. Dhingra and S. C. Fishman, The Metallurgical Society, Inc., p.121.
- 82 Mondolfo, L. F. (1976), *Aluminium Alloys, Structures and Properties*, Butterworth, 1st edition, London.
- 83 Wang, R. W., Surappa, M. K., Tao, C. H., Li, C. Z. and Yan, M. G., 1998, *Mater. Sci. Engng*, **A254**, 219.
- 84 Rohatgi, P. K., (1986) in *Interfaces in Metal-Matrix Composites*, ed. by A. K. Dhingra and S. C. Fishman, The Metallurgical Society, Inc., p.185.
- 85 Lloyd D. J., Jin, I. and Weatherly, G. C., 1994, *Scripta Metall. Mater.*, **31**, 393.
- 86 Athana, R., 1998, *J. Mater. Sci.*, **33**, 1959.
- 87 Dudek, H. J., Kleine, A., Borath, R. and Neite, G., 1993, *Mater. Sci. Engng*, **A167**, 129.
- 88 Wang, S., Dudek, H. J., and Kaysser, W. A., 1995, *Z. Metallkd.*, **86(2)**, 141.
- 89 Wang, S., and Dudek, H. J. 1996, *Mater. Sci. Engng*, **A205**, 180.
- 90 Lee, J.-C., Kim, G.-H., Lee, J.-i., and Lee, H.-I., 1997, *Metall. Mater. Trans.*, **28A**, 1251.
- 91 Han, D. S. , Jones, H. and Atkinson, H. V. , 1993, *J. Mater. Sci.*, **28**, 2654.
- 92 Iseki, T., Kameda, T. and Maruyama, T. , 1984, *J. Mater. Sci.*, **19**, 1692
- 93 Lin, R. Y. , 1995, *Key Engng Mater.*, **104-107**, 507.
- 94 Peteves, S. D. , Tambuyser, P. , Helbach, P. , Audier, M. , Laurent, V. and Chatain, D.,1990, *J. Mater. Sci.*, **25**, 3765.
- 95 Noble, B.,Trowsdale, A. J. and Harris, S. J.,1997, *J. Mater. Sci.*, **32**, 5969.
- 96 Lee, J. C. , Byun, J. Y. , Park, S. B. and Lee, H. I. ,1998, *Acta Mater.*, **46**, 1771.
- 97 Kannikeswaran, K. and Lin, R. Y. , 1987, *JOM*, **39**, 17.

BIBLIOGRAPHY

- 98 Viala, J. C. , Fortier, P. and Bouix, J., *J. Mater. Sci.*, 1990, **25**, 1842.
- 99 Barin, I. , (1989), *Thermochemical Data of Pure Substances*, VCH, Weinheim.
- 100 Cui, Y. , Geng, L. and Yao, C. K., 1997, *J. Mater. Sci. Letters*, **16**, 788.
- 101 Weiland, A., Hultman, L., Wahlström, U., Persson, C. and Johannesson, T., 1998, *Acta Mater.*, **46**, 5271.
- 102 Johnson, P. K. , Rehman, F. U. , Fox, S. , Flower, H. M. and West, D. R. F. , *Mater. Sci. Forum*, 1995, **189-190**, 291.
- 103 Knacke, O., Kubaschewski, O. and Hesselmann, H., (1991) *Thermochemical Properties of Inorganic Substance*, Springer-Verlag, Berlin.
- 104 Lupis, C. H., (1983), *Chemical Thermodynamics of Materials*, Elsevier Science Publishing Co., New York.
- 105 Cayron, C., Hertz, J., Buffat, P. A. and Beffort, O., to be published in *J. Mater. Sci.*
- 106 Cayron, C., Long, S., Buffat, P. A. and Beffort, O., Unpublished results.
- 107 Romero, J. C. and Arsenault, R. J., 1995 , *Acta Metall. Mater.*, **43**, 849.
- 108 Jepps, N. W. and Page, T. F., (1983), *Progress in Crystal Growth and Characterization vol. 7*, ed. by P. Krishna, Pergamon Press, pp. 259-307.
- 109 Peteves, S. D. , Tambuyser, P. , Helbach, P. , Audier, M. , Laurent, V. and Chatain, D. , 1990, *J. Mater. Sci.*, **25**, 3765.
- 110 Laird, C. and Aaronson, H. I., 1968, *Trans. Metall. Soc. AIME*, **242**, 1383.
- 111 Hull, D., (1975), *An Introduction to Dislocations*, 2^d ed., Pergamon Press Ltd., Oxford, pp. 79-81.
- 112 Rosenbaum, H. S., and Turnbull, D., 1958, *Acta metall.*, **6**, 653.
- 113 Dubost, B., Bouvaist, J. and Reboul, M., 1986, *Proceedings of the 1st International Conference on Aluminium Alloys*, ed. by E. A Starke and T. H. Sanders. p.° 1109.
- 114 Sagalowicz, L., Lapasset, G., and Hug, G., 1996, *Phil. Mag. Letters*, **74**, 57.
- 115 Vivas, M., Lours, P., Levailant, C., Couret, A., Casanove, M. J. and Coujou, A., 1997, *Mater. Sci. Engng*, **A234-236**, 664.
- 116 Vivas, M., Lours, P., Levailant, C., Couret, A., Casanove, M. J. and Coujou, A., 1997, *Phil. Mag. A*, **76**, 921.
- 117 Polmear, I. J. (1995). *Light Alloys. Metallurgy of the Light Metals*, Arnold, London.

Chapter 5 Introduction to Order-Disorder Transitions

- 118 Rao, C. N. R. and Rao, K. J. (1978), *Phase Transitions in Solids: an approach to the study of the chemistry and physics of solids*, McGraw-Hill, New York.
- 119 Tolédano, J. C. and Tolédano, P., (1987), *The Landau theory of Phase Transitions*, World Scientific, Singapore.
- 120 Tol dano, P., Dmitriev, V. (1996), *Reconstructive Phase Transition in Crystals and Quasicrystals*, World Scientific, Singapore.
- 121 Buerger, M. J., 1951, *Phase Transitions in Solids*, John Wiley, New York., p. 183.

BIBLIOGRAPHY

- 122 Landau, L. D., 1937, *Phys. Z. Sowjetunion*, **11**, 26.
- 123 Ising, E., 1925, *Z. Phys.*, **31**, 253.
- 124 Onsager, L., 1944, *Phys. Rev.*, **65**, 117.
- 125 Chandler, D. (1987), *Introduction to Modern Statistical Mechanics*, Oxford University Press, Oxford.
- 126 Heermann, D. W. (1990), *Computer Simulation Methods in Theoretical Physics*, 2^d ed., Springer-Verlag, Berlin.
- 127 Metropolis, N., Rosenbluth, A. W., Rosenbluth, M. N., Teller, A. H. and Teller, E., 1953, *J. Chem. Phys.*, **21**, 108.
- 128 Ducastelle, F. (1991), *Order and Phase Stability in Alloys*, ed. by F. R. Boer and D. G. Pettifor, North Holland, Amsterdam.
- 129 Kanamori, J., 1966, *Prog. Theor. Phys.*, **35**, 16.
- 130 Kudo, T. and Katsura, S., 1976, *Prog. Theor. Phys.*, **56**, 435.
- 131 Careri, G. (1984), *Order and Disorder in Matter*, The Benjamin/Cummings Publishing Company, Inc., Reading, Massachusetts.
- 132 Wilson, K. G., 1979, *Scientific American*, **241(2)**, 140.
- 133 Hawking, S. W. (1998), *A Brief History of Time*, Updated and expanded 10th anniversary ed., Bantam Books, New York.
- 134 Bragg, W. L. and Williams, E. J., 1934, *Proc. Roy. Soc. (London)*, **A145**, 699.
- 135 Weiss, P., 1907, *J. Phys. Paris*, **6**, 661.
- 136 Bethe, H. A., 1935, *Proc. Roy. Soc. (London)*, **A150**, 1935.
- 137 Kikuchi, R., 1951, *Phys. Rev.*, **81**, 988.
- 138 Kikuchi, R., 1977, *J. Physique Colloq.*, **38**, p. 307 (C-7).
- 139 Wilson, K. G., 1972, *Phys. Rev. Lett.*, **28**, 584.
- 140 Scheika, W. (1956), *Disordered Alloys, Diffuse Scattering and Monte Carlo Simulations*, Springer-Verlag, Berlin.
- 141 Cowley, J. M. (1984), *Diffraction Physics*, 2^d ed., North-Holland, Amsterdam.
- 142 Welberry, T. R. (1998), *Lectures on Diffuse X-ray Scattering and Disorder*, Troisième cycle de la physique en Suisse Romande, Lausanne.
- 143 Withers, R. L., Proffen, Th. and Welberry T. R., 1999, *Phil. Mag. A.*, **79**, 753.
- 144 Cusack, N. E. (1987), *The Physics of Structurally Disordered Matter, an Introduction*, ed. by D. G. Brewer, Graduate Student Series in Physics, IOP Publishing Ltd.
- 145 Van Dyck, D., Van Tandeloo, G. and Amelinckx, S., 1982, *Ultramicroscopy*, **10**, 263.
- 146 Horiuchi, S., 1982, *Ultramicroscopy*, **10**, 229.
- 147 Shindo, D. and Hiraga, K. (1998), *High-Resolution Electron Microscopy for Materials Science*, Springer-Verlag, Tokyo.
- 148 Hata, S., Matsumura, S., Kuwano, N. and Oki, K., 1998, *Acta mater.*, **46**, 881.
- 149 Hiraga, K., Hirabayashi, M., Terasaki, O. and Watanabe, D., 1982, *Acta Cryst.*, **A38**, 269.

BIBLIOGRAPHY

- 150 Terasaki, O., Watanabe, D., Hiraga, K., Shindo, D. and Hirabayashi, M., *J. Appl. Cryst.*, **14**, 392.

Chapter 6 Order-Disorder Transition in the AlCuMgSi and AlMgSi Alloys

- 151 Sagalowicz, L., Lapasset, G., and Hug, G., 1996, *Phil. Mag. Letters*, **74**, 57.
- 152 Arnberg, L. and Aurivillius, B., 1980, *Acta. Chem. Scand.*, **A 34**, 1.
- 153 Cayron, C., Sagalowicz, L., Beffort, O. and Buffat, P. A., 1999, *Phil. Mag. A*, **79**, 2833.
- 154 Dubost, B., Bouvaist, J. and Reboul, M., 1986, *Proceedings of the 1st International Conference on Aluminium Alloys*, ed. by E. A. Starke and T. H. Sanders. p. 1109.
- 155 Dumolt, S. D., Laughlin, D. E., and Williams, J. C., 1984, *Scr. Metall.*, **18**, 1347.
- 156 Matsuda, K., Uetani, Y., Anada, H., Tada, S. and Ikeno, S., 1992, *Proceedings of the 3rd International Conference on Aluminium Alloys*, edited by L. Arnberg, O. Lohne, E. Nes and N. Ryum, **1**, 272.
- 157 Edwards, G. A., Stiller, K. and Dunlop, G. L., 1994, *Appl. Surf. Sci.*, **76/77**, 219.
- 158 Naoi, T., Matsuda, K., Sato, T., Kamio, A. and Ikeno, S., 1998, *Proceedings of the 6th International Conference on Aluminium Alloys ICAA6*, edited by T. Sato and S. Kumai, (Toyohashi: The Japan Institute of Light Metals), **2**, p. 861.
- 159 Matsuda, K., Sakaguchi, Y., Miyata, Y., Uetani, Y., Sato, T., Kamio, A. and Ikeno, S., 2000, *J. Mater. Sci.*, **35**, 179.
- 160 Andersen, S. J., Zandbergen, H. W., Jansen, J., Trholt, C., Tundal, U. and Reiso, O., 1998, *Acta Mater.*, **46**, 3283.
- 161 Jacobs, M. H., 1972, *Phil. Mag.*, **26**, 1.
- 162 Epicier, T., Guichon, G., Dafir, D. and Merle, P., 1993, *Mater. Sci. Forum*, **126-128**, 121.
- 163 Edwards, G. A., Stiller, K., Dunlop, G. L. and Couper, M. J., 1998, *Acta Mater.*, **46**, 3893.
- 164 Tsuda, K. and Tanaka, M., 1995, *Acta Cryst.*, **A51**, 7.
- 165 Press, W. H., Teukolsky, S. A., Vetterling, W. T. and Flannery, B. P., (1992), *Numerical Recipes in C.*, Cambridge Press University, Cambridge, p. 499.
- 166 Lodgaard, S. and Ryum, N., 2000, *Mater. Sci. Engng*, **A283**, 144.
- 167 Cayron, C. and Buffat, P. A., 2000, *Acta mater.*, **48**, 2639.
- 168 Megaw, H. D. (1973), *Crystal Structures, a Working Approach*, ed. by R. Stevenson and M. A. Whitehead, W. B. Saunders, Philadelphia, PA, pp. 312-316.
- 169 Kanamori, J., 1984, *J. Phys. Soc. Japan*, **53**, 250.
- 170 Buffat, P. A. and Borel, J. P., 1975, *Phys. Rev. A*, **13**, 2287.
- 171 Jaccard, J., Kanzig, W. and Peter, M., 1953, *Helv. Phys. Acta*, **26**, 521.
- 172 Zhong, W. L., Wang, Y. G., Zhang P. L. and Qu, B. D., 1994, *Phys. Rev. B.*, **50**, 698.

BIBLIOGRAPHY

Annex A

Electronic Diffusion Factor, Radial Potential, Projected Potential

A.1 Inversion of the Diffusion Factor Formula

The electronic diffusion factor is the 3-D Spatial Fourier Transform of the atomic potential

$$f^e(\mathbf{u}) = \int V(\mathbf{r}) \exp[2\pi i \mathbf{u} \cdot \mathbf{r}] d\mathbf{v} \quad (\text{A.1})$$

If we assume that the atomic potential is radial $V(\mathbf{r}) = V(r)$, the integration can be calculated in the following way:

$$\begin{aligned} f^e(u) &= \int V(r) \exp[2\pi i \mathbf{u} \cdot \mathbf{r}] d\mathbf{v} \\ &= 2\pi \int_{r=0}^{\infty} \int_{\theta=-\pi/2}^{\pi/2} V(r) r^2 \exp[2\pi i u r \cos \theta] d\cos \theta dr \\ &= 2\pi \int_{r=0}^{\infty} V(r) r^2 \frac{\sin[2\pi u r]}{\pi u r} dr \end{aligned} \quad (\text{A.2})$$

This formula has been used by Doyle and Turner to calculate the atomic diffusion factors $f^B(u) = K_0 \int V(r) \exp[2\pi i \mathbf{u} \cdot \mathbf{r}] d\mathbf{v} = K_0 f^e(u)$ from the numeral values of the atomic potentials given by relativist Hartree-Fock calculations [A.1]. $K_0 = 2, m_0 e / h^2$ is an electron-atom interaction constant. These values have been interpolated by a sums of 4 Gauss functions $a_i \exp[-b_i u^2]$ by Doyle and Turner [A.2] or by a sum of 6 functions $a_i (1 - \exp[-b_i u^2]) / u^2$ by Weickenmeier and Kohl [A.3]. Since these analytical interpolation functions are easy to find in literature [A.4], which is not the case for the atomic potentials, we decided to use them to calculate the atomic potential. Therefore, we have inverted equation (A.2) :

$$\begin{aligned} f^e(u) &= 2\pi \int_{r=0}^{\infty} V(r) r^2 \frac{\sin[2\pi u r]}{\pi u r} dr \\ \frac{1}{2\pi} u f^e(u) &= \int_{r=0}^{\infty} V(r) r^2 \frac{\sin[2\pi u r]}{\pi r} dr \end{aligned} \quad (\text{A.3})$$

applying the Parseval theorem on \mathfrak{R}^+ (pair functions),

with $\mathfrak{S} \frac{\sin[2\pi ur]}{\pi r} = \mathfrak{S}^{-1} \frac{\sin[2\pi ur]}{\pi r} = \text{slit}(r, u)$ ($\mathfrak{S} = \mathfrak{S}^{-1}$ because $\frac{\sin[2\pi ur]}{\pi r}$ is a real pair function), it follows that

$$\begin{aligned} \frac{1}{2\pi} u f^e(u) &= \int_{r=0}^{\infty} \mathfrak{S}[V(r)r^2] \text{slit}(r, u) du \\ &= \int_{r=0}^u \mathfrak{S}[V(r)r^2] du \end{aligned} \quad (\text{A.4})$$

therefore
$$\mathfrak{S}[V(r)r^2] = \frac{1}{2\pi} \frac{d}{du} [u f^e(u)] \quad (\text{A.5})$$

so that

$$\begin{aligned} V(r) &= \frac{1}{2\pi r^2} \mathfrak{S}^{-1} \frac{d}{du} [u f^e(u)] \\ &= \frac{1}{2\pi r^2} 2\pi i r \mathfrak{S}^{-1} [u f^e(u)] \\ &= \frac{-1}{2\pi r} \frac{d}{dr} \mathfrak{S}^{-1} [f^e(u)] \end{aligned} \quad (\text{A.6})$$

and since $f^e(u)$ is a real pair function, it follows that $\mathfrak{S}^{-1} = \mathfrak{S}$, and if we note the Fourier Transform with the \sim :

$$V(r) = \frac{-1}{2\pi r} \frac{d}{dr} f^{\sim}(r) \quad (\text{A.7})$$

A.2 Radial Atomic Potentials Deduced from Doyle and Turner Diffusion Factors Fit

Equation (A.7) allows us to calculate the radial potential of atoms with the electronic diffusion factors from the atomic diffusion factors calculated by Doyle and Turner $f_{DT}^B(u)$

$$V(r) = \frac{-1}{2\pi K_0 r} \frac{d}{dr} f^{\sim}(r) \quad (\text{A.8})$$

$$f_{DT}^B(s) = \sum_{i=1}^4 a_i \exp[-b_i s^2] \quad (\text{A.9})$$

with $s = u/2$

$$f_{DT}^B(u) = \sum_{i=1}^4 a_i \exp\left[-\frac{b_i u^2}{4}\right] \quad (\text{A.10})$$

$$V(r) = \frac{1}{K_0} \sum_{i=1}^4 \left(\frac{4\pi}{b_i}\right)^{3/2} a_i \exp\left[-\frac{4\pi^2 r^2}{b_i}\right] \quad (\text{A.11})$$

Since no thermal effect has been included in the expression (A.11) of the potentials ($T = 0$ K), these ones are very sharp. The thermal effect can be included by multiplying equation (A.9) by $\exp[-Bs^2]$, where B the Debye-Waller factor defined by $B = 8, \langle u^2 \rangle$ with $\langle u^2 \rangle$ the mean square thermal vibration amplitude. Therefore, *thermal diffuse scattering* (TDS) is straight included by replacing the b_i factors by $b_i + B$ in (A.11). Equation (A.11) has also been given by Peng after applying the inverse Fourier Transform on the particular expression (A.9) [A.5]. Radial potentials with and without thermal effects ($B = 0.3 \text{ \AA}^2$) are represented for Mg, Al, Si and Cu in Fig. A.1.

A.3 Calculus of the Projected Potentials

The projected potentials in (x, y) along z are calculated by

$$V_p(x, y) = \int_{-\infty}^{\infty} V(x, y, z) dz \quad (\text{A.12})$$

$$\begin{aligned} \text{with } x^2 + y^2 + z^2 = r^2 &\Rightarrow 2zdz = 2rdr \\ &= 2 \int_{\sqrt{x^2+y^2}}^{\infty} \frac{rV(r)}{z} dr \end{aligned}$$

so that

$$V_p(x, y) = 2 \int_{\sqrt{x^2+y^2}}^{\infty} \frac{rV(r)}{\sqrt{r^2 - (x^2 + y^2)}} dr \quad (\text{A.13})$$

A.4 Projected Atomic Potential Deduced from Doyle and Turner Diffusion Factors Fit

We have seen that the radial atomic potential deduced for the Doyle and Turner interpolation takes the form

$$V(r) = \sum_{i=1}^4 A_i \exp[-B_i r^2] \quad (\text{A.14})$$

with

$$\begin{cases} A_i = \frac{1}{K_0} \left(\frac{4\pi}{b_i} \right)^{3/2} a_i \\ B_i = \frac{4\pi^2}{b_i} \end{cases} \quad \text{with } b_i \text{ replaced by } b_i + B \text{ for thermal diffuse effects} \quad (\text{A.15})$$

noting $d = \sqrt{x^2 + y^2}$ and applying equation (A.13)

$$V_p(d) = \sum_{i=1}^4 \int_d^{\infty} \frac{2rA_i \exp[-B_i r^2]}{\sqrt{r^2 - d^2}} dr \quad (\text{A.16})$$

with a primitive of $\frac{2rA \exp[-B r^2]}{\sqrt{r^2 - d^2}}$ being $A \sqrt{\frac{\pi}{B}} \exp[-B r^2] \text{Erfc}[\sqrt{b(r^2 - d^2)}]$

knowing that $\text{Erfc}[0] = 0$ and $\text{Erfc}[\infty] = 1$, and it follows that

$$V_p(d) = \sum_{i=1}^4 A_i \sqrt{\frac{\pi}{B_i}} \exp[-B_i d^2] \quad (\text{A.17})$$

which can be directly express in function of the a_i and b_i coefficients

$$V_p(d) = \frac{4\pi}{K_0} \sum_{i=1}^4 \frac{a_i}{b_i} \exp\left[-\frac{4\pi^2}{b_i} d^2\right] \quad (\text{A.18})$$

with a_i, b_i the coefficients given by Doyle and Turner for the interpolation of the diffusion factors [A.2] and $1/K_0 = 47.877 \text{ V.}\text{\AA}^2$.

The projected potential are represented in 2D in Fig. A.1c and in 1D in Fig. A.2c. Equation (A.18) will be used for the simulations of diffuse scattering patterns by disordered particles.

A.5 References

- A.1 Doyle, P. A. and Turner, P. S., 1967, *Acta Cryst.*, **22**, 153.
- A.2 Doyle, P. A. and Turner, P. S., 1968, *Acta Cryst.*, **A24**, 390.
- A.3 Weickenmeir, A. and Kohl, H., 1991, *Acta Cryst.*, **A47**, 590.
- A.4 *International Tables for X-ray Crystallography, vol. IV* (1974), ed. by J. A. Ibers and W. C. Hamilton, International Union of Crystallography, Kynoch Press, Birmingham. Table 2.4.6A.
- A.5 Peng, M. G., 1999, *Micron*, **30**, 625.
- A.6 *International Tables for X-ray Crystallography, vol. III* (1974), ed. by J. A. Ibers and W. C. Hamilton, International Union of Crystallography, Kynoch Press, Birmingham. Table 3.3.3A.

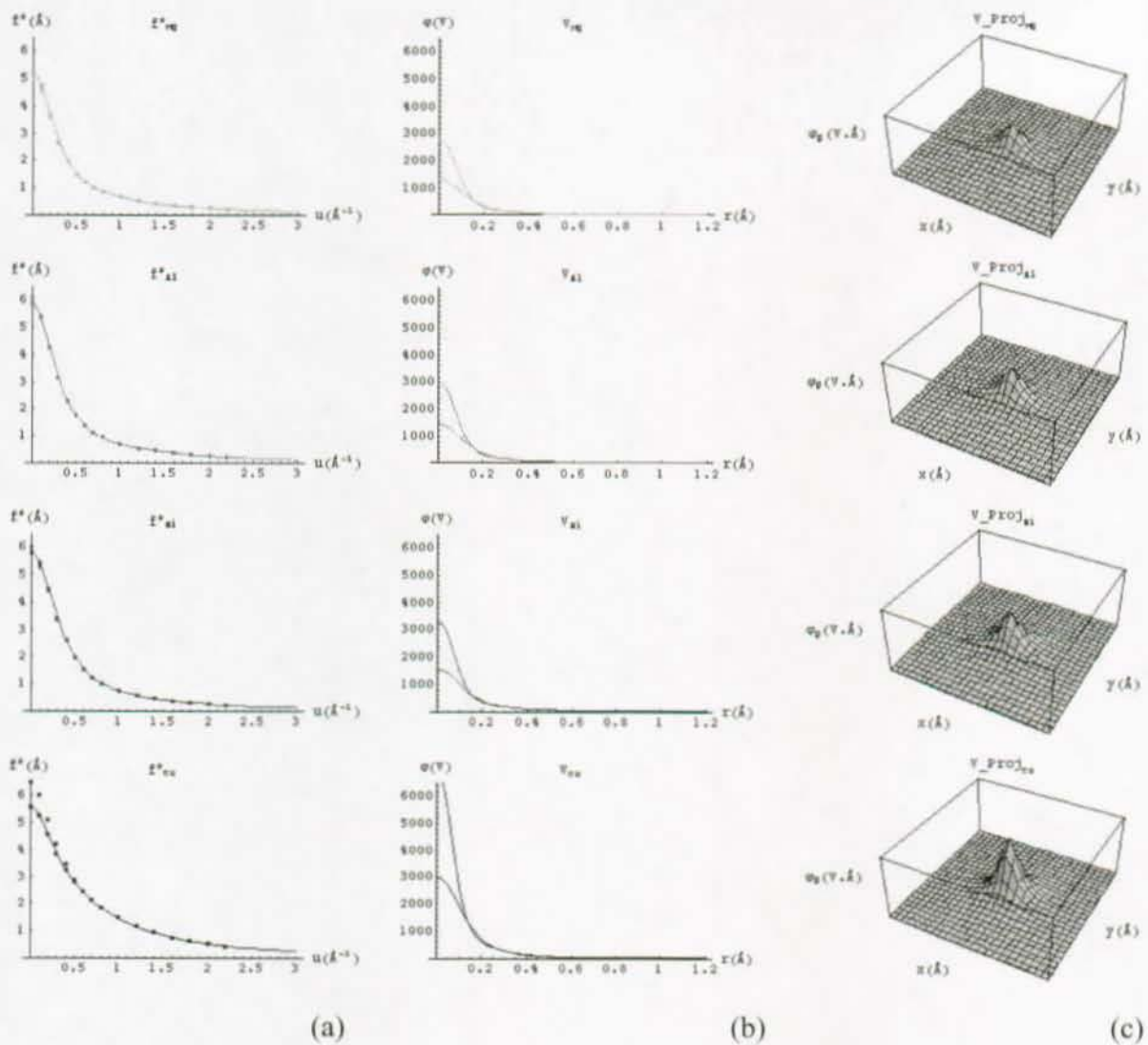
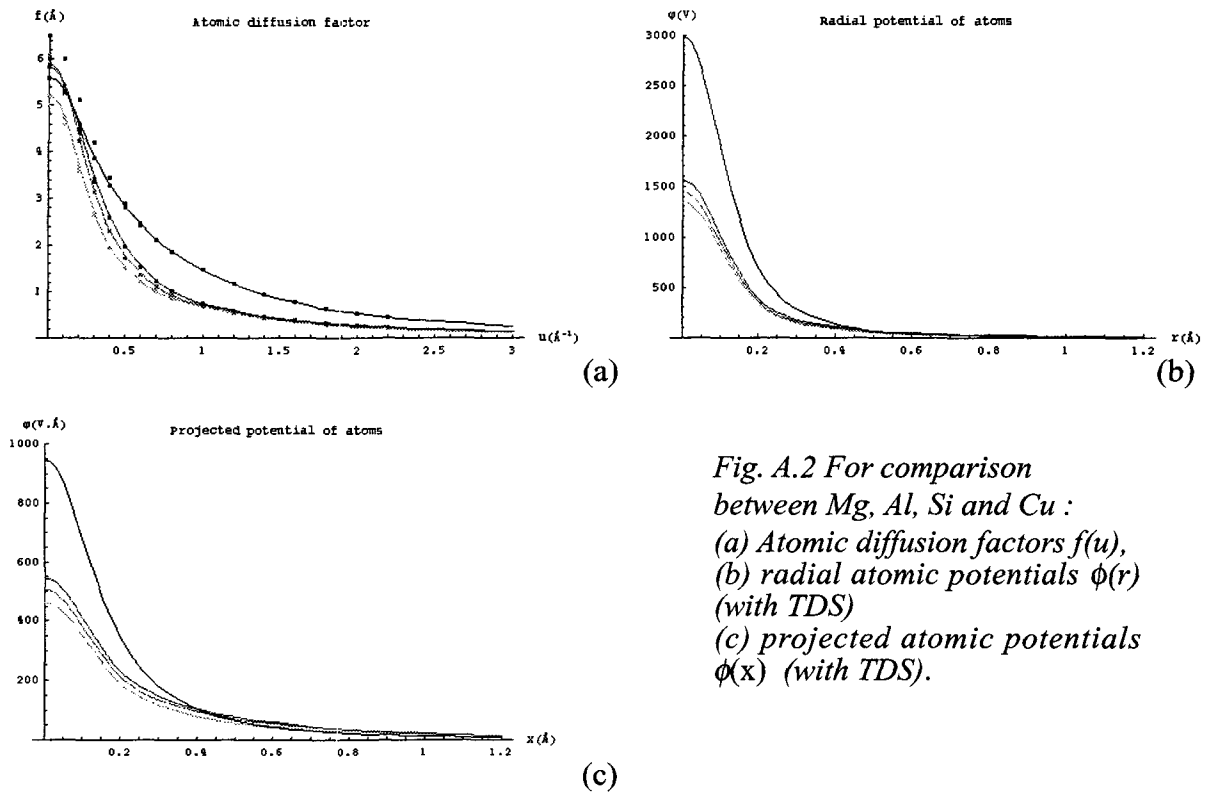


Fig. A.1 For Mg, Al, Si and Cu:

(a) Atomic diffusion factors $f(u)$: the upper serie of points have been deduced from X-ray sacttering factors by the Mott formula [A.6], the upper serie by Doyle and Turner[A.1, A.4], the line corresponds to the Doyle and Turner fit by a sum of 4 Gauss functions [A.2].
 (b) Radial atomic potentials $V(r)$ deduced from the Doyle and Turner fit. The upper/lower curves are respectively without/with TDS effect.
 (c) Projected atomic potentials $V(x,y)$ (with TDS).



*Fig. A.2 For comparison between Mg, Al, Si and Cu :
 (a) Atomic diffusion factors $f(u)$,
 (b) radial atomic potentials $\phi(r)$ (with TDS)
 (c) projected atomic potentials $\phi(x)$ (with TDS).*

Annex B

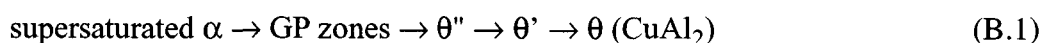
Precipitation in the 2xxx and 6xxx Aluminum Alloys

The 2xxx series, the 6xxx and the 7xxx (AlZnMg, AlZnMgCu) represent most of the heat-treatable aluminum alloys. These ones are widely used in building, construction, containers, packaging, electrical conductors and transportation. This annex presents the crystallographic information about the stable and metastable phases in the 2xxx and 6xxx aluminum alloys. The 2xxx are AlCu alloys possibly with Mg, Ag, Si, Fe, Cr, Zn, Ti. The 6xxx alloys are AlMgSi alloys possibly with Cu, Mn, Fe, Cr, Zn, Ti. This annex is based on the general Mondolfo's book about aluminum alloys [B.1], on the Lorimer's review paper [B.2], and on an up-to-date outline of age hardening in light alloys published by Polmear [B.3]; it also includes more recent works and our personal points of view.

B.1 Precipitation in the 2xxx Alloys

B.1.1 In the AlCu Alloys

Although there is some debate on the existence of various metastable precipitates in the first stage of precipitation, the most generally accepted aging sequence is:



- GP zones

Understanding of the precipitation sequence was not reached until two independent notes appeared side by side in *Nature*, by Guinier [B.4] and Preston [B.5] in 1938. They found from streaks observations by different X-ray techniques what is now called GP zones. In their models, Guinier and Preston analyzed the GP zones as Cu-rich thin platelets coherent with the $\{100\}_\alpha$ planes. Because of the smaller size of the Al and Cu atoms (with radius of 0.143 and 0.128 nm respectively), the matrix planes surrounding the GP zones collapse toward the Cu layers. More elaborated models were proposed by Gerold [B.6] and Toman [B.7]. Recent analyses by HREM confirm the Cu monolayer model [B.8] and an APFIM study precises that 50% of the layers contain 100% Cu, and the other more than 65% [B.9].

- θ''

The θ'' phase was firstly reported by Guignier [B.10] who observed that upon extended aging the streaks associated with GP zones developed intensity maxima. They are also called GPII. He proposed that θ'' is fully coherent with the matrix, with a tetragonal structure with $a =$

0.404 nm and $c = 0.79$ nm. The OR with the matrix is:

$$(100)_{\theta''} // (001)_{\alpha} \text{ and } [001]_{\theta''} // [001]_{\alpha} \quad (\text{B.2})$$

He was unsure whether the platelets were modifications of primary GP zones (GP II) or a separated phase θ'' . Baur reported that the structure of θ'' phase was consistent with a sequence of 1 copper layer and 3 aluminum layers, and that during aging at 130°C the c parameter of the precipitates decreased from 0.808 nm to 0.765 nm [B.11].

• θ'

The θ' phase has a distorted CaF_2 structure [B.12], tetragonal with $a = 0.404$ nm, $c = 0.58$ nm, with the following atomic positions:

Al (0,0,0), (0,0,1/2), (1/2,1/2,0), (1/2,1/2,1/2)

Cu (0,1/2,3/4), (1/2,0,1/4).

Its composition is CuAl_2 and the orientation relationship with the matrix is

$$(001)_{\theta'} // (001)_{\alpha} \text{ and } [001]_{\theta'} // [001]_{\alpha} \quad (\text{B.3})$$

It preferentially nucleates on $a/2 \langle 110 \rangle$ dislocations, which can act to relieve the misfit in two $\langle 100 \rangle_{\alpha}$ matrix directions. The initial distribution of θ' is highly heterogeneous and reflects the initial dislocation density in a particular grain. The nucleation and expansion is completely independent of GP zones or θ'' . The broad faces of θ' plates can remain fully coherent with the matrix even after extended aging. The precipitates present antiphase domain boundaries during their growing [B.13].

• θ - CuAl_2

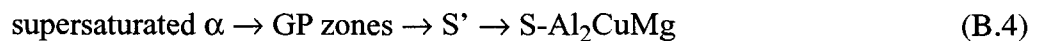
The equilibrium θ phase is BC tetragonal with $a = 0.6066$ nm and $c = 0.4874$ nm [B.14]. Guignier catalogued 5 ORs between θ precipitates and the Al matrix [B.15]. Laird and Aaronson reported that three reactions occur simultaneously during the dissolution θ' and the formation of θ crystals [B.16]:

- (1) θ was nucleated at α/θ' boundaries and then consumed the θ' plate,
- (2) θ once nucleated, grew into surrounding α ,
- (3) θ' dissolved while θ precipitates grew at some distance away.

A representation of the precipitation sequence is given in Fig. B.1 (from Ashby [B.17]).

B.1.2 In the AlCuMg Alloys

These alloys date from the accidental discovery of the phenomenon of age hardening by Alfred Wilm, working in Berlin in 1906. His work led to the production of an alloy known as Duralumin (Al-3.5Cu-0.5Mg-0.5Mn) used in aircraft industry. The Al-Cu-Mg alloy with a weight ratio of 2.2/1 forms the pseudo-binary aluminum-S system with the following precipitation sequence:



• GPB zones

The term GPB zones was introduced by Silcock [B.18] who showed that in quenched pseudo-binary alloys with a 7/1 Cu/Mg ratio, some zones are formed as cylinders along

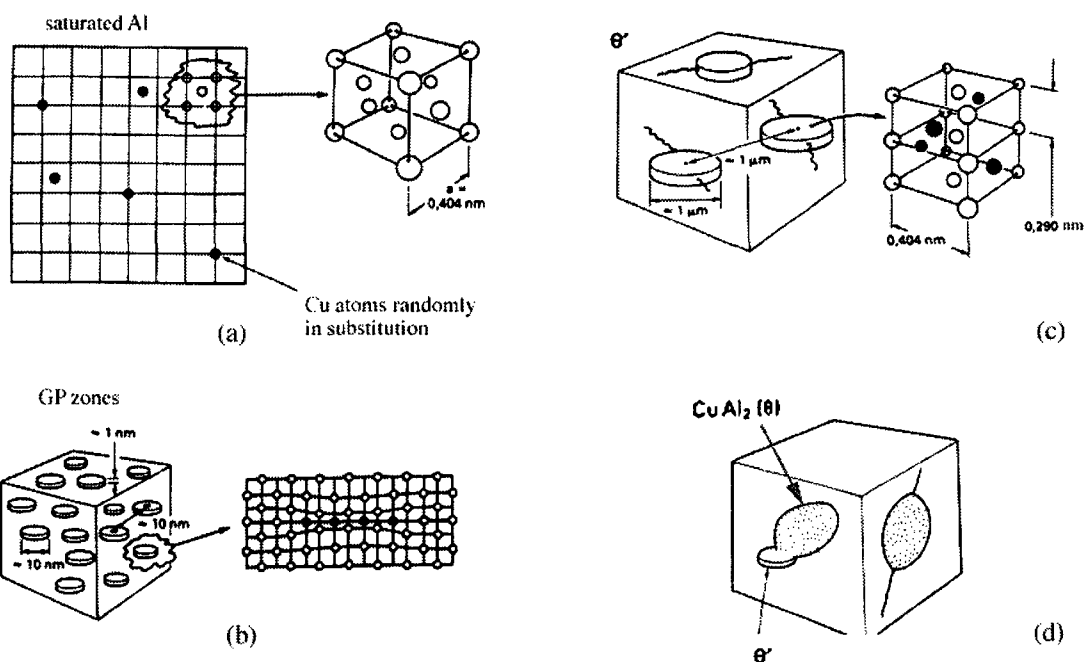


Fig. B.1 GP \rightarrow θ'' \rightarrow θ' \rightarrow θ precipitation sequence. (a) Cu atoms in a saturated Al matrix, (b) formation of the GP and θ'' zones, (c) nucleation and growth of the θ' plate, (d) dissolution of the θ' plates and appearance of the θ plates. From [B.17].

$\langle 100 \rangle_\alpha$ directions, 10-20 in diameter and 40 long. These zones are probably ordered clusters of Cu and Mg atoms. The observed zones were a mixture of those observed in Al-Cu alloys and those detected in the pseudo-binary aluminum (S). Charai has studied by HREM and calorimetry the first stage of precipitation [B.19], he made the distinction between atomic clusters firstly analyzed by APFIM by Ringer [B.20], the GPB zones and the S'' phase firstly reported by Bagaryatsky [B.21]. He concluded that S'' is an ordered form of the GPB zones. From their blurred HREM images, we actually think that S'' is disordered form of S', such as QP is a disordered form of QC or Q. This assumption is confirmed by the HREM study of Ratchev who showed that HREM images of disordered zones can be indexed by their FFTs as S'' [B.22]. As for the GP zones in 6xxx alloys, we seriously doubt about the existence of GPB zones (which by definition would not produce spots in the FFTs).

• $\underline{S'}$

S' is orthorhombic with $a = 0.404$ nm, $b = 0.925$ nm, $c = 0.718$ nm [B.23]. Slightly different parameters were given by Charai [B.19]. The OR with the matrix is:

$$[100]_{S'} // [100]_\alpha, [010]_{S'} // [021]_\alpha \text{ and } [001]_{S'} // [012]_\alpha \quad (\text{B.5})$$

S' precipitates heterogeneously nucleate on dislocations and grow as laths on $\{210\}_\alpha$ in $\langle 001 \rangle_\alpha$ directions.

• \underline{S} -CuMgAl₂

The S phase is orthorhombic with lattice parameters similar to those given for S': $a = 0.400$ nm, $b = 0.923$ nm, $c = 0.714$ nm [B.24]. Let us notice that these parameters are close to

a_α , $\sqrt{5} a_\alpha$ and $\sqrt{3} a_\alpha$. By HREM simulations, Radmilovic [B.25] proposed a crystallographic structure corresponding to a slight modification of a previous one found by Perlitz and Westgren from X-ray diffraction [B.24]. Weatherly and Nicholson concluded that the loss of coherency of the laths is due to the attraction of a matrix dislocation to the lath followed by the formation of an array of loops with Burgers vectors of the type $a/2 \langle 101 \rangle$ spaced along the lath [B.26].

- σ -Al₅Cu₆Mg₂

This phase was firstly reported by Weatherly in an Al-2.7Cu-1.36Mg-0.2Si alloy [B.27]. It was later reported by Schueller in Al-4.3Cu-1.36Mg/SiC composites [B.28]. This phase can also be obtained in Al alloys without Si such as Al-3.2Cu-0.45Mg-0.4Ag alloys [B.29]. Actually, it seems that it needs Ag or Si to nucleate. Since its coarsening is lower than the for θ' , this phase could be used to harden the Al alloys. Its structure is cubic with $a = 0.831$ nm [B.30]. The OR is

$$[100]_\sigma // [100]_\alpha \text{ and } (010)_\sigma // (021)_\alpha \quad (\text{B.6})$$

It appears as cubes easily identifiable from the moiré fringes along the $\langle 100 \rangle_\alpha$ directions (see Fig. 4.21 for instance).

B.1.3 In the AlCuMgAg Alloys

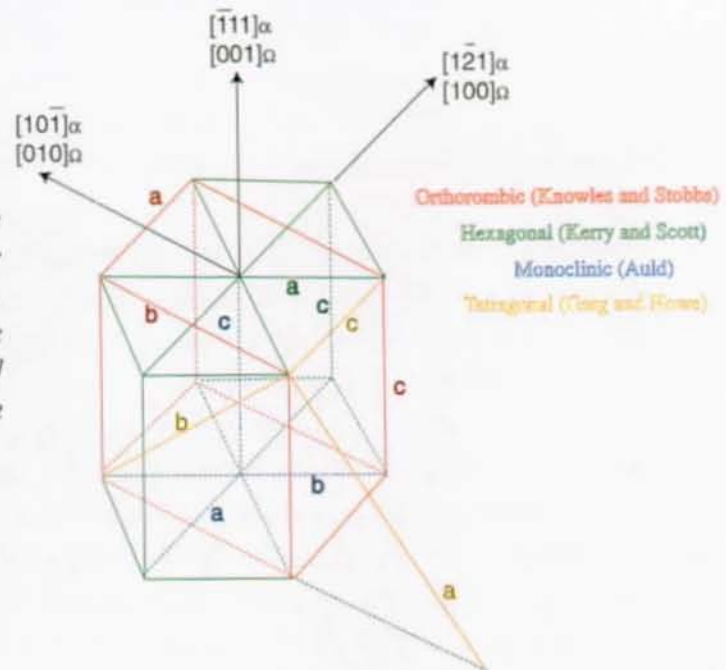
- Ω -CuAl₂

In 1966 Polmear and coworkers showed that the precipitation state of Al-Cu-Mg alloys, with compositions in the $\alpha+\theta+S$ or $\alpha+\theta$ regions of the phase diagram, is modified by the addition of Ag: in addition to θ' another phase named Ω is formed [B.31, B.32] (they firstly thought that the phase was the T-Al₆CuMg₄ phase). This phase is detectable at very early stages of aging and emerges as thin hexagonal plates parallel to $\{111\}_\alpha$ planes. It improves the mechanical properties (strength, stress corrosion) at high temperature due to its high thermal stability. Its chemistry is very close to CuAl₂, Mg and Ag would be required to favor the nucleation of the phase, as confirmed by the APFIM study of Murayama [B.33]. The growing of this phase and the role of Ag has been studied by Hutchinson using Z-contrast microscopy [B.34]. The structure of Ω phase has proven to be controversial: the phase is hexagonal for Kerry and Scott [B.35], monoclinic for Auld [B.36], orthorhombic for Knowles and Stobbs [B.37] confirmed by Muddle and Polmear [B.38]. More recently a tetragonal structure corresponding to a slight modification of the stable θ -CuAl₂ structure was proposed by Howe and coworkers [B.39], and they proposed other names such as θ_M [B.39] or $\theta_{\{111\}}$ [B.40]. The lattice parameters of the FC orthorhombic structure are $a = 0.496$ nm, $b = 0.859$ nm, $c = 0.848$ nm. We can notice that the parameters are close to $\sqrt{3}/2 a_\alpha$, $\sqrt{9}/2 a_\alpha$ and $3/2 a_\alpha$. The OR is:

$$(001)_\Omega // (111)_\alpha \text{ and } [010]_\Omega // [101]_\alpha \quad (\text{B.7})$$

If we look at the four proposed structures and the lattice parameters given by the authors, we must be aware that the proposed lattices in fact are identical as shown in Fig. B.2: it is only the symmetry given by atomic positions in the unit cell which changes the point group.

Fig. B.2 Representation of the different unitary cells proposed for the Ω phase. Orthorhombic [B.37], hexagonal [B.35], monoclinic [B.36] or tetragonal [B.39] structures are based on the same lattice.



B.1 Precipitation in the 6xxx Alloys

AlMgSi alloys are widely used as medium-strength structural alloys which have the additional advantages of good weldability, corrosion resistance and immunity to stress corrosion cracking. They are used as the majority of extrusions, with smaller quantities being available as sheet and plate. We can distinguish two groups, the first one with balanced Mg/Si ratio (Mg and Si between 0.8 and 1.2%) and the second one with Si in excess. An addition of 0.25% Cu improves their mechanical properties, even if 0.2% Cr is required to offset the adverse effect that Cu may have in the corrosion resistance.

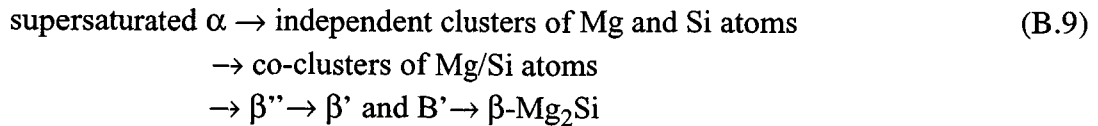
B.1.1 Without Si in Excess

The sequence of precipitation was firstly investigated by TEM by Thomas [B.41] and Pashley [B.42]. The often reported precipitation sequence [B.2] is



GP zones were firstly reported by Geisler and Hill [B.43], Guinier and Lambot [B.44] and Lutts [B.45] with X-ray diffraction techniques. Their existence is now seriously questioned after the works of Edwards [B.46], Bigot [B.9], Ringer [B.47], and Murayama [B.48]. Indeed, these authors showed by APFIM that the pre-precipitation zones are actually clusters of Mg atoms, clusters of Si atoms, and further during the aging co-clusters of Mg/Si atoms with Mg/Si \approx 1. Recently, Edwards proposed another precipitation sequence for a 6061 alloys

(containing 0.18%Cu) [B.49]:



The B' comes from the presence of Cu, as it will be shown in section B.1

• β''

This phase takes the form of rod-shaped precipitates along the $\langle 100 \rangle_\alpha$ directions. It was also called GPII, but this name is not appropriated since it has a structure different from Al. The name β'' and the transformation $\beta'' \rightarrow \beta'$ was firstly introduced by Shchegoleva from a X-ray study in 1968 [B.50]. She determined its structure to be monoclinic with $a = b = 0.616$ nm, $c = 0.71$ nm and $\beta = 82^\circ$. This structure was confirmed by TEM by Wahi and von Heimendahl in 1974 [B.51]. Nevertheless, it exists in their article a great confusion between the name they gave and the actual names which are now usually used. They thought that β' had a structure very close to the stable β . They found it tetragonal with $a = 0.642$ nm and $c = 0.646$ nm, and therefore refused the β' structure proposed by Jacobs in 1972 [B.57], which is now widely accepted and checked by modern TEM and HREM techniques. In consequence, their idea of what we call now β' is wrong and we think that even the well accepted $\beta'' \rightarrow \beta'$ they proposed should be checked by in-situ TEM experiments. Moreover, many structures now given for β'' , and all of them in agreement together (even if the parameters of the unit cell sometimes are multiple from one author to other) differ from the one proposed by Shchegoleva and Wahi. The latest studies are even more convincing (clear SAED and HREM images) than the Shchegoleva's X-ray results and the short Wahi's TEM study. Let us give some of the structures recently proposed:

Lynch [B.52]	monoclinic	$a = 0.30$ nm, $c = 0.33$ nm, $b = 0.40$ nm, $\beta = 71^\circ$
Edwards [B.53]	based centered monoclinic	$a = 1.534$ nm, $c = 0.689$ nm, $b = 0.405$ nm, $\beta = 106^\circ$
Murayama [B.54]	monoclinic	$a = 0.714$ nm, $c = 0.658$ nm, $b = 0.405$ nm, $\beta = 75^\circ$
Naoi [B.55]	monoclinic B2/m	$a = 0.77$ nm, $c = 0.67$ nm, $b = 0.203$ nm, $\beta = 75^\circ$
Andersen [B.56]	monoclinic C2/m	$a = 1.516$ nm, $c = 0.674$ nm, $b = 0.405$ nm, $\beta = 105.3^\circ$

In the Andersen's study, a crystallographic structure with the atomic positions was proposed from exit wave reconstructed images. However, we think that confirmations by other methods are required, as explained in section 3.7.2. The OR is

$$[001]_{\beta''} // [310]_\alpha, [100]_{\beta''} // [230]_\alpha \text{ and } [010]_{\beta''} // [001]_\alpha \quad \text{(B.10)}$$

Edwards reported from APFIM measurements that the composition has an [Mg]/[Si] ratio smaller than the one of the stable β phase, between 1 and 1.2 even if preferential evaporation of the Mg is suspected to have slightly decreased the ratio [B.46]. After extraction of one of the β'' precipitate from the matrix, Naoi reported from EDS measurements that the phase contains a high content of Al, and gave the ratios Si:Al:Mg = 6:3:1 [B.55]. A deep study of the chemical composition by APFIM [B.9] confirms the presence of Al in the precipitates (50% which decreases to 30% during aging), and reports [Mg]/[Si] ratio close to 1.6.

• β'

This phase takes also the form of rod-shaped precipitates along the $\langle 100 \rangle_\alpha$ directions (the section can be elliptic or rectangular). By a detailed TEM study, Jacobs proposed in 1972 a hexagonal structure for the β' phase with $a = 0.705$ nm and $c = 0.405$ nm [B.57]. As explained before, this structure is now confirmed by HREM images [B.58, B.49] and widely accepted. In 1991, Matsuda proposed a crystallographic structure for β' and explained that its a lattice parameter should be at 0.407 nm [B.59]. He checked that his structure was in agreement with the positions of the SAED spots (not the intensities). Nevertheless, the structure he proposed has actually a lattice parameter of 0.705 nm (he misunderstood how to determine the unit cell). Moreover, even if we accept his structure with the correction $a = 0.705$ nm, this one seems very unrealistic due to the very large interatomic distances between the atoms. From the present work, a crystallographic structure has been proposed for β' in agreement with quantitative microdiffraction patterns and HREM images (section 6.3). Two ORs were found:

$$(100)_{\beta'} // (100)_\alpha \text{ and } [001]_{\beta'} // [001]_\alpha \quad (\text{B.11})$$

$$(100)_{\beta'} // (110)_\alpha \text{ and } [001]_{\beta'} // [001]_\alpha \quad (\text{B.12})$$

The chemical composition of this phase seems to be variable. Matsuda reported $[\text{Mg}]/[\text{Si}] \approx 1.68$ [B.61], whereas Edwards reported $[\text{Mg}]/[\text{Si}] \approx 1-1.2$ [B.46].

• β - Mg_2Si

The equilibrium phase is FCC with the CaF_2 structure with a lattice parameter of $a = 0.639$ nm. Jacobs [B.57] found that β phase is formed as platelets on the $\{100\}_\alpha$ planes with the OR:

$$(001)_\beta // (100)_\alpha \text{ and } [110]_\beta // [100]_\alpha \quad (\text{B.13})$$

It is now widely accepted that the phase is formed after dissolution of the β' phase, and does not correspond to a modification of the β' phase, which can be explained by the fact that these two phases have completely different crystallographic structures.

• u-phase

This phase has been recently reported by Lodgaard and Ryum [B.62]. It nucleates on the β' needles during heating at 580°C, the typical homogenization temperature. It takes the form of rod-shaped precipitates along the $\langle 100 \rangle_\alpha$ directions. Its structure is hexagonal with $a = 0.670$ nm and $c = 0.808$ nm. Its OR is

$$[100]_u // [100]_\alpha \text{ and } [001]_u // [001]_\alpha \quad (\text{B.14})$$

This phase contains Si, Al, Mg, but also Mn and Fe. We actually think that its structure could be very similar to the QC structure [B.74], with Mn and Fe in the interstitial sites (section 6.3.1).

B.1.2 With Si in Excess

The metastable phases in an Al-1%Mg₂Si-0.4%Si alloy have been extensively investigated by TEM, HREM and EDS chemical analyses by Matsuda [B.60, B.61]. Matsuda

reported three phases in addition to the β' phases taking also the form of rod-shaped precipitates along the $\langle 100 \rangle_\alpha$ directions.

- type-A

A complete TEM analysis of this phase, after extraction of one the precipitate from the Al matrix, is given in [B.63]. Matsuda reported a hexagonal structure with $a = 0.405$ nm and $c = 0.67$ nm. Nevertheless, the crystal structure he proposed in [B.61] is fanciful. The OR is

$$\bar{1}(20)_A // (001)_\alpha \text{ and } ([001]_A, [001]_\alpha) = 20^\circ \quad (\text{B.15})$$

The chemical composition he reported is Si:Al:Mg = 5:4:1.

- type-B

Matsuda reported in [B.64] a structure orthorhombic with $a = 0.684$ nm, $b = 0.793$ and $c = 0.405$ nm. However, the crystal structure he proposed in [B.61] is also fanciful. The OR is

$$(001)_B // (001)_\alpha \text{ and } ([010]_B, [010]_\alpha) = 20^\circ \quad (\text{B.16})$$

The chemical composition he reported is Si:Al:Mg = 5:4:2. This type-B phase is in agreement with the rectangular centered arrangement ($b \approx 0.8$ nm, $a \approx 0.7$ nm) found by Sagalowicz on a phase that he called L [B.65].

- type-C

The type-C phase was reported by Matsuda in 1996 [B.60]. Its structure is hexagonal with $a = 1.04$ nm and $c = 0.405$ nm. The OR is

$$(001)_B // (001)_\alpha \text{ and } ([\bar{2}10]_B, [100]_\alpha) = 10^\circ \quad (\text{B.17})$$

Actually this phase is the same that the one reported by Sagalowicz in 1996 and called M [B.66]. Matsuda reported a ratio $[\text{Si}]/[\text{Mg}] \approx 1.2$. It was clearly shown by EDS measurements by Matsuda and Sagalowicz that this phase does not contain Cu. That is why they gave it an other name than B' found by Dumolt in 1984 [B.67], a phase that has the same structure and may contain Cu (but we do not think so). As shown during our work, we also think that this phase is similar to the stable Q-Al₅Cu₂Mg₈Si₆ phase, but without Cu (section 6.2.3).

B.1 Precipitation in the AlCuMgSi Alloys

The stable phases of the quaternary alloy, such as θ and Si, are reported in a quaternary phase diagram (with 4% Cu) in Fig. 4.19. In the following, we will just give some information about the rod-shaped precipitates.

- Q'

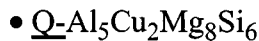
It is known from [B.68] and [B.69], that addition of Cu improves the mechanical properties of the 6xxx alloys by a refinement of their precipitation state. It was shown by Miao and Laughlin [B.70] that Cu induces the formation of lathlike Q precipitates and of its precursors called Q'. Actually, the rod-shaped precipitates in the 6xxx alloys that contain Cu are the same that those found in 2xxx alloys that contain Si. Dubost firstly reported that the AlCuMgSi rod-shaped precipitates are precursors of the stable Q-Al₅Cu₂Mg₈Si₆ phase, and he called these precipitates λ' [B.71]. Its structure is the same than the Q phase one, i.e.

hexagonal with $a = 1.03$ nm and $c = 4.04$ nm. Its OR is

$$(210)_{Q'} // (001)_{\alpha} \text{ and } [001]_{Q'} // [001]_{\alpha} \quad (\text{B.18})$$

In the present work we did not make the difference between Q' and Q as explained in section 6.2.2.

The real link between the β'' , β' phases and the λ' or Q phases was given during this study. We showed that in fact the precursors of the Q rods are QC and QP, such as the precursors of B' are β' and βP , the only difference between the two Q and β families being the Cu incorporated in the interstices of the QP clusters (chapter 6, [B.74] and [B.75]).



This phase is the stable phase of the AlCuMgSi alloys. It is known as $\underline{\text{Q}}$ [B.1], W, λ or h [B.72, B.73]. Its structure is known from X-ray studies: it is hexagonal P6 with $a = 1.03932$ nm and $c = 0.40173$ nm, the atomic positions are given in [B.73].

B.1 References

- B.1 Mondolfo, L. F. (1976), *Aluminium Alloys, Structures and Properties*, Butterworth, 1st edition, London.
- B.2 Lorimer, G. W., (1978), Precipitation in aluminum alloys in *Precipitation processes in Solids*, TMS-AIME Warrendale, PA, pp. 87-119.
- B.3 Polmear, I. J. (1995). *Light Alloys. Metallurgy of the Light Metals*, Arnold, London.
- B.4 Guinier, A, 1938, *Nature.*, **142**, 569.
- B.5 Preston, G. D., 1938, *Nature*, **142**, 570.
- B.6 Gerold, V., 1954, *Z. Metall.*, **45**, 593 & 599.
- B.7 Toman, K., 1957, *Acta cryst.*, **10**, 187.
- B.8 Karlik, M. and Jouffrey, B., 1997, *Acta mater.*, **8**, 3251.
- B.9 Bigot, A., 1998, *Etude par sonde atomique de la precipitation durcissante d'alliage d'aluminium des series 2xxx, 6xxx et 7xxx*, Thèse de doctorat, Faculté des Sciences de l'Université de Rouen.
- B.10 Guinier, A., 1952, *Acta cryst.*, **5**, 51.
- B.11 Baur, R., 1966, *Z. Metall.*, **57**, 181.
- B.12 Preston, G. D., 1938, *Phil. Mag.*, **26**, 855.
- B.13 Wheatherly, G. C., 1970, *Acta metall.*, **18**, 15.
- B.14 Bradley, A. J. and Jones, P., 1933, *J. Inst. Met.*, **51**, 131.
- B.15 Guinier, A., 1939, *Ann. Physique*, **12**, 161.
- B.16 Laird, C. and Aaronson, H. I., 1966, *Acta metall.*, **14**, 171.
- B.17 Ashby, M. F., Jones, D. R. H. (1996), *Materiaux*, Dunod.
- B.18 Silcock, J. M., 1961, *J. Inst. Metals*, **89**, 203.

- B.19 Charai, A., Walther, T., Alfonso, T., Zahra, A. M. and Zahra, C. Y., 2000, *Acta mater.*, **48**, 2751.
- B.20 Ringer, S. P., Sakurai, T., and Polmear, I. J., 1997, *Acta Mater.*, **45**, 3731.
- B.21 Bagaryatsky, Yu A., 1959, *Dokl. Akad. Nauk SSSR*, **50**, 568.
- B.22 Ratchev, P., Verlinden, B., De Smet, P. and Van Houtte, P., 1998, *Acta mater.*, **46**, 3523.
- B.23 Wilson, R. N., and Partridge, P. G., 1965, *Acta metall.*, **13**, 1321.
- B.24 Perlitz, H. and Westgren, A., 1943, *Ark. Kemi. Miner. Geol. B.*, **16**, 13.
- B.25 Radmilovic, V., Kilaas, R., Dahmen, U., and Shiflet G. J., 1999, *Acta mater.*, **47**, 3987.
- B.26 Weatherly, G. C. and Nicholson, R. B., 1968, *Phil. Mag.*, **17**, 801.
- B.27 Weatherly, G. C., PhD thesis, University of Cambridge, 1966.
- B.28 Schueller, R. D., Wawner, F. E. and Sachdev, A. K., 1994, *J. Mater. Sci.*, **29**, 424.
- B.29 Li, Qiong and Wawner, F. E., 1997, *J. Mater. Sci.*, **32**, 5363.
- B.30 Schueller, R. D., Sachdev, A. K. and Wawner, F. E., 1992, *Scripta Metall. Mater.*, **27**, 617.
- B.31 Auld, J. H., Vietz, J. T. and Polmear I. J., 1966, *Nature*, **209**, 703.
- B.32 Vietz, J. T. and Polmear, I. J., 1966, *J. Inst. Metals*, **94**, 410.
- B.33 Murayama, M. and Hono, K., 1998, *Scripta mater.*, **38**, 1315.
- B.34 Hutchinson, C. R., Fan, X., Pennycook, S. J. and Shiflet, G. J., 2000, *Mat. Sci. Forum*, **331-337**, 965.
- B.35 Kerry, S. and Scott, V. D., 1984, *Metal Sci.*, **18**, 289.
- B.36 Auld, J. H., 1986, *Mater. Sci. Tech.*, **2**, 784.
- B.37 Knowles, K. M. and Stobbs, W. M., 1988, *Acta cryst.*, **B44**, 207.
- B.38 Muddle, B. C. and Polmear, I. J., 1989, *Acta metall.*, **37**, 777.
- B.39 Garg, A. and Howe, J. M., 1991, *Acta metall.*, **39**, 1939.
- B.40 Benson, W. E. and Howe, J. M., 1997, *Phil. Mag. A*, **75**, 1641.
- B.41 Thomas, G., 1961-62, *J. Inst. Metals*, **90**, 57.
- B.42 Pashley, D. W., Jacobs, M. H. and Vietz J. T., 1967, *Phil. Mag. A*, **51**.
- B.43 Geisler, A. H. and Hill, J. K., 1948, *Acta cryst.*, **1**, 283.
- B.44 Guinier, A. and Lambot, H., 1950, *Rev. metall.*, **47**, 709.
- B.45 Lutts, A., 1961, *Acta metall.*, **9**, 577.
- B.46 Edwards, G. A., Stiller, K. and Dunlop, G. L., 1994, *Appl. Surf. Sci.*, **76/77**, 219.
- B.47 Ringer, S. P., Swenser, S. P., Muddle, B. C., Polmear, I. J. and Sakurai, T., 1996, *Mater. Sci. Forum*, **217-222**, 689.
- B.48 Murayama, M. and Hono, K., 1999, *Acta mater.*, **47**, 1537.
- B.49 Edwards, G. A., Stiller, K., Dunlop, G. L. and Couper, M. J., 1998, *Acta Mater.*, **46**, 3893.
- B.50 Shchegoleva, T., 1968, *Phys. Met. and Metallogr*, **25**, 56.
- B.51 Wahi, R. P. and von Heimendahl, M., 1974, *phys. stat. sol. a*, **24**, 607.

- B.52 Lynch, J. P., Brown, L. M. and Jacobs, M. H., 1982, *Acta metall.*, **30**, 1389.
- B.53 Edwards, G. A., Dunop, G. L. and Couper, M. J., 1994, *Proceedings of the 4th International Conference on Aluminium Alloys ICAA4*, ed. T. H. Sanders and E. A. Starke. Georgia Institute of Technology, Atlanta, GA, 1994, **1**, p. 620.
- B.54 Murayama, N., Uemori, R., Hashimoto, N., Saga, M. and Kikuchi, M., 1997, *Scripta mater.*, **36**, 89.
- B.55 Naoi, T., Matsuda, K., Sato, T., Kamio, A. and Ikeno, S., 1998, *Proceedings of the 6th International Conference on Aluminium Alloys ICAA6*, edited by T. Sato and S. Kumai, (Toyohashi: The Japan Institute of Light Metals), **2**, p. 861.
- B.56 Andersen, S. J., Zandbergen, H. W., Jansen, J., Tr holt, C., Tundal, U. and Reiso, O., 1998, *Acta Mater.*, **46**, 3283.
- B.57 Jacobs, M. H., 1972, *Phil. Mag.*, **26**, 1.
- B.58 Matsuda, K., Tada, S. and Ikeno, S., 1993, *J. Electron Microsc.*, **42**, 1.
- B.59 Matsuda, K., Ikeno, S., and Tada, S., 1993, *J. Japan Inst. Metals*, **57**, 1107.
- B.60 Matsuda, K., Uetani, Y., Anada, H., Tada, S. and Ikeno, S., 1992, *Proceedings of the 3rd International Conference on Aluminium Alloys*, edited by L. Arnberg, O. Lohne, E. Nes and N. Ryum, **1**, 272.
- B.61 Matsuda, K., Sakaguchi, Y., Miyata, Y., Uetani, Y., Sato, T., Kamio, A. and Ikeno, S., 2000, *J. Mater. Sci.*, **35**, 179.
- B.62 Lodgaard, S. and Ryum, N., 2000, *Mater. Sci. Engng*, **A283**, 144.
- B.63 Matsuda, K., Tada, S., Ikeno, S., Sato, T., and Kamio, A., 1995, *Scr. Metall. Mater.*, **32**, 1175.
- B.64 Matsuda, K., Ikeno, S., Sato, T., and Kamio, A., *Mater. Sci. Forum*, 1996, **217-222**, 707.
- B.65 Sagalowicz, L., Hug, G., Bechet, D., Saintfort, P. and Lapasset, G., 1994, *Proceedings of the 4th International Conference on Aluminium Alloys ICAA4*, ed. T. H. Sanders and E. A. Starke. Georgia Institute of Technology, Atlanta, GA, **1**, p. 636.
- B.66 Sagalowicz, L., Lapasset, G., and Hug, G., 1996, *Phil. Mag. Letters*, **74**, 57.
- B.67 Dumolt, S. D., Laughlin, D. E., and Williams, J. C., 1984, *Scr. Metall.*, **18**, 1347.
- B.68 Sakurai, T., and Eto, K., 1992, in *Proceedings of the 3rd International Conference on Aluminium Alloys ICCA3*, ed. by L. Arnberg, O. Lohne, E. Nes and N. Ryum, **1**, p. 208.
- B.69 Tamizifar, M., and Lorimer, G. W., 1992, in *Proceedings of the 3rd International Conference on Aluminium Alloys ICCA3*, ed. by L. Arnberg, O. Lohne, E. Nes and N. Ryum, **1**, p. 220.
- B.70 Miao, W. F. and Laughlin, D. E., 2000, *Met. Mater. Trans. A.*, **31A**, 361.
- B.71 Dubost, B., Bouvaist, J. and Reboul, M., 1986, *Proceedings of the 1st International Conference on Aluminium Alloys*, ed. by E. A. Starke and T. H. Sanders. p. 1109.
- B.72 Phragm n, G. J., 1950, *J. Inst. Met.*, **77**, 521.
- B.73 Arnberg, L. and Aurivillius, B., 1980, *Acta. Chem. Scand.*, **A 34**, 1.
- B.74 Cayron, C. and Buffat, P. A., 2000, *Acta mater.*, **48**, 2639.
- B.75 Cayron, C., Sagalowicz, L., Beffort, O. and Buffat, P. A., 1999, *Phil. Mag. A*, **79**, 2833.

Annex C

Simulation of Electron Diffraction Patterns of Orientated Precipitates

C.1 Notions of Crystallography

C.1.1 Punctual Groups

Crystallography is based on the translational order of the crystals. A crystal can be considered as a *cell* translated periodically in 3 directions along a *lattice*. The only symmetries coherent with the lattice are the rotational axes of order $p = 1, 2, 3, 4, 6$ and $\overline{1}, \overline{2}, \overline{3}, \overline{4}, \overline{6}$ (the overline designs a composition of a rotation with a central symmetry) and can be combined to form the 32 *punctual groups*. They correspond to *orientation symmetries* (symmetries of the crystal faces).

The 11 *Laue classes* are the centrosymmetric punctual groups. They are the only punctual groups obtainable from the ZOLZ patterns in kinematical conditions because of the Friedel's law.

The 7 *crystal systems* are the Laue classes that in addition to be centrosymmetric are in total compatibility with the lattice symmetries.

The 14 *Bravais modes* are built from the 7 crystal systems by considering larger multiple cells based on the initial lattice but with higher symmetries. It is shown that only centered lattices (I) or face centered lattices (F) are possible. For details, see for instance [C.1]

C.1.2 Space Groups

The punctual groups contain only orientation information of the crystal lattice (vectorial symmetries). Based on these 32 punctual groups, we can consider the symmetries of the patterns which are compatible with punctual group (allowing translations by a vector smaller than the 3 lattice vectors). It is shown that only certain helicoidal axes based on the p -rotational axes and glide planes based on half the base vectors of the lattice are possible. Their combination form the 230 *space groups*. They correspond to *positional symmetries*.

C.1.3 Reciprocals Spaces and Associated Matrices

Let us choose for a *direct space* a base ($\mathbf{a}, \mathbf{b}, \mathbf{c}$). Its *reciprocal space* has a base ($\mathbf{a}^*, \mathbf{b}^*$,

\mathbf{c}^*) so that $\mathbf{a}^* \cdot \mathbf{a} = \mathbf{b}^* \cdot \mathbf{b} = \mathbf{c}^* \cdot \mathbf{c} = 1$ and $\mathbf{a}^* \cdot \mathbf{b} = \mathbf{a}^* \cdot \mathbf{c} = \dots = 0$. The main property of the reciprocal lattice is that if $\mathbf{n} = [u, v, w]$ is a vector in the direct space and $\mathbf{n}^* = [h, k, l]$ a vector in the reciprocal space, the scalar product is $\mathbf{n} \cdot \mathbf{n}^* = hu + vk + lw$.

The *metric tensor* \mathbf{G} is the transformation matrix $(\mathbf{a}, \mathbf{b}, \mathbf{c}) \rightarrow (\mathbf{a}^*, \mathbf{b}^*, \mathbf{c}^*)$:

$$G = \begin{bmatrix} a^2 & abc \cos \gamma & acc \cos \beta \\ abc \cos \gamma & b^2 & bcc \cos \alpha \\ acc \cos \beta & bcc \cos \alpha & c^2 \end{bmatrix} \text{ useful for the scalar product: } n_1 \cdot n_2 = [u_1, v_1, w_1] G \begin{bmatrix} u_2 \\ v_2 \\ w_2 \end{bmatrix}.$$

The *structure matrix* \mathbf{S} is a transformation matrix from the $(\mathbf{a}, \mathbf{b}, \mathbf{c})$ base to an orthonormal base. The exact way to built it is described for example in [C.2]. This matrix ia useful to link two crystals of different structures with an OR between them.

C.1 Simulation Program

During our work, many SAED patterns were acquired in many different matrix zone axes to identify unknown precipitates with many different structures. Some of the SAED correspond to the diffraction of the matrix and several different precipitates. Their understanding is complicated by the high number of possible precipitates such as θ' , Si, S' , Ω . At the beginning of the work, for one matrix zone axis, all the possible diffracting precipitates with their equivalent zone axis had to be calculated. Soon, we have decided to write a program to simulate the diffraction pattern of both the matrix and the precipitate in OR with it. Firstly, we wrote a program in Mathematica[□] for a cubic matrix and for only one variant. In collaboration with P. H. Jouneau, we have generalized the program to any matrix structure with the generation of all the equivalent variants of a precipitate in OR with the matrix. P.H. Jouneau completely rewrote the program in Python[□] language. The program is available on request [C.3]. The algorithm we used is similar to that used an independent work of Akbay [C.4]. The number of variants of a precipitate phase depends not only on the OR itself but also on the crystal symmetries of the matrix and precipitate phases. The number of variants increases with higher symmetry of the matrix and with reduced symmetry of the precipitate crystal structures. It also decreases with an OR along high symmetry axes. Let us succinctly explain how the program works.

(1) The matrix and precipitates crystallographic structures are built with the *bul* routine of EMS, a general program of electron microscopy simulation [C.5].

(2) The matrix zone axis \mathbf{Z}_{mat} and the OR are entered in the program. The OR can be specified in the form of parallel directions $\mathbf{U}_p // \mathbf{U}_m, \mathbf{V}_p // \mathbf{V}_m$, or parallel planes (Fig. C.1).

(3) The structure files generated by *bul* are read to extract the metric tensors \mathbf{G}_{mat} and \mathbf{G}_{prec} , the structure matrices \mathbf{S}_{mat} and \mathbf{S}_{prec} and the symmetry classes (punctual group) which have the form of a list of matrices $\{\mathbf{T}_{\text{mat}}\}$ and $\{\mathbf{T}_{\text{prec}}\}$, for the matrix and precipitates phases.

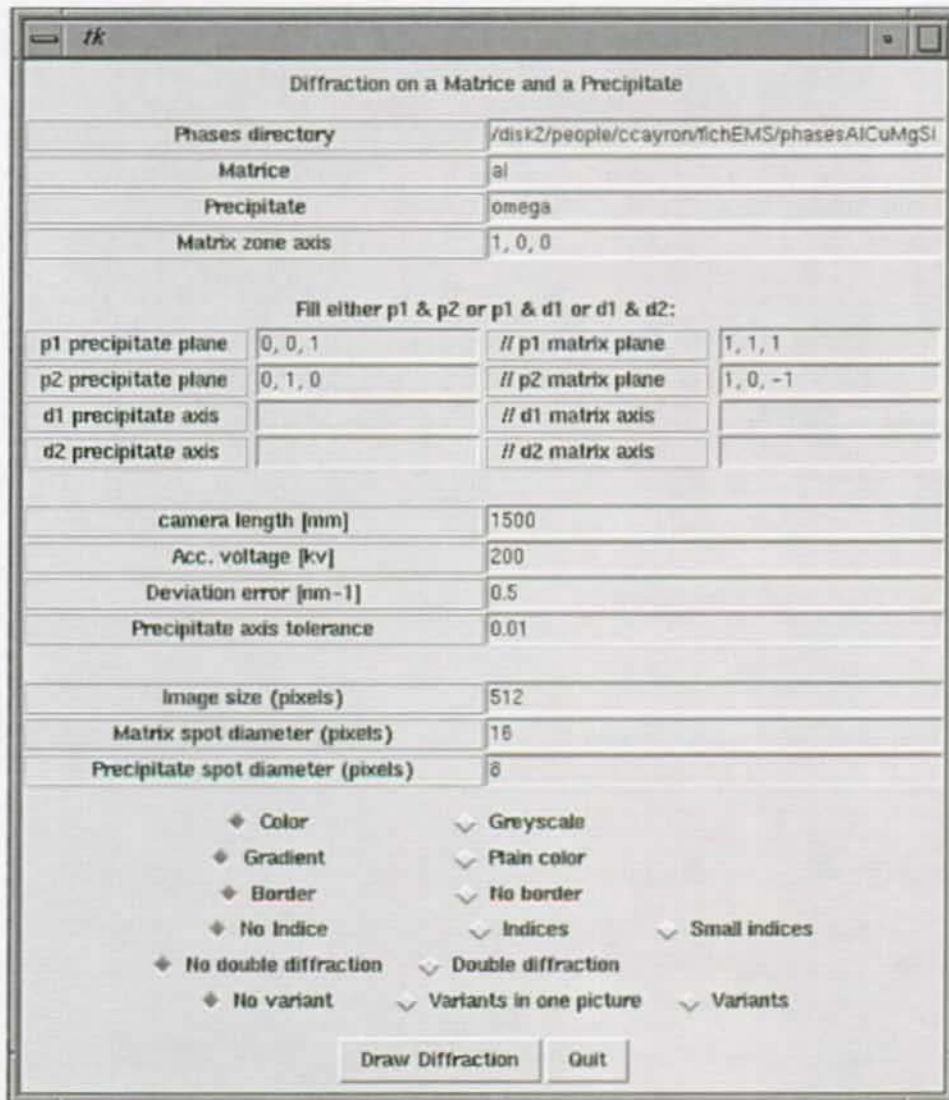


Fig. C.1 Main window of the program of electron diffraction simulation of orientated precipitates in OR with the matrix.

(4) Direct bases are built for the matrix and the precipitate phases by $(\mathbf{U}, \mathbf{V}, \mathbf{S}^{-1}(\mathbf{S} \cdot \mathbf{U} \otimes \mathbf{S} \cdot \mathbf{V}))$. We will name them \mathbf{M} and \mathbf{P} for matrix and precipitates respectively.

(5) The transformation matrix from the matrix to the precipitate is calculated $\mathbf{Pass} = \mathbf{M} \cdot \mathbf{P}^{-1}$.

(6) The zone axis of the matrix is calculated in the precipitate base by $\mathbf{Z}_{\text{prec}} = \mathbf{Pass}^{-1} \cdot \mathbf{Z}_{\text{mat}}$. The axis in real numbers form (r_1, r_2, r_3) is transformed in integer numbers form (i_1, i_2, i_3) .

(7) This operation is repeated for all the zones axes equivalent by the matrix symmetries $\{\mathbf{Z}_{\text{prec}}\} = \mathbf{Pass}^{-1} \cdot \{\mathbf{T}_{\text{mat}}\} \cdot \mathbf{Z}_{\text{mat}}$

(8) The list $\{\mathbf{Z}_{\text{prec}}\}$ is reduced by the precipitate symmetries: \mathbf{Z}_{prec} is excluded of the list $\{\mathbf{Z}_{\text{prec}}\}$ if $\exists \mathbf{Z}_{\text{prec}}^0 \in \{\mathbf{Z}_{\text{prec}}\}, \mathbf{Z}_{\text{prec}} / \mathbf{Z}_{\text{prec}}^0 \in \{\mathbf{T}_{\text{prec}}\} \cdot \mathbf{Z}_{\text{prec}}^0$.

(9) For \mathbf{Z}_{mat} and all the $\{\mathbf{Z}_{\text{prec}}\}$, the diffraction files are generated by the *di5* routine of EMS [C.5] with the acceleration voltage, deviation error, and camera length parameters. They are

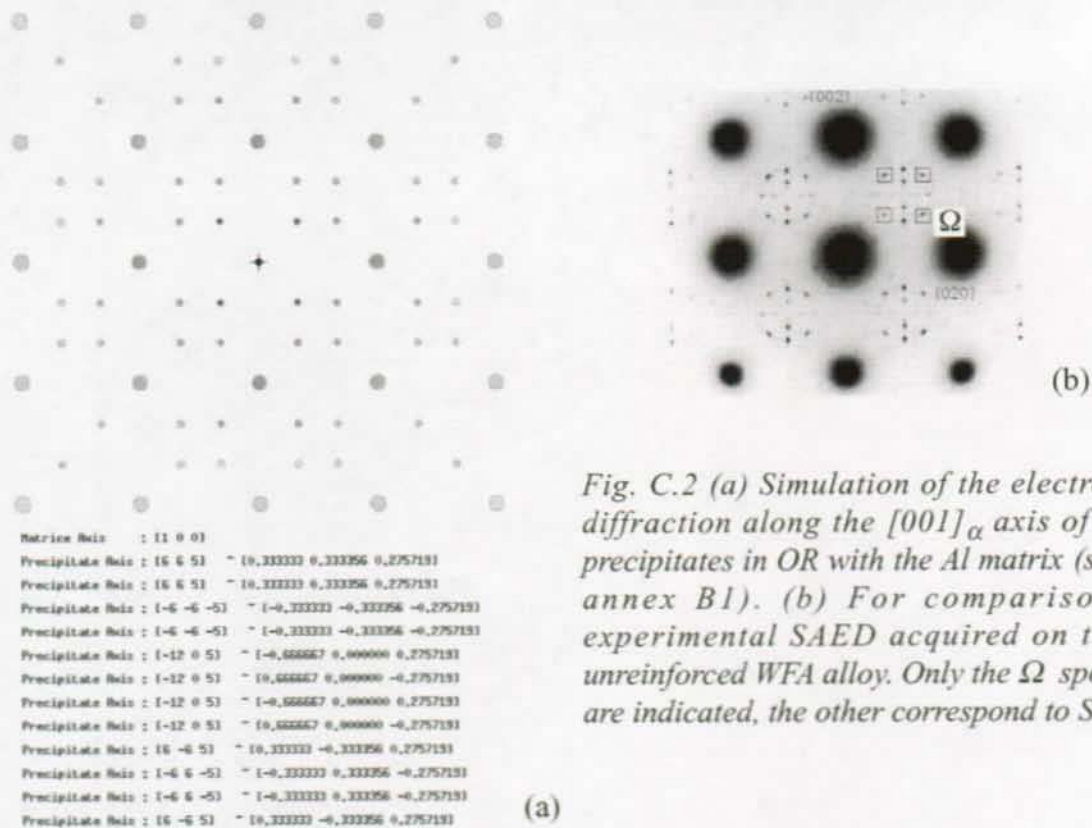


Fig. C.2 (a) Simulation of the electron diffraction along the $[001]_{\alpha}$ axis of Ω precipitates in OR with the Al matrix (see annex B1). (b) For comparison, experimental SAED acquired on the unreinforced WFA alloy. Only the Ω spots are indicated, the other correspond to S' .

read as a list of positions $\{\mathbf{g}\}$ and intensities of the spots.

(10) For the matrix and each of the precipitate variant diffraction files, one \mathbf{g} is extracted and the angle of rotation α between the matrix diffraction pattern and the precipitate diffraction pattern is calculated by $\alpha = (\mathbf{G}_{\text{mat}}^{-1} \cdot \mathbf{g}_{\text{mat}}, \mathbf{Pass.} (\mathbf{G}_{\text{prec}}^{-1} \cdot \mathbf{g}_{\text{prec}}))$.

(11) The diffraction patterns of the matrix and precipitate variants are drawn, possibly with double diffraction generated by a translation of the $\{\mathbf{g}\}_{\text{prec}}$ pattern by the most intense spots of the matrix $\mathbf{g}_{\text{mat}} \in \{\mathbf{g}\}_{\text{mat}}$ and by multiplying the intensities.

We have extensively used this program during our work (Fig. 6.17). We also report in Fig. C.2 an example where the identification of the precipitate spots was not obvious.

C.1 References

- C.1 Giacobozzo, C., Monaco, H. L., Viterbo, D., Scordari, F., Gilli, G., Zanotti, M. and Catti, M., (1992), *Fundamentals of Crystallography*, edited by C. Giacobozzo, Oxford University Press.
- C.2 Bollmann, W. (1982) *Crystal lattices, Interfaces, Matrices*, published by the author.
- C.3 Please contact us: jouneau@gemppm.insa-lyon.fr or cyril.cayron@epfl.ch
- C.4 Akbay, T., Aydinol, K and Bor, A. S., 1994, *J. Appl. Cryst.*, **27**, 379.
- C.5 Stadelmann, P., 1987, *Ultramicroscopy*, **21**, 131.

Remerciements

En tout premier lieu je tiens à remercier Prof. Philippe-André Buffat pour m'avoir offert la possibilité d'effectuer cette recherche au CIME, mais aussi pour sa gentillesse, son ouverture d'esprit ainsi que ses conseils avisés. Je remercie aussi chaleureusement le Dr. Olivier Beffort pour m'avoir ouvert les portes de l'EMPA-Thun et m'avoir fait découvrir le monde des composites à matrices métalliques. Son bon-sens et ses conseils judicieux m'ont plus d'une fois été d'un grand recours. Encore mille remerciements Olivier et Philippe, pour les relations de confiance que nous avons eues durant ces quatre années de thèse qui ont constitué un facteur de motivation très important pour ce travail.

Je remercie bien sûr le Prof. Pierre Stadelmann pour sa disponibilité que ce soit pour des problèmes théoriques, expérimentaux ou informatiques. Aucun programme développé durant ce travail n'aurait pu se faire sans son aide avisée. Mes remerciements vont aussi au Dr. Laurent Sagalowicz pour m'avoir fait connaître les alliages d'aluminium et pour toutes les discussions et idées que nous avons partagées sur le sujet. Je ne saurai oublier de remercier le Dr. Pierre-Henri Jouneau pour son aide tant aussi bien théorique qu'informatique qui a été indispensable à l'écriture d'un programme de simulation de diffraction de précipités. Toute ma reconnaissance va à mes collègues de travail, le Dr. Alain Sfera, pour le temps qu'il a passé sur le manuscrit de thèse, pour son œil implacable à y détecter les inexactitudes scientifiques, mais aussi pour la bonne humeur qu'il répand naturellement autour de lui, le Dr. Michael Foeth pour le temps qu'il a passé sur l'anglais de mes écrits, sans oublier le Dr. Klaus Leifer, le Dr. Marco Cantoni et les petits nouveaux, Mlle Silviya Gradecak, M. Ollivier Pujol et M. Joël Cagnon. Un merci spécial à l'EPFL qui a organisé des cours de 3ème cycles libres d'accès et intéressants!

Rien n'aurait été possible sans les conseils de Mlle Danièle Laub et Mlle Fabienne Bobard quant à la préparation des lames minces TEM, et sans l'aide d'étudiants de l'EPFL, M. Stéphane Bonjour, M. Arnaud Merglen, M. Vincent Bouchard et M. Alexandre Soguel. Je tiens bien sûr à remercier la disponibilité et l'appui technique de M. Gaston Peter, M. Bernard Garoni et maintenant M. Guido Milanesi, tous indispensables au fonctionnement des microscopes. Merci aussi au Dr. François Pashoud et M. Brian Senior qui m'ont formé respectivement aux microscopes à transmission et à balayage. Je remercie toutes les personnes de l'EMPA qui ont élaboré les composites de cette étude et mis tous leurs efforts pour tenter de produire la phase Q si chère à mon cœur, je veux citer entre autres le Dr. Christian Hausmann et le Dr. Siyuan Long. Je remercie aussi chaleureusement Mme Ruth Rouquier et Mme. Esther Gacoïn pour leur aide dans toutes mes démarches administratives.

Enfin, j'aimerais aussi témoigner toute ma reconnaissance à mes parents, à ma soeur MéliSSa et à mon épouse Samantha, pour leur affection, leur soutien, et leur compréhension lors de ces quatre années de dur labeur.

Remerciements

Curriculum Vitae

Cyril CAYRON

* Av. d'Yverdon 5	* 1, rue principale
1004 Lausanne (Suisse)	21110 Tart-Le-Haut (France)
' bureau 00.41.21.693.48.30	' domicile 00.33.3.80.31.58.94
' domicile 00.41.21.624.19.69	

Email cyril.cayron@epfl.ch

né le 05/09/1972
marié, sans enfant
nationalité française

INGENIEUR CIVIL DES MINES

Diplômé de l'Ecole Nationale Supérieure des Mines de Nancy

DEA Science et Génie des Matériaux

FORMATION

- 1996-2000 Thèse à l'Ecole Polytechnique Fédérale de Lausanne EPFL, au Centre Interdépartemental de Microscopie Electronique CIME, en collaboration avec le Laboratoire Fédéral d'Essai des Matériaux et de Recherche EMPA (Suisse)
- 1994-1995 Diplôme d'Etudes Approfondies DEA (classé 1er, mention Bien) en Science et Génie des Matériaux à la faculté de Nancy (54).
- 1992-1995 Formation d'ingénieur généraliste à l'Ecole Nationale Supérieure des Mines de Nancy EMN.
- 1990-1992 Classes préparatoires aux Grandes Ecoles (math sup, math spé M') au lycée Carnot à Dijon (21) : mathématiques et physique.
- 1990 Baccalauréat C (scientifique), mention Très Bien.

EXPERIENCE PROFESSIONNELLE

- 1999-2000 Participation au projet européen sur les composites à matrices métalliques MMC-ASSESS (<http://mmc-assess.tuwien.ac.at/>)
- 1996-20005 Formation des utilisateurs du microscope électronique à transmission CM20.
- 1995-1996 Service National Scientifique (12 mois) à la Compagnie Générale d'Innovation et de Développement COGIDEV à Rueil-Malmaison (92) : « Développement d'un procédé de fabrication d'écrans plats matriciels électrochromes ».
- 1995 Stage de fin d'études (6 mois) à la Société Nationale d'Etudes et de Construction de Moteurs d'Avions SNECMA à Corbeil (91) : « Etude de l'influence des carbures primaires sur la tenue en fatigue du superalliage INCONEL 718 grains fins en vue d'un dimensionnement des aubes de turbine ».

Curriculum Vitae

Scientific Publications

ARTICLES

Cayron, C., Buffat, P.-A., Beffort, O., and Long, S. (1999). "SiO₂ binder effect on the precipitation state of an AlCu4MgAg/Al₂O₃ composite". *J. Mater. Sci.*, **34**, 905-915.

Cayron, C., Sagalowicz, L., Beffort, O., and Buffat, P.-A. (1999). "Structural phase transition in Al-Cu-Mg-Si alloys by a TEM study of the precipitation state of the AlCuMgAg alloy reinforced by SiC particles". *Phil. Mag. A.*, **79**, 2833-2851.

Cayron, C., Hausmann, C., Buffat, P.-A., and Beffort, O. (1999). "About the epitaxial growth of Mg-subgrains on Al₂MgC₂ interfacial carbides in a squeeze cast Mg4Al/T300 metal matrix composite". *J. Mater. Sci. Letters*, **18**, 1671-1674.

Long, S., Beffort, O., Cayron, C. and Bonjour, C. (1999). "Microstructure and mechanical properties of a high volume fraction SiC particles reinforced AlCu4MgAg squeeze casting". *Mater. Sci. Engng.*, **A269**, 175-185.

Cayron, C., and Buffat, P.-A. (2000). "Structural Phase Transition in Al-Cu-Mg-Si and Al-Mg-Si Alloys: Ordering Mechanisms and Crystallographic Structures". *Mater. Sci. Forum*, **331-337**, 1001-1006.

Cayron, C., and Buffat, P.-A. (2000). "TEM study of the β' phase (Al-Mg-Si alloys) and QC phase (Al-Cu- Mg-Si alloys): Ordering mechanism and crystallographic structures". *Acta Mater.*, **48**, 2639.

CONFERENCES

Cayron, C., Buffat, P.-A., Beffort, O., and Long, S. (1997). "Effect of the fibre binder chemistry on the microstructure of Saffil/AlCu4MgAg composite". *IPCM 97, Interfacial Phenomena in Composite Materials*, Hungary, 14-16 Septembre.

Long, S., Cayron, C., Kübler, J. and Beffort, O., (1998). "Structure and properties of SiC-AlCuMgAg composites for structural applications" *CIMETEC 98, 9th Int. Conf. on Modern Materials and Technology*, Italy.

Moser, B., Cayron, C., Hausamann, C. and Beffort, O., (1998). "A comparative study on the mechanical failure mechanisms of unidirectional continuous fibre reinforced light metals". *CIMETEC 98, 9th Int. Conf. on Modern Materials and Technology*, Italy.

Cayron, C., Buffat, P. A., Hausamann, C. and Beffort, O., (1998). "Etude par microscopie électronique de la réaction d'interface dans un composite MgAg4/C" *Trinoculaire des microscopies, Société française des Microscopies, Strasbourg, France, 29 Juin-3 Juillet*.

Cayron, C., Buffat, P. A., Beffort, O. and Long. S., (1998). "Caractérisation par microscopie électronique de l'état de précipitation d'un composite AlCuMgAg/Al₂O₃" *Trinoculaire des microscopies, Société française des Microscopies*, Strasbourg, France, 29 Juin-3 Juillet.

Cayron, C., Buffat, P. A., Beffort, O. and Long. S., (1998). "TEM study of the precipitation state of a squeeze-cast AlCuMgAg/SiC composite" *ICEM-14, Int. Conf. on Electron Microscopy*, Cancun, Mexico, August 31-September 4, Symp. Z, vol. II, p. 709.

Cayron, C. and Buffat. P. A., (2000). "Order and Disorder in the AlMgSi(cu) Alloys", *Forum on Advanced Materials*, Rehovot, Israël, February 20-22.

Cayron, C., (2000). "Investigation of Al and Mg MMCs by transmission electron microscopy", *19 èmes Journées des Matériaux*, EPFL-Lausanne, Suisse, 29 Février -1 Mars.

Cayron, C., and Buffat, P.-A. (2000). "Structural Phase Transition in Al-Cu-Mg-Si and Al-Mg-Si Alloys: Ordering Mechanisms and Crystallographic Structures". *ICAA7, 7th Int. Conf. on Aluminium Alloys*, Charlottesville, Virginia, USA, April 9-14.